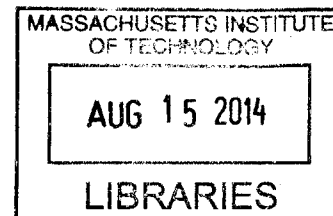


**The Linear and Nonlinear Rheology of Multiscale
Complex Fluids**

ARCHIVES

by

Aditya Jaishankar



B.Tech., Indian Institute of Technology Madras (2009)
S.M., Massachusetts Institute of Technology (2011)

Submitted to the Department of Mechanical Engineering
in partial fulfillment of the requirements for the degree of

Doctor of Philosophy in Mechanical Engineering

at the

MASSACHUSETTS INSTITUTE OF TECHNOLOGY

June 2014

©Massachusetts Institute of Technology 2014. All rights reserved.


Signature redacted

Author

Department of Mechanical Engineering
May 27, 2014

Signature redacted

Certified by


Gareth H. McKinley
Professor, Mechanical Engineering
Thesis Supervisor

Signature redacted

Accepted by

David E. Hardt
Graduate Officer, Department Committee on Graduate Students

The Linear and Nonlinear Rheology of Multiscale Complex Fluids

by
Aditya Jaishankar

Submitted to the Department of Mechanical Engineering
on May 27, 2014, in partial fulfillment of the
requirements for the degree of
Doctor of Philosophy in Mechanical Engineering

Abstract

The microstructures of many complex fluids are typically characterized by a broad distribution of internal length scales. Examples of such multiscale materials include physically and chemically cross-linked gels, emulsions, soft colloidal glasses and concentrated suspensions. Due to the complex microstructure, these materials exhibit multiscale power law relaxation under externally imposed deformation. Compact constitutive frameworks that can accurately describe and predict both the linear as well as the nonlinear rheology of such complex fluids have remained elusive. Moreover, the rheological behavior of these materials under extensional deformations, which is important in applications such as spraying and fiber spinning, is relatively poorly understood.

The primary contribution of this thesis is the development of a compact constitutive modeling framework to quantitatively describe the rheology of multiscale complex fluids. In the linear limit of small deformations, fractional constitutive equations in conjunction with the concept of quasi-properties have been shown to provide accurate physical descriptions of the broad power law relaxation dynamics exhibited by multiscale materials. In this thesis we very generally show how fractional constitutive equations enable the prediction of the rheological response of multiscale fluids under complex deformation profiles. As a specific example, we analyze the damped inertio-elastic oscillations exhibited at early times by viscoelastic interfacial layers upon the imposition of a constant stress, and the subsequent long time power law creep. We also analyze the small strain lubrication flow regime of a typical tack experiment performed on a crosslinked power law gel, where the extensional deformation of the complex material plays an important role.

We extend these models to the large strain nonlinear regime using an integral K-BKZ framework coupled with a strain damping function. We demonstrate in a general manner that nonlinear rheological responses such as shear-thinning and positive first normal stress coefficients can be predicted a priori from linear viscoelastic data and a single additional nonlinear parameter introduced through the damping function. We also demonstrate that well-known empirical rheological models utilized to describe nonlinear behavior such as the Herschel-Bulkley, Cross and Carreau models can be derived using the K-BKZ framework by selecting a suitable fractional relaxation kernel and an appropriate damping func-

tion. Additionally, we derive expressions for linear viscometric functions as well as the first normal stress coefficient for materials that exhibit steady shear flow behavior predicted by the above empirical models. Our approach also quantifies the applicability of widely known empirical rheological rules for nonlinear rheology such as the Cox-Merz rule.

The second contribution of this thesis is in increasing the understanding of the rheological behavior of multiscale complex fluids in extensional flow fields. For this purpose we utilize a variety of experimental extensional rheology techniques such as Capillary Breakup Extensional Rheometry (CaBER), Filament Stretching Extensional Rheometry (FiSER) and an Optimized Shape Cross-slot Extensional Rheometer (OSCER). Due to their ubiquity in industrial applications as well as in biologically relevant complex fluids, we primarily study aqueous polysaccharide systems (for example Mamaku gum). With the help of these detailed experiments, we investigate and quantify the strength of hydrogen-bonding interactions in this multiscale physically associated gel. We also investigate the extensional rheology of Hyaluronic acid, which has been shown to be an important factor in proper synovial fluid function.

The findings of this thesis are widely applicable given the widespread use of multiscale complex fluids in industrial, and biological applications. The fractional constitutive framework derived here overcomes the limitations of current modeling approaches that invoke a large number of empirical constitutive parameters. Our simple models will be useful for quantitative material diagnostics and quality control comparisons as well as for computational simulations. Moreover, the experimental findings on the extensional rheology of multiscale polysaccharide systems will help in the formulation of biologically relevant complex fluids for the treatment of physiological conditions such as osteoarthritis and dysphagia.

Thesis Supervisor: Gareth H. McKinley
Title: Professor, Mechanical Engineering

Acknowledgments

This thesis could not have been completed without the guidance and friendship I have received over the last five years from numerous people, some of whom I mention below. These words of acknowledgment only bring out a small fraction of the heartfelt gratitude I feel for them.

Firstly, I would like to thank my advisor Gareth McKinley, who has left an indelible mark on me, both personally and professionally. This thesis has benefited greatly by his depth of knowledge, in the areas of, amongst many others, complex fluids and rheology. His excitement about research and all things scientific is truly infectious, and was a big source of motivation. In addition to his invaluable research guidance, his good sense of humor and razor-sharp wit were always available around the corner to help see me through those inevitable days when research progress seemed slow. I feel privileged to have had the opportunity to learn from him not only about the science of my thesis area, but also about the *art* of scientific research itself. Perhaps Liberty Hyde Bailey, the great American botanist, had a teacher such as Gareth in mind when he said ‘A good teacher is better than all the laboratories and apparatus’. I am also thankful to Professors Roger Kamm, Krystyn Van Vliet and Konstantin Turitsyn for serving on my thesis committee and taking a keen interest in my work.

The Non-Newtonian Fluids group has been a very satisfying and enjoyable environment in which to work. I would like to acknowledge Johannes Soulages for helping me perform my first ever rheology experiment and for teaching me about the various tricks rheometers can play. I thank May Wee and Professors Goh and Matia-Merino of Massey University for introducing me to Mamaku gum, and being great research collaborators. My colleagues and friends at the NNF — Alex, Caroline, Divya, Michela and Setareh have contributed much to the high level of camaraderie in the lab. Special thanks go out to Bavand Keshavarz, Chris Dimitriou and Laura Casanellas; the many evenings spent discussing everything and nothing at the Miracle of Science provided the perfect way to end a day’s work. I have many fond memories of discussing British comedy over beer with Simon Haward. In addition to being a helpful and dependable friend, he is also an excellent experimentalist and a source of research inspiration. Some of the birefringence experiments I performed with his help have been amongst the most enjoyable times in the lab. Thanks are also due to Marc Fardin for his friendship over the years. As a scientist, I hold him in very high regard; but he is equally capable in many other spheres of creativity. Be it critiquing Impressionist and Renaissance art, or identifying wild flora from memory while hiking in New Hampshire’s White Mountains, much thanks are due to him for giving me a wider sense of perspective about science, research and other human endeavors.

The coffee breaks with Radhika Marathe were an ideal diversion when research ideas were reluctant to present themselves. I am grateful for the continuing friendship of my undergraduate friends Vikas, Chirranjeevi, Nirmal and Sudharshan. Thanks also to Steve Sando for being a wonderful room-mate over the last few years. Finally, I would like to

express my deepest gratitude to my parents and sister. I owe everything to them, and no words are sufficient to describe the importance of their unbounded love and support, not just through my PhD, but throughout my life.

This thesis is dedicated to my parents and my sister.

Contents

1	Introduction	39
1.1	Multiscale Systems in Nature	39
1.2	Complex Fluids and their Rheology	41
1.3	Multiscale Complex Fluids	44
1.4	Aims of This Thesis	55
2	Mathematical Background	59
2.1	Linear Viscoelasticity	59
2.1.1	The Linear Viscoelastic Maxwell Model	59
2.2	Fractional Derivatives and the Springpot	64
2.3	The Canonical Fractional Models: FMM and FKVM	73
2.3.1	The Fractional Maxwell Model (FMM)	73
2.3.2	The Fractional Kelvin Voigt Model (FKVM)	79
2.4	A Case Study: Capillary Suspensions	80
3	Linear Shear Deformations	85
3.1	Introduction	85
3.2	Techniques and Materials	88
3.2.1	Interfacial Rheology	88

3.3	Results	92
3.3.1	Stress Relaxation and Creep without Inertia	92
3.3.2	Interfacial Dynamics	95
3.3.3	The FMM in Small Amplitude Oscillatory Shear (SAOS) Deformations	97
3.3.4	Creep Ringing and Power-Law Responses	101
3.4	Conclusions	107
4	Nonlinear Shear Deformations	109
4.1	Introduction	110
4.2	Materials and Methods	114
4.3	Results and Discussion	115
4.3.1	Linear Viscoelasticity	115
4.3.2	Nonlinear Viscoelasticity and the K-BKZ Model	118
4.3.3	Empirical Relationships for Nonlinear Viscoelasticity	128
4.3.4	The Delaware-Rutgers Rule for Power-Law Materials	134
4.3.5	Fractional Zener Model (FZM) and Carreau-Type Flow Curves	141
4.4	Conclusions	146
5	Small Strain Extensional Deformations:	
	Tacky Polymer Gels	149
5.1	Introduction	150
5.2	The Fractional Kelvin-Voigt Model	151
5.2.1	SAOS Fitting and Parameter Determination	151
5.2.2	Determination of the Normal Force for a Probe Tack Test: Constant Velocity Applied Deformation	153

5.2.3	Determination of the normal force for a constant strain rate applied deformation	170
5.3	The Fractional Maxwell Model	176
5.3.1	Determination of the normal force for a constant strain rate applied deformation	176
5.3.2	Determination of the normal force for a constant velocity applied deformation	185
5.3.3	Experimental verification of analytical results	187
5.4	Conclusions	193
6	Large Strain Extensional Deformations:	
	Polysaccharide Systems	195
6.1	Mamaku Gum	195
6.1.1	Introduction	196
6.1.2	Experimental	200
6.1.3	Results and Discussion	202
6.1.4	Filament Stretching Extensional Rheometry	219
6.1.5	Conclusions	223
6.2	Hyaluronic Acid	224
6.2.1	Introduction	225
6.2.2	Modeling the Squeeze flow of HA in Joints	230
6.2.3	Test Fluids and their Rheological Characterization	239
6.2.4	Extensional Flow Apparatus	241
6.2.5	Flow Induced Birefringence Measurement	242
6.2.6	Results and Discussion	243

7	Conclusions	249
	Appendix A List of Useful Formulas Related to the Fractional Calculus	255
A.1	Definitions and Properties of Fractional Derivatives	255
A.2	Frequently Encountered Special Functions	257
A.3	Laplace and Fourier Transforms of Fractional Derivatives	258
A.4	Constitutive Equations and their Linear Viscometric Functions	259
	Appendix B Supplementary Information to Chapter 3	265
B.1	Thermodynamic inconsistency of the higher-order Nutting equation . . .	265
B.2	Confidence interval estimate discussion	266
B.3	Asymptotic analysis of the interfacial creep compliance $J_s(t)$	267
B.3.1	Small t limit	267
B.3.2	Large t limit	271
B.4	Fractional calculus and the Soft Glassy Rheology (SGR) model	273
B.5	Creep ringing and the linear Jeffreys model	275
	Appendix C Supplementary Information to Chapter 4	277
	Appendix D Supplementary Information to Chapter 5	281
D.1	Determination of $I_n(t)$	281
D.2	Boundary condition for determining C_1	283
	Appendix E An analytical solution to the extended Navier-Stokes equations using the Lambert W function.	285
E.1	Introduction	285
E.2	The Extended Navier Stokes Equations (ENSE)	289

E.3	Results and Discussion	291
E.3.1	Comparison with Data	295
E.3.2	The Conductance	298
E.3.3	Velocity Field in the Channel	301
E.3.4	Boundary Layer Analysis	305
E.4	Conclusion	308

List of Figures

1.1.1	Examples of multiscale systems in nature. (a) A satellite image of the Lena river delta located in the far north of eastern Siberia. We observe the river breaking up into smaller streams which in turn break up into still smaller streams. Image credit: NASA/USGS EROS. (b) Cloud formation around Guadalupe Island in the Pacific Ocean. Here too we see the signatures of a multiscale system; the clouds consist of big whorls, that break up into smaller and smaller whorls at the perimeter, and this process continues across many different length scales. Also visible in this image, is a von Karman vortex street [5] produced due to the presence of the island in the south west corner.	40
1.2.1	Ludwig Eduard Boltzmann, who made a number of important contributions to various branches of physics, including thermodynamics, kinetic theory, statistical mechanics, and viscoelasticity. Many current theories of viscoelasticity are generalization of his initial linear superposition equation [24]. Markovitz notes that he seems to be amongst the first to propose a power law relaxation kernel $G(t) = B/t$, where B is a constant [23]. Image is in the public domain.	43
1.2.2	List of standard shearing flows used to determine the material functions of complex fluids, from Bird et al. [24]. The left and right columns depict the flow state of the fluid for time $t < 0$ and $t > 0$ respectively. For definitions of the material functions for each flow, see Refs. [24] and [26]. We provide definitions and expressions for many of these material functions at appropriate locations of this thesis.	45

1.3.1 Examples of experimentally measured relaxation moduli $G(t)$ that exhibit multiscale power law response. In both cases, we observe broad relaxation spectra with no easily discernible characteristic timescale. (a) Data for 0.5 wt.% Xanthan gum solutions. Each curve corresponds to a different value of strain amplitude γ_0 , whose value is given in the legend. (b) Data for commercial low density polyethylene melt at 160°C. Adapted from Ref. [28]. Similar to (a), each curve corresponds to a different value of strain amplitude: $\gamma_0 = 1$ (hollow circles), $\gamma_0 = 3$ (filled circles), $\gamma_0 = 5$ (hollow square), $\gamma_0 = 7$ (filled squares) and $\gamma_0 = 9$ (hollow triangles). The decrease in $G(t)$ with increasing γ_0 is a nonlinear effect which we describe in detail in Chapter 4. 46

1.3.2 Examples of experimentally measured relaxation moduli $G(t)$ that exhibit multiscale power law response. (a) Thermoreversible colloidal gel consisting of organophilic silica below the gel temperature $T = 23$ °C. Adapted from Ref. [29]. Each symbol corresponds to a different strain amplitude, and a master curve has been constructed using a damping function $h(\gamma_0)$ (see Chapter 4 for details). (b) Data obtained for gluten gels, which is a branched biopolymer matrix with starch globules occupying the pores of the matrix. Figure adapted from Ref. [30]. As in the previous figure, the decrease in $G(t)$ with increasing γ_0 is a nonlinear effect. 47

1.3.3 Cryo scanning electron microscopy images of (a1,a2) a gel obtained by coagulating milk through the addition of rennet, (b1,b2) curds obtained by cooking the resultant gel under gentle stirring and (c1,c2) cheese produced by aging the cooked curds for one week under mechanically applied pressure. Column 1 has a scale bar of 20 μm and column 2 has a scale bar of 10 μm . The multiscale nature of these materials is clearly visible, and there is a broad distribution of pore and globule sizes. Images reproduced from Ref. [31]. 50

- 1.3.4 A simulated example of a 2D random walk, with the walker taking steps of equal length at constant intervals of time in a randomly chosen direction. The green and red dots indicate the starting and ending locations of the walk, and the black dots connected by blue lines represent the intermediate steps. For a 2D random walk with a large number of steps, the MSD $\langle \Delta r^2 \rangle \sim t$ 51
- 1.3.5 Comparison of a regular random walk (left), and a Continuous Time Random Walk (right) exhibited by subdiffusive systems. The blue curve and red curves indicate MSD of the form $\langle \Delta x^2 \rangle^{1/2} \sim t^{1/2}$ and $\langle \Delta x^2 \rangle^{1/2} \sim t^{1/4}$ respectively. The yellow shaded regions plot the probability $P(x, t)$ of finding the walker at location x at time t . We observe that a CTRW covers less ground for the same interval of elapsed time. Figure reproduced from Ref. [49]. 53
- 1.3.6 (a) Relaxation modulus data and multimode Maxwell fit (Prony series, Equation (1.3.7)) reproduced from Laun [51]. Eight modes were required to fit the data, whose relaxation times τ_i were chosen arbitrarily. The fit is shown by a solid black line and the values are shown in (b). Note the waviness in the fit introduced by the multimode Maxwell model for $1 \leq t \leq 200$. In this thesis, we present models that circumvents the need to introduce a large number of modeling parameters for broad multiscale relaxation spectra. 54
- 2.1.1 James Clerk Maxwell, Scottish physicist who is widely considered as one of the greatest classical physicists [22]. His most important work was the unification of electricity and magnetism, and proving that visible light is part of a much larger electromagnetic spectrum. He also made important contributions in the kinetic theory of gases and in linear viscoelasticity. His proposal of a viscoelastic model containing both elasticity and viscosity [75], now referred to as the linear viscoelastic Maxwell model has led to various linear, nonlinear and frame invariant generalized models that can capture a wide range of rheological behavior. Examples of these models are the generalized Maxwell model (Equations 2.1.10, 2.1.11), the upper and lower convected Maxwell models [24] and the Wagner model [76]. Image is in the public domain. 60

2.1.2	Schematic figures of the simplest two element mechanical models used in rheology. (a) the linear viscoelastic Maxwell model, with a spring of modulus G_0 and a dashpot of viscosity η_0 connected in series and (b) the linear viscoelastic Kelvin Voigt model, with the spring and the dashpot connected in parallel. The representation of linear viscoelasticity in terms of mechanical models with multiple elements is a useful aid to thinking.	60
2.1.3	A schematic figure of the generalized (multimode) Maxwell model. The model consists of multiple Maxwell modes connected in parallel. Each parallel mode represents a mode of relaxation of modulus G_i and relaxation time τ_i . Using this model, a broad <i>continuous</i> relaxation spectrum can be modeled by approximating it as a set of <i>discrete</i> relaxation modes. Figure reproduced from Ref. [77].	63
2.2.1	The schematic representation of a springpot as an element that interpolates between a spring ($\alpha = 0$) and a dashpot ($\alpha = 1$).	67
2.2.2	The geometric representation of a springpot, in which it is interpreted as a vector \vec{S}_1 of magnitude $ \vec{S}_1 = \mathbb{V}\omega^\alpha$ that makes an angle $\pi\alpha/2$ with the horizontal axis. Purely elastic responses lie on the horizontal axis, and purely viscous responses lie on the vertical axis. Typical magnitudes for different complex fluids are indicated schematically on each axis. A springpot, on the other hand has projections on both axes and therefore captures intermediate responses. A second springpot \vec{S}_2 of magnitude $ \vec{S}_2 = \mathbb{G}\omega^\beta$ and making the angle $\pi\beta/2$ with the horizontal is also shown.	68
2.2.3	Schematic figure of an infinite ladder model adapted from Schiessel and Blumen [81]. Setting the box B to be a spring, and then letting $n \rightarrow \infty$, it can be shown that the constitutive equation of such an infinite ladder model is exactly that of the springpot [95]. To intuitively see why this is the case, one may imagine the ladder model as containing n different relaxation modes, each with its own characteristic relaxation time τ_i . Setting $n \rightarrow \infty$ decreases the spacing between these relaxation modes and converts the discrete relaxation spectrum of the finite ladder model to a continuous relaxation spectrum.	70

2.3.1	Schematic figures of the (a) Fractional Maxwell Model (FMM) and (b) Fractional Kelvin Voigt Model (FKVM). These models are generalizations of their linear counterparts (shown in Figure 2.1.2) and the springs and dashpots are replaced by springpots.	74
2.3.2	Stress relaxation data for bread dough reproduced from Ref. [50]. The original data is from Ref. [110]. A stretched exponential relaxation function (dashed line) captures the rheological behavior at short times, while at long times, the dough exhibits power law-like stress relaxation (dotted line). The Mittag-Leffler relaxation kernel (solid line) smoothly interpolates between these two asymptotic material responses.	76
2.4.1	A micrograph reproduced from Ref. [113] of a capillary suspension consisting of hydrophobically modified glass beads ($r = 9.6 \mu\text{m}$) suspended in diisononyl phthalate. The second immiscible liquid is 1 wt.% water. The inset figure schematically shows the nature of the capillary bridging, with water (orange shading) preferentially occupying the pores between the particles. The yellow lines in the main figure outline water trapped between these pores. More details can be found in Refs. [111–114]. . . .	80
2.4.2	Magnitude of the complex shear modulus $ G^*(\omega) $ as a function of frequency ω obtained by Koos and Willenbacher [111] in a small amplitude oscillatory shear experiment performed on the capillary suspensions described in Ref. [111]. The legend indicates the weight % of added water. The lines are fits of Equation 2.4.2 to the data (symbols). With just three parameters, we are able to capture the transition of the suspensions from a sol state to a gel-like material possessing a yield stress.	81
2.4.3	Model parameters obtained by fitting the FKVM expression for $ G^*(\omega) $ derived in Equation 2.4.2 to the SAOS data of Koos and Willenbacher [111]. One of the springpot elements has been set to be a spring ($\beta = 0$). These data and fits are shown in Figure 2.4.2. As the amount of water is increased, we observe that both G and \mathbb{V} progressively increase.	82
3.2.1	Schematic figures of the Double Wall Ring (DWR) fixture used to perform the interfacial rheology.	90

3.3.1	Rheological data for ‘highly anomalous’ butyl rubber taken from [80]. The solid line depicts the FMM fit with one of the elements set to be a spring ($\beta = 0$). For comparison, the fit obtained from a linear Maxwell model is shown as a dashed line. (b) Creep data at two different stresses for the same ‘highly anomalous’ butyl rubber. The solid line represents the prediction of the FMM based on the quasi-properties determined from the stress relaxation fit.	94
3.3.2	Interfacial small amplitude oscillatory shear data of 3 wt.% Acacia gum solutions carried out using the DWR. (a) Strain amplitude sweep performed at $\omega = 1 \text{ rad s}^{-1}$. (b) Frequency sweep performed at a strain amplitude $\gamma_0 = 1\%$, which lies in the linear regime. The viscoelastic interface shows weak power-law behaviour.	96
3.3.3	The FMM fitted (lines) to interfacial storage $G'_s(\omega)$ and loss $G''_s(\omega)$ moduli data (symbols) obtained from (a),(b) 3 wt.% Acacia gum solutions and (c),(d) 50 mg/ml BSA solutions. $G'_s(\omega)$. The FMM fits are given by equations 3.3.5 and 3.3.6 respectively. Cole-Cole plot of (b) the same Acacia gum solution and (d) the same BSA solution showing the fractional Maxwell fit as a solid line with a linear Maxwell fit shown for comparison by the dashed line.	100
3.3.4	Creep compliance for 3 wt.% Acacia gum solutions performed at various values of imposed interfacial stress σ_s^0 . All experiments collapse onto a single curve as expected for a linear viscoelastic response. The interfacial viscoelasticity is coupled with instrument inertia giving rise to creep ringing at early times. The inset plot shows that at long times the creep compliance exhibits power-law behaviour with $J_s(t) \sim t^{0.13}$	103

3.3.5	(a) Experimentally measured values of the interfacial compliance response (symbols), and the short and long time asymptote in the FMM coupled with instrument inertia. At early times, we retrieve the expected quadratic response of $J_s(t) \sim \frac{1}{2} \frac{t^2}{I/b_s}$ which is in accordance with the equation of motion at very early times. At long times, the effect of inertia only appears as a higher order correction (equation 3.3.14). (b) The predicted interfacial creep compliance from solving equation 3.3.11 numerically using the exponents and quasi-properties found from the SAOS experiments that characterize the Acacia gum solutions. The prediction made by the model is in excellent agreement with the measured data, and it captures both the creep ringing at early times as well as the power-law behaviour observed at long times.	106
4.1.1	Flowchart showing the pathways described in this paper to arrive at viscometric material functions for multiscale materials. Beginning with a simple linear viscoelastic experiment such as Small Amplitude Oscillatory Shear (SAOS), and characterizing the power-law responses of material using a fractional constitutive model, we can make accurate predictions of other linear material functions such as the creep compliance $J(t)$ and the relaxation modulus $G(t)$. We also show in this paper that by measuring the damping function $h(\gamma)$ and using a K-BKZ framework in conjunction with the previously determined quasi-properties, nonlinear material functions such as the steady shear viscosity $\eta(\dot{\gamma})$ and the first normal stress coefficient $\Psi_1(\dot{\gamma})$ can be evaluated accurately.	113
4.2.1	The various industrial applications of Xanthan gum. Reproduced from Ref. [68].	115
4.3.1	Small Amplitude Oscillatory Shear (SAOS) experiments performed on different concentrations of Xanthan gum. Data are shown by filled symbols (storage modulus) and hollow symbols (loss modulus), while the solid lines are fits to the storage modulus $G'(\omega)$ (Eq.2.3.15) and the dashed lines are fits to the loss modulus $G''(\omega)$ (Eq.2.3.16). The parameter values determined for each fluid are given in Table 1.	116

4.3.2	Creep experiments performed on different concentrations of Xanthan gum (symbols) and the corresponding predictions of the linear viscoelastic creep compliance $J(t)$ (Eq. (2.3.13)). The applied stress is $\sigma_0 = 0.5$ Pa. The values of the constitutive parameters $\alpha, \beta, \mathbb{V}$ and \mathbb{G} used to make the prediction are obtained directly from the SAOS experiments (Table 1). The initial quadratic response at short times is given by $J(t) = (b/2I)t^2$ and occurs due to the coupling of the instrument inertia with viscoelasticity, and is shown as a black dashed line.	117
4.3.3	Relaxation modulus $G(t)$ obtained from step strain experiments performed on a 0.5 wt.% Xanthan gum solution at different strain amplitudes. The legend box shows the strain amplitude γ_0 at which the stress relaxation test was performed. Increasing the strain amplitude causes a progressive decrease in the relaxation modulus, which can be quantified using a damping function of the form given by Eq.(4.3.11).	121
4.3.4	The damping function $h(\gamma) = G(t, \gamma)/G(t)$ for different concentrations of Xanthan Gum. The damping function is independent of concentration and is well described by a function of the form $h(\gamma) = 1/(1 + 0.3\gamma^2)$	122
4.3.5	Predictions of nonlinear material functions using the K-BKZ type model (lines) compared with measured data (symbols); (a) steady shear viscosity $\eta(\dot{\gamma})$, and (b) first normal stress coefficient $\Psi_1(\dot{\gamma})$. The model parameters for each fluid are given in Tab. I. The dashed lines in (a) show the viscosity given by the asymptotic simplification in Eq.4.3.22.	124
4.3.6	Comparison of the agreement between the Cox-Merz rule and the Gleissle mirror relations for the FMM. The predicted values of the steady shear viscosity from the two different rules virtually overlap. $\alpha = 0.64, \beta = 0.19, \mathbb{V} = 71.65 \text{ Pa s}^\alpha, \mathbb{G} = 7.82 \text{ Pa s}^\beta$	131
4.3.7	Predictions of the Gleissle mirror relations for the FMM (lines) compared to measured data for Xanthan gum(symbols); (a) steady shear viscosity $\eta(\dot{\gamma})$ prediction (Eq.4.3.38) and (b) first normal stress co-efficient $\Psi_1(\dot{\gamma})$ prediction (Eq.4.3.42). There is a consistent offset between the prediction and measured data, which increases with increasing concentration. Values of $\alpha, \beta, \mathbb{V}$ and \mathbb{G} used to make the model predictions were taken from Table 4.3.1.	132

- 4.3.8 The offset factor f (Eq. 4.3.43) as a function of the shear rate $\dot{\gamma}$ for different values of the damping function parameter a . $0 < f < 1$ indicating that the steady shear viscosity is lower than the complex viscosity. This arises from damage accumulated at the large strains imposed during a steady shear experiment. The values of the FMM parameters are $\alpha = 0.60$, $\beta = 0.14$, $\mathbb{V} = 208.54 \text{ Pa s}^\alpha$ and $\mathbb{G} = 22.46 \text{ Pa s}^\beta$ corresponding to the 1 wt.% Xanthan gum solution with characteristic timescale $\tau = (\mathbb{V}/\mathbb{G})^{1/(\alpha-\beta)} = 1846 \text{ s}$ 133
- 4.3.9 The irreversibility assumption. The green line shows $|\gamma(t)| = \gamma_0 |\sin \omega t|$. The blue dashed line is the damping function without the irreversibility assumption, and there is instant microstructural recovery of accumulated damage in the material when $\gamma < \gamma_c$. The red circles denote the damping function we use in Equation 4.3.63, which accounts for irreversibility and assumes zero recovery after the strain first exceeds the critical strain γ_c . . . 138
- 4.3.10 A special case of the Fractional Zener Model (FZM) which we refer to as the Fractional Viscoelastic Cross Model (FVCM). 142
- 4.3.11 Simulations of the viscosity predicted by the FVCM model plotted in dimensionless form as a function of the Weissenberg number $Wi = \tau \dot{\gamma}$. (a) Effect of varying the value of the springpot exponent β , which controls the slope of the shear-thinning region. (b) Effect of varying the damping function parameter a . For $a = 0$, no shear-thinning is observed. 144
- 4.3.12 Simulations of the the steady shear viscosity $\eta(\dot{\gamma})$ as a function of shear rate $\dot{\gamma}$ obtained from the FVCM model. For all curves, $\eta_p = 100 \text{ Pa s}$ and $\eta_s = 1 \text{ Pa s}$. The FCVM (Cross) prediction was obtained using a damping function of the form $h(\gamma) = 1/(1 + 0.1\gamma^2)$ and a springpot with $\beta = 0.3$ and $\mathbb{G} = 10 \text{ Pa s}^\beta$, and $\tau = (\eta_p/\mathbb{G})^{1/(1-\beta)} = 26.83 \text{ s}$. To generate the Cross model simulation, the same values of $(\dot{\gamma}^*)^{-1} = 26.83 \text{ s}$ and $n = 0.3$ were chosen. 145

5.1.1	A diagram of a typical tack experiment showing the variation of the normal force as a function of displacement, reproduced from Ref. [196]. The tack force is also frequently plotted as a function of the strain. We observe that at small strains there is a peak in force, followed by a large strain flow regime, sometimes exhibiting strain hardening. In this Chapter, we show that this peak in the tack force arises from the lubrication flow of the polymer at small strains. The inset plot schematically shows a tack experiment.	150
5.2.1	SAOS data of the polymer gels (symbols) shown along with the FKVM fits (dashed lines). (a) Cole-Cole plot. (b) The same SAOS data plotted against angular frequency ω	152
5.2.2	The definition of the axes used in this document. The upper plate (diameter 8 mm) is shown in gray, and the polymer gel is shown in blue. The initial aspect ratio depicted here is to scale.	154
5.2.3	The profiles of the deforming filament of polymer gel at different instances of time during a tack experiment for contact force $F_c = 300\text{g}$. (a) $t = 0$ (b) $t = 5t_p$ and (c) $t = 20t_p$. Here $t_p \approx 1\text{ s}$ was determined based on the observation of the experimental data. This diagram is to scale, with the upper plate of diameter 8 mm.	156
5.2.4	Comparison of the analytically derived solution for the tack force (equation 5.2.50 with a numerical solution obtained from solving $I_3(t)$ in 5.2.45 numerically. The numerical and analytical solutions coincide exactly. $\alpha = 0.59$, $\beta = 0$, $\mathbb{V} = 433.50\text{ Pa s}^\alpha$, $\mathbb{G} = 108.27\text{ Pa}$, $R_0 = 4\text{ mm}$, $h_0 = 0.159\text{ mm}$, $u_0 = 0.1\text{ mm s}^{-1}$	161
5.2.5	Predictions of the tack force based on 5.2.50, with each contact force value represented by a different color. Predictions are lines and measured data are symbols. The value of h_0 for each contact force was obtained from measurements as the value of h when the force on the plate changes sign, and $u_0=0.13\text{ mm/s}$	162
5.2.6	Prediction of the tack force based on equation 5.2.50. These are the same predictions as shown in the previous figures, but plotted here on a log-log scale to exemplify the goodness of the prediction for short times $t \leq 20\text{ s}$ and small strains.	163

5.2.7	The prediction of the SAOS response (equations 2.3.22 and 2.3.23) of the low modulus polymer gel based on the values of α, \mathbb{V} and G determined from the short and long time asymptotes of the tack experiment (equations 5.2.55 and 5.2.67).	168
5.2.8	Comparison of the composite force F_{comp} given by equation 5.2.69 (symbols) against the full analytic solution given by equation 5.2.50 (solid line). The short and long time asymptotes are represented as dashed lines. The peak force F_p and it's temporal location t_p are labeled.	169
5.2.9	Prediction of the magnitude (equation 5.2.73) and location of the peak force (equation 5.2.72) as determined by the composite function constructed from the asymptotic analysis. Measured data (■) is for the low modulus gels ($\alpha = 0.59, \mathbb{V} = 433.50 \text{ Pa s}^{0.59}$ and $G = 108.27 \text{ Pa}$.) taken from N.B. Wyatt, A.M. Grillet, L.G. Hughes, <i>Macromolecules</i> , submitted, 2012.	170
5.2.10	Comparison of the analytically derived solution for the tack force (equation 5.2.88) and the solution from solving $Q(t)$ (cf. 5.2.78 and 5.2.79) numerically. It is observed that the analytical and numerical solutions coincide exactly. $\alpha = 0.59, \mathbb{V} = 433.50 \text{ Pa s}^{0.59}, G = 108.27 \text{ Pa}, R_0 = 4 \text{ mm}, u_0 = 0.1 \text{ mm/s}$ and $h_0 = 0.159 \text{ mm}$	173
5.2.11	The composite force obtained from equation 5.2.100 (solid line) compared against the exact analytic solution for the force derived in equation 5.2.88 (symbols). Also shown are the short time (blue dashed line) and long time asymptotes (red dashed line) determined by equations 5.2.95 and 5.2.99 respectively. The composite force is seen to approximate the exact analytic solution excellently. $\alpha = 0.59, \mathbb{V} = 433.50 \text{ Pa s}^{0.59}, G = 108.27 \text{ Pa}, R_0 = 4 \text{ mm}, u_0 = 0.1 \text{ mm/s}$ and $h_0 = 0.159 \text{ mm}$	176
5.3.1	Comparison of the numerically determined value of the force given by equations 5.3.13 and 5.3.16 (symbols) against the approximate analytical solution given by equation 5.3.25 (line). The parameters were chosen to be $\alpha = 0.59, \beta = 0, \mathbb{V} = 100 \text{ Pa s}^\alpha$ and $\mathbb{G} = 400 \text{ Pa}$. For the purposes of illustration, $R_0 = 4 \text{ mm}, u_0 = 0.1 \text{ mm/s}$ and $h_0 = 0.1 \text{ mm}$	181

- 5.3.2 An example of predicting the SAOS response of a fractional Maxwell-like viscoelastic material from the asymptotic analysis of a tack experiment performed on the material. Here, the values of the parameters used are $\alpha = 0.59$, $\beta = 0$, $\mathbb{V} = 100 \text{ Pa s}^\alpha$, $\mathbb{G} = 400 \text{ Pa}$. For the purposes of illustration, $R_0 = 4 \text{ mm}$, $u_0 = 0.1 \text{ mm s}^{-1}$ and $h_0 = 0.1 \text{ mm}$ 183
- 5.3.3 The composite force determined in equation 5.3.38 (solid line) compared to the exact numerical solution for the tack force as given by equation 5.3.13 (symbols). Also shown here are the short time (black dashed line) and long time (blue dashed line) asymptotes, determined in equations 5.3.32 and 5.3.36 respectively. Note that the approximate composite force is a good approximation to the exact numerically determined solution. The parameters were chosen to be $\alpha = 0.59$, $\beta = 0$, $\mathbb{V} = 100 \text{ Pa s}^\alpha$ and $\mathbb{G} = 400 \text{ Pa}$. For the purposes of illustration, $R_0 = 4 \text{ mm}$, $u_0 = 0.1 \text{ mm s}^{-1}$ and $h_0 = 0.1 \text{ mm}$ 184
- 5.3.4 Comparison of the numerically determined value of the force given by equation 5.3.40 (symbols) against the approximate analytic solution determined in equation 5.3.43 (line). The analytical solution is a good approximation to the exact numerically determined force. $\alpha = 0.59$, $\beta = 0$, $\mathbb{V} = 100 \text{ Pa s}^\alpha$ and $\mathbb{G} = 400 \text{ Pa}$ 186
- 5.3.5 The composite force determined by equation 5.3.50 (solid line) compared to the numerically determined exact solution for the tack force given in equation 5.3.40 (symbols). Also shown here are the short time (red dashed line) and long time (blue dashed line) asymptotes derived in equations 5.3.47 and 5.3.48 respectively. It is observed that the composite force is a very good approximation to the exact value of the tack force. The parameters were chosen to be $\alpha = 0.59$, $\beta = 0$, $\mathbb{V} = 100 \text{ Pa s}^\alpha$ and $\mathbb{G} = 400 \text{ Pa}$, with $R_0 = 4 \text{ mm}$, $u_0 = 0.1 \text{ mm s}^{-1}$, and $h_0 = 0.1 \text{ mm}$ for purposes of illustration. 188
- 5.3.6 SAOS measurements performed on 2 wt.% LBG solutions. (a) The material responds linearly at least until a strain amplitude of 10%. (b) Frequency sweep at a strain amplitude of $\gamma_0 = 5\%$. Also shown are the FMM fits (equations 2.3.15 and 2.3.16) and the corresponding fit parameters. 190

5.3.7	Steady shear viscosity $\eta(\dot{\gamma})$ of 2 wt.% LBG. The fluid approaches a zero-shear plateau at low shear rates and is shear-thinning at high shear rates. The complex modulus $\eta^*(\omega)$ agrees well with $\eta(\dot{\gamma})$ at $\omega = \dot{\gamma}$, as suggested by the empirical Cox-Merz rule. Deviations to the rule are seen at higher rates.	191
5.3.8	A time-sequence of snapshots of a tack experiment performed on 2 wt.% LBG solutions using a plate of radius $R_0 = 4$ mm. The profile of the fluid filament close to breakup indicates the existence of an elasto-capillary balance of forces. Image analysis of the video gives us the true velocity of the upper plate $u_0 _{\text{true}} = 0.539$ mm s ⁻¹ , and the mid-plane radius R_{mid} as a function of time. $u_0 _{\text{imposed}} = 0.5$ mm s ⁻¹ , $h_0 = 0.5$ mm, $t_b = 7.9$ s.	191
5.3.9	The reciprocal of the experimentally measured mid-plane radius R_{mid} (suitably scaled with the initial radius R_0) obtained from video analysis plotted against the stretch ratio λ . It is observed that except near breakup, assumptions made about the kinematics of the fluid filament (equation 5.2.43) agree closely with experiment.	192
5.3.10	The measured tack force exerted by a 2 wt.% LBG solution (symbols) compared to the corresponding analytical prediction derived in equation 5.3.40 (line). It is observed that the prediction agrees very closely with the experimental data. The deviation of the measured force from the data close to breakup is due to additional elastic stresses retarding the breakup leading to a change in the kinematics of the flow.	193
6.1.1	Effect of changing the salt environment of Mamaku gum solutions. (a) Adding different concentrations of NaCl does not drastically influence the shear viscosity of Mamaku gum solutions. (b) Varying the salt composition only minimally influences the steady shear viscosity of Mamaku gum solutions. Data from Ref. [73].	199
6.1.2	Zero shear viscosity η_0 of a 7 wt. % Mamaku gum solution as a function of pH. Changing the pH leaves η_0 relatively unchanged, except at very alkaline pH. This could be due to structural changes induced in the polysaccharide chains at very alkaline pH. Data from Ref. [73].	199

6.1.3	<p>(a) The zero shear viscosity η_0 of Mamaku gum solutions as a function of concentration showing the different power law scalings characteristic of the dilute and semidilute regimes. In the semidilute regime, $\eta_0 \sim c^{4.464}$.</p> <p>(b) The shear rheology of different concentrations of Mamaku gum in the absence of urea, reproduced with permission from Goh et al.[71] For Mamaku gum, $c^* \approx 2.2$ wt. %. At some critical shear rate $\dot{\gamma}_p$, which depends on the Mamaku gum concentration, a shear thickening regime appears for $c > c^*$, followed by strong shear thinning.</p>	203
6.1.4	<p>Effect of the addition of urea on the viscosity of a 5 wt.% Mamaku gum solution. Upon the addition of urea, three changes are observed, namely, the zero shear viscosity plateau drops, the onset of shear thickening is pushed to higher shear rates, and the extent of shear thickening also drops.</p>	204
6.1.5	<p>Dependence of the characteristic timescale τ_p (squares) and the peak viscosity η_p (circles) on the concentration of added urea for a 5 wt. % Mamaku gum solution. An identical exponential dependence (differing only by a constant pre-factor) is observed in the variation of η_p as well as τ_p with urea concentration. We measure the same exponential sensitivities for 2.5 wt. % and 5.0 wt. % Mamaku gum solutions.</p>	205
6.1.6	<p>Snapshots of CaBER experiments for 2.5 wt. % (top row) and 5.0 wt. % (bottom row) Mamaku gum solutions. In both cases, it can be seen that the onset of the elasto-capillary regime, characterized by a uniform cylindrical fluid filament, occurs at around $t/t_b \approx 0.15$. For the 2.5 wt.% solution, the break-up time $t_b = 0.80$ s, while for the 5 wt.% solution, $t_b = 55.30$ s. The initial gap is $L_0 = 2$ mm, the final gap $L_f = 8$ mm, and the plate diameter $D_0 = 6$ mm. This yields an initial aspect ratio of $\Lambda_0 = 0.33$ and a final aspect ratio of $\Lambda_f = 1.33$.</p>	207
6.1.7	<p>Diameter of the fluid filament as a function of time for CaBER experiments performed on different concentrations of Mamaku gum. The relaxation times shown in the figure is determined by fitting equation 6.1.2 to the elasto-capillary regime of the experiment. The relaxation time τ increases with increasing Mamaku concentration.</p>	208

6.1.8	(a) Transient extensional viscosity of different concentrations of Mamaku gum calculated using equation 6.1.4. (b) Trouton ratio $Tr = \eta_E^+/\eta_0$ for the same concentrations of Mamaku gum shown in (a). Whereas the extensional viscosity increases with increasing Mamaku gum concentration c , the Trouton ratio is nearly independent of c	210
6.1.9	The transient extensional viscosity η_E^+ of 2.5 wt. % (a) and 5.0 wt. % (b) Mamaku gum solutions measured in a CaBER device. In both solutions, η_E^+ drops by nearly two orders of magnitude when the urea concentration is increased from 0 M to 5 M.	211
6.1.10	The diameter $D(t)$ as a function of time t of 2.5 wt. % (a) and 5.0 wt. % (b) Mamaku gum solutions measured during CaBER experiments, plotted on a log-linear scale. Increasing the urea concentration leads to earlier breakup and a drop in viscoelasticity. The magnitude of the slope of the $D(t)$ vs. t curves is inversely related to the relaxation time τ ; for both Mamaku concentrations, the relaxation time decreases upon increasing urea concentration.	213
6.1.11	(a) The normalized relaxation time $\bar{\tau} = \tau/\tau^0$ for Mamaku/urea mixtures calculated from CaBER experiments, where τ^0 is the relaxation time of the pure Mamaku solution (0 M urea). The relaxation times fall onto a master curve given by $\bar{\tau} = \exp(-0.8c)$, independent of the Mamaku concentration. (b) An identical exponential dependence is observed in the variation of the peak shear viscosity with urea concentration, as well as the reciprocal of the critical shear rate at which the peak shear viscosity is observed, shown here for a 5 wt.% solution of Mamaku.	214
6.1.12	(a) The values of $G_r'(\omega)$ (solid symbols) and $G_r''(\omega)$ (hollow symbols) measured in an SAOS experiment for a 5 wt. % Mamaku gum solution with different concentrations of added urea. The curves have been shifted along the frequency axis using a shift factor a_c to generate a master curve. (b) The values of the shift factor a_c as a function of urea concentration required to generate the master curves of $G_r'(\omega)$ and $G_r''(\omega)$. There is an exponential relationship between a_c and urea concentration c . However, the dependence of the shift factor on urea concentration is stronger in the nonlinear experiments (black squares) as compared to the linear SAOS experiments.	218

- 6.1.13 A schematic figure of the FiSER device. In a FiSER experiment, a fluid filament is set up between two parallel plates (shown in blue) and the bottom plate is then pulled apart in an exponential manner, to obtain a desired strain rate. A laser sheet (shown in red) continuously measures the mid-plane diameter of the filament and a force transducer measures the normal force during the stretch. 220
- 6.1.14 Snapshots of the fluid filament during a FiSER experiment. The top row of images is of a 5 wt. % Mamaku gum solution, while the bottom row corresponds to a 5 wt. % Mamau gum solution with urea added at a concentration of 3 M. The Hencky strains ϵ_H at which the images were taken are given at the top of the figure. Upon the addition of urea, the viscoelasticity of the polysaccharide gum is dramatically decreased, and the breakup of the fluid filament occurs at much smaller stretch ratios compared to the urea-free solutions. 221
- 6.1.15 Stress vs. Hencky strain ((a),(c),(e)) and modulus vs. Hencky strain ((b),(d),(f)) obtained from filament stretching experiments for different Mamaku/urea mixtures. In all cases, the Mamaku/urea mixtures are strain hardening. The stress is strain-rate independent for small strains, and shows rate dependency as the Hencky strain increases. The stress (and correspondingly the modulus) increase with increasing nominal strain rate for the 0 M urea and 1 M urea mixtures. However, no clear trend is observed for the 3 M urea mixture. This is because the relaxation time of the 3 M urea solutions is so low ($\lambda = 0.31$ s.) that the maximum experimentally impossible Weissenberg number is not high enough to exhibit any rate dependence. 222
- 6.2.1 (a) Schematic drawing of a synovial joint highlighting the important anatomic features. (b) Simplified picture of the squeeze flow in a synovial joint undergoing a compressive deformation (such as occurs in the knees during locomotion). The black arrows indicate the flow of the synovial fluid being squeezed outwards orthogonal to the compression axis, resulting in a biaxial extensional flow at the mid-plane between joint surfaces and a stagnation point at the center of symmetry (marked by the red 'x'). 226

6.2.2	Flow velocity magnitudes and direction for shear-thinning power-law fluids in a squeeze flow with $R/h = 10$. The power-law exponents are: (a) $n = 1$, (b) $n = 0.5$, (c) $n = 0.2$, and (d) $n \rightarrow 0$	233
6.2.3	Flow velocity magnitudes and direction for shear-thinning power-law fluids in a squeeze flow with $R/h = 100$. The power-law exponents are: (a) $n = 1$, (b) $n = 0.5$, (c) $n = 0.2$, and (d) $n \rightarrow 0$	234
6.2.4	Velocity as a function of non-dimensional height in the channel z at fixed values of radius r and for $R/h = 10$. The power-law exponent is: (a) $n = 1$, (b) $n = 0.5$, (c) $n = 0.2$, and (d) $n \rightarrow 0$	235
6.2.5	Velocity as a function of non-dimensional height in the channel z at fixed values of radius r and for $R/h = 100$. The power-law exponent is: (a) $n = 1$, (b) $n = 0.5$, (c) $n = 0.2$, and (d) $n \rightarrow 0$. As n decreases the velocity field becomes increasingly independent of z and approaches plug-like flow. . .	236
6.2.6	The flow type parameter ψ as a function of spatial position for $R/h = 10$ and (a) $n = 1$, (b) $n = 0.5$, (c) $n = 0.2$, and (d) $n \rightarrow 0$. $\psi = 1$ corresponds to pure extensional flow, while $\psi = 0$ corresponds to simple shear flow. . . .	237
6.2.7	The flow type parameter ψ as a function of spatial position for $R/h = 100$ and (a) $n = 1$, (b) $n = 0.5$, (c) $n = 0.2$, and (d) $n \rightarrow 0$	238
6.2.8	Steady shear viscosity of HA/PBS solutions measured using an AR-G2 stress-controlled cone-and-plate rheometer (closed symbols) and an m-VROC microfluidic rheometer (open symbols). The viscosity is well-described by a Carreau- Yasuda model (solid lines), except for the fluid containing BSA and γ -globulin at low shear rates.	240
6.2.9	(a) 3D view of the OSCER geometry showing the upstream and downstream characteristic channel dimension H and the uniform depth d . (b) Light micrograph of the actual OSCER geometry. The inflow is along the y - and the outflow along the x -direction. At the center of the geometry there is a stagnation point, here marked as the origin of coordinates. . . .	242

6.2.10	Streak imaging showing the nature of the flow field in the OSCER with a Newtonian fluid at $U = 0.01 \text{ m s}^{-1}$, with superimposed colored hyperbolae for comparison. The superimposed white lines indicate the symmetry axes of the geometry, which coincide at the stagnation point. Flow enters through the top and bottom channels and exits through the left- and right-hand channels.	244
6.2.11	Flow induced birefringence measured over a range of extension rates in solutions of HA1.6: (a) 0.1 wt. %, (b) 0.3 wt. %, (c) 0.3 wt. % + BSA + γ -globulin. The color scale bar represents retardation in the range of $R = 0 - 10 \text{ nm}$	245
6.2.12	(a) Measured birefringence Δn as a function of the strain rate $\dot{\epsilon}$ for HA1.6 solutions in the OSCER. In the 0.1 wt. % solution the experiment is curtailed at lower $\dot{\epsilon}$ due to the onset of an inertio-elastic instability that distorts the birefringent strand (as illustrated by the inserted image for $U = 0.36 \text{ m s}^{-1}$). (c) Extensional viscosity η_E as a function of $\dot{\epsilon}$, determined from birefringence measurements using the stress-optical rule.	247
B.5.1	Interfacial creep data obtained with a 50 mg/ml BSA solution. A viscously damped inertio-elastic ringing is present at early times and a power-law behaviour is exhibited at long times. The solid line shows the linear Maxwell fit to the entire time range of the experiment, and the dashed line shows the linear Maxwell fit only to the ringing regime. Neither fit performs adequately at capturing both the ringing phenomenon as well as the long-time power-law behaviour.	276
E.1.1	The different regime classifications of micro channel flows based on Knudsen number Kn . Figure is reproduced from [329].	287
E.3.1	Evolution in the non-dimensional pressure $\bar{P}(\bar{x}) = P(\bar{x})/P_c$ as a function of non-dimensional position $\bar{x} = x/L$ along the micro channel analytically determined from equation E.3.5. We observe that the pressure is a non-monotonic function of \bar{P}_i , and saturates for high inlet pressures \bar{P}_i . Furthermore, an inflection point is present in the curves, some of which are not readily apparent in the plots above on account of being very close to the exit.	295

- E.3.2 Analytically determined pressure gradient $d\bar{P}/d\bar{x}$ as a function of \bar{x} (equation E.3.20) for a fixed value of the outlet pressure. There exists a point in the channel where the pressure gradient is most favorable (most negative), and the magnitude of the favorable pressure gradient increases with \bar{P}_i . The location \bar{x} at which this occurs is also shifted towards $\bar{x} = 1$ as the pressure is increased (cf. equation E.3.21). 297
- E.3.3 Prediction of the analytically derived solution to the ENSE compared to the experimental measurements taken directly from the values reported by Maurer et al. [343]. The agreement between the prediction and the data is good. The parameters used here are from Maurer et al. $\mu = 19.9 \times 10^{-6}$ Pa s, $h = 0.6 \mu\text{m}$, $w = 200 \mu\text{m}$, $L = 10$ cm, $T = 293$ K. The outlet pressure was held constant at $P_o = 12$ kPa. The black dashed line shows the CNSE solution for the mass flux. 298
- E.3.4 (a) The conductance κ of the micro channel as a function of the average pressure in the channel. In contrast to the prediction in the classical case in which the conductance increases linearly with average pressure, the CNSE predicts that the conductance varies non-monotonically with $\langle \bar{P} \rangle$. (b) The Knudsen number at minimum conductance calculated using the average pressure as a function of outlet pressure. The Knudsen number at minimum conductance varies non-monotonically with the imposed pressure. 300
- E.3.5 Comparison of the prediction of the analytical expression obtained in the present work for the conductance of a micro channel (equation E.3.24) against experimental data obtained by Maurer et al. [343]. The outlet pressure as well as fluid properties and micro channel geometry is the same as that in [343]. The prediction is very good and closely agrees with the experimental data. The black dashed line shows the CNSE solution. . . . 301
- E.3.6 Velocity profiles in the micro channel at different locations \bar{x} . (a) $\bar{P}_i = 1$ and $\bar{P}_o = 0.25$ ($\mathcal{P} = 4$). The contribution of the diffusive velocity terms is a significant proportion of the total velocity and increases along the channel. (b) $\bar{P}_i = 10$ and $\bar{P}_o = 0.25$ ($\mathcal{P} = 40$). In this case, there is still slip at the walls, but its contribution to the total mass flux is negligibly small. . . . 302

E.3.7	Magnitude of the scaled velocity \mathcal{U} in the micro channel as a function of spatial position for different values of inlet pressure: (a) $\bar{P}_i = 0.3$, (b) $\bar{P}_i = 1.0$, (c) $\bar{P}_i = 5.0$, (d) $\bar{P}_i = 10$ at fixed outlet pressure $\bar{P}_o = 0.25$. For larger values of \bar{P}_i , the fluid undergoes a sudden increase in velocity in the vicinity of $\bar{x}=1$. Color scale bar shows values of \mathcal{U} ranging from 0 to 1.	304
E.3.8	Scaled profiles of the centerline velocity along the micro channel for different values of \bar{P}_i . Increasing \bar{P}_i leads to a steep increase in the scaled velocity close to $\bar{x} = 1$. The red dashed line shows the boundary layer approximation given in Table E.3.1 for $\bar{P}_i = 10 \gg 1$, $\bar{P}_o = 0.25 \ll 1$	305
E.4.1	The different flow regimes for micro channel gas flows. Of note is the boundary layer flow regime, in which steep gradients in the pressure field as well as velocity field are localized in the vicinity of the channel exit. . .	309

List of Tables

2.3.1 Asymptotic behaviour of $G'(\omega)$ and $G''(\omega)$ in the FMM. Because $0 < \beta < \alpha < 1$, G' and G'' reduce identically to 0 for the cases $\beta = 1$ and $\alpha = 0$ respectively, and the result holds for all frequencies.	78
4.3.1 Values of the model parameters $\alpha, \beta, \mathbb{V}$ and \mathbb{G} of the FMM for different concentrations of Xanthan Gum.	117
6.1.1 The various uses of polysaccharides in the food industry. Most frequently they are used as thickeners and gelling agents. Thickening is important not only to provide better texture and mouthfeel to foods, but also to help patients suffering from dysphagia. More information on molecular structure and applications of polysaccharides in foods can be found in Ref. [225]. . .	198
6.2.1 Parameters used to fit the Carreau-Yasuda model to the steady shear rheology data.	241
E.3.1 Limiting expressions for pressure $\bar{P}(\bar{x})$ and velocity $u^T(\bar{x})$ for the case $\bar{P}_o \ll 1$. The expressions in the second column, in which $\mathcal{P} \rightarrow 1$, is obtained by expanding the logarithm for $\mathcal{P} \approx 1$. Equation numbers are given within parentheses.	306
E.3.2 Limiting expressions for pressure $\bar{P}(\bar{x})$ and velocity $u^T(\bar{x})$ for the case $\bar{P}_o \gg 1$. Although there is no exponential behavior in this case, when $\mathcal{P} \gg 1$, the functional dependence of the expressions for pressure and velocity are such that steep gradients occur near the channel exit. As before, the expressions in the second column, in which $\mathcal{P} \rightarrow 1$, is obtained by expanding the logarithm for $\mathcal{P} \approx 1$. Equation numbers are given within parentheses. . . .	307

How can it be that writing down a few simple and elegant formulae, like short poems governed by strict rules such as those of the sonnet or the waka, can predict universal regularities of Nature?

Perhaps we see equations as simple because they are easily expressed in terms of mathematical notation already invented at an earlier stage of development of the science, and thus what appears to us as elegance of description really reflects the interconnectedness of Nature's laws at different levels.

-MURRAY GELL-MANN, From his 1969 Nobel Prize in Physics banquet speech.

1 | *Introduction*

1.1 *Multiscale Systems in Nature*

Many systems in nature contain patterns or networks with multiple length scales. For example, the rocky faces of the great mountain ranges of the Earth exhibit cracks, fractures and fissures that are of many different sizes [1, 2]. There are long and thick cracks that run down the face of the mountain, from which shorter and thinner cracks branch off. From these smaller cracks, in turn, still smaller cracks originate, and this process continues over many different size scales (or length scales) along the mountain side. We term such systems that possess features across multiple length scales as *multiscale* systems. In figure 1.1.1 we show two examples of multiscale systems found in nature: river deltas, with streams breaking up into smaller and smaller tributaries [3] and the perimeter of rain clouds [4]. Other examples of multiscale patterns found in nature are in viscous fingering phenomena [6], continental or island coastlines [7] and galaxy clustering in the cosmos [8].

Such multiscale systems often share the properties of *self-similarity*, or being invariant under a change of scale. In other words, they look the same when inspected “from nearby or from far” [9]. The mathematical ideal of such scale-invariant systems are fractal geometries [1]. These geometries theoretically possess every possible length scale, and are hence truly scale-free. Mathematicians have considered the concepts of scale-invariance and scale-free patterns through various striking and beautiful geometrical constructions such as the Koch snowflake, the Sierpinski Gasket, and Peano curves [10]. Many of these fractal geometrical constructions contain infinitely many length scales, and are perfectly non-random. However, physical systems do not conform to the mathematical ideal of non-random fractals. Physical systems are random fractals, and only look *approximately* the same at different length scales [11]. Furthermore, they only exhibit scale-free behavior over a bounded range

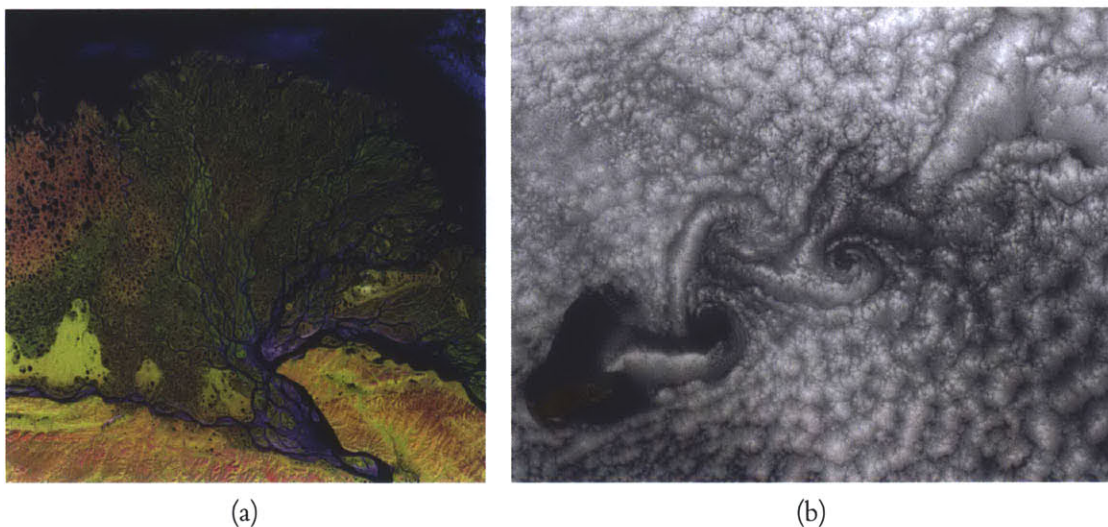


Figure 1.1.1: Examples of multiscale systems in nature. (a) A satellite image of the Lena river delta located in the far north of eastern Siberia, Russia. We observe the river breaking up into smaller streams which in turn break up into still smaller streams. Image credit: NASA/USGS EROS. (b) Cloud formation around Guadalupe Island in the Pacific Ocean. Here too we see the signatures of a multiscale system; the clouds consist of big whorls, that break up into smaller and smaller whorls at the perimeter, and this process continues across many different length scales. Also visible in this image, is a von Karman vortex street [5] produced due to the presence of the island in the south west corner.

of length scales, and cannot be fractal in the strictest sense.¹ Therefore, we will term all physical systems as being multiscale, rather than scale-free or fractal.

In this thesis we study in detail the rheological behavior of complex fluids with multiscale microstructures. Indeed, a single polymer chain is well modeled as a self similar random fractal, with the fractal dimension depending on factors such as the branching of the polymer chain or interactions between individual chains [11]. However, rather than consisting of single component polymers, complex fluids used by Nature or in consumer products and industrial applications are often multi-component systems with a wide distribution of length and time scales. Examples of such systems include, amongst many others, crosslinked polymer networks [13], microgel dispersions [14], foams [15], colloidal sus-

¹At the lower end, length scales are bounded by either the atomic, or small aggregate scale, and at the upper end sample size, for example.[12] Moreover, as Avnir et al. [12] caution, we need a sufficiently large range of experimental data to be able to make any conclusion about the fractal, scale-free nature of patterns found in nature.

pensions [16, 17] and soft glassy materials [18]. This sort of microstructure consisting of a broad distribution of length and time scales leads to a broad multiscale rheological response under mechanically applied deformations. In this thesis, one of our aims is to develop compact constitutive models to characterize, describe and predict the rheological behavior of multiscale complex fluids. But before we address this problem, we first need to address some more fundamental questions: What is the hallmark characteristic of a multiscale complex fluid in a rheological experiment? Indeed, what do we mean by a *complex* fluid, what is *rheology* and why is it important?

1.2 Complex Fluids and their Rheology

Rheology is defined as the study of the flow and deformation of materials [19]. On a very basic level, materials are classified into Hookean solids and Newtonian fluids [19]. The shear stress $\sigma^{(s)}(t)$ in a Hookean solid is given by

$$\sigma^{(s)}(t) = G_0\gamma(t) \quad (1.2.1)$$

in which G_0 is a modulus (units: Pa) and $\gamma(t)$ is the shear strain, while in a Newtonian fluid, the stress $\sigma^{(d)}(t)$ is given by

$$\sigma^{(d)}(t) = \eta\dot{\gamma}(t) \quad (1.2.2)$$

in which $\dot{\gamma}(t)$ is the shear rate, and η_0 is the coefficient of viscosity (units: Pa s). These responses of the Hookean solid and Newtonian liquid can be represented by analogous mechanical elements, namely the spring and dashpot respectively, and this is denoted by the superscripts s and d in Equations (1.2.1) and (1.2.2) respectively. If a shear stress is applied on a cube of a Hookean solid, it indefinitely remembers its original cubical shape and will return to it once the shearing stress is removed. In this sense, Hookean solids exhibit perfect memory [20]. At the opposite end of the spectrum is a Newtonian fluid, which has zero memory. When a shear stress is applied to a material element of a Newtonian fluid, its previous configuration is instantly forgotten and there is continuous flow for as long as the shear stress is applied. It is a case of scientific irony that these two opposing material responses are associated with the names of Hooke and Newton, between whom

perhaps one of the biggest scientific feuds in history took place². Gribbin provides a concise account of the events that transpired over the many years they were active scientists and beyond [22].

These two canonical material responses lie at opposite ends of a range of material responses that are experimentally observed. Most real materials, however, do not conform to the definitions of ‘solids’ and ‘fluids’, and lie between these canonical idealizations. Such complex, or *non-Newtonian* fluids (because they are not well-described by Equation (1.2.2)) have fading memory; they remember their previous configuration over some characteristic timescale known as the relaxation time τ . Due to the fading, time-varying memory, the stress at any given instant of time depends on the entire deformation history of the material over all past times. Such materials are known as *viscoelastic*, i.e., they exhibit both viscous fluid-like response as well as elastic solid-like response, whose relative magnitudes depend on the timescale of the applied deformation. Many everyday materials are viscoelastic complex fluids, and examples include foodstuffs, pastes and slurries, polymeric melts and solutions, gels, particulate and colloidal suspensions, biofluids and personal care products [20]. Given the myriad uses of complex fluids, measuring and modeling their rheology is of paramount importance.

To account for the fading memory of complex fluids, the stress $\sigma(t)$ at any given time t can be written in a general manner as [19]

$$\sigma(t) = \int_{-\infty}^t G(t-t') \dot{\gamma}(t') dt' \quad (1.2.3)$$

in which $G(t)$ is a relaxation modulus, and $\dot{\gamma}(t)$ is the shear rate as before. Equation (1.2.3) has been attributed to Ludwig Boltzmann (see Figure 1.2.1), and is hence known as the Boltzmann superposition principle [23]. Equations (1.2.1), (1.2.2) and (1.2.3) are examples of *constitutive equations*, which are equations that relate the stress $\sigma(t)$ in a continuum material to the deformation $\gamma(t)$ and/or deformation rate $\dot{\gamma}(t)$. Whereas equations (1.2.1) and (1.2.2) are instantaneous in time and do not depend on the deformation history of the

²This could possibly be the source of Hooke’s secrecy and jealousy with many of his scientific discoveries. When he discovered his law of elasticity, he wanted to make sure it was applicable to a wide range of elastic systems, and at the same time, establish himself as being the first to discover it. He therefore published his law as an anagram: *ceiiinosssttu* which was an encryption of *Ut tensio sic vis*, the Latin for ‘As the extension, so the force’ [21]



Figure 1.2.1

Ludwig Eduard Boltzmann, who made a number of important contributions to various branches of physics, including thermodynamics, kinetic theory, statistical mechanics, and viscoelasticity. Many current theories of viscoelasticity are generalization of his initial linear superposition equation [24]. Markovitz notes that he seems to be amongst the first to propose a power law relaxation kernel $G(t) = B/t$, where B is a constant [23]. Image is in the public domain.

material, the Boltzmann superposition integral is a linear superposition integral; the total stress contribution is a sum of past contributions over all times³.

The relaxation modulus $G(t)$ can be experimentally measured from a stress relaxation experiment. We apply on the sample a step shear strain deformation of amplitude γ_0 given by

$$\gamma(t) = \gamma_0 H(t) \quad (1.2.4)$$

where $H(t)$ is the Heaviside step function [25], and we measure the resulting stress response $\sigma(t)$ as a function of time. $G(t)$ is then calculated as

$$G(t) = \frac{\sigma(t)}{\gamma_0}. \quad (1.2.5)$$

In the linear regime, the relaxation modulus $G(t)$ is independent of the strain amplitude (we discuss nonlinear rheological response in detail in Chapter 4), and is an example of a *material function* [24]. These functions enable us to characterize the rheological behavior of a complex fluid by applying standard shearing or extensional flows. We show a list of shear flows (linear and nonlinear) used to characterize complex fluids in Figure 1.2.2, which we have adapted from the classic text *Dynamics of Polymeric Liquids* by Bird et al. [24]. Each

³To intuit the integral in Equation (1.2.3), consider $\dot{\gamma}(t') dt'$ to be an infinitesimal strain, $G(t - t')$ is the instantaneous relaxation modulus and hence the integrand is an infinitesimal stress contribution. The integral then sums over all these small contributions to yield the total stress. We emphasize that the Boltzmann superposition integral can only model linear deformations.

kind of applied deformation yields a different shear material function; however it can be shown that all the linear material functions are related [26], and the knowledge of any one of them is sufficient to derive all others. Note that the steady shear viscosity $\eta(\dot{\gamma})$ (top-most entry in Figure 1.2.2) is a nonlinear material function.

For some complex fluids, upon performing a step strain experiment and measuring the relaxation modulus $G(t)$, one may be able to identify a single or a few characteristic relaxation times, for example semidilute worm-like micelle solutions [27]. Such fluids are called Maxwell-like (See Chapter 2 for more details on the single mode and multi-mode Maxwell models). However multiscale complex fluids, on account of the multiscale nature of their microstructures, do not possess an easily discernible relaxation time. Instead, $G(t)$ exhibits a broad power law-like response, with $G(t) \sim t^{-\alpha}$, $0 < \alpha < 1$. In the next section, we examine the microstructure of multiscale complex fluids in more detail, and discuss the need for compact constitutive models for this class of materials.

1.3 Multiscale Complex Fluids

In Figures 1.3.1 and 1.3.2, we show examples of power law relaxation spectra of various complex fluids. A brief description of the fluids is given in the corresponding figure captions. We observe that in all cases, the relaxation modulus $G(t)$ has a power law dependence with time, i.e., $G(t) \sim t^{-\alpha}$. The figures show stress relaxation experiments performed at various strain amplitudes. At larger strain amplitudes, the relaxation modulus decreases progressively with increasing amplitude γ_0 . This is a nonlinear effect, and we describe the quantification of such nonlinear effects in Chapter 4. In this introduction, we will focus our attention on $G(t)$ obtained in the linear regime, where it is independent of strain amplitude.

A single power law is the simplest form of multiscale response to a step strain (given by Equation (1.2.4)). It is often the case that more complex multiscale power law response is experimentally observed. For example, the relaxation modulus for the organophilic silica colloidal gel [29] shown in Figure 1.3.2(a) shows a power law of the form $G(t) \sim t^{-\beta}$ and short times, and this transitions to a power law of the form $G(t) \sim t^{-\alpha}$ at long times, with $\alpha > \beta$. We discuss in detail how to characterize and model more complex multiscale response such as the dual power law behavior of Xanthan gum in the following chapters of the thesis. For the purposes of this introduction, it suffices to note that the key feature of stress relaxation in multiscale materials is *one or more broad power law regions in the stress relaxation*


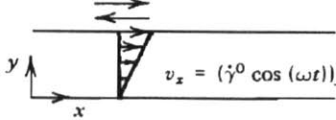
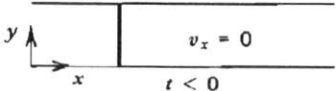

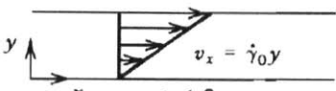
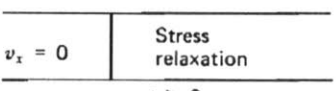
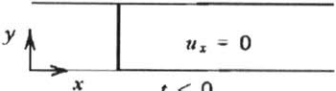
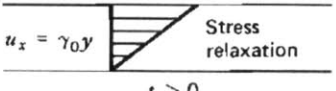
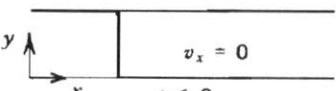
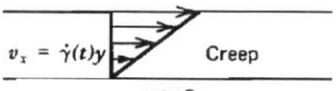
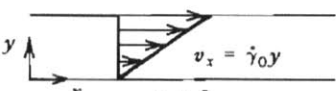
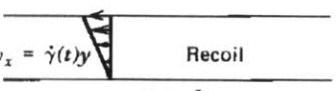
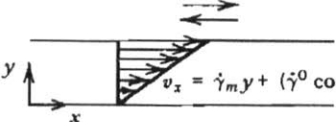
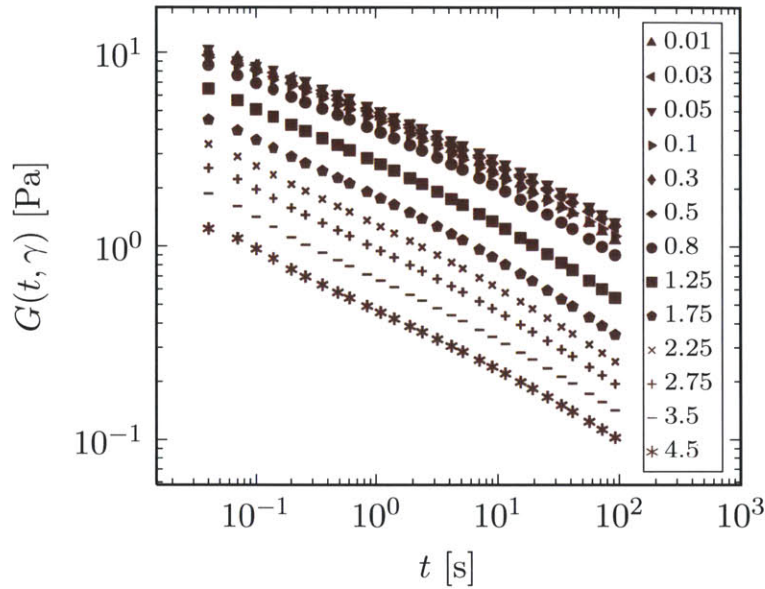
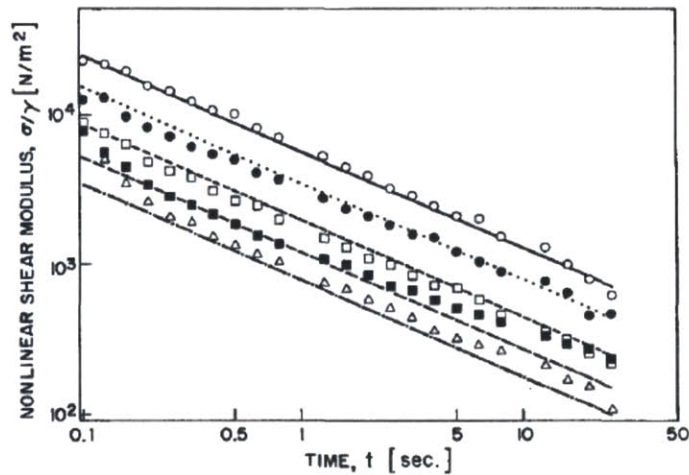
<p>a. Steady shear flow</p>		<p>v_x = velocity in x-direction $\dot{\gamma}$ = shear rate</p>
<p>b. Small-amplitude oscillatory shear</p>		<p>$\dot{\gamma}^0$ = shear rate amplitude ω = angular frequency</p>
<p>c. Stress growth upon inception of steady shear flow</p>	<p>Fluid at rest</p> 	<p>Steady shear flow</p> 
<p>d. Stress relaxation after cessation of steady shear flow</p>	<p>Steady shear flow</p> 	<p>Motion suddenly stopped</p> 
<p>e. Stress relaxation after a sudden shearing displacement</p>	<p>Fluid at rest</p> 	<p>Fluid at rest</p> 
<p>f. Creep</p>	<p>Fluid at rest</p> 	<p>Constant shear stress applied</p> 
<p>g. Constrained recoil after steady shear flow</p>	<p>Steady shear flow</p> 	<p>Shear stress suddenly removed</p> 
<p>h. Parallel superposition of steady shear flow and small-amplitude oscillations</p>		<p>$\dot{\gamma}_m$ = mean value of shear rate $\dot{\gamma}^0$ = amplitude of superposed oscillations ω = angular frequency of oscillations</p>

Figure 1.2.2: List of standard shearing flows used to determine the material functions of complex fluids, from Bird et al. [24]. The left and right columns depict the flow state of the fluid for time $t < 0$ and $t > 0$ respectively. For definitions of the material functions for each flow, see Refs. [24] and [26]. We provide definitions and expressions for many of these material functions at appropriate locations of this thesis.

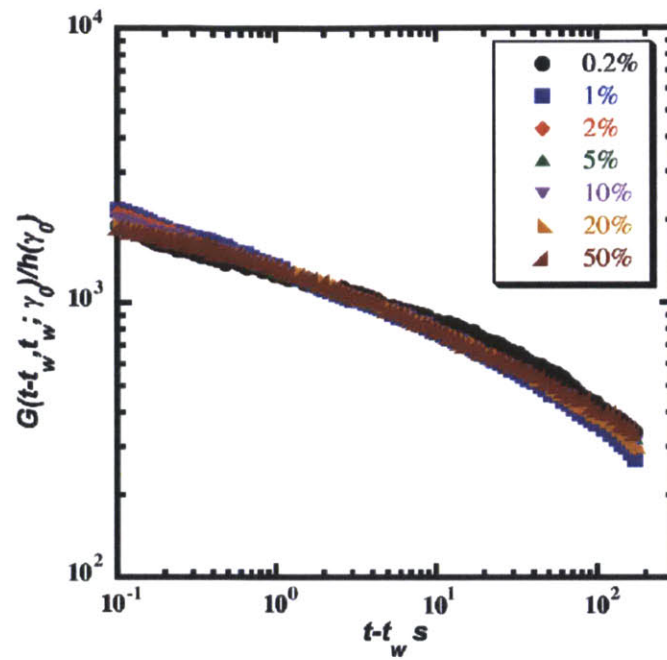


(a)

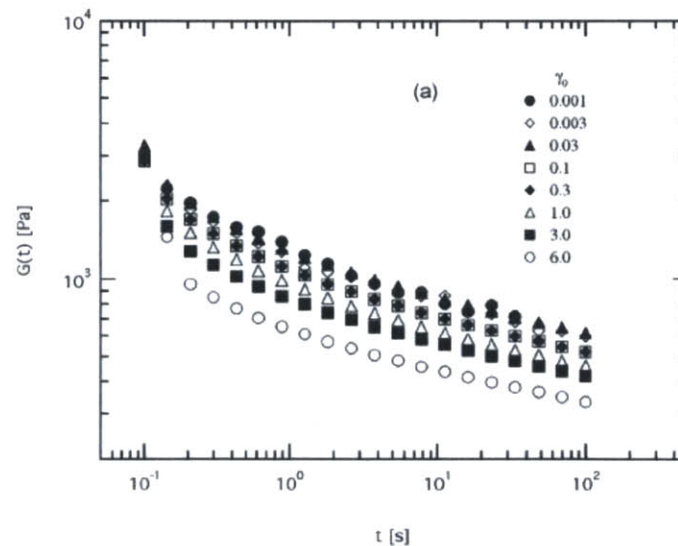


(b)

Figure 1.3.1: Examples of experimentally measured relaxation moduli $G(t)$ that exhibit multiscale power law response. In both cases, we observe broad relaxation spectra with no easily discernible characteristic timescale. (a) Data for 0.5 wt.% Xanthan gum solutions. Each curve corresponds to a different value of strain amplitude γ_0 , whose value is given in the legend. (b) Data for commercial low density polyethylene melt at 160°C . Adapted from Ref. [28]. Similar to (a), each curve corresponds to a different value of strain amplitude: $\gamma_0 = 1$ (hollow circles), $\gamma_0 = 3$ (filled circles), $\gamma_0 = 5$ (hollow square), $\gamma_0 = 7$ (filled squares) and $\gamma_0 = 9$ (hollow triangles). The decrease in $G(t)$ with increasing γ_0 is a nonlinear effect which we describe in detail in Chapter 4.



(a)



(b)

Figure 1.3.2: Examples of experimentally measured relaxation moduli $G(t)$ that exhibit multiscale power law response. (a) Thermoreversible colloidal gel consisting of organophilic silica below the gel temperature $T = 23$ °C. Adapted from Ref. [29]. Each symbol corresponds to a different strain amplitude, and a master curve has been constructed using a damping function $h(\gamma_0)$ (see Chapter 4 for details). (b) Data obtained for gluten gels, which is a branched biopolymer matrix with starch globules occupying the pores of the matrix. Figure adapted from Ref. [30]. As in the previous figure, the decrease in $G(t)$ with increasing γ_0 is a nonlinear effect.

response, with no easily discernible characteristic timescale. A power law relaxation modulus $G(t)$ also implies power law behavior in other linear viscoelastic material functions such as the creep compliance $J(t)$ or the elastic and viscous moduli, $G'(\omega)$ and $G''(\omega)$ respectively, because of the nature of the inter-relations between these material functions [26].

Such multiscale power law response can arise from different underlying microstructural physical mechanisms. For example, the polyethylene melt shown in Figure 1.3.1(b) is highly polydisperse [28]. Each molecular weight has its own characteristic relaxation time associated with it, and given a polymer solution with a broad and continuous distribution of molecular weights, a unique relaxation time cannot be identified. As a first approximation, one may think about the origin of the power law response in terms of the existence of a large number of relaxation modes, one each for a particular molecular weight in the distribution. However, because of the polydispersity, these multiple modes are very closely spaced. This leads to a broad, multiscale power law response in which no unique characteristic time scale can be identified. Therefore, in the case of polydisperse polymer solutions, the power law relaxation arises from multiple length scales existing at molecular scales.

On the other hand, power law relaxation could also arise due to multiple length scales that exist at scales larger than molecular. For example, consider Figure 1.3.3, in which we show the microstructure of (a) a gel obtained by coagulating milk through the addition of rennet, (b) curds obtained by cooking the resultant gel under gentle stirring and (c) cheese produced by aging the cooked curds for one week under mechanically applied pressure. These figures have been reproduced from the work of Ong et al. [31]. The scale bar in the left and right columns of figures (marked a1, b1 & c1, and a2, b2 & c2) is 20 μm and 10 μm respectively. We observe that in addition to length scale distributions at the molecular level arising from the various proteins and polysaccharides present in milk and cheese, the microstructure itself consists of a wide distribution of holes, pores and domains of fat and protein. At these microstructural scales too, we see the signature of multiscale systems: it looks the same when inspected from nearby or from far [9] (within reasonably physical length scales, as discussed previously). Such a microstructural distribution of length scales also leads to power law stress relaxation upon the imposition of a mechanical deformation. The rationale here is identical to the soft glassy rheology model [18, 32], which applies to materials that consist of discrete and numerous coarse-grained blobs of material [33] that interact with each other weakly. In such multiscale materials, if the energy landscape around a coarse-grained blob of material is such that the distribution of energy wells around

a blob has an exponential tail, it can be shown that this distribution of energy wells leads to a power law distribution of relaxation timescales i.e. multiscale stress relaxation.

There are other molecular or microstructural physical mechanisms that give rise to multiscale stress relaxation, characterized by the broad power law rheological response observed in Figures 1.3.1 and 1.3.2. For example, in crosslinked networks with dangling chain ends, Curro and Pincus [34] have assumed that the stress contribution due to each chain end at time t is proportional to the length of the chain $l(t)$ that has not relaxed at time t . By estimating $l(t) \approx \alpha^{-1} \ln(t/\tau_1)$, where α and τ_1 are material constants, and a distribution of polymeric chain lengths, they are able to show that such crosslinked networks exhibit power law stress relaxation. Indeed, it has been experimentally verified that crosslinked gels often exhibit power law stress relaxation in bulk rheological experiments [35, 36].

A more direct measurement of the multiple length scales present in power law materials such as gels and soft glasses is through microrheological experiments [37, 38]. In these experiments, a tracer particle is introduced into the bulk of the complex fluid and its thermally driven motion is tracked as a function of time. As long as the particle is much larger than the length scale of heterogeneities in the fluid, the viscoelastic spectrum $\tilde{G}(s)$ can be calculated from the Mean Squared Displacement (MSD) $\langle \Delta \tilde{r}^2(s) \rangle$ traveled by the tracer particle, where s is the Laplace domain variable. $\tilde{G}(s)$ is related to the relaxation modulus $G(t)$ through the relationship [26, 39]

$$\tilde{G}(s) = s\mathcal{L}[G(t)] \quad (1.3.1)$$

where $\mathcal{L}[G(t)]$ is the Laplace transform of the relaxation modulus $G(t)$ given by

$$\mathcal{L}[G(t)] = \int_0^{\infty} G(t') e^{-st'} dt' \quad (1.3.2)$$

We find $\tilde{G}(s)$ from the generalized Stokes-Einstein equation: [37]

$$\tilde{G}(s) = \frac{k_B T}{\pi a s \langle \Delta \tilde{r}^2(s) \rangle} \quad (1.3.3)$$

in which k_B is the Boltzmann's constant, T is the absolute temperature, a is the radius of the tracer particle and s is the Laplace frequency. As we have discussed previously, a Newtonian (purely viscous) fluid has no memory and hence the relaxation modulus $G(t) = \eta_0 \delta(t)$, η_0

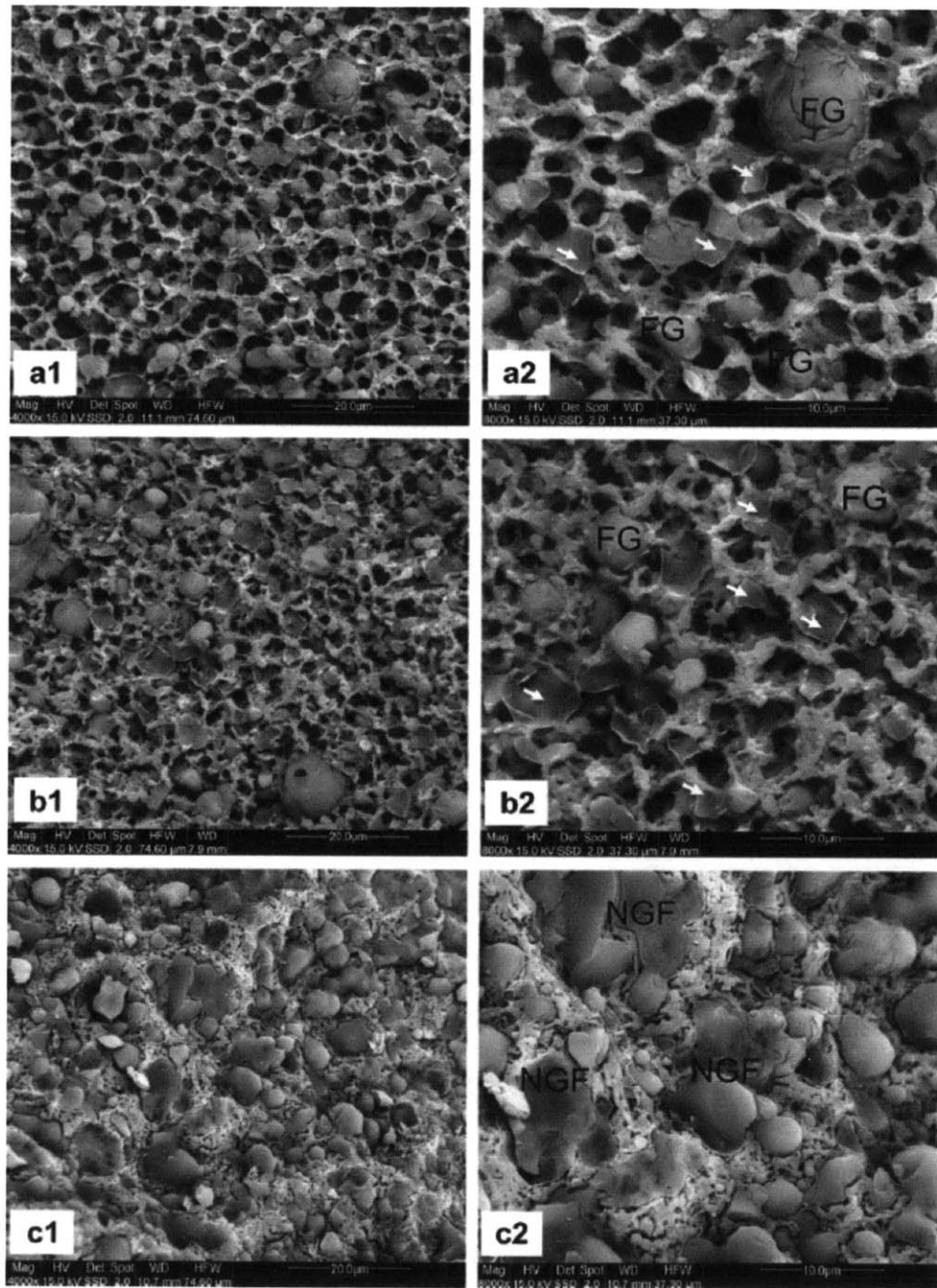


Figure 1.3.3: Cryo scanning electron microscopy images of (a1,a2) a gel obtained by coagulating milk through the addition of rennet, (b1,b2) curds obtained by cooking the resultant gel under gentle stirring and (c1,c2) cheese produced by aging the cooked curds for one week under mechanically applied pressure. Column 1 has a scale bar of 20 μm and column 2 has a scale bar of 10 μm . The multiscale nature of these materials is clearly visible, and there is a broad distribution of pore and globule sizes. Images reproduced from Ref. [31].

being the viscosity of the fluid, and $\delta(t)$ is the Dirac-Delta function [25]. Substituting this expression for $G(t)$ into Equation (1.3.3) and inverting the Laplace transform to solve for $\langle \Delta r^2(t) \rangle$ we obtain

$$\langle \Delta r^2(t) \rangle = 6Dt \quad (1.3.4)$$

where $D = k_B T / 6\pi a \eta_0$ is the coefficient of diffusion, i.e., the MSD of a thermally diffusing spherical particle in a Newtonian fluid varies linearly with time. This is a familiar classical result known derived by Einstein for particles diffusing through Brownian motion [40]; the motion of a diffusing particle can be modeled as a random walk.⁴

We consider a particle (called a walker) that takes steps of fixed length at a fixed intervals of time. However, the direction of motion at each step is chosen at random. The important point to note here is that each step is not correlated with the previous step. In this case, it can be shown that the probability of finding the walker at a distance r away from the origin is given by a Gaussian distribution. Equation (1.3.4) for the MSD can then be found from the second moment of this Gaussian distribution [41]. In Figure 1.3.4 we show an example of a random walk generated computationally.

However, the MSD of a diffusing tracer particle in a very large number of multiscale complex fluids does not obey Equation (1.3.4) [42]. Instead, such materials are *subdiffusive*,

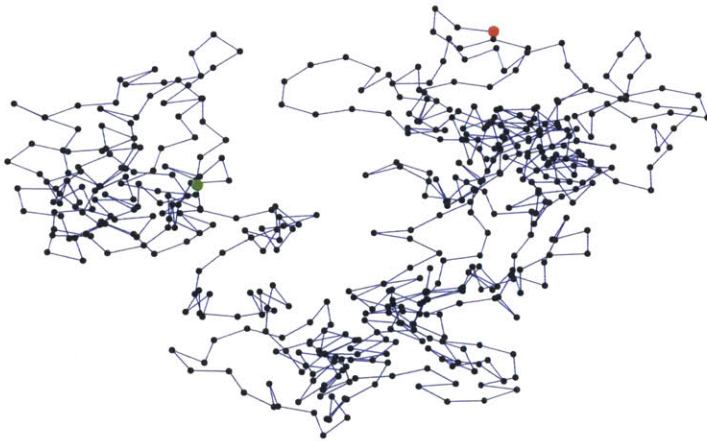


Figure 1.3.4

A simulated example of a 2D random walk, with the walker taking steps of equal length at constant intervals of time in a randomly chosen direction. The green and red dots indicate the starting and ending locations of the walk, and the black dots connected by blue lines represent the intermediate steps. For a 2D random walk with a large number of steps, the MSD $\langle \Delta r^2 \rangle \sim t$.

⁴Einstein's paper on Brownian motion is part of his so-called *Annus Mirabilis* papers, published in the journal *Annalen der Physik* in 1905. The other papers that he published that year include those on the photoelectric effect, special relativity and the mass-energy equivalence, all of which have since revolutionized physics.

and the MSD varies with time as [43, 44]

$$\langle \Delta r^2(t) \rangle \sim t^\alpha \quad (1.3.5)$$

where $0 < \alpha < 1$. Examples of complex fluids that exhibit such anomalous subdiffusive behavior are colloidal gels [17], cytoskeletal networks [45], semidilute polymer solutions [37], and soft glasses [32]. This anomalous diffusion is a direct consequence of the presence of a broad distribution of length scales in the microstructure of multiscale complex fluids. The diffusion process in these materials is now hindered by the distribution of length scales, and a tracer particle is liable to get *trapped* at certain locations [42, 46], i.e., trapped at certain energy wells, and has to wait at that location until it can jump out of the energy well it is trapped in. Such an intermittent jumping diffusion mechanism has been experimentally visualized, for example in entangled F-actin networks [47]. The trapping process followed by subsequent jumping can be modeled by a *Continuous Time Random Walk* (CTRW); rather than the walker making discrete steps at fixed intervals of time, the random walk is characterized by a waiting-time distribution $\psi(t)$ [48]. For a multiscale complex fluid, an analytical form for the waiting-time distribution $\psi(t)$ that models experimentally observed material response is given by

$$\psi(t) \sim \left(\frac{t}{\tau} \right)^{-(1+\alpha)} \quad (1.3.6)$$

where τ is a constant and $0 < \alpha < 1$. This form of $\psi(t)$ captures the fact that multiscale materials contain a broad distribution of length scales, which leads to a broad, scale-free waiting-time distribution. It can be shown for this form of $\psi(t)$ that the CTRW predicts a MSD of the power law, subdiffusive form given in Equation (1.3.5) [42, 49]. Using Equation (1.3.3), it is then straightforward to derive power law stress relaxation from the power law subdiffusion predicted by a CTRW. We show the difference between the regular random walk proposed by Einstein and a CTRW in Figure 1.3.5, adapted from Sokolov et al. [49]. This is a 1-D random walk, with the walker restricted only to the x -dimension. The position of the walker is plotted as a function of time as a black curve. The blue and red curves are plots of, respectively, $\langle \Delta x^2 \rangle^{1/2} \sim t^{1/2}$ (regular random walk, left figure) and $\langle \Delta x^2 \rangle^{1/2} \sim t^{1/4}$ (CTRW with $\alpha = 1/2$, right figure) [49]. We observe that a CTRW, due to its subdiffusive nature, covers less ground than a regular random walk for the same value of elapsed time. The filled yellow curves show the probability $P(x, t)$ of finding the particle

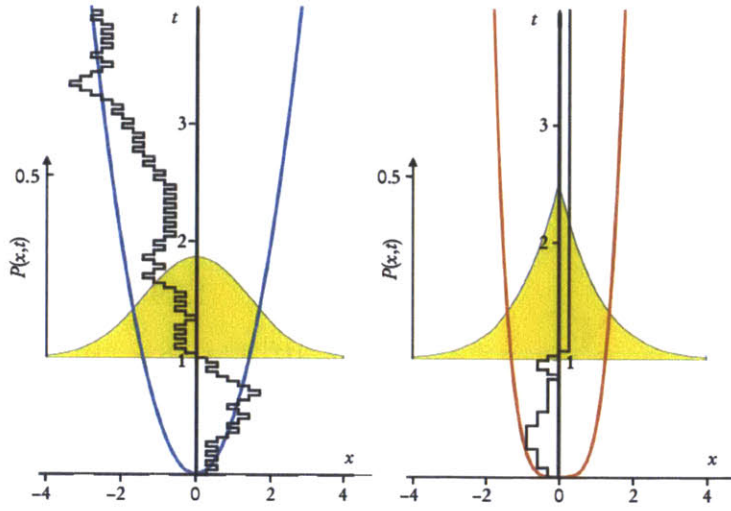


Figure 1.3.5

Comparison of a regular random walk (left), and a Continuous Time Random Walk (right) exhibited by subdiffusive systems. The blue curve and red curves indicate MSD of the form $\langle \Delta x^2 \rangle^{1/2} \sim t^{1/2}$ and $\langle \Delta x^2 \rangle^{1/2} \sim t^{1/4}$ respectively. The yellow shaded regions plot the probability $P(x, t)$ of finding the walker at location x at time t . We observe that a CTRW covers less ground for the same interval of elapsed time. Figure reproduced from Ref. [49].

at position x at time t . The CTRW has a characteristic cusp [42, 49], and is a *narrower* distribution, indicating that a particle starting at the origin $x = 0$ is likely to be nearer to the origin after time t in the CTRW.

The preceding arguments and discussions demonstrate that there are various physical mechanisms taking place at the molecular or microstructural level that lead to power law behavior. Because of this diversity, a very wide range of complex fluids exhibit such a mechanical response under externally applied deformations. Given the ubiquity of multiscale materials in fundamental research and industrial applications, it is of vital importance to possess models for their material response in order to obtain an quantitative understanding of the material, and perhaps more importantly, make predictions of the rheological response of these complex fluids under arbitrary linear and nonlinear deformations. We next discuss the approaches currently used to model multiscale materials, and discuss some of their shortcomings.

A widely used technique to model multiscale rheological response is the so called Prony series, in which the relaxation modulus $G(t)$ is given by a sum of exponentials [26]:

$$G(t) = \sum_{i=0}^{\infty} G_i e^{-t/\tau_i} \quad (1.3.7)$$

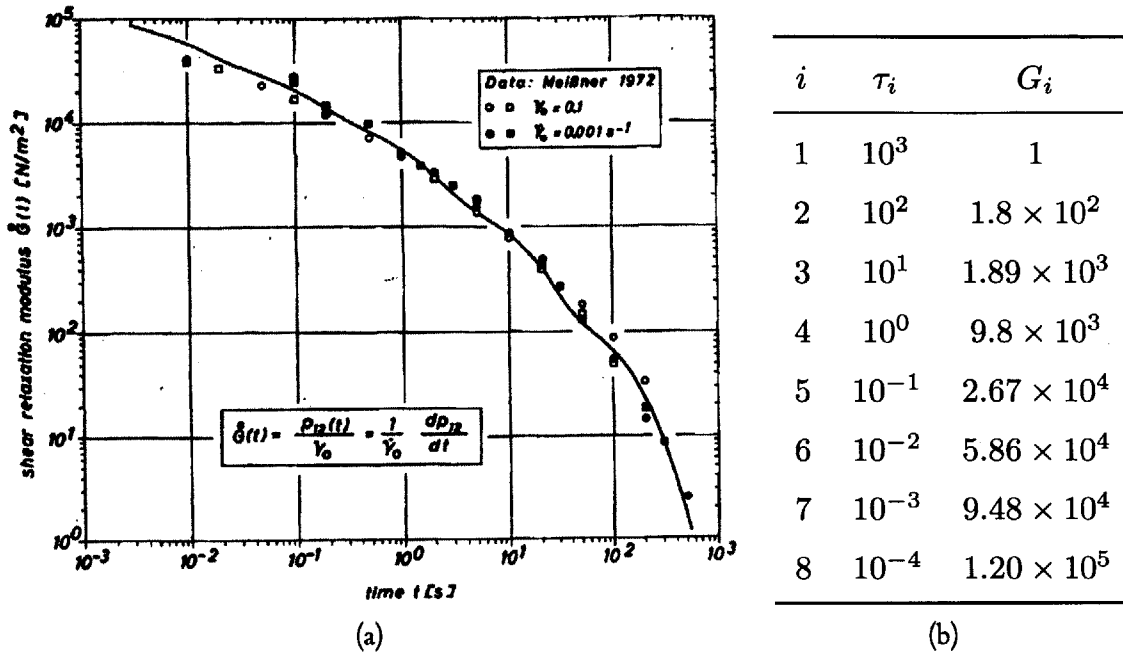


Figure 1.3.6: (a) Relaxation modulus data and multimode Maxwell fit (Prony series, Equation (1.3.7)) reproduced from Laun [51]. Eight modes were required to fit the data, whose relaxation times τ_i were chosen arbitrarily. The fit is shown by a solid black line and the values are shown in (b). Note the waviness in the fit introduced by the multimode Maxwell model for $1 \leq t \leq 200$. In this thesis, we present models that circumvents the need to introduce a large number of modeling parameters for broad multiscale relaxation spectra.

where G_i is the modulus and τ_i is the relaxation time of the i -th mode.⁵ A Prony series generalizes the idea of a single-mode exponential Maxwell-Debye response [50], which we discuss in greater detail in the next chapter. The rationale for the form of $G(t)$ given in Equation (1.3.7) is that there are multiple stress relaxation processes simultaneously taking place in the material, each taking place exponentially with its own characteristic relaxation time τ_i and modulus G_i . We therefore discretize the overall relaxation spectrum as being composed of a sum of these individual relaxation modes. In Figure 1.3.6a we show some classic measurements for the relaxation modulus $G(t)$ (symbols) of a Low Density Polyethylene (LDPE) melt due to Laun [51]. The black line is a fit to the data obtained from a Prony series (Equation (1.3.7)) consisting of 8 modes. We tabulate the fit param-

⁵In practice, the number of modes N over which the fit is performed is finite. N depends on the range of available data, and the behavior of the spectrum.

ters in Figure 1.3.6(b). This approach seems to work in practice and we are able to obtain a reasonably good fit over five decades of time. However, we often require to determine a large number of fitting parameters. Furthermore, the specific values of τ_i were chosen arbitrarily (in this case at every decade of time), and even after this choice, we are still left with an eight parameter fit⁶. Because of this choice, the values of the relaxation times τ_i and moduli G_i are not unique [19], and it becomes meaningless to assign a physical basis for the moduli G_i and relaxation times τ_i [33]. Perhaps more importantly, in multiscale complex fluids such as emulsions, colloidal gels and soft glasses, assuming a discrete set of relaxation modes is not an accurate physical description of the relaxation process taking place in the material which are metastable, non-equilibrium systems [52]; the relaxation process is more accurately described by the Soft Glassy Rheology model (SGR), in which coarse-grained material domains are continuously hopping between a distribution of energy states in the system [18], and relaxation takes place when elastic energy released during hopping between energy states is viscously dissipated. This relaxation process implies that elasticity and viscosity, rather than being independent, are intricately connected. This has been experimentally observed in various multiscale systems showing power law behavior, for example in crosslinking gels at criticality [35]. Again, this indicates that the discretization of elasticity into springs, and viscosity into dashpots—as in the Prony series given in Equation (1.3.7)—is not a true description of the physics of the relaxation mechanism in these multiscale complex fluids.

1.4 *Aims of This Thesis*

The discussions in this chapter have highlighted the ubiquity of multiscale complex fluids. They include such diverse classes of complex fluids such as colloidal gels, soft glasses, emulsions, physically and chemically crosslinked gels, and viscoelastic interfaces [53, 54]. This makes them critical materials in a multitude of industrial, biological and fundamental research applications. It is thus of vital importance to possess compact constitutive frameworks that enable the quantitative description of multiscale complex fluids, and subsequently make

⁶Under the assumptions of the Rouse model for dilute polymer solutions [24], the relaxation time τ_i of the i -th mode is given by $\tau_i = \tau_0/i^2$ and the modulus of the i -th mode is given by $G_i = G_0\tau_i/\sum_k \tau_k$. This reduces the number of parameters to be fit to two. However, the Rouse model is applicable to a relatively limited class of complex fluids [20], and in general, the Prony series involves fitting a large number of material parameters.

predictions of material response under complex and arbitrary deformation profiles.

The chief goal of this thesis is to develop compact constitutive frameworks for multiscale complex fluids. Fractional constitutive equations have been shown to be particularly good models to describe the rheological response of complex fluids that exhibit broad power law responses [55–57]. The subdiffusion observed at the microscale is well modeled by the fractional Fokker–Plank equation [49, 58]. We adopt a continuum approach, and formulate fractional constitutive equations by modeling the viscoelasticity of multiscale complex fluids in terms of mechanical models. In particular, fractional constitutive equations make use of a mechanical element known as the springpot [59], which interpolates between the canonical responses of a spring (Equation (1.2.1)) and a dashpot (Equation (1.2.2)). We show how these models capture the complex multiscale response exhibited by a diverse variety of complex fluids using only a small number of parameters, and enable us to make predictions of material response in both the linear and nonlinear regimes under complex externally applied deformation profiles. Possessing the *analytical* expressions to make such predictions of material response is of immense utility when direct experimental measurements are likely to have artifacts, for example materials that exhibit wall slip under steady shearing deformations [60].⁷

A complete description of the rheology of complex fluids involves the characterization of their *shear* as well as *extensional* rheology. The extensional properties of a complex fluid are often vastly different from their shear properties [61]. In extensional flows, fluid material elements are primarily elongated, and the deformation is essentially shear-free [24]. These flows are important in various industrial processes such as fiber spinning, extrusion, film blowing and spraying, and in applications such as enhanced oil recovery, turbulent drag reduction and atomization [61]. They are also critical to the function of various biologically relevant fluids such as saliva [62] and Hyaluronic acid [63]. Moreover, due to the complex multi-component nature of biological fluids, their microstructures possess multiple length scales and they exhibit broad power law relaxation spectra in viscometric flows. A brief survey of the literature indicates that the extensional rheology of multiscale complex fluids is relatively unexplored.

⁷In Appendix A, we provide an example of the utility of possessing an analytical expression for the solution of a physical problem. We analytically solve the problem of microchannel gas flows with Knudsen number $Kn \sim 1$, where momentum transport due to self-diffusion can be a significant fraction of the total momentum flux. The analytical expressions enable us to examine a boundary layer-like flow regime that appears under certain conditions of inlet and outlet pressures across the microchannel.

Therefore, in this thesis, we also experimentally characterize the extensional rheology of multiscale complex fluids. We focus our attention on aqueous polysaccharide solutions given their immense industrial and biological applications [64]. For example, the swallowing and digestive process, as the food bolus moves from the mouth through the digestive tract involves extensional deformations, and fluid elements are stretched or elongated [65, 66]. Patients suffering from dysphagia, which is defined as a difficulty or inability to swallow, do not possess the muscular control required for the swallowing process [67]. Thickening agents are hence added to foods to slow down the process of bolus transport, and hence allow more time for musculature control. These thickening agents are very frequently aqueous polysaccharides such as Xanthan gum [68], which also exhibit broad multiscale rheological response [69]. A detailed understanding of the extensional rheology of power law aqueous polysaccharides will therefore help in the formulation of better food thickeners and treatments for dysphagia.

Polysaccharides are also critical in other biological fluids such as Hyaluronic acid (HA) found in mammalian synovial fluid (SF) [70]. Synovial fluid has been identified as being a critical component in the lubrication of mammalian joints. In everyday activities such as running or jumping, the synovial fluid in joints can be modeled as undergoing a squeeze flow⁸ with strong extensional components [63]. It has been observed that in the joints of patients suffering from osteoarthritis, the molecular weight of the HA in synovial fluid is decreased, leading to decreased extensional viscosities. As a result, the lubricating ability of SF is decreased. A characterization of the extensional rheology of HA will therefore help in diagnostics as well as treatments for osteoarthritis.

The remainder of this thesis is organized as follows: in the next chapter, we provide the necessary mathematical background and describe in detail the basic principles of fractional constitutive equations and fractional derivatives. We develop the canonical fractional constitutive models that we will use throughout this thesis. In Chapter 3, we demonstrate the ability of fractional constitutive equations to quantitatively describe the linear viscoelastic behavior of multiscale complex fluids. We take the specific example of the viscoelastic air-solution interfaces formed by globular protein solutions, and show how predictions of material response can be obtained under complex externally applied deformations. Chapter 4 extends the capabilities of fractional constitutive equations to nonlinear shear deforma-

⁸We present a quantitative analysis for this in Chapter 6

tions, and we show how predictions of nonlinear rheological response can be obtained from characterizing the material in a linear viscoelastic experiment. We use the fractional model framework to assess the performance of heuristic nonlinear rules and quantify the systematic offsets, or shift factors, that can be observed between experimental data and the heuristically predicted nonlinear response. In this chapter, we also demonstrate how one can obtain various empirically proposed and widely employed nonlinear flow relationships starting with a suitable fractional constitutive framework.

We transition to the study of the extensional rheology of multiscale power law materials in Chapter 5. We specifically examine tack experiments performed on pressure sensitive adhesives, which are often chemically crosslinked gels exhibiting multiscale response. We show that combining a fractional constitutive equation with the lubrication flow kinematics of a Newtonian fluid, we obtain accurate predictions of the tack forces generated in the small strain limit.

Chapter 6 focuses on an experimental study of the extensional rheology of multiscale complex fluids under large strains. Using the techniques of Capillary Breakup Extensional Rheometry (CaBER) and Filament Stretching Extensional Rheometry (FiSER), we probe the nature of intermolecular interactions in an aqueous polysaccharide solution known as Mamaku gum [71–73] which has potential applications as a food thickener and as a treatment for dysphagia. These interactions also lead to broad power law response in shear rheological experiments. We also use the recently developed Optimized Shape Cross-Slot Extensional Rheometer (OSCER) [74] to measure and characterize the extensional rheology of Hyaluronic acid solutions. Finally, we conclude in Chapter 7 and present some avenues for future research.

2 | *Mathematical Background*

In this chapter, we begin our discussion of fractional constitutive equations. We introduce the notion of the fractional derivative as a generalization of integer order derivatives. We then construct a mechanical element called the springpot, and then incorporate it into continuum based mechanical models to construct fractional constitutive equations. We pay particular attention to the Fractional Maxwell model and Fractional Kelvin-Voigt model (FMM and FKVM respectively), both of which we frequently use throughout this thesis. Some of the important mathematical relationships and results given in this chapter are tabulated in Appendix B.

2.1 Linear Viscoelasticity

2.1.1 The Linear Viscoelastic Maxwell Model

In Chapter 1, we introduced the notions of springs (Equation 1.2.1) and dashpots (Equation 1.2.2) as the most elementary constitutive equations, which are relationships that relate stress to the state of deformation in the material. The springs are purely elastic, while dashpots are purely viscous. One of the simplest mechanical models that captures viscoelastic material response is the Maxwell model, which consists of a spring and a dashpot connected in series [26]. This model was introduced by James Clerk Maxwell (cf. Figure 2.1.1) in the context of a theory of gases [75]. [b] We show a schematic figure of the Maxwell model in Figure 2.1.2. The constitutive equation of the Maxwell model can be derived by considering equality of the stress in the elements ($\sigma(t) = \sigma^{(s)}(t) = \sigma^{(d)}(t)$) and additivity of strains

**Figure 2.1.1**

James Clerk Maxwell, Scottish physicist who is widely considered as one of the greatest classical physicists [22]. His most important work was the unification of electricity and magnetism, and proving that visible light is part of a much larger electromagnetic spectrum. He also made important contributions in the kinetic theory of gases and in linear viscoelasticity. His proposal of a viscoelastic model containing both elasticity and viscosity [75], now referred to as the linear viscoelastic Maxwell model has led to various linear, nonlinear and frame invariant generalized models that can capture a wide range of rheological behavior. Examples of these models are the generalized Maxwell model (Equations 2.1.10, 2.1.11), the upper and lower convected Maxwell models [24] and the Wagner model [76]. Image is in the public domain.

$(\gamma^{(s)} = \gamma^{(d)})$ and we obtain [26]

$$\sigma(t) + \frac{\eta_0}{G_0} \frac{d\sigma(t)}{dt} = \eta \frac{d\gamma}{dt} \quad (2.1.1)$$

in which $\sigma(t)$ is the instantaneous stress (units: Pa), $\gamma(t)$ is the instantaneous strain (dimensionless), G_0 is the modulus of the spring (units: Pa) and η_0 is the coefficient of viscosity of the dashpot (units: Pa s).

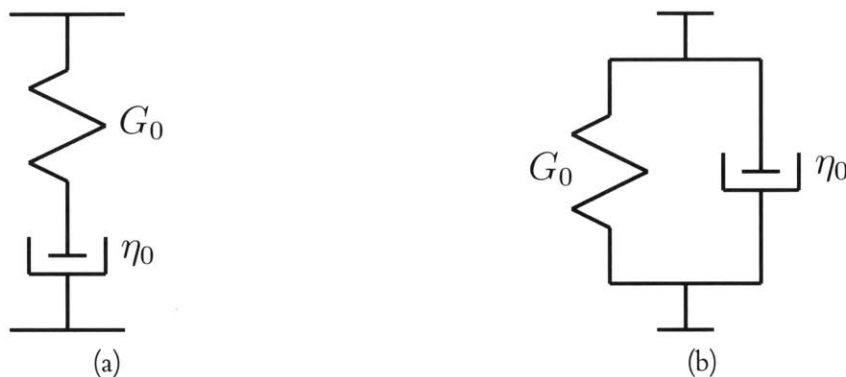


Figure 2.1.2: Schematic figures of the simplest two element mechanical models used in rheology. (a) the linear viscoelastic Maxwell model, with a spring of modulus G_0 and a dashpot of viscosity η_0 connected in series and (b) the linear viscoelastic Kelvin Voigt model, with the spring and the dashpot connected in parallel. The representation of linear viscoelasticity in terms of mechanical models with multiple elements is a useful aid to thinking.

The advantage of an explicit constitutive relationship such as Equation 2.1.1 that relates the stress and the strain in the material is that it is straightforward to derive the standard linear viscoelastic shear material functions. We describe below the material functions that we will often use in this thesis. However this is by no means exhaustive; detailed expressions of the various material functions obtained for different constitutive equations may be found in standard textbooks [19, 24, 77].

As described in Chapter 1, we may obtain the relaxation modulus $G(t)$ of the Maxwell model by imposing a shear strain of the form $\gamma(t) = \gamma_0 H(t)$ (see Equation 1.2.4) and measuring the resulting stress response as a function of time. Substituting this strain deformation profile into Equation 2.1.1 we obtain

$$\sigma(t) + \frac{\eta_0}{G_0} \frac{d\sigma(t)}{dt} = \eta\gamma_0\delta(t) \quad (2.1.2)$$

where $\delta(t)$ is the Dirac Delta function [25]. Solving for $G(t) = \sigma(t)/\gamma_0$, with the initial condition $G(0) = G_0$, we obtain

$$G(t) = G_0 e^{-t/\tau} \quad (2.1.3)$$

where

$$\tau = \eta_0/G_0 \quad (2.1.4)$$

is a relaxation time. This is the classic Maxwell-Debye response [42].

Much insight into the linear viscoelastic response of complex fluids can also be obtained through small amplitude oscillatory shear (SAOS) deformation [77]. In this dynamic experiment a sinusoidally varying deformation profile of the form

$$\gamma(t) = \gamma_0 \sin(\omega t) \quad (2.1.5)$$

is applied to the sample, in which ω is the frequency of the oscillation. Note that substituting this deformation profile into an elastic Hookean spring (Equation 1.2.1) and a viscous Newtonian dashpot (Equation 1.2.2) we obtain a stress response that is perfectly in-phase (phase angle $\delta = 0$ rad) and quarter cycle out of phase (phase angle $\delta = \pi/2$ rad), respectively, with the applied deformation. For a material that is both elastic as well as vis-

cous (i.e. viscoelastic), the stress response is phase shifted compared to the the strain profile ($0 < \delta < \pi/2$), and we can in general write (for linear deformations) [19]

$$\sigma(t) = G'(\omega)\gamma_0 \sin(\omega t) + G''(\omega)\gamma_0 \cos(\omega t) \quad (2.1.6)$$

in which $G'(\omega)$ is the elastic (or storage) modulus and $G''(\omega)$ is the viscous (or loss) modulus. $G'(\omega)$ is a measure of the energy stored and $G''(\omega)$ is a measure of the energy dissipated in the material per unit volume in one cycle of deformation. The phase difference δ can be written in terms of the linear viscoelastic moduli $G'(\omega)$ and $G''(\omega)$ as

$$\delta = \tan^{-1} \left(\frac{G''(\omega)}{G'(\omega)} \right) \quad (2.1.7)$$

If we substitute the sinusoidal deformation profile of Equation 2.1.5 into the the constitutive equations of a spring and dashpot, Equations 1.2.1 and 1.2.2 respectively, we note that for a spring $G''(\omega) = 0$ whereas for a dashpot $G'(\omega) = 0$, which is the expected purely elastic and purely viscous responses respectively. The process of decomposition of stress into a elastic and viscous components as shown in Equation 2.1.6 holds for all constitutive equations. Taking the specific case of the Maxwell model we substitute Equation 2.1.5 into Equation 2.1.1 to obtain

$$G'(\omega) = G_0 \frac{(\tau\omega)^2}{1 + (\tau\omega)^2} \quad (2.1.8)$$

$$G''(\omega) = G_0 \frac{\tau\omega}{1 + (\tau\omega)^2} \quad (2.1.9)$$

Expressions for the other linear viscoelastic material functions such as the creep compliance $J(t)$ can be found in textbooks [19, 24, 77].

The linear Maxwell, with a single mode exponential relaxation response (Equation 2.1.3) is too simplistic a model for most complex fluids. To capture more complex stress relaxation phenomena, a model that consists of a *superposition* of Maxwell modes can be constructed by placing many linear Maxwell elements in parallel [24]. We show a schematic diagram of this model in Figure 2.1.3, which is called the Generalized (or multimode) Maxwell model. Because stresses add, when elements are placed in parallel, the relaxation modulus $G(t)$ of this model identical to the Prony series given in Chapter 1 (see Equation 1.3.7), with the total modulus being simply a sum of the individual contributions from each parallel arm.

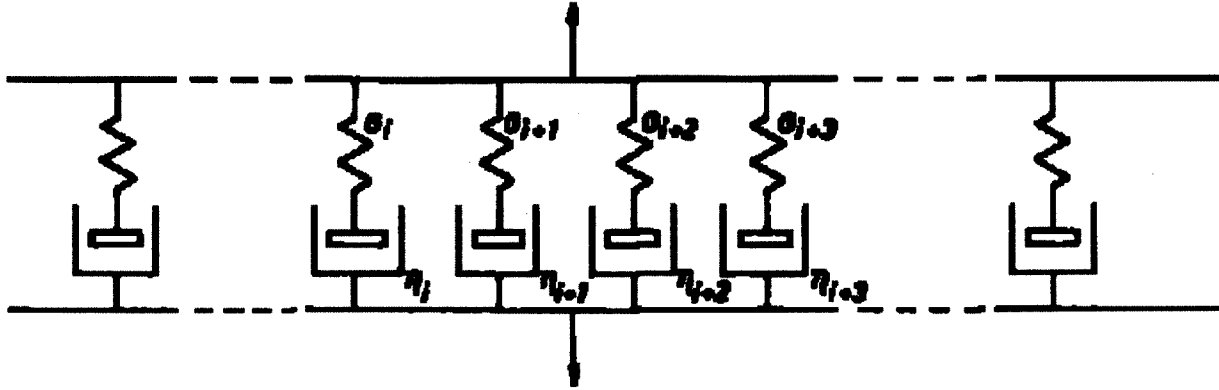


Figure 2.1.3: A schematic figure of the generalized (multimode) Maxwell model. The model consists of multiple Maxwell modes connected in parallel. Each parallel mode represents a mode of relaxation of modulus G_i and relaxation time τ_i . Using this model, a broad *continuous* relaxation spectrum can be modeled by approximating it as a set of *discrete* relaxation modes. Figure reproduced from Ref. [77].

The linear viscoelastic storage and loss moduli, $G'(\omega)$ and $G''(\omega)$ respectively, are given by a superposition of the moduli of the individual modes [19]:

$$G'(\omega) = \sum_{k=0}^{\infty} G_k \frac{(\tau_k \omega)^2}{1 + (\tau_k \omega)^2} \quad (2.1.10)$$

$$G''(\omega) = \sum_{k=0}^{\infty} G_k \frac{\tau_k \omega}{1 + (\tau_k \omega)^2} \quad (2.1.11)$$

Therefore, to describe complicated material response with broad spectra, one may add progressively more mechanical elements in series or parallel to the initial Maxwell element [26], and in the process provide additional modes of relaxation. We thus obtain a broad spectrum of discrete relaxation times that characterize the material response. Most real systems can thus be described in an *ad hoc* way using a sum of exponentials [35]. This has proved to be a very successful modeling approach for the linear viscoelasticity of many complex fluids, for example polymer solutions [78, 79].

However, we have already noted the deficiencies of such an approach in Chapter 1, especially for multiscale complex fluids with broad relaxation spectra; it becomes difficult to assign physical meaning to the model parameters, and the number of parameters to be fit in order to capture the relaxation spectra can be very large, making this approach impractical. Perhaps most importantly, grouping the elastic and viscous contributions to

the stress into springs and dashpots, respectively are abstractions, because there are no real springs or dashpots in the complex fluids. In soft glassy materials, in which each coarse-grained material domain has multiscale, crowded environments, elasticity and viscosity are intricately connected and are not independent [18, 33]. The separation of these properties into springs and dashpots, and reducing what is in reality a continuous relaxation spectrum into discrete modes is an approximation. To quote from the work of G. W. Scott Blair, one of the founding fathers of modern rheology [80],

Normally, one is faced with the choice of selecting a large number of true properties or a smaller number of quasi-properties, since it is nearly always possible to express rheological behavior in terms of true properties provided enough constants are fitted. It is hoped to show that the latter course is by no means always the best.

Motivated by these arguments, in this thesis we present a generalized constitutive framework to model the rheological response multiscale complex fluids. The fundamental concepts in our framework are *fractional derivatives*, *springpots* and *quasi-properties*, which we explore in detail next.

2.2 Fractional Derivatives and the Springpot

We have mentioned in section 1.2 that for linear viscoelastic response, Boltzmann derived a general superposition integral that relates the stress $\sigma(t)$ in the material to the history of the deformation $\gamma(t)$ experienced by a material, which we reproduce here for convenience:

$$\sigma(t) = \int_{-\infty}^t G(t-t') \dot{\gamma}(t') dt' \quad (2.2.1)$$

For example, for the case of a Hookean spring, $G(t) = G_0$ and for a Newtonian dashpot, $G(t) = \eta_0 \delta(t)$ where $\delta(t)$ is the Dirac Delta function [25]. Substituting these into the

Boltzmann superposition integral, we obtain, respectively

$$\begin{aligned}\sigma^{(s)}(t) &= \int_{-\infty}^t G_0 \dot{\gamma}(t') dt' = G_0 \gamma(t) \\ &= G_0 \frac{d^0 \gamma(t)}{dt^0}\end{aligned}\quad (2.2.2)$$

$$\begin{aligned}\sigma^{(d)}(t) &= \int_{-\infty}^t \eta_0(t-t') \dot{\gamma}(t') dt' = \eta_0 \dot{\gamma}(t) \\ &= \eta_0 \frac{d\gamma(t)}{dt}\end{aligned}\quad (2.2.3)$$

in which the superscripts s and d represent, respectively, the mechanical analogues of springs and dashpots as before. For a multiscale complex fluid exhibiting power law behavior (for example chemically crosslinking gels at the sol-gel transition [35, 81]), we experimentally observe that $G(t) = ct^{-\alpha}$ where c (units: Pa s $^\alpha$) and $0 < \alpha < 1$ are constants. Substituting this form of the relaxation modulus into Equation 2.2.1, we obtain

$$\sigma(t) = \int_{-\infty}^t c(t-t')^{-\alpha} \dot{\gamma}(t') dt' \quad (2.2.4)$$

At this point we note that Equation 2.2.4 is mathematically identical to the operation known as the fractional derivative. The Caputo definition of the fractional derivative is given by [82–84]

$$\frac{d^\alpha f(t)}{dt^\alpha} \equiv \frac{1}{\Gamma(m-\alpha)} \int_0^t (t-t')^{m-\alpha-1} f^{(m)}(t') dt' \quad (2.2.5)$$

in which $m-1 \leq \alpha < m$, m is an integer, and $f^{(m)}(t)$ indicates an integer order differentiation of the function $f(t)$ to order m . In rheology, we experimentally find that for multiscale power law relaxation, $0 < \alpha < 1$, and therefore $m = 1$. This enables us to

simplify Equation 2.2.5 as

$$\frac{d^\alpha f(t)}{dt^\alpha} = \frac{1}{\Gamma(1-\alpha)} \int_0^t (t-t')^{-\alpha} \dot{f}(t') dt' \quad (2.2.6)$$

where the overdot indicates a derivative to order 1. Because the Caputo definition of the fractional derivative is defined in terms of a linear integral, the operator itself is linear, and

$$\frac{d^\alpha}{dt^\alpha} (bf(t) + g(t)) = b \frac{d^\alpha f(t)}{dt^\alpha} + \frac{d^\alpha g(t)}{dt^\alpha} \quad (2.2.7)$$

where b is any scalar and f and g are appropriate function [85]. We note that we have provided only *one* definition of the fractional derivative, namely the Caputo derivative. However, other definitions exist, such as the Riemann–Liouville and the Grunwald–Letnikov derivatives. The latter is a fractional generalization of the limit definition of an integer order derivative, and is therefore especially useful in numerical implementations of fractional calculus [86]. In this thesis, we will exclusively use the Caputo definition because it enables the formulation of initial conditions in terms of integer order derivatives. For more information on other definitions, the textbooks by Podlubny [82] and Miller and Ross [85] are good references to consult.¹

A careful inspection of Equations 2.2.6 and 2.2.4 indicate that the latter can be written in terms of a fractional derivative², and we obtain

$$\sigma^{(sp)}(t) = \mathbb{V} \frac{d^\alpha \gamma(t)}{dt^\alpha} \quad (2.2.8)$$

Here we have replaced c of Equation 2.2.4 by the quasiproperty \mathbb{V} , whose meaning we explain in more detail below. It can be shown that in the limits of $\alpha = 0$ and $\alpha = 1$,

¹The field of fractional derivatives has a long and rich history in the mathematics literature. Mathematicians such as Euler [87], Lagrange [88], Laplace [89], Fourier [90], Abel [91], Hardy and Weyl have all studied and worked on these operators. Abel seems to be the first to have used fractional calculus to solve a physical problem (the previous excursions were purely mathematical): he solved the tautochrone problem, which involves finding the shape of the curve for which the time taken by a bead sliding down it without friction and under the influence of gravity is independent of the location of the curve at which the bead is released. Ross [92] provides an excellent historical account of the development of fractional calculus.

²Here we assume that the lower limit of the integral in the definition of the fractional derivative is zero i.e. for $t' < 0$, $\dot{\gamma}(t') = 0$.

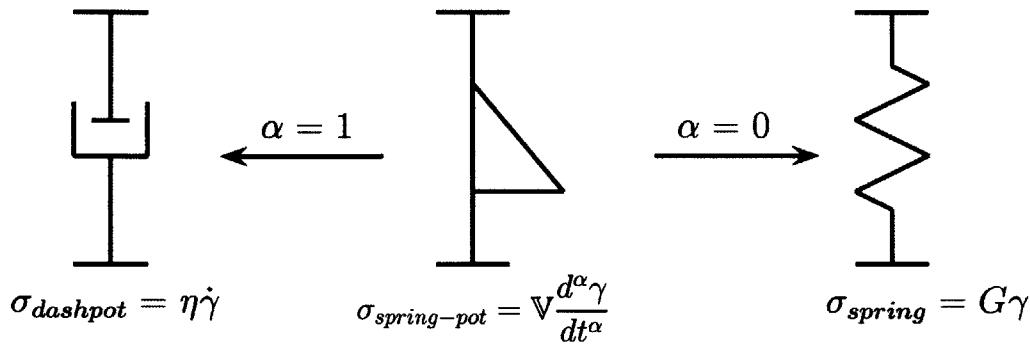


Figure 2.2.1: The schematic representation of a springpot as an element that interpolates between a spring ($\alpha = 0$) and a dashpot ($\alpha = 1$).

Equation 2.2.8 reduces to the constitutive equations of a Hookean spring (Equation 2.2.2) and Newtonian dashpot (Equation 2.2.3) respectively [93]. Therefore, for all other values of $0 < \alpha < 1$, Equation 2.2.8 represents a mechanical element that interpolates between the mechanical responses of a spring and a dashpot [80]. For this reason, Koeller [59] has termed this element the *springpot*. We have schematically shown this intermediate nature of the springpot in Figure 2.2.1.

The two parameters \mathbb{V} and α are the only parameters required to characterize a springpot. For dimensional consistency, the constant \mathbb{V} must have the units (Pa s^α) where $0 \leq \alpha \leq 1$, and can be equated to Scott-Blair's concept of a quasi-property [80]. The quasi-property \mathbb{V} also reduces respectively to the limits of a modulus G_0 (units: Pa) or a viscosity η_0 (units: $[\text{Pa s}]$) in the limiting cases of $\alpha = 0$ and $\alpha = 1$ respectively. The formulation of fractional constitutive equations in terms of quasi-properties has fallen out of use in the recent rheological literature. It is often preferred to write the constitutive equation of a springpot (Equation 2.2.8) as $\sigma^{(sp)}(t) = G_0 \lambda_0^\alpha \frac{d^\alpha \gamma}{dt^\alpha}$, where the modulus G_0 has units of [Pa] and λ_0 has units of [s] (see for example [94]). While this initially seems simply to be a matter of notational convenience, the latter formulation draws attention away from the fact that the fundamental material property that characterizes the behaviour of power law-like materials is the unique quasi-property $\mathbb{V} = G_0 \lambda_0^\alpha$, which characterizes the magnitude of the material response in terms of a single material parameter. In fact it can be shown that it is not possible from simple rheological tests to isolate the individual components (G_0, λ_0, α) , but only the product $G_0 \lambda_0^\alpha$.

The preferred term proposed by Blair et al. for a constitutive law exhibiting springpot

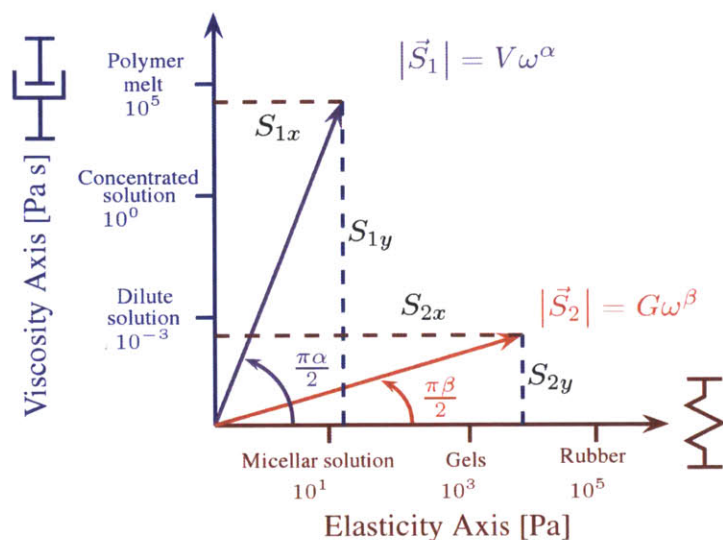


Figure 2.2.2

The geometric representation of a springpot, in which it is interpreted as a vector \vec{S}_1 of magnitude $|\vec{S}_1| = V\omega^\alpha$ that makes an angle $\pi\alpha/2$ with the horizontal axis. Purely elastic responses lie on the horizontal axis, and purely viscous responses lie on the vertical axis. Typical magnitudes for different complex fluids are indicated schematically on each axis. A springpot, on the other hand has projections on both axes and therefore captures intermediate responses. A second springpot \vec{S}_2 of magnitude $|\vec{S}_2| = G\omega^\beta$ and making the angle $\pi\beta/2$ with the horizontal is also shown.

like behaviour was *the principle of intermediacy* [80]. To understand the intermediate nature of a springpot, it is instructive to think about the springpot response graphically as depicted in figure 2.2.2. The horizontal axis represents an ideal elastic response (with S.I. units of [Pa]), and the vertical axis represents a purely viscous response (with S.I. units of [Pa s]). We represent each springpot on this plot as a vector with magnitude $\vec{S}_1 = V\omega^\alpha$, $\vec{S}_2 = G\omega^\beta$ and making an angle $\frac{\pi}{2}\alpha$ or $\frac{\pi}{2}\beta$ with the horizontal axis (ω is the frequency in an SAOS experiment). In such a representation, all Hookean springs and purely elastic responses ($\alpha = 0$) lie on the horizontal axis, and all Newtonian dashpots and purely viscous responses ($\alpha = 1$) lie on the vertical axis. A springpot, on the other hand, has projections S_{1x} and S_{1y} on both the elastic axis as well as the viscous axis respectively, and hence is intermediate between a spring and a dashpot. Such a vectorial representation emphasizes that a springpot spans the parameter space bounded by the purely elastic and purely viscous axes, and in the process generalizes the notions of elastic and viscous material response. For example, a typical power-law gel or elastomeric material may be predominantly elastic in nature (with $G' \gg G''$) but will still have some dissipative character (i.e $\tan \delta = G''/G' \neq 0$), corresponding to a nonzero value of the power law coefficient α . Figure 2.2.2 captures graphically Scott-Blair's concept that was expressed in words as "the use of complex entities as lying a certain

distance between the prototypes” [80, pp. 74]. This vectorial representation also reminds us that the elastic nature and the viscous nature of a single springpot are interrelated and have a constant ratio, as is experimentally observed in a number of gels [13] and soft glassy materials [32].

Schiessel and Blumen [81, 95] have shown that a mechanical equivalent of the springpot exists in terms of an infinite ladder model, shown schematically in Figure 2.2.3. The authors show that for such an arrangement of springs and dashpots, the Laplace-transformed stress is related to the Laplace-transformed strain through a continued fraction expression. In the limit of infinitely many elements, this continued fraction sums to a power law, yielding the constitutive equation of the springpot. Therefore, one physical way to interpret the springpot element is in terms of an infinite ladder model that consists of an infinite number of very closely spaced relaxation modes. We have already explained a microstructural interpretation of the springpot in terms of substituting a power law relaxation kernel in the Boltzmann superposition integral (Equation 2.2.4). The power law kernel itself arises from the multiscale microstructure and the existence of multiple length scales, as explained in Chapter 1.

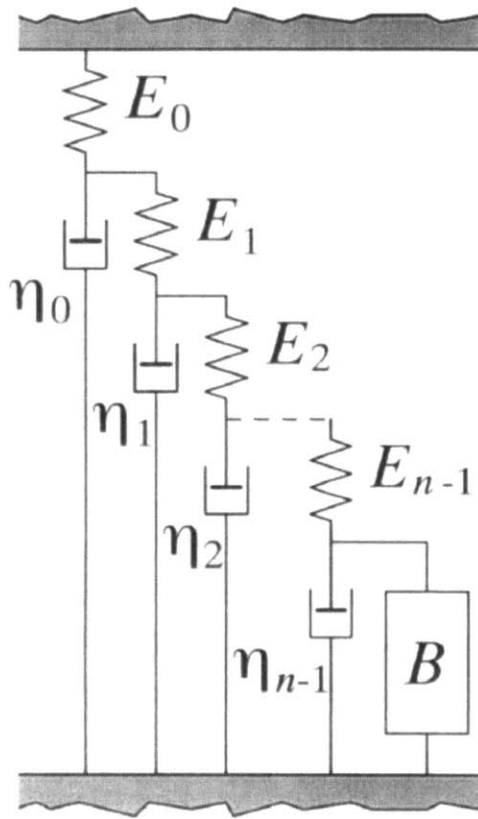
It is relatively straightforward to calculate the linear viscoelastic material functions for the springpot. To calculate the relaxation modulus $G(t)$, we substitute a step strain deformation of the form $\gamma(t) = \gamma_0 H(t)$ (Equation 1.2.4) into the constitutive equation of the springpot (Equation 2.2.8) to obtain

$$\sigma(t) = \mathbb{V} \gamma_0 \frac{d^\alpha H(t)}{dt^\alpha} \quad (2.2.9)$$

We now require to solve this fractional differential equation and find $G(t) = \sigma(t)/\gamma_0$. In our opinion, the easiest way to solve Equation 2.2.9 is through the Laplace transform technique. We exploit the fact that the definition of the fractional derivative involves a linear integral and therefore, the techniques of Laplace and Fourier transforms are applicable [85]. The Laplace transform of the Caputo definition of the fractional derivative is given by [82, 83, 85]

$$\mathcal{L} \left[\frac{d^\alpha f(t)}{dt^\alpha}; s \right] = s^\alpha \tilde{f}(s) - \sum_{k=0}^{n-1} s^{\alpha-k-1} f^{(k)}(0), \quad n-1 < \alpha \leq n \quad (2.2.10)$$

in which $\tilde{f}(s) = \mathcal{L}[f(t); s]$ is the Laplace transform of the function $f(t)$ (defined in Equ-

**Figure 2.2.3**

Schematic figure of an infinite ladder model adapted from Schiessel and Blumen [81]. Setting the box B to be a spring, and then letting $n \rightarrow \infty$, it can be shown that the constitutive equation of such an infinite ladder model is exactly that of the springpot [95]. To intuitively see why this is the case, one may imagine the ladder model as containing n different relaxation modes, each with its own characteristic relaxation time τ_i . Setting $n \rightarrow \infty$ decreases the spacing between these relaxation modes and converts the discrete relaxation spectrum of the finite ladder model to a continuous relaxation spectrum.

tion 1.3.2) and s is the Laplace domain variable. Note that the initial conditions enter into Equation 2.2.10 in terms of integer order derivatives. Therefore, Laplace-transforming Equation 2.2.9, we obtain

$$\tilde{\sigma}(s) = \mathbb{V} \gamma_0 s^{\alpha-1} \quad (2.2.11)$$

which upon rearrangement and inverting the transform³, we obtain the relaxation modulus $G(t)$ of the single springpot as [59]

$$G(t) = \frac{\mathbb{V} t^{-\alpha}}{\Gamma(1-\alpha)} \quad (2.2.12)$$

³We list useful identities related to the Laplace and inverse Laplace transforms of fractional derivatives in Appendix A.

where $\Gamma(z)$ is the Gamma function defined as [25]

$$\Gamma(z) = \int_0^{\infty} x^{z-1} e^{-x} dx \quad (2.2.13)$$

A creep experiment is one in which a stress of the form

$$\sigma(t) = \sigma_0 H(t) \quad (2.2.14)$$

is applied on the material, and the resulting strain response $\gamma(t)$ is measured as a function of time. We define the creep compliance $J(t)$ as

$$J(t) \equiv \frac{\gamma(t)}{\sigma_0} \quad (2.2.15)$$

We can also find $J(t)$ for a single springpot using the Laplace transform technique described above. Substituting Equation 2.2.14 into Equation 2.2.8, we obtain

$$\sigma_0 H(t) = \mathbb{V} \frac{d^\alpha \gamma(t)}{dt^\alpha} \quad (2.2.16)$$

Again, we can solve the above equation by taking its Laplace transform, rearranging the equation to solve for $\tilde{\gamma}(s)$ in the Laplace domain, and then inverting the transform. Performing these steps, we obtain the creep compliance $J(t)$ of a springpot as [59]

$$J(t) = \frac{\mathbb{V} t^\alpha}{\Gamma(1 + \alpha)} \quad (2.2.17)$$

To find the complex shear modulus $G^*(\omega) = G'(\omega) + iG''(\omega)$, the most convenient technique is to use the Fourier transform method. The Fourier transform $\tilde{f}(\omega)$ of a function $f(t)$ is defined by [25]

$$\mathcal{F}[f(t)] \equiv \tilde{f}(\omega) \equiv \int_{-\infty}^{\infty} f(t) e^{i\omega t} dt \quad (2.2.18)$$

and for the Caputo fractional derivative, the following relationship holds [55]:

$$\mathcal{F} \left[\frac{d^\alpha f(t)}{dt^\alpha}; \omega \right] = (i\omega)^\alpha \tilde{f}(\omega) \quad (2.2.19)$$

Therefore, to find the elastic and loss moduli $G'(\omega)$ and $G''(\omega)$ respectively, we simply Fourier transform the constitutive equation 2.2.8 to obtain

$$\tilde{\sigma}(\omega) = \mathbb{V}(i\omega)^\alpha \tilde{\gamma}(\omega) \quad (2.2.20)$$

We know that $G^*(\omega) = \tilde{\sigma}(\omega)/\tilde{\gamma}(\omega)$ [26], and hence for a single springpot $G^*(\omega) = \mathbb{V}(i\omega)^\alpha$. Separating the real and imaginary parts of $G^*(\omega)$ we obtain the linear viscoelastic moduli as⁴

$$G'(\omega) = \mathbb{V}\omega^\alpha \cos(\pi\alpha/2) \quad (2.2.21)$$

$$G''(\omega) = \mathbb{V}\omega^\alpha \sin(\pi\alpha/2) \quad (2.2.22)$$

The above demonstration of using the Laplace transform technique to solve for the relaxation modulus $G(t)$, and the Fourier transform to find $G'(\omega)$ and $G''(\omega)$ was meant to be instructive; we have worked these out in detail here because we will repeatedly use this technique to solve for the linear viscoelastic material functions throughout this thesis. In fact, we show in Chapter 3, that these techniques can be used to solve more complicated fractional differential equations.

In Equations 2.2.21 and 2.2.22, setting $\alpha = 1$ yields $G'(\omega) = 0$ and $G''(\omega) = \mathbb{V}\omega$ which is the correct limit of the Newtonian dashpot. Similarly, it can be shown that for $\alpha = 0$, the equations reduce to the limit of the Hookean spring. For all other values of $0 < \alpha < 1$, $G'(\omega)$ and $G''(\omega)$ are pure power laws, with a constant phase angle $\delta = \pi\alpha/2$. This kind of linear viscoelastic behavior has been measured experimentally in many gel like systems [13, 35].

With this background, we are now ready to use these springpot elements to construct more complex constitutive models. This approach has been discussed in some detail in the literature, notably by Bagley and Torvik [56], Torvik and Bagley [96], Koeller [59],

⁴In deriving the expressions for $G'(\omega)$ and $G''(\omega)$, we only consider the solutions that lie on the principal branch.

Nonnenmacher [57], Friedrich [97], [95] Schiessel and Blumen and Heymans and Bauwens [98]; we therefore summarize the primary results without detailed derivations.

2.3 *The Canonical Fractional Models: FMM and FKVM*

The two canonical models that we study in this section are the Fractional Maxwell model (FMM) and the Fractional Kelvin-Voigt Model (FKVM). These are fractional generalizations of the linear viscoelastic Maxwell and Kelvin-Voigt models respectively, and we replace all the springs and dashpots by springpots. Both the FMM as well as the FKVM are characterized by only four parameters — two power law exponents, which control the scaling for the temporal and frequency response, and two quasi-properties, which set the scales for magnitude of the stresses in these multiscale materials. Examples of the successful application of these two canonical fractional models to describe the linear rheology of complex multiscale materials include red blood cell membranes [99], smooth muscle cells [100], food gums [101] and comb-shaped polymers [94].

2.3.1 *The Fractional Maxwell Model (FMM)*

Many multiscale materials typically exhibit a broad power law regime of stress relaxation over many decades of timescales, but at sufficiently long times (or low frequencies) ultimately transition into a sol-like flow regime. This response can be modeled by the Fractional Maxwell Model (FMM), which consists of two springpot elements in series [94]. We show a schematic drawing of the FMM in Figure 2.3.1(a). The FMM compactly describes the rheological properties of multiscale materials that exhibit sol-like flow at long timescales. In Chapter 3, we show using the example of viscoelastic interfaces formed from globular protein solutions that the FMM can quantitatively predict the *linear* rheological behavior of complex fluids under a range of different deformation conditions [93]. The constitutive equation for the FMM can be obtained from assuming equality of the stress ($\sigma = \sigma_1 = \sigma_2$) in the springpots, and additivity of the strains ($\gamma = \gamma_1 + \gamma_2$) to give

$$\sigma(t) + \frac{\mathbb{V}}{\mathbb{G}} \frac{d^{\alpha-\beta} \sigma(t)}{dt^{\alpha-\beta}} = \mathbb{V} \frac{d^{\alpha} \gamma(t)}{dt^{\alpha}} \quad (2.3.1)$$

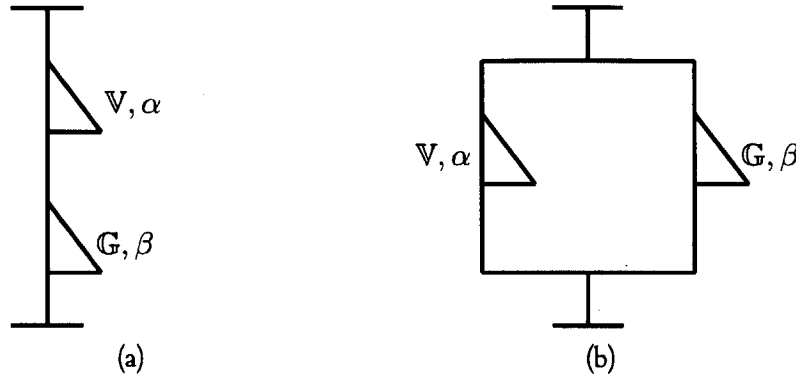


Figure 2.3.1: Schematic figures of the (a) Fractional Maxwell Model (FMM) and (b) Fractional Kelvin Voigt Model (FKVM). These models are generalizations of their linear counterparts (shown in Figure 2.1.2) and the springs and dashpots are replaced by springpots.

where we take $\alpha > \beta$ without loss of generality⁵ [55]. The ratio

$$\tau = (\mathbb{V}/\mathbb{G})^{1/(\alpha-\beta)} \quad (2.3.2)$$

is a measure of a characteristic timescale in this model. Each of the springpots in the FMM has its own asymptotic power law behavior (depending on α and β), and τ represent a characteristic time scale at which the power law transitions from one to the other. We discuss the asymptotic behavior of the FMM in more detail below⁶. For the case of $\alpha = 1$ and $\beta = 0$, the FMM reduces to a dashpot and a spring in series, and therefore reduces to the linear viscoelastic Maxwell model. This can be verified by substituting these limits for α and β in Equation 2.3.1, and noticing that it reduces to Equation 2.1.1, with $\mathbb{V} \rightarrow \eta_0$ and $\mathbb{G} \rightarrow G_0$. Friedrich [102] has shown that this model results in a nonnegative internal work and a nonnegative rate of energy dissipation, and is hence consistent with the laws of thermodynamics. Lion has argued more generally that a constitutive model containing fractional elements is thermodynamically admissible only if the resulting constitutive equation represents some physically realizable combination of springs, dashpots and springpots [103]. In other words, models that do not have mechanical analogues are thermodynamically inadmissible.

⁵Some authors use the notation $c = \alpha - \beta$ and $d = \alpha$, and use these parameters c and d to formulate their constitutive equations. See, for example, Ref. [94].

⁶Also see table 2.3.1

As before, to find the relaxation modulus $G(t)$, we substitute a step strain deformation (Equation 1.2.4) in the constitutive equation of the FMM 2.3.1, and use the Laplace transform technique to solve for $G(t) = \sigma(t)/\gamma_0$. Performing these steps, we obtain the following analytical expression for $G(t)$ [55]

$$G(t) = Gt^{-\beta} E_{\alpha-\beta, 1-\beta} \left(-\left(\frac{t}{\tau}\right)^{\alpha-\beta} \right) \quad (2.3.3)$$

where $E_{a,b}(z)$ is the two-parameter Mittag-Leffler function defined as [82]

$$E_{a,b}(z) = \sum_{k=0}^{\infty} \frac{z^k}{\Gamma(ak + b)}; \quad (a, b > 0) \quad (2.3.4)$$

and the characteristic timescale τ is given by equation 2.3.2. Note that in equation 2.3.3 we have written the expression for $G(t)$ in terms of the quasi-properties \mathbb{V} and \mathbb{G} of the two springpot elements, and the power-law exponents α, β . For $\alpha = 1$ and $\beta = 0$, Equation 2.3.3 reduces to the correct Maxwell-Debye relaxation pattern of the linear viscoelastic Maxwell model (Equation 2.1.3).

The Mittag-Leffler function, named after its originator the Swedish mathematician Gosta Mittag-Leffler, finds use in various fields of physics such as control theory, electric circuit theory, diffusion, electrochemistry, and as we will describe in detail in this thesis, viscoelastic complex fluids [82]. The relaxation modulus of the FMM given in Equation 2.3.3 has the interesting property of interpolating between a stretched exponential, or Kohlrausch-Williams-Watts [104, 105], relaxation process at short times and a power law relaxation process [106] at long times. The stretched exponential relaxation process is of the form

$$G(t) = G \exp \left[-\left(\frac{t}{\tau}\right)^{\xi} \right] \quad (2.3.5)$$

where G is a modulus, τ is a characteristic timescale, and $0 < \xi < 1$ is a stretching exponent. This kind of stress relaxation response, exhibiting a transition from stretched exponential behavior to power law behavior, is frequently observed in rheological experiments involving multiscale complex fluids [107–109]. In Figure 2.3.2 we show a stress relaxation experiment performed on bread dough (figure adapted from Ref. [50], original data from Ref. [110]). The dashed line is a fit of a stretched exponential of the form given in Equation 2.3.5

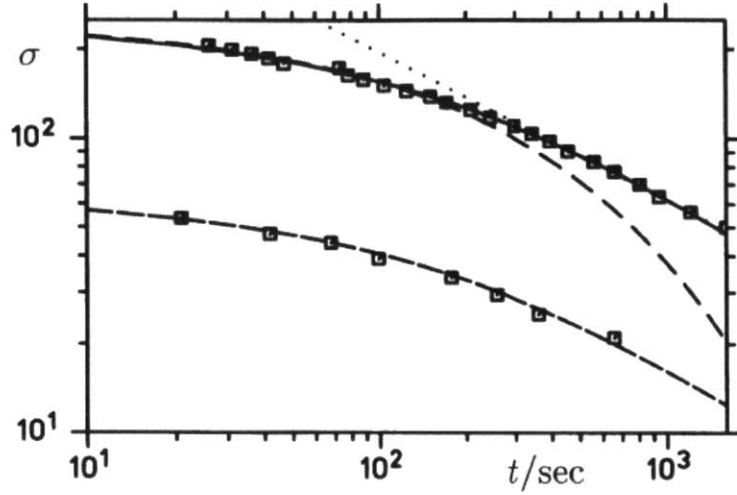


Figure 2.3.2

Stress relaxation data for bread dough reproduced from Ref. [50]. The original data is from Ref. [110]. A stretched exponential relaxation function (dashed line) captures the rheological behavior at short times, while at long times, the dough exhibits power law-like stress relaxation (dotted line). The Mittag-Leffler relaxation kernel (solid line) smoothly interpolates between these two asymptotic material responses.

to the data (hollow symbols) at early times. The dotted line indicates a fit of a power law relaxation kernel at long times. The Mittag-Leffler function, which smoothly interpolates between these two asymptotic responses, is shown by the solid black line.

To better understand this interpolatory nature of the Mittag-Leffler function, we examine the various asymptotes of the stretched exponential (KWW) relaxation kernel as well as those of the Mittag-Leffler relaxation kernel. At short times $t/\tau \ll 1$, we expand Equation 2.3.5 using a Taylor series to obtain

$$G(t) \approx G \left[1 - \left(\frac{t}{\tau} \right)^\xi \right] \quad (2.3.6)$$

We also determine the asymptotic behavior of the Mittag-Leffler function at $z = t/\tau \ll 1$ and $z = t/\tau \gg 1$ respectively [82]:

$$E_{a,b}(-z) \approx \sum_{k=0}^N \frac{z^k}{\Gamma(ak + b)} + O(z^{N+1}); z \ll 1 \quad (2.3.7)$$

$$E_{a,b}(-z) \approx \sum_{k=1}^N \frac{z^{-k}}{\Gamma(b - ak)} + O(z^{-(N+1)}); z \gg 1 \quad (2.3.8)$$

Using these equations, it can be shown that for the FMM the relaxation modulus $G(t)$ of

the FMM has the following asymptotic behavior:

$$G(t) \approx \mathbb{G}t^{-\beta} \left(\frac{1}{\Gamma(1-\beta)} + \frac{(t/\tau)^{\alpha-\beta}}{\Gamma(1+\alpha-2\beta)} \right) t/\tau \ll 1 \quad (2.3.9)$$

$$G(t) \approx \frac{(t/\tau)^{-\alpha}}{\Gamma(1-\alpha)}; t/\tau \gg 1 \quad (2.3.10)$$

and for the special case of $\beta = 0$ (i.e. one of the elements in the FMM is a spring) we obtain,

$$G(t) \approx \mathbb{G} \left(1 - \frac{(t/\tau)^\alpha}{\Gamma(1+\alpha)} \right); t/\tau \ll 1 \quad (2.3.11)$$

$$G(t) \approx \frac{(t/\tau)^{-\alpha}}{\Gamma(1-\alpha)}; t/\tau \gg 1 \quad (2.3.12)$$

Comparing Equations 2.3.6 and 2.3.11 demonstrates that the short time behavior of the KWW relaxation function and the Mittag-Leffler type function are identical. Equation 2.3.12 demonstrates that at long times, the Mittag-Leffler function asymptotically behaves like a power law.

We also derive the creep compliance $J(t)$ by substituting a step stress of the form $\sigma(t) = \sigma_0 H(t)$ into the constitutive equation 2.3.1, and solving the resulting equation using the Laplace transform technique described previously, we obtain [55]

$$J(t) \equiv \frac{\gamma(t)}{\gamma_0} = \left(\frac{1}{\mathbb{V}} \frac{t^\alpha}{\Gamma(1+\alpha)} + \frac{1}{\mathbb{G}} \frac{t^\beta}{\Gamma(1+\beta)} \right) \quad (2.3.13)$$

where $\Gamma(z)$ is the Gamma function defined in Equation 2.2.13. In deriving Equation 2.3.13, the necessary initial conditions are determined from the fact that the sample is initially at rest, and we have $\dot{\gamma}(0) = 0$. Moreover, the state of zero strain may be fixed arbitrarily, and we set the material strain to be $\gamma(0) = 0$ at $t = 0$.

To find the linear viscoelastic moduli $G'(\omega)$ and $G''(\omega)$, we simply Fourier transform the constitutive equation of the FMM (Equation 2.3.1) as explained previously to obtain [55, 93]

$$G^*(\omega) = \frac{\mathbb{V}(i\omega)^\alpha \cdot \mathbb{G}(i\omega)^\beta}{\mathbb{G}(i\omega)^\alpha + \mathbb{V}(i\omega)^\beta} \quad (2.3.14)$$

	G' (Pa m)	G'' (Pa m)
$\lim_{\omega \rightarrow 0}$	$\mathbb{V}\omega^\alpha \cos\left(\frac{\pi}{2}\alpha\right)$, if $\alpha \neq 1$ $\frac{\mathbb{V}^2}{\mathbb{G}}\omega^{2-\beta} \cos\left(\frac{\pi}{2}\beta\right)$, if $\alpha = 1$	$\mathbb{V}\omega^\alpha \sin\left(\frac{\pi}{2}\alpha\right)$, if $\alpha \neq 0$ $0 (\mathbb{V}\omega)$, if $\alpha = 0$
$\lim_{\omega \rightarrow \infty}$	$\mathbb{G}\omega^\beta \cos\left(\frac{\pi}{2}\beta\right)$, if $\beta \neq 1$ $0 (\mathbb{V}\omega)$, if $\beta = 1$	$\mathbb{G}\omega^\beta \sin\left(\frac{\pi}{2}\beta\right)$, if $\beta \neq 0$ $\frac{\mathbb{G}^2}{\mathbb{V}}\omega^{-\alpha} \sin\left(\frac{\pi}{2}\alpha\right)$, if $\beta = 0$

Table 2.3.1: Asymptotic behaviour of $G'(\omega)$ and $G''(\omega)$ in the FMM. Because $0 < \beta < \alpha < 1$, G' and G'' reduce identically to 0 for the cases $\beta = 1$ and $\alpha = 0$ respectively, and the result holds for all frequencies.

and separating out the real and imaginary parts to find $G'(\omega)$ and $G''(\omega)$ respectively, we obtain

$$G'(\omega) = \mathbb{V}\tau^{-\alpha} \frac{(\omega\tau)^\alpha \cos(\pi\alpha/2) + (\omega\tau)^{2\alpha-\beta} \cos(\pi\beta/2)}{(\omega\tau)^{2(\alpha-\beta)} + 2(\omega\tau)^{\alpha-\beta} \cos(\pi(\alpha-\beta)/2) + 1} \quad (2.3.15)$$

$$G''(\omega) = \mathbb{V}\tau^{-\alpha} \frac{(\omega\tau)^\alpha \sin(\pi\alpha/2) + (\omega\tau)^{2\alpha-\beta} \sin(\pi\beta/2)}{(\omega\tau)^{2(\alpha-\beta)} + 2(\omega\tau)^{\alpha-\beta} \cos(\pi(\alpha-\beta)/2) + 1} \quad (2.3.16)$$

The asymptotic behaviours of equations 2.3.15 and 2.3.16 in the limit of low and high frequencies are given in table 2.3.1. Several different limits can be distinguished in the special cases corresponding to $\beta = 0, 1$ and $\alpha = 0, 1$ respectively. These limits reduce correctly to those of the linear Maxwell model when $\alpha = 1$ and $\beta = 0$. When multiple Maxwell modes are used to generate a satisfactory description of the behaviour of power-law materials, we often require a very large number of discrete relaxation times [26], something that can be readily circumvented with the use of a fractional model such as equation 2.3.1. The fractional calculus description captures the dynamics of the broad spectrum of relaxation times very succinctly, by collapsing them into a single springpot [95].

The FMM is better suited to model complex fluids that exhibit sol-like flow response at long time. Complex fluids exhibiting a gel-like plateau regime in the long time scale limit are better modeled by the Fractional Kelvin-Voigt Model (FKVM). We examine this model and provide the linear viscoelastic material functions for this model next.

2.3.2 The Fractional Kelvin Voigt Model (FKVM)

This second canonical fractional constitutive equation comprises of two springpots arranged in parallel. We show a schematic diagram of the FKVM in Figure 2.3.1(b). The linear viscometric functions $G(t)$ and $J(t)$ can be derived as before using the Laplace transform technique, which we have described in detail for the case of the FMM. Therefore, we will simply present the final results without derivation [55]. The constitutive equation of the FKVM is given by

$$\sigma(t) = \mathbb{V} \frac{d^\alpha \gamma(t)}{dt^\alpha} + \mathbb{G} \frac{d^\beta \gamma(t)}{dt^\beta} \quad (2.3.17)$$

The relaxation modulus of the FKVM is given by

$$G(t) = \frac{\mathbb{V} t^{-\alpha}}{\Gamma(1-\alpha)} + \frac{\mathbb{G} t^{-\beta}}{\Gamma(1-\beta)} \quad (2.3.18)$$

and the creep compliance $J(t)$ is given by

$$J(t) = \frac{t^\alpha}{\mathbb{V}} E_{\alpha-\beta, 1+\alpha} \left(- \left(\frac{t}{\tau} \right)^{\alpha-\beta} \right) \quad (2.3.19)$$

We may use the asymptotic forms of the Mittag-Leffler function given in Equations 2.3.7 and 2.3.8 to find the short and long time asymptotes of the creep compliance in the FKVM, and we obtain

$$J(t) \approx \frac{t^\alpha}{\mathbb{V}\Gamma(1+\alpha)}; t/\tau \ll 1 \quad (2.3.20)$$

$$J(t) \approx \frac{t^\beta}{\mathbb{G}\Gamma(\beta+1)}; t/\tau \gg 1 \quad (2.3.21)$$

To find the linear viscoelastic elastic and viscous moduli, $G'(\omega)$ and $G''(\omega)$ respectively, we Fourier transform the constitutive equation 2.3.17 and separate the real and imaginary

parts to obtain

$$G'(\omega) = \mathbb{V}\omega^\alpha \cos(\pi\alpha/2) + \mathbb{G}\omega^\beta \cos(\pi\beta/2) \quad (2.3.22)$$

$$G''(\omega) = \mathbb{V}\omega^\alpha \sin(\pi\alpha/2) + \mathbb{G}\omega^\beta \sin(\pi\beta/2) \quad (2.3.23)$$

In this section, we have the derived linear viscometric functions of the simplest two element fractional models: the FMM and the FKVM. These fractional constitutive models can capture a very diverse variety of multiscale rheological response. We next show an example of the capabilities of this model by analyzing capillary suspensions [111].

2.4 A Case Study: Capillary Suspensions

Capillary suspensions are complex fluids which consist of particles that are suspended in a continuous fluid medium with a small amount of second immiscible liquid added [111, 112]. Due to the immiscibility of the second liquid, it preferentially occupies the pores between the suspended particles, and in the process bridges particles to form a network. This network can span the entire sample, leading to the increase of the yield stress of the fluid by several orders of magnitude with just a small amount of second liquid (1 vol.%) [113, 114]. In Figure 2.4.1 we reproduce a micrograph of a capillary suspension from Ref. [113]. The inset figure schematically shows the nature of the bridges formed by the second immiscible fluid in capillary suspensions, with the pores between particles occupied. The

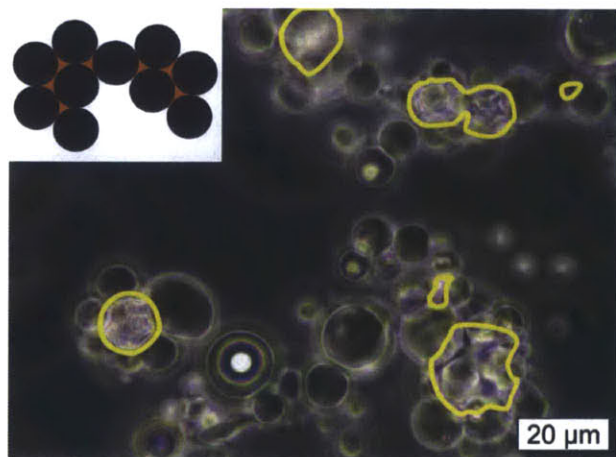
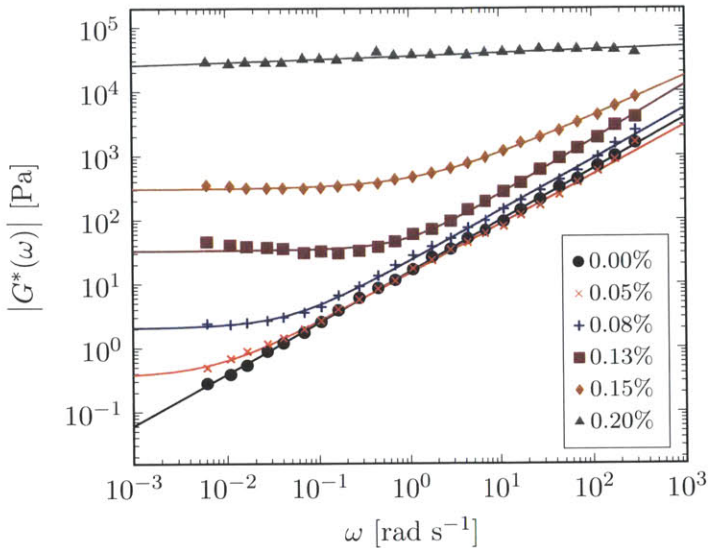


Figure 2.4.1

A micrograph reproduced from Ref. [113] of a capillary suspension consisting of hydrophobically modified glass beads ($r = 9.6 \mu\text{m}$) suspended in diisononyl phthalate. The second immiscible liquid is 1 wt.% water. The inset figure schematically shows the nature of the capillary bridging, with water (orange shading) preferentially occupying the pores between the particles. The yellow lines in the main figure outline water trapped between these pores. More details can be found in Refs. [111–114].


Figure 2.4.2

Magnitude of the complex shear modulus $|G^*(\omega)|$ as a function of frequency ω obtained by Koos and Willenbacher [111] in a small amplitude oscillatory shear experiment performed on the capillary suspensions described in Ref. [111]. The legend indicates the weight % of added water. The lines are fits of Equation 2.4.2 to the data (symbols). With just three parameters, we are able to capture the transition of the suspensions from a sol state to a gel-like material possessing a yield stress.

yellow lines in the micrograph outline areas of capillary bridging [113].

In Figure 2.4.2, we replot the shear rheology data of Koos and Willenbacher [111] obtained for a suspension of hydrophobically modified calcium carbonate particles in silicone oil (volume fraction of particles $\phi = 17.3\%$). The immiscible liquid used here is water, and each curve in Figure 2.4.2 represents a different weight percentage of water, whose values are shown in the legend. We observe that when there is no added water, the complex modulus $|G^*(\omega)|$ displays no low frequency (or long time) plateau, indicating that at long times the suspensions flows continuously, and therefore any stress in the suspension ultimately relaxes. However, as the volume fraction of water is progressively increased, we observe the appearance of a low frequency plateau modulus, whose value increases with increasing water weight %. At higher frequencies, $|G^*(\omega)|$ increases as a power law, with $|G^*(\omega)| \sim \omega^\alpha$ and by inspection we see that $\alpha < 1$. At a water weight percentage of 0.20 %, the rheology becomes gel-like, with a broad multiscale spectrum response. Further details on the experimental parameters and the rheology of these systems may be found in Refs. [111–114].

We now seek to model these linear viscoelastic data to quantify the changes induced upon increasing the weight percentage of water. We allow the shape of the $|G^*(\omega)|$ versus ω curves to guide our intuition. Observing that the curves show a low frequency plateau

and a high frequency power law regime⁷, we begin with the fractional Maxwell model with one of the springpots set to be a spring, i.e. $\beta = 0$ and $\mathbb{G} \rightarrow G$. For this case we calculate the complex modulus to be

$$|G^*(\omega)| = \sqrt{[G + \mathbb{V}\omega^\alpha \cos(\pi\alpha/2)]^2 + [\mathbb{V}\omega^\alpha \sin(\pi\alpha/2)]^2} \quad (2.4.1)$$

$$\Rightarrow |G^*(\omega)| = G\sqrt{1 + 2(\omega\tau)^\alpha \cos(\pi\alpha/2) + (\omega\tau)^{2\alpha}} \quad (2.4.2)$$

We fit Equation 2.4.2 to the data shown in Figure 2.4.2; these fits are shown as solid lines. We observe that the fits are very good, and the FKVM (with only three parameters G , \mathbb{V} and α) is able to describe the relaxation spectrum of these capillary suspensions over nearly five decades of frequency. We present the values of the model parameters for the different values of the weight percentage of water in Figure 2.4.3. With increasing weight percentage of water, \mathbb{V} and G , which set the scale for the magnitude of stresses increase very rapidly.

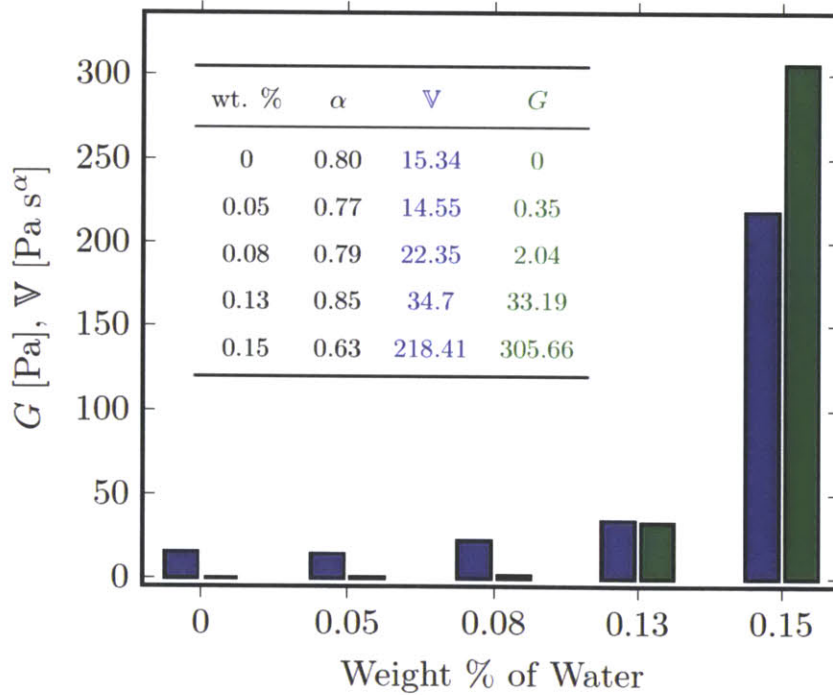


Figure 2.4.3

Model parameters obtained by fitting the FKVM expression for $|G^*(\omega)|$ derived in Equation 2.4.2 to the SAOS data of Koos and Willenbacher [111]. One of the springpot elements has been set to be a spring ($\beta = 0$). These data and fits are shown in Figure 2.4.2. As the amount of water is increased, we observe that both G and \mathbb{V} progressively increase.

⁷We encounter this kind of relaxation spectrum again in Chapter 5 in the context of chemically crosslinked adhesive gels.

However, the value of α changes over a much smaller relative amount, indicating that the nature of the branched network structure formed on introducing the immiscible liquid remains relatively unchanged. For the suspension with 0.20 % water (not shown here), a single springpot with just two parameters is enough to capture the rheological spectrum, and we find that $\alpha = 0.05$ and $\mathbb{V} = 3.15 \times 10^4 \text{ Pa s}^\alpha$. The high value of quasi-property and the drastic drop in α means that the material behaves nearly like a Hookean solid (for which $\alpha = 0$), indicating that there is a drastic change in the microstructure of the capillary suspension at this weight percentage of water, possibly in the nature of the percolation structure formed by the capillary bridges.

This case study has presented just one example of the successful application of fractional constitutive equation to model broad multiscale rheological response. Once a material has been characterized, i.e., the power law exponents and corresponding quasi-properties have been determined, we may use the fractional framework to make predictions of material response in other kinds of deformation profiles. In the next chapter we demonstrate how fractional models can be used to make predictions of multiscale material response not just under a standard viscometric flow, but under more complex externally applied deformations, such as a creep experiment with appreciable instrument inertia.

3 | *Linear Shear Deformations*

Consumer products like foods contain numerous polymeric and particulate additives that play critical roles in maintaining their stability, quality and function. The resulting materials exhibit complex bulk and interfacial rheological responses, and often display a distinctive power-law response under standard rheometric deformations. As we have seen in the previous two chapters, these power-laws are not conveniently described using conventional rheological models, without the introduction of a large number of relaxation modes. In this chapter, we present a constitutive framework utilizing fractional derivatives to model the power-law responses often observed experimentally. We revisit in greater detail the concept of quasi-properties briefly discussed in Chapter 1 and their connection to the fractional Maxwell model (FMM). Using Scott-Blair's original data, we demonstrate the ability of the FMM to capture the power-law response of 'highly anomalous' materials. We extend the FMM to describe the viscoelastic interfaces formed by bovine serum albumin and solutions of a common food stabilizer, Acacia gum. Fractional calculus allows us to model and compactly describe the measured frequency response of these interfaces in terms of their quasi-properties. Finally, we demonstrate the predictive ability of the FMM to quantitatively capture the behaviour of complex viscoelastic interfaces by combining the measured quasi-properties with the equation of motion for a complex fluid interface to describe the damped inertio-elastic oscillations that are observed experimentally.

3.1 Introduction

A multitude of consumer products, especially foods, owe their structure, stability and function to the presence of interfaces. Common examples include foams and emulsions such as milk, soups, salad dressings, mayonnaise, ice cream and butter (see Ref. [115] and the

references therein). Although many of these foams and emulsions are thermodynamically unstable, the kinetics of phase separation can be controlled with the addition of various proteins, surfactants, gums and other stabilizing agents, which have very important implications for the shelf-life of foods [116]. However, the presence of these additives often leads to complex rheological properties and give rise to distinctive power-laws in the creep response (i.e. the strain varies as $\gamma(t) \sim t^\alpha$) and also in the corresponding frequency response (i.e. the elastic modulus varies with frequency as $G'(\omega) \sim \omega^\alpha$). Such power-law responses are not well described by canonical rheological models such as the Maxwell or Kelvin-Voigt models [26]. The sensory perception of foods in terms of textural parameters plays an important role in the assessment of food quality, and is strongly related to the viscoelastic properties of the interfacial layers present [117]. New rheological tools such as the double wall ring (DWR) interfacial rheometer [53, 118] enable us to experimentally quantify such responses with unprecedented accuracy over a wide range of frequency and time scales. We now seek a framework for modeling these power-law responses in a simple yet robust constitutive theory that can then be used to predict the material response in other, more complex, flows.

The irregular nature of relaxation events in complex fluids such as foods and consumer products leads to stress relaxation that is not exponential, and is best represented as a power law in time. i.e. $G(t) \sim t^\beta$. As we have seen in Chapter 1, non-exponential stress relaxation in the time domain also implies power-law behaviour in the viscoelastic storage modulus, $G'(\omega)$, and loss modulus, $G''(\omega)$, measured in the frequency domain using small amplitude oscillatory shear deformations. This broad spectral response is indicative of the wide range of distinct relaxation processes available to the microstructural elements that compose the material, and there is no single characteristic relaxation time [106]. For power-law materials to be modeled accurately, it is often found that a very large number of corresponding mechanical elements are required. For many complex fluids, this approach is frequently impractical from a modeling point of view. Moreover, the values of the fitted parameters in any model with a finite array of relaxation modes depend on the timescale of the experiment over which the fit is performed. Consequently the model parameters obtained lack physical meaning [33].

Blair [119] pioneered a framework that enabled the power-law equation proposed by [120] to be made more general through the use of fractional calculus. With analogy to the classical ideas of (i) the Hookean spring, in which the stress in the spring is proportional to

the zero-th derivative of the strain and (ii) the Newtonian dashpot, in which the stress in the dashpot is proportional to the first derivative of the strain, he proposed a constitutive equation in terms of a *fractional derivative*

$$\sigma(t) = \mathbb{V} \frac{d^\alpha \gamma(t)}{dt^\alpha} \quad (3.1.1)$$

where $0 < \alpha < 1$, effectively creating an element that interpolates between the constitutive responses of a spring and a dashpot. Here the material property \mathbb{V} is a *quasi-property*, and d^α/dt^α is the fractional derivative operator [85], both of which are discussed in further detail below. Scott-Blair and co-workers used equation 3.1.1 as a constitutive equation in itself; Koeller [59] later equated this canonical modal response to a mechanical element called the *spring-pot*¹ and identified it as the fundamental building block from which more complex constitutive models could be constructed.

One of the consequences of Scott-Blair and coworkers' detailed study into these so-called fractional models is the emergence of the concept of material *quasi-properties*, denoted in equation 3.1.1 by the quantity \mathbb{V} (with SI units of Pa s^α). Quasi-properties differ from material to material in the dimensions of mass M, length L and time T, depending on the power α . It may thus be argued that they are not true material properties because they contain non-integer powers of the fundamental dimensions of space and time. However, such quasi-properties appear to compactly describe textural parameters such as the “firmness” of a material [122]. They are numerical measures of a dynamical process such as creep in a material rather than of an equilibrium state. In the present chapter we show how we can compactly represent the wide range of microstructural relaxation processes in the material in terms of these so-called quasi-properties and the associated fractional derivatives with only a few parameters.

Bagley and Torvik were able to demonstrate that, for long chain molecules with many submolecules per chain, the Rouse molecular theory [124] is equivalent to a fractional constitutive equation, and compactly represented the polymer contribution to the total stress in terms of the fractional half-derivative of the strain [123]. The Fractional Maxwell Model (FMM) and other fractional constitutive models have been considered in detail in the literature [55, 57, 59, 95, 125].

¹The springpot is also sometimes referred to as the Scott Blair element [121].

We demonstrate in this chapter that fractional stress-strain relationships are also applicable to viscoelastic interfaces, and result in simple constitutive models that may be used to quantitatively describe the power-law rheological behaviour exhibited by such interfaces. We first connect the fractional calculus framework to the studies of Scott-Blair and coworkers [80, 122] and show, using Blair et al.'s 1947 original data on 'highly anomalous butyl rubber', how the use of the fractional Maxwell model to extract the quasi-properties of this material is superior to the use of conventional spring-dashpot models that characterize creep and stress-relaxation. Next, we emphasize the utility of fractional constitutive models, and highlight the shortcomings of linear constitutive models for describing complex fluid interfaces using interfacial rheology data obtained from highly viscoelastic bovine serum albumin and Acacia gum interfaces. Finally, we present a discriminating comparison of linear and fractional viscoelastic constitutive models using the phenomenon of creep ringing that arises from the coupling between surface elasticity and instrument inertia. We show that combining fractional constitutive models with the concept of material quasi-properties enables the quantitative description of complex time-dependent interfacial phenomena.

3.2 *Techniques and Materials*

3.2.1 *Interfacial Rheology*

Interfacial rheology or '2D rheology' studies the dynamics and structure of interfacial viscoelastic thin films or skins formed by solutions containing surface active molecules [126]. Understanding the mechanics of viscoelastic interfaces is critical to a number of applications including the use of food additives and stabilizers [116, 127], medicine, physiology and pharmaceuticals [128, 129]. Although static surface tension measurements are sufficient to characterize the interfacial properties of surfactant-free solutions with clean interfaces, accurate descriptions of solutions or dispersions containing surface active molecules with dynamically evolving interfaces necessitate correct accounting of the mass and momentum transport processes occurring at the interface [130]. Interfacial rheometry probes the microstructure and dynamics of thin layers or films or skins formed on interfaces of surfactant, protein or macromolecular solutions, by measuring the response to either a compressional/dilational deformation or a shear deformation [126, 127, 131–133]. In this chapter,

we will only concern ourselves with the interfacial response of surface-active solutions to shearing deformations, although dilatational interfacial phenomena can also be important in other modes of deformation [134].

At equilibrium, the interface exhibits a state of tension, which is quantified in terms of a force per unit length or surface tension, s (units: N m^{-1} or Pa m). For a given solution, the interfacial tension varies with concentration, temperature and bulk-phase pressure, and any gradient in these parameters creates a surface tension gradient that can drive so-called Marangoni flows at the interface as well as in bulk [126, 131]. These flows encounter additional dampening by viscous stresses generated at the interface, which can be parameterized by an interfacial viscosity η_s (units: Pa s m), characterizing the surface drag [126]. A constitutive relation between the interfacial shear stress σ_s (Pa m), and interfacial shear rate $\dot{\gamma}$ (s^{-1}), was first proposed by Boussinesq, and the Boussinesq-Scriven surface stress tensor for Newtonian-like interfaces is given by [126, 133, 135]

$$\sigma_s = [(\kappa_s - \eta_s)\nabla_s \vec{v}_s] \mathbf{P}_{st} + 2\eta_s \mathbf{D}_s \quad (3.2.1)$$

where κ_s is the interfacial dilational viscosity, \mathbf{D}_s is the rate of deformation tensor, $\nabla_s \vec{v}_s$ is the divergence of the interfacial velocity, and \mathbf{P}_{st} is a projection tensor that transforms the vector contributions into the component tangential to the interface. In the more general non-Newtonian case that is expected when high molecular weight solutes such as proteins are adsorbed on the surface, the relation between interfacial stress and interfacial deformation is nonlinear [126, 132] and the interfacial viscosity depends upon the two principal invariants of the surface deformation tensor. In addition to an interfacial viscosity, η_s , viscoelastic interfaces also exhibit an interfacial viscoelasticity, G_s^* (units Pa m). By analogy with bulk oscillatory measurements, the linear response of the interface to an oscillatory shear strain, $\gamma(t) = \gamma_0 \sin(\omega t)$ can be quantified at small amplitudes in terms of a frequency-dependent dynamic surface elasticity, $G_s^*(\omega) = G_s'(\omega) + iG_s''(\omega)$ where the real and imaginary part correspond to the interfacial storage and loss modulus respectively. The different methods used traditionally for measuring interfacial rheology for food proteins, surfactant-protein mixtures and biofluids used in medical diagnostics are detailed in Refs. [126, 132, 133, 136]. Here we limit the discussion to the interplay between the interfacial and bulk rheology of surfactant-free globular proteins.

As a result of the boundary conditions at the interface, in typical rheological measurements, the deformation imposed on the interface becomes coupled with a corresponding

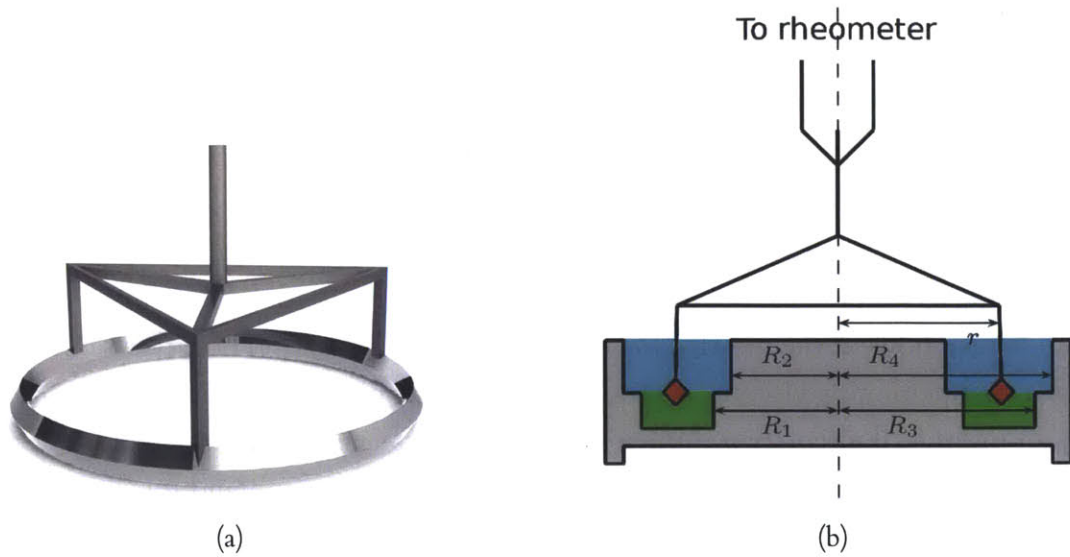


Figure 3.2.1: Schematic figures of the Double Wall Ring (DWR) fixture used to perform the interfacial rheology.

deformation or flow in the bulk phases [126, 132]. The challenge is to deconvolute the bulk and the interfacial contributions. The contribution of surface drag relative to bulk drag for a steady shear flow is described by the Boussinesq number, Bo_s , defined as

$$Bo_s = \frac{(\eta_s V / L_s) P_s}{(\eta V / L_B) A_B} = \frac{\eta_s}{\eta l_s} \quad (3.2.2)$$

where V is a characteristic velocity (units: $m s^{-1}$), L_s and L_B are the characteristic length scales for shear flow in the interface and bulk sub-phase respectively, P_s is the contact perimeter between the interface and the probe (units: m) and A_B is the contact area between the geometry and the sub-phase (units: m^2). The effects of interfacial viscosity dominate only for $Bo_s \gg 1$ and can be maximized by choosing a geometry that maximizes the wetted perimeter for a given contact area, or equivalently by minimizing the characteristic length scale, $l_s \approx A_B / P_s$ [126].

In this thesis, we use the Double Wall Ring fixture (DWR) developed by Vandebril et al. [118]. The DWR is an annular ring made of platinum-iridium alloy with a diamond-shaped cross-section that sits at the air-liquid or liquid-liquid interface and undergoes in-plane torsional displacements. We show images of the DWR in Figures 3.2.1(a) and 3.2.1(b). In the DWR set-up [118], the ratio $l_s \approx A_B / P_s = 0.7 \text{ mm}$, which results in a reasonably

high Boussinesq number, even for moderate values of η_s/η . Specifically, the characteristic length scale is 48 times smaller than the corresponding value for a bi-cone geometry with a radius of 34 mm [133], thus allowing higher values of Bo_s and improved instrumental sensitivity to interfacial effects. The corresponding expressions for the Boussinesq number in the cone-and-plate geometry, $Bo_s^{CP} = 2\eta_s/\eta R$ and double-gap geometry, $Bo_s^{DG} = \eta_s/\eta L$ indicate that interfacial contributions will always be much smaller than those for the DWR fixture, because the cylinder length L in the double gap and cone radius R in the cone-and-plate are at least an order of magnitude greater than l_s for the DWR fixture. However, whether interfacial effects can be safely neglected entirely in these geometries depends intimately on the measured values of η_s/η .

Two common examples of surface active materials are Acacia gum solutions and BSA solutions, which form the focus of the present study. The surface characteristics of BSA solutions at the air-water interface have been studied extensively using multiple techniques and it is well established that these solutions form rigid viscoelastic interfaces [54, 134, 137, 138]. On the other hand, although some interfacial studies have been performed on Acacia gum solutions [139–141], there is comparatively less literature available for these solutions. Furthermore, there is significant variability present between Acacia gums extracted from different sources.

To demonstrate the ability of the fractional models discussed above to describe viscoelastic interfaces, we performed interfacial rheological experiments on bovine serum albumin (BSA) and Acacia gum solutions. The surface characteristics of BSA solutions at the air-water interface have been studied extensively using multiple techniques and it is well established that these solutions form rigid viscoelastic interfaces [134, 137, 138, 142]. On the other hand, although some interfacial studies have been performed on Acacia gum solutions [139–141], there is comparatively less literature available for these solutions. Furthermore, there is significant variability present between Acacia gums extracted from different sources. Bovine serum albumin, extracted by agarose gel electrophoresis, was obtained from Sigma-Aldrich Corp (St. Louis, MO USA) in the form of a lyophilized powder. 0.01 M phosphate buffered saline (PBS) solution (NaCl 0.138 M; KCl 0.0027 M; pH 7.4, at 25 °C.) was prepared by dissolving dry PBS powder obtained from Sigma-Aldrich Corp. A precisely weighed quantity of BSA was dissolved in the PBS and the solution was brought up to the required volume in a volumetric flask to finally obtain solutions with a BSA concentration of 50 mg ml⁻¹. The uncertainty in composition from solution preparation was

determined to be only 0.002%. The prepared solutions were stored under refrigeration at 4 °C and were allowed to slowly warm up to room temperature before being used for experiments. All BSA solutions used in this study had a concentration of 50 mg ml⁻¹ unless otherwise specified.

Acacia gum in powdered form was also obtained from Sigma-Aldrich Corp (SKU:G9752). Using the same weighing technique described above, a known quantity of Acacia gum was dissolved in deionized water by slow stirring for approximately 6 hours to make solutions at a concentration of 3 wt.%. The solutions were then double-filtered using Whatman filter paper grade #595 (pore-size: 4 – 7 μm) to remove any residual insoluble material. Prior to rheological testing, all solutions were stored at 4°C for 24 hours to ensure biopolymer hydration ([143]).

3.3 Results

3.3.1 Stress Relaxation and Creep without Inertia

We first consider the stress relaxation in a complex material after the imposition of a step strain. The broad spectrum of relaxation times exhibited by power-law materials often present challenges in modeling such experiments [144]. It has already been noted in Chapter 1 that the inclusion of additional relaxation modes, which is equivalent to including additional Maxwell or Voigt units in parallel, gives improved fits to experimental data. The resulting expression for linear viscoelastic stress relaxation is a Prony series [20, 145]

$$G(t) \equiv \frac{\sigma(t)}{\gamma_0} = \sum_{k=1}^{N_m} G_k e^{-\frac{t}{\tau_k}} \quad (3.3.1)$$

where G_k and τ_k are fitting constants. The number of modes N_m required to fit experimental data varies depending on the time scale over which the relaxation modulus is measured and the degree to which the experimental data deviates from the exponential Maxwell-Debye response. Although describing data in this manner is a well-posed exercise, it is often cumbersome because of the large number of fitting parameters required. Tschoegl [26] remarks presciently

If the number of Maxwell of Voigt units is increased to the minimum number

required for a series-parallel model to represent such a [power-law] distribution at all adequately, the simplicity of the standard models is lost and, in addition, arbitrary decisions must be made in assigning suitable values to the model elements.

Another empirical approach often used to describe experimental observations of power-law-like relaxation is a stretched exponential response, known as the Kohlrausch-Williams-Watts expression (KWW) [20], given by $\sigma(t) = G\gamma_0 e^{-(t/\tau)^\beta}$ where the characteristic relaxation time τ , the exponent β and the modulus scale G are the fitting constants. The KWW expression works well in practice for describing the step strain excitation; However it is in general not possible using standard procedures to find the underlying form of the constitutive model that could subsequently be used to predict the response of the material to another mode of excitation [26]. Blair et al. [80] attempted to model measurements of anomalous stress relaxation in a range of materials using a higher-order Nutting equation of the form

$$\gamma = \sigma^\beta (At^{k'} + Bt^{k'-1} + Ct^{k'-2} \dots) \quad (3.3.2)$$

with $A \gg B, C, \dots$. However, we show in Appendix B that this equation is not thermodynamically admissible.

To demonstrate the ability of properly-formulated fractional constitutive models and the resulting quasi-properties to compactly describe the complex time-dependent properties of real viscoelastic materials, we revisit Blair et al.'s original stress relaxation data and fit the measurements with the FMM discussed in Chapter 2. In figure 3.3.1 we re-plot representative data reported for the original stress relaxation and creep experiments performed by Blair et al. [80]. We plot the relaxation modulus $G(t)$ and the corresponding creep compliance $J(t)$ for compactness, instead of the original stress and strain values respectively. It can be seen that the data collapse onto a rheological master-curve as expected for experiments performed in the limit of linear deformations. We now fit equation 2.3.3 to the measured $G(t)$ values shown in figure 3.3.1a. We set one of the elements in the FMM to be a spring, (i.e. $\beta = 0$); this accounts for the instantaneous elastic response in the stress at the start of the experiment. The FMM fit (solid line) describes the material response extremely well over a wide range of timescales ($10 \text{ s} \leq t \leq 400 \text{ s}$) in terms of just three material parameters $\alpha = 0.60 \pm 0.04$, $\mathbb{V} = 2.7 \pm 0.7 \times 10^7 \text{ Pa s}^{0.60}$ and $\mathbb{G} = 2.3 \pm 0.2 \times 10^6 \text{ Pa}$, (with $\beta = 0$). The error bars in the figure and the error estimates of the individual parameters α, \mathbb{V} and \mathbb{G} correspond to 95% confidence intervals for the nonlinear least square parameter

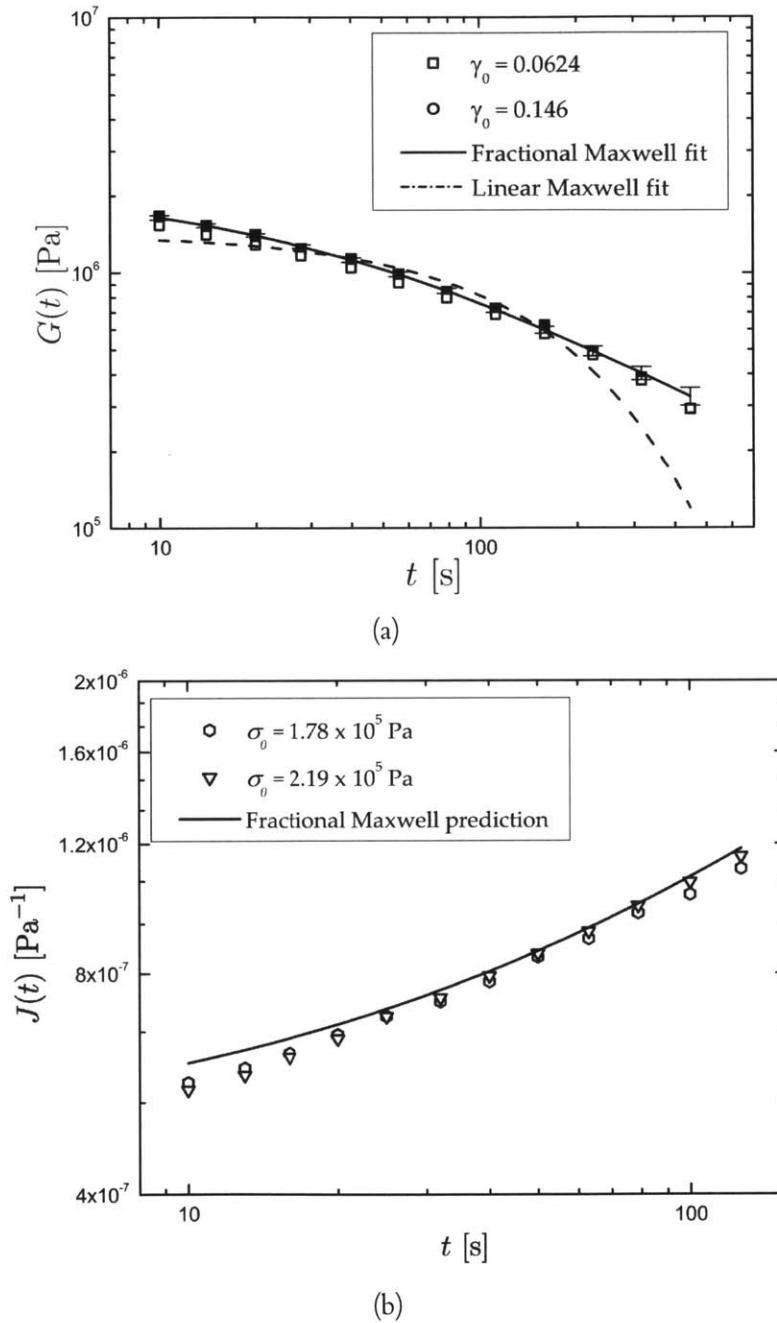


Figure 3.3.1: Rheological data for ‘highly anomalous’ butyl rubber taken from [80]. The solid line depicts the FMM fit with one of the elements set to be a spring ($\beta = 0$). For comparison, the fit obtained from a linear Maxwell model is shown as a dashed line. (b) Creep data at two different stresses for the same ‘highly anomalous’ butyl rubber. The solid line represents the prediction of the FMM based on the quasi-properties determined from the stress relaxation fit.

fits. A satisfactory fit using a sum of relaxation modes (equation 3.3.1) is obtained only if three relaxation modes are used, leading to the use of six fitting parameters, instead of the three required in the fractional Maxwell case.

If the values of the quasi-properties found above truly characterize the material, then we should be able to *predict* the constitutive response of the material to other deformations using the same rheological equation of state. To demonstrate this, we next consider the creep data for the same ‘highly anomalous’ rubber presented by Blair et al. which has been plotted as the creep compliance $J(t)$ in Figure 3.3.1(b). We can use Equation 2.3.13 to predict the creep response of the ‘highly anomalous’ rubber based on the power-law exponent and quasi-properties found from fits to the relaxation modulus. Substituting these values into Equation 2.3.13 leads to the solid curve shown in Figure 3.3.1(b). It can be seen that the prediction of the model again agrees very well with measured data, indicating that the FMM quantitatively describes the power-law-like behaviour observed by Scott-Blair in these anomalous materials.

From this analysis of some previously-published data, the superiority of fractional models in compactly describing the broad power-law like response of real materials is apparent. Similar power-law creep responses are commonly observed in both microrheological experiments [17, 146] and macroscopic experiments [140, 147]. Scott-Blair’s concept of quasi-properties is intimately connected to the framework of fractional calculus models and provides a physical material interpretation of the predictive power of these apparently abstract constitutive models.

3.3.2 *Interfacial Dynamics*

For each sample, we first performed interfacial time sweep experiments at a fixed frequency of $\omega = 1 \text{ rad s}^{-1}$ and a fixed strain amplitude of $\gamma_0 = 1 \%$ to monitor the time evolution of interfacial viscoelasticity at the interface. We find that the interfacial viscoelastic storage and loss moduli, $G'_s(\omega)$ and $G''_s(\omega)$ respectively, reach equilibrium about 2.5 hours after sample loading, indicating that the interfacial structure has reached steady-state. It is observed that $G'_s(\omega) > G''_s(\omega)$ indicating that the interfacial microstructures formed is predominantly elastic. The solid-like nature of the microstructures formed at the interface can also be observed in the strain sweep performed at an angular frequency of $\omega = 1 \text{ rad s}^{-1}$ shown in figure 3.3.2a. In the linear regime, we measure $G'_s \approx 0.025 \text{ Pa m} > G''_s \approx 5 \times 10^{-3} \text{ Pa m}$. The interfacial structure yields at a strain amplitude of about $\gamma_0 \approx 3\%$. In figure 3.3.2b

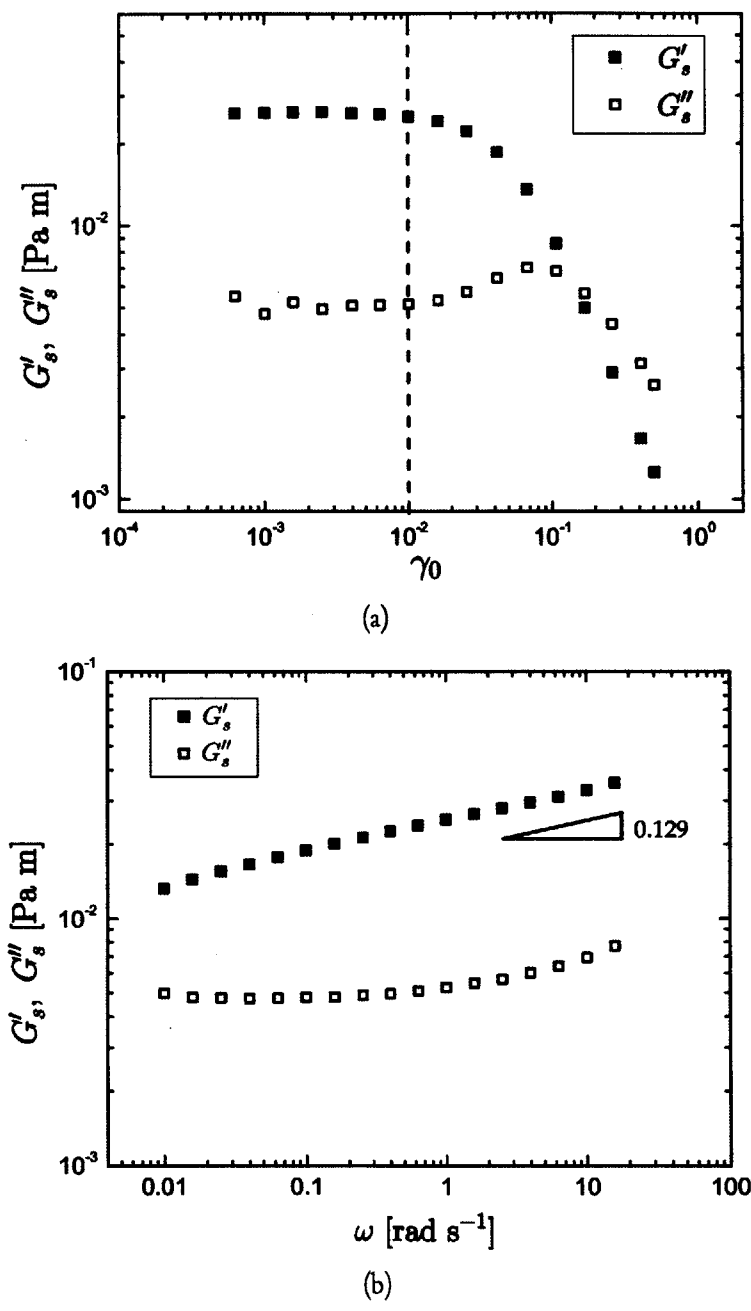


Figure 3.3.2: Interfacial small amplitude oscillatory shear data of 3 wt.% Acacia gum solutions carried out using the DWR. (a) Strain amplitude sweep performed at $\omega = 1 \text{ rad s}^{-1}$. (b) Frequency sweep performed at a strain amplitude $\gamma_0 = 1\%$, which lies in the linear regime. The viscoelastic interface shows weak power-law behaviour.

we show the values of the interfacial moduli as a function of excitation frequency for the 3 wt.% Acacia gum solution. Throughout the frequency range tested, $G'_s(\omega) > G''_s(\omega)$ signifying that viscoelastic solid-like behaviour persists even at lower frequencies. Testing at frequencies lower than $\omega = 10^{-2} \text{ rad s}^{-1}$ was avoided to prevent evaporation effects from interfering with the measurements. Erni et al. have reported that the values of G'_s and G''_s measured in a frequency sweep are unchanged upon changing the concentration of Acacia gum in the subphase from 10 wt.% to 20 wt.%, which has been attributed to the saturation of the interface by Acacia gum molecules [140].

The viscoelastic data obtained from the frequency sweep exhibits a weak power-law behaviour, which is typical of many physical and chemical gels [13] as well as soft glassy materials [18]. Numerous recent reports of bulk rheology in soft solids have shown examples of such power-law behaviour in small amplitude oscillatory shear deformations (for example Refs. [33, 147, 148]). We have already demonstrated the utility of fractional models in describing bulk creep and stress relaxation experiments in the previous section. We next examine the ability of the FMM to describe the power-law responses observed in interfacial oscillatory deformations.

3.3.3 *The FMM in Small Amplitude Oscillatory Shear (SAOS) Deformations*

The complex fluid examples discussed above, including the Acacia gum and bovine serum albumin interfaces tested in this study exhibit broad power-law responses when subjected to small amplitude oscillatory shear experiments. Winter and Mours have presented a model for critical gels in which the storage and loss moduli in the bulk are described by the power laws $G'(\omega) = S\Gamma(1-n)\cos(n\pi/2)\omega^n$ and $G''(\omega) = S\Gamma(1-n)\sin(n\pi/2)\omega^n$ respectively, where S is the gel strength parameter (units of Pa s^n) [13]. It may be shown by inverse Fourier transforming the complex modulus $G^*(\omega) = G'(\omega) + iG''(\omega)$ and finding the resulting constitutive equation that this is equivalent to a constitutive model consisting of a single spring-pot and the gel strength parameter is closely related to the quasi-property of the spring-pot $\mathbb{V} = S\Gamma(1-n)$.

We may achieve a more versatile constitutive model for describing foods and other gels and soft glasses that show power-law-like rheology by considering the FMM depicted schematically in figure 2.3.1(a). For a viscoelastic interface the corresponding interfacial

constitutive equation is equation

$$\sigma_s(t) + \frac{\mathbb{V}_s}{\mathbb{G}_s} \frac{d^{\alpha-\beta} \sigma_s(t)}{dt^{\alpha-\beta}} = \mathbb{V}_s \frac{d^\alpha \gamma(t)}{dt^\alpha} \quad (3.3.3)$$

which is the same as Equation 2.3.1, expect for the subscript s on all quantities indicating that the constitutive equation has been written out for interfacial quantities. Following the procedure outlined by Friedrich [97], and Schiessel et al. [55], we evaluate the complex modulus of the interface by Fourier transforming equation 3.3.3 using equation 2.2.19 to obtain

$$G_s^*(\omega) = \frac{\mathbb{V}_s (i\omega)^\alpha \cdot \mathbb{G}_s (i\omega)^\beta}{\mathbb{G}_s (i\omega)^\alpha + \mathbb{V}_s (i\omega)^\beta} \quad (3.3.4)$$

and finding the real and imaginary parts of $G_s^*(\omega)$ we obtain

$$G_s'(\omega) = \mathbb{V}_s \tau_s^{-\alpha} \frac{(\omega \tau_s)^\alpha \cos(\pi\alpha/2) + (\omega \tau_s)^{2\alpha-\beta} \cos(\pi\beta/2)}{(\omega \tau_s)^{2(\alpha-\beta)} + 2(\omega \tau_s)^{\alpha-\beta} \cos(\pi(\alpha-\beta)/2) + 1} \quad (3.3.5)$$

$$G_s''(\omega) = \mathbb{V}_s \tau_s^{-\alpha} \frac{(\omega \tau_s)^\alpha \sin(\pi\alpha/2) + (\omega \tau_s)^{2\alpha-\beta} \sin(\pi\beta/2)}{(\omega \tau_s)^{2(\alpha-\beta)} + 2(\omega \tau_s)^{\alpha-\beta} \cos(\pi(\alpha-\beta)/2) + 1} \quad (3.3.6)$$

Again, we note that Equations 3.3.4, 3.3.5 and 3.3.6 are the interfacial counterparts of Equations 2.3.14, 2.3.15 and 2.3.16 respectively.

One limitation of the critical gel model is that the elastic and viscous moduli remain parallel to each other over all frequencies, and the loss tangent $\tan \delta = \tan(\pi n/2)$ is independent of frequency. In contrast, many experiments show broad power-law signatures over some frequency range but ultimately a cross-over at low enough frequencies to a limiting viscous-like material response. The existence of a characteristic timescale in the FMM enables such a material response to be described. The crossover frequency ω_c at which $G_s' = G_s''$ for the FMM is found by equating equations 3.3.5 and 3.3.6 and we then find

$$\omega_c = \left(\frac{\mathbb{G}_s}{\mathbb{V}_s} \left[\frac{\sin \frac{\pi}{2} \alpha - \cos \frac{\pi}{2} \alpha}{\cos \frac{\pi}{2} \beta - \sin \frac{\pi}{2} \beta} \right] \right)^{\frac{1}{\alpha-\beta}} \quad (3.3.7)$$

Equation 3.3.7 makes it evident that the characteristic relaxation timescale in this model is $\tau_s \simeq \omega_c^{-1} \sim (\mathbb{V}_s/\mathbb{G}_s)^{\frac{1}{\alpha-\beta}}$, provided the argument in square brackets is positive. However there

is no crossover predicted by the model if $0 < \beta < \alpha < 0.5$ or if $0.5 < \beta < \alpha < 1$ (the total model response is then predominantly elastic or viscous, respectively, at all frequencies). For such materials no clear characteristic timescale exists.

In Figure 3.3.3 we show SAOS measurements of the interfacial viscoelasticity for 3 wt. % Acacia gum solutions and 50 mg/ml BSA solutions. The black solid lines in Figures 3.3.3(a) and 3.3.3(c) show the fit of the FMM for the elastic interfacial modulus $G'_s(\omega)$ (equation 3.3.5) for the 3 wt.% Acacia gum solutions and 50 mg/ml BSA solutions respectively. The dashed lines show the predicted values of the interfacial loss modulus $G''_s(\omega)$ (equation 3.3.6). From these fits, the power-law exponents that characterize the Acacia gum solution are determined to be $\alpha = 0.8 \pm 0.2$, $\beta = 0.124 \pm 0.003$, and the corresponding quasi-properties are $\mathbb{V}_s = 3 \pm 2 \text{ Pa m s}^{0.8}$, $\mathbb{G}_s = 0.027 \pm 0.003 \text{ Pa m s}^{0.124}$ (In Appendix B, we discuss the reason for the large confidence interval estimates for \mathbb{V}). The material parameters of the 50 mg/ml BSA solution are $\alpha = 0.80 \pm 0.07$, $\beta = 0.11 \pm 0.02$, $\mathbb{V}_s = 0.048 \pm 0.008 \text{ Pa m s}^{0.80}$, $\mathbb{G}_s = 0.017 \pm 0.001 \text{ Pa m s}^{0.11}$. When the loss modulus is plotted against the storage modulus in a Cole-Cole representation, we do not observe the simple semicircular response expected from a linear Maxwell material but instead power-law materials produce Cole-Cole plots with more complicated elliptical shapes [94]. It can be seen from the figures that the FMM captures the frequency dependence of the interfacial material functions accurately. On the other hand, the single-mode linear Maxwell model (indicated by broken lines in Figures 3.3.3(b) and 3.3.3(d)) is unable to capture the power-law behaviour of these viscoelastic interfaces.

It is possible to estimate the crossover point and hence the relaxation time of the viscoelastic interface from the FMM fit. Calculating the value of ω_c using equation 3.3.7, we find that for the Acacia gum solution $\omega_c = 7.0 \times 10^{-4} \text{ rad s}^{-1}$ corresponding to a characteristic time constant of $t_c \approx 1430 \text{ s}$. As we have noted previously, it is challenging to measure linear viscoelastic properties at such low frequencies and at room temperature due to the long times it takes for test completion, which can result in solvent evaporation. In the case of the BSA solutions the interfacial relaxation time is shorter and the crossover point can be measured directly using the DWR fixture giving $\omega_c = 0.16 \text{ rad s}^{-1}$ ($t_c \approx 6.4 \text{ s}$). This crossover to a viscously dominated response is also captured accurately by the FMM. Acacia gum clearly produces a predominantly elastic interface with a very long relaxation time.

The values of the interfacial quasi-properties of the Acacia gum and BSA solutions we have found here fully characterize the linear viscoelastic interfacial properties of the two

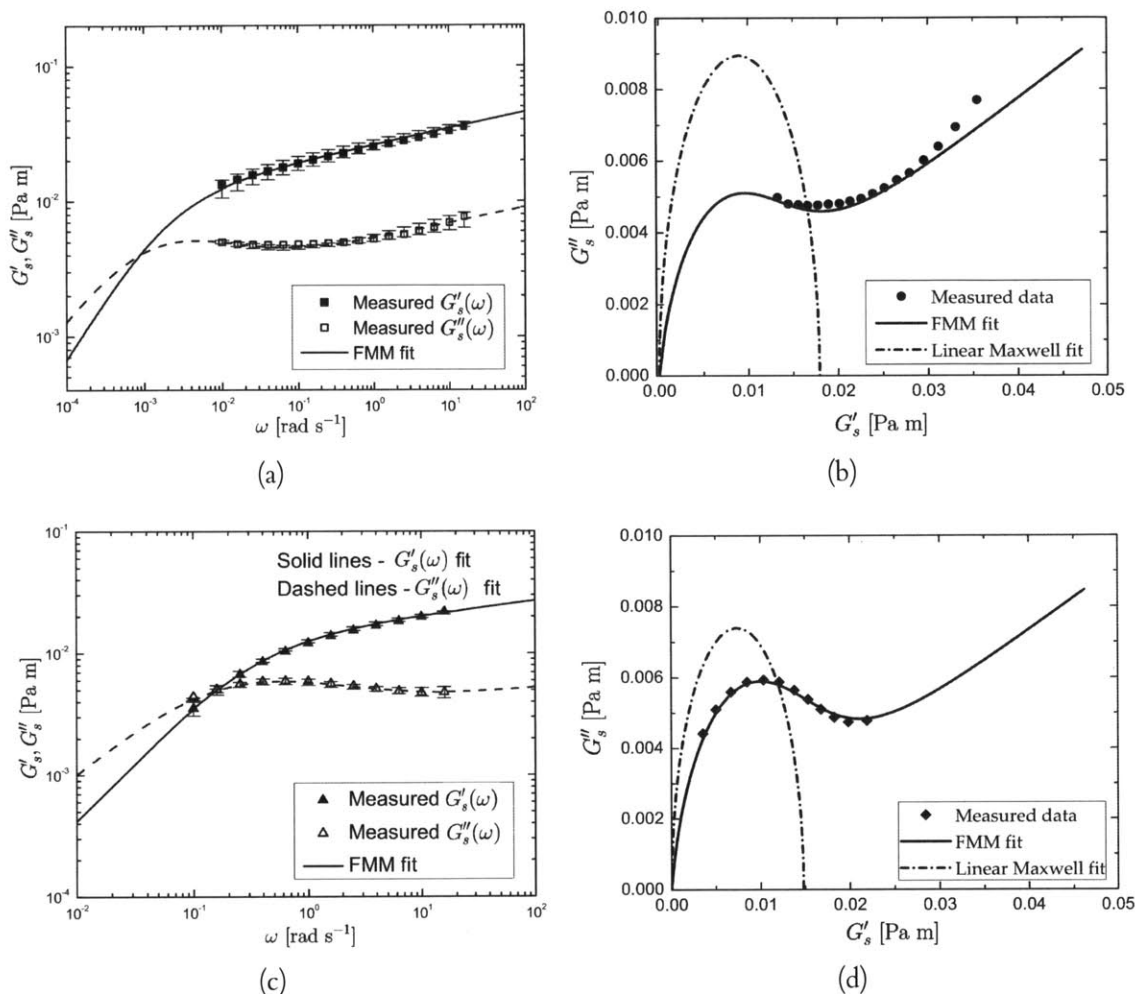


Figure 3.3.3: The FMM fitted (lines) to interfacial storage $G'_s(\omega)$ and loss $G''_s(\omega)$ moduli data (symbols) obtained from (a),(b) 3 wt.% Acacia gum solutions and (c),(d) 50 mg/ml BSA solutions. $G'_s(\omega)$. The FMM fits are given by equations 3.3.5 and 3.3.6 respectively. Cole-Cole plot of (b) the same Acacia gum solution and (d) the same BSA solution showing the fractional Maxwell fit as a solid line with a linear Maxwell fit shown for comparison by the dashed line.

solutions, and these parameters may now be used to predict the response of these rheologically complex materials to other modes of excitation. In the next subsection we discuss the transient response of the materials in creep experiments when inertial effects in the flow cannot be neglected.

3.3.4 Creep Ringing and Power-Law Responses

Inertial effects are almost always unavoidable in controlled-stress rheometry, especially in step-stress and impulse-response experiments [149]. The angular acceleration of the fixture is retarded by the moment of inertia I (units: kg m^2) of the spindle of the torsional rheometer, and the attached geometry. The coupling between this moment of inertia and the fluid viscoelasticity is seen in the general equation of motion of the fluid in step-stress experiments [150]

$$\frac{I}{b}\ddot{\gamma} = H(t)\sigma_0 - \sigma(t) \quad (3.3.8)$$

Where $\gamma(t)$ is the strain in the sample, $H(t)$ is the Heaviside step function, σ_0 is the magnitude of the step in the applied stress and $\sigma(t)$ is the retarding stress exerted by the sample on the fixture. The double over-dot indicates the second derivative with respect to time. The parameter $b = F_\gamma/F_\sigma$ is a combination of geometric factors (units: m^3) and is determined by the specific instrument and geometry used. The factors $F_\gamma = \dot{\gamma}/\Omega$ (dimensionless) and $F_\sigma = \sigma/T$ (units: m^{-3}) are geometric parameters that convert the measured variables of angular velocity Ω and torque T to shear rate $\dot{\gamma}$ and shear stress σ respectively. It can instantly be seen from Equation 3.3.8 that due to the non-zero inertia of the system, $\sigma(t) \neq H(t)\tau_0$.

For a Newtonian fluid with viscosity η , $\sigma(t) = \eta\dot{\gamma}(t)$, and in the absence of inertia, the solution to Equation 3.3.8 gives the expected linear response $\gamma(t) = (\sigma_0/\eta)t$. However, for non-zero inertia, the strain $\gamma(t)$ is given by

$$\gamma(t) = \frac{\sigma_0}{\eta} \left[t - \frac{I}{b\eta} \left(1 - \exp\left(-\frac{b\eta}{I}t\right) \right) \right] \quad (3.3.9)$$

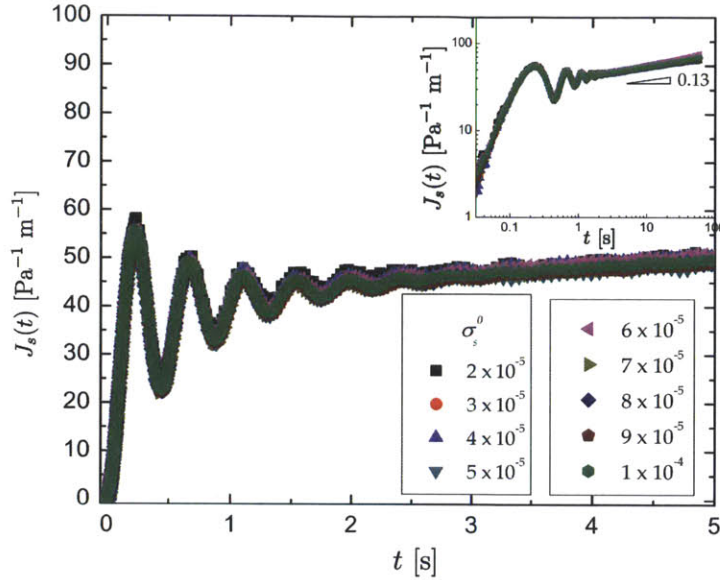
The characteristic time constant for this exponential response is $t_c = I/b\eta$. At long times $t > 3I/b\eta$ the expected linear system response is recovered but the strain is retarded by a factor $I/b\eta$ and $\gamma(t) = (\sigma_0/\eta)(t - t_c)$. For $t \ll I/b\eta$, the exponential term in Equation 3.3.9 can be expanded to obtain $\gamma(t) = (\sigma_0 b/2I)t^2 + O(t^3)$ and hence the short time response is quadratic as expected from Newton's second law. It should be noted that this short-time creep response is independent of the fluid rheology and is valid for all test fluids at sufficiently early times.

When the equation of motion (Equation 3.3.8) is coupled with a viscoelastic constitutive model, the presence of the inertial term leads to a damped oscillatory response during

creep experiments. (See Refs. [150, 151] and the Results section of this chapter for the exact form of this strain response). These oscillatory dynamics often cloud the short time creep response and are generally considered undesirable. However, Struik and others have described procedures from which one can extract bulk viscoelastic storage and loss moduli using this ‘creep-ringing’ or free oscillation [151, 152]. In this chapter, we show how this bulk analysis can also be adapted in order to use creep ringing measurements with the DWR fixture to extract the interfacial viscoelastic properties of an adsorbed protein film. Larsen et al. have observed creep ringing while studying the interfacial properties of a metal oxide film [153]. However, their analysis does not include the coupling of the inertia equation 3.3.8 with a viscoelastic model. In this paper, we adapt the bulk creep ringing formulation outlined above to the extraction of interfacial moduli using a three-parameter linear viscoelastic Jeffreys model.

In previous work using BSA solutions exhibiting interfacial viscoelasticity [53], we have shown that this technique of extracting interfacial properties even presents certain advantages over the conventional technique of conducting frequency sweep measurements to high frequencies. In this earlier study we also noted that solutions of BSA exhibit a power-law creep response at long times, which could not be adequately captured with the linear Maxwell–Jeffreys model that was considered analytically. In Appendix B, we show a creep experiment performed on 50 mg/ml BSA solutions with significant inertial effects as well as the best fit prediction of the Maxwell–Jeffreys model [26] with an added inertial mass. It is evident from the figure that linear models such as this are incapable of capturing the full viscoelastic response of the material. In the current work, we extend the creep ringing analysis to fractional viscoelastic constitutive models for the interface; we aim to predict the power-law creep behaviour over the entire time range of the experiment using the material power exponents and quasi-properties determined previously in frequency sweep experiments (Figure 3.3.3).

In figure 3.3.4 we show measurements of the interfacial creep compliance $J_s(t)$ (with units of $[\text{Pa}^{-1} \text{m}^{-1}]$) of 3 wt. % Acacia gum solutions for different values of the imposed interfacial stress σ_s^0 . We observe that the interfacial compliance $J_s(t) \equiv \gamma(t)/\sigma_s^0$ measured at different stresses collapse onto a single curve indicating the measurements are in the linear viscoelastic regime. The inset plot shows the creep compliance response at long times on logarithmic axes, which exhibits a power-law scaling in time with $J_s(t) \sim t^{0.13}$, instead of the slope of unity or zero expected from, respectively, a purely viscous or purely elastic


Figure 3.3.4

Creep compliance for 3 wt.% Acacia gum solutions performed at various values of imposed interfacial stress σ_s^0 . All experiments collapse onto a single curve as expected for a linear viscoelastic response. The interfacial viscoelasticity is coupled with instrument inertia giving rise to creep ringing at early times. The inset plot shows that at long times the creep compliance exhibits power-law behaviour with $J_s(t) \sim t^{0.13}$.

material response.

To overcome the poor predictions achieved from single mode linear viscoelastic models, and without resorting to the *ad-hoc* introduction of a large number of superposed relaxation modes, we instead use the FMM (equation 3.3.3) coupled with the inertia of the test fixture to describe both the ringing observed in the creep experiment at short times, as well as the power-law behaviour seen at long times. We begin with the equation of the motion of the spindle of the stress-controlled rheometer [150, 151],

$$\frac{I}{b_s} \frac{d^2\gamma}{dt^2} = H(t)\sigma_s^0 - \sigma_s(t) \quad (3.3.10)$$

where I is the total moment of inertia of the spindle of the rheometer and the attached test geometry (i.e. the DWR fixture), $\sigma_s(t)$ is the retarding interfacial stress applied by the sample on the spindle and $\gamma(t)$ is the resulting strain. The factor $b_s = F_\gamma/F_\sigma$ (units of m^2) is a geometric factor determined by the specific instrument and geometry used. The quantities $F_\gamma = \dot{\gamma}/\Omega$ (dimensionless) and $F_\sigma = \sigma_s/T$ (units: m^{-2}) convert the measured quantities of torque T and angular velocity Ω into the rheologically-relevant quantities of interfacial stress σ_s and strain rate $\dot{\gamma}$ respectively. Equation 3.3.10 can now be coupled with

Equation 3.3.3 to yield the fractional differential equation

$$\mathbb{V}_s \frac{d^\alpha \gamma}{dt^\alpha} + A \frac{\mathbb{V}_s}{\mathbb{G}_s} \frac{d^{2+\alpha-\beta} \gamma}{dt^{2+\alpha-\beta}} = H(t) \sigma_s^0 + \frac{\mathbb{V}_s}{\mathbb{G}_s} \frac{d^{\alpha-\beta}}{dt^{\alpha-\beta}} H(t) \sigma_s^0 \quad (3.3.11)$$

where we introduce $A = I/b_s$ for compactness. In the above equation we have used the composition rule for fractional derivatives, which states that $\frac{d^q}{dt^q} \frac{d^p f}{dt^p} = \frac{d^{p+q} f}{dt^{p+q}}$ provided $f^{(k)}(0) = 0$ where $k = 0, 1, \dots, m-1$; $m < p < m+1$ [82]. The fractional differential equation 3.3.11 is of order $2+\alpha-\beta$, and Heymans and Podlubny [154] have shown that a fractional differential equation of arbitrary real order k requires k^* initial conditions, where k^* is the lowest integer greater than k . Because we have $0 \leq \beta \leq \alpha \leq 1$, we find that we need three initial conditions. The spindle is initially at rest and hence $\gamma(0) = \dot{\gamma}(0) = 0$. However the step in stress causes an instantaneous acceleration and the third initial condition is $\sigma_s(0) = 0$ which is equivalent to $\ddot{\gamma}(0) = \sigma_s^0/A$ from equation 3.3.10.

Before we solve equation 3.3.11 for $\gamma(t)$, we first seek to determine its asymptotic behaviour in the limits of early times and long times. Evaluating the Laplace transform of equation 3.3.11 using equation 2.2.10 and employing the three initial conditions given above, we find that

$$\tilde{\gamma}(s) = \frac{\sigma_s^0}{s} \left(\frac{1 + \frac{\mathbb{V}_s}{\mathbb{G}_s} s^{\alpha-\beta}}{\mathbb{V}_s s^\alpha + A s^2 + A \frac{\mathbb{V}_s}{\mathbb{G}_s} s^{2+(\alpha-\beta)}} \right) \quad (3.3.12)$$

It may be shown (see Appendix B) that at short times equation 3.3.12 yields

$$\gamma(t) \Big|_{t \rightarrow 0} \approx \frac{1}{2} \frac{\sigma_s^0}{A} t^2 + \dots \quad (3.3.13)$$

This quadratic response is independent of the fractional orders of the spring-pots α and β as expected, because the short time response in the equation of motion 3.3.10 is dictated solely by the inertial response of the fixture; at very early times the interface has not had time to build-up any stress and hence $\sigma_s(t) \approx 0$. The solution of equation 3.3.10 under the condition $\sigma_s(t) = 0$ yields the quadratic expression in equation 3.3.13. Similarly, at long times we obtain (see Appendix B for details)

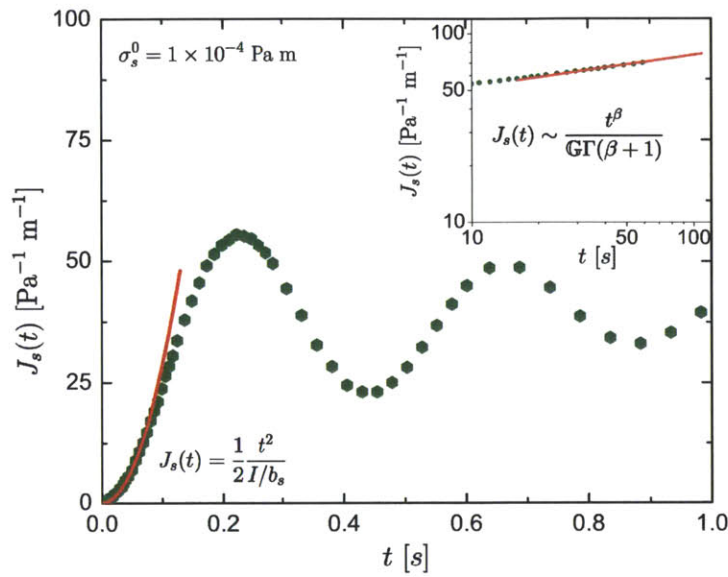
$$\gamma(t) \Big|_{t \rightarrow \infty} \approx \sigma_s^0 \left(\frac{t^\alpha}{\mathbb{V}_s \Gamma(\alpha+1)} + \frac{t^\beta}{\mathbb{G}_s \Gamma(\beta+1)} \right) + \dots \quad (3.3.14)$$

which is, to the leading order, the same as the inertia-free creep response derived in equation 2.3.13. This means that the effects of inertia become unimportant at long times, as observed in the experimental measurements shown in Figure 3.3.4.

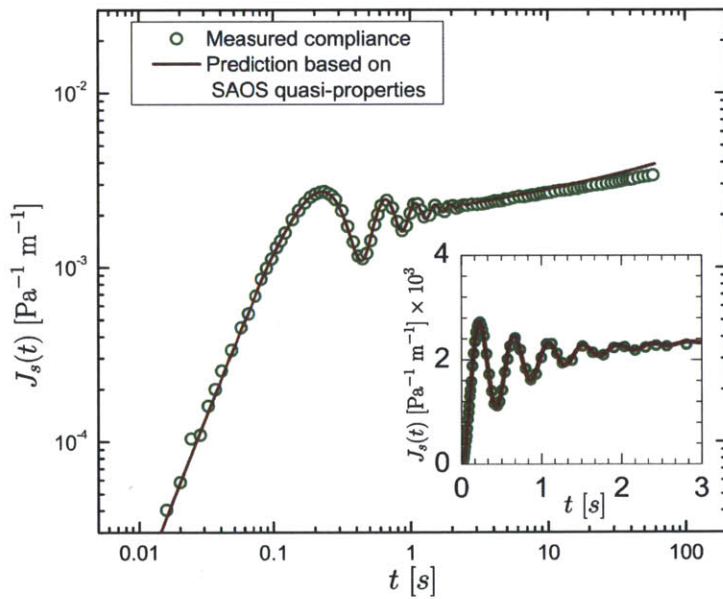
The value of $A = I/b_s$ can be calibrated once the rheometer fixture is selected and in our case was found to be $A = 1.72 \times 10^{-4}$ kg. Figure 3.3.5(a) shows the asymptotic short time response (line) given by equation 3.3.13 plotted against the measured interfacial creep compliance of a 3 wt. % Acacia gum solution (filled symbols). It can be seen that the short time asymptotic response agrees very well with the measured data. The inset plot also shows the value of the long time asymptote derived in equation 3.3.14. From the fractional Maxwell Cole-Cole fits shown in figure 3.3.3, the fit values that characterize the Acacia gum solutions are found to be $\alpha = 0.8 \pm 0.2$, $\beta = 0.124 \pm 0.003$, $\mathbb{V}_s = 3 \pm 2$ Pa s^{0.8}, $\mathbb{G}_s = 0.027 \pm 0.003$ Pa s^{0.124}. Because $\frac{t^\beta}{\mathbb{G}_s} \approx 6 \frac{t^\alpha}{\mathbb{V}_s}$ at $t = 60$ s, we find that the first term in equation 3.3.14 is smaller than the second. Therefore, to a first approximation, at long times $\gamma(t) \approx \frac{\sigma_s^0}{\mathbb{G}_s} \frac{t^\beta}{\Gamma(1+\beta)}$. Calculating the value of the coefficient $\frac{1}{\mathbb{G}_s \Gamma(1+\beta)}$, we find it equals 39.3 Pa⁻¹ m⁻¹ s^{-0.124}. When we fit a power-law of the form $\gamma(t) = at^b$ directly to the measured data, where a and b are fitting constants, we find that the measured data at long times is described by $J_s(t) \approx 40.4t^{0.130}$ Pa⁻¹ m⁻¹, which is in excellent agreement with the analytically derived asymptotic predictions for long times. This asymptotic power-law creep behaviour, shown as the solid line in the inset plot in Figure 3.3.5, cannot be conveniently captured using conventional spring-dashpot models.

We now proceed to predict the interfacial creep response of the Acacia gum solutions based on the FMM fit parameters and quasi-properties found previously. To this end, we solve equation 3.3.11 for the strain $\gamma(t)$ with the values of \mathbb{V}_s , \mathbb{G}_s , α and β determined from the fits of the FMM to the small amplitude oscillatory shear data. Equation 3.3.11 is amenable to an analytical solution and can be found by calculating the inverse Laplace transform of equation 3.3.12, in terms of the Mittag-Leffler function defined in equation 2.3.4. However the resulting expression is cumbersome to evaluate because it contains a double infinite sum. Instead, we circumvent this difficulty by solving equation 3.3.11 numerically using the procedure outlined by Podlubny et al. and a modified version of a MATLAB code freely available from the same group. We refer the reader to Ref. [86] for details of the numerical scheme used.

The resulting numerical solution of equation 3.3.11 obtained using the quasi-properties found from SAOS is plotted in figure 3.3.5(b) as a solid line overlaid onto the experimentally



(a)



(b)

Figure 3.3.5: (a) Experimentally measured values of the interfacial compliance response (symbols), and the short and long time asymptote in the FMM coupled with instrument inertia. At early times, we retrieve the expected quadratic response of $J_s(t) \sim \frac{1}{2} \frac{t^2}{I/b_s}$ which is in accordance with the equation of motion at very early times. At long times, the effect of inertia only appears as a higher order correction (equation 3.3.14). (b) The predicted interfacial creep compliance from solving equation 3.3.11 numerically using the exponents and quasi-properties found from the SAOS experiments that characterize the Acacia gum solutions. The prediction made by the model is in excellent agreement with the measured data, and it captures both the creep ringing at early times as well as the power-law behaviour observed at long times.

measured compliance data. It is observed that the prediction of $J_s(t)$ based on the previously fitted quasi-property values is in very good agreement with the measured temporal response over the entire range of the creep experiment, indicating that the quasi-properties of the FMM characterize the rheological response of the material over a wide range of timescales. This fractional constitutive model can predict the response to other excitations once the quasi-properties have been found from SAOS fits. This would not be possible using empirical laws such as the KWW expression, or the critical gel equation, although these laws are able to capture power-law behaviour. It is noteworthy that the FMM contains only two additional parameters (α, β) beyond a simple Kelvin or Maxwell response and yet enables excellent predictions accounting for the damped inertio-elastic effects at short times as well as the long time power-law response.

3.4 Conclusions

We have revisited the concept of quasi-properties for describing the rheology of complex microstructured materials and interfaces, and demonstrated how their inclusion in fractional constitutive models containing spring-pot mechanical elements leads to the natural and quantitative description—using only a few constitutive parameters—of power-law behaviour frequently observed experimentally. Not only is this fractional constitutive approach more compact than the traditional approach of using a multi-mode Prony series, it is also more physical; in the latter approach, the number of fitted parameters as well as their magnitudes depend on the timescale of the experiment used for model fitting.

In the spring-pot constitutive equation, the elastic modulus, $G'(\omega)$, and the loss modulus, $G''(\omega)$, increase as a function of frequency while maintaining a constant ratio between them. This is reminiscent of the behaviour observed in critical gels and soft glassy materials [18]. In fact it can be shown that the soft glassy rheology (SGR) model under certain conditions yields exactly the same constitutive relationship as a single spring-pot defined in the Caputo sense, and the ‘effective noise temperature’ x in the SGR model is intimately related to the fractional exponent α (or β). Both these aspects are discussed in Appendix B.

Not only can fractional models accurately model the complex relaxation behaviour exhibited by bulk materials (as demonstrated here using Scott-Blair’s (1947) original data on ‘highly anomalous’ butyl rubber), they can also be extended to describe complex viscoelastic interfaces as well. Using small amplitude oscillatory shear experiments, we measured

the power-law linear viscoelastic behaviour exhibited by interfaces formed from adsorbed films of bovine serum albumin and Acacia gum. By fitting the data to the FMM, we could extract the quasi-properties \mathbb{V}_s , \mathbb{G}_s and exponents α, β that characterize these rheologically-complex interfaces. We then considered the transient flow generated by an interfacial creep experiment in which inertial contributions are significant. We were able to predict *a priori* the inertio-elastic creep ringing observed at short times as well as the long-time power-law response using the values of the quasi-properties determined previously. There is excellent agreement between the model predictions and the experimental data across a wide range of timescales. These measurements demonstrate that once the quasi-properties of a material have been determined from one particular excitation they characterize this rheologically-complex interface and help determine the material response to other modes of deformation.

Finally we note that all of the models presented here describe the linear viscoelastic limit and cannot describe non-linear viscoelastic behaviour (for example the onset of shear thinning or strain softening) exhibited by many complex fluids and interfaces at large strains. In the next chapter we turn our attention to extending these models to the nonlinear regime and develop a frame invariant fractional constitutive equation that involves a finite strain measure.

4 | *Nonlinear Shear Deformations*

We have seen that the relaxation processes of a wide variety of soft materials frequently contain one or more broad regions of power law-like or stretched exponential relaxation in time and frequency. Fractional constitutive equations have been shown to be excellent models for capturing the linear viscoelastic behavior of such materials, and their relaxation modulus can be quantitatively described very generally in terms of a Mittag-Leffler function. However, these fractional constitutive models cannot describe the non-linear behavior of such power-law materials. In this chapter, we use the example of Xanthan gum to show how predictions of non-linear viscometric properties such as shear-thinning in the viscosity and in the first normal stress coefficient can be quantitatively described in terms a nonlinear fractional constitutive model. We adopt an integral K-BKZ framework and suitably modify it for power-law materials exhibiting Mittag-Leffler type relaxation dynamics at small strains. Only one additional parameter is needed to predict nonlinear rheology, which is introduced through an experimentally measured damping function. Empirical rules such as the Cox-Merz rule and Gleissle mirror relations are frequently used to estimate the non-linear response of complex fluids from linear rheological data. We use the fractional model framework to assess the performance of such heuristic rules and quantify the systematic offsets, or shift factors, that can be observed between experimental data and the predicted nonlinear response. We also demonstrate how an appropriate choice of fractional constitutive model and damping function results in a nonlinear viscoelastic constitutive model that predicts a flow curve identical to the elastic Herschel-Bulkley model. This new constitutive equation satisfies the Rutgers-Delaware rule, that is appropriate for yielding materials. This K-BKZ framework can be used to generate canonical three-element mechanical models that provide nonlinear viscoelastic generalizations of other empirical inelastic models such as the Cross model. In addition to describing nonlinear viscometric responses, we are also able to provide accurate expressions for the linear viscoelastic behavior of complex materials

that exhibit strongly shear-thinning Cross-type or Carreau-type flow curve. The findings in this chapter provide a coherent and quantitative way of translating between the linear and nonlinear rheology of multiscale materials, using a constitutive modeling approach that involves only a few material parameters.

4.1 Introduction

Many multiscale materials typically exhibit a broad power-law regime of stress relaxation over many decades of timescales, but at sufficiently long times (or low frequencies) ultimately transition into either a sol-like flow regime or a gel-like plateau regime. Both of these responses can be captured by appropriate two element fractional constitutive models arranged in series or parallel. The Fractional Maxwell Model (FMM) consists of two springpot elements in series [155]. The FMM compactly describes the rheological properties of multiscale materials that exhibit sol-like flow at long timescales. In Chapter 3, we have shown using the example of viscoelastic interfaces formed from globular protein solutions that the FMM can quantitatively predict the *linear* rheological behavior of complex fluids under a range of different deformation conditions [93]. The relaxation modulus in the FMM takes the analytical form of a Mittag-Leffler function, which exhibits stretched exponential (KWW) behavior at short times, and power-law behavior at long timescales [106].

On the other hand, complex fluids exhibiting a gel-like response in the long timescale limit are better modeled by the Fractional Kelvin-Voigt Model (FKVM). This second canonical fractional constitutive equation comprises of two springpots arranged in parallel. Both the FMM as well as the FKVM are characterized by only four parameters — two power-law exponents, which control the scaling for the temporal and frequency response, and two quasi-properties, which set the scales for magnitude of the stresses in these multiscale materials. However we note that while the linear viscoelastic predictions of fractional models have now been extensively studied, there is an absence of fractional constitutive equations that are able to predict the *nonlinear* rheological response of these complex materials observed at large strain. Yang et al. provide an overview of previous attempts at developing appropriate frame invariant models utilizing fractional derivatives and also list their shortcomings [156]. They develop an appropriate finite strain measure coupled with the Mittag-Leffler relaxation kernel, and this leads to a frame-invariant Fractional Upper

Convected Maxwell formulation. However, this model suffers from the same limitations of all quasi-linear models [24] and is unable to predict shear-thinning in the viscosity, and also predicts a constant first normal stress coefficient $\Psi_1(\dot{\gamma})$ at all shear rates. This absence of shear-thinning effects is in stark contrast to the very broad shear-thinning response observed in common complex multiscale materials such as Xanthan gum.

Larson has previously shown that by using the integral form of the K-BKZ type equation with a simple power-law relaxation kernel and a suitable strain dependent damping function, the nonlinear rheology of polydisperse polymer melts can be accurately predicted [28]. However as we have noted above, a single power-law type relaxation kernel of the form $G(t) = ct^{-\alpha}$, in which c and $0 < \alpha < 1$ are the only material constants that characterize the linear response, does not adequately characterize the viscoelastic response of many complex materials that show two or more distinct power-law regimes during relaxation. One commonly employed experimental technique for gaining insight into nonlinear rheological properties of complex materials is through the use of empirical rules such as the Cox-Merz rule [157], Laun's rule [158] or the Gleissle Mirror Relations [24, 159]. These empirical rules connect the progressive shear-thinning behavior observed in many complex multiscale materials to the very broad relaxation spectra observed in linear viscoelastic tests such as small amplitude oscillatory shear flow ([24, 160]). Booij and Leblans have shown that irrespective of the particular form of the relaxation spectrum, viscoelastic materials will obey the Cox-Merz rule when the shear component of the nonlinear strain measure $S_{12}(\dot{\gamma}s)$ satisfies [161]

$$S_{12}(\dot{\gamma}s) = \int_0^{\dot{\gamma}s} J_0(v) dv \quad (4.1.1)$$

in which $J_0(v)$ is the zeroth order Bessel function of the first kind and $\dot{\gamma}s$ is the total shear strain accumulated in the time interval s . However, Renardy [162] notes that this relation is not plausible; he demonstrates that under the assumption of a very broad spectrum of relaxation modes such that the same modes participate in linear as well as nonlinear response, along with the simplest possible strain-dependent damping function, materials do indeed obey rules like the Cox-Merz rule to within a *constant factor*. This assumption of a broad spectrum of relaxation times holds true for a power-law material and we should thus expect that a suitable nonlinear generalization of fractional viscoelastic models can be used

to understand the predictive capabilities of these empirical rheological rules.

In this chapter, we use the K-BKZ framework together with Scott Blair's ideas of quasi properties and the fractional calculus to quantify the magnitude of this offset factor in the Cox-Merz rule and interpret its existence in terms of the accumulated damage in a multi-scale material arising from the nonlinear response to the applied deformation. In Fig. 4.1.1 we present a flowchart of the various pathways discussed in this paper to predict nonlinear material response, including the application of the empirically based Cox-Merz rule and the Gleissle mirror relations. We discuss these relationships in more detail in Section 4.3.3. We also demonstrate using our K-BKZ model how one may quantify the systematic offset that is commonly observed between these empirical relationships and experimentally measured data.

We begin with the Fractional Maxwell Model [93] and extend Larson's K-BKZ approach to include relaxation kernels of Mittag-Leffler type. Incorporating Renardy's arguments for broad relaxation spectra, we show that by using an appropriate damping function that accurately captures the transition to nonlinear shear-thinning behavior, one can make accurate predictions of both steady shear viscosity $\eta(\dot{\gamma})$ as well as first normal stress coefficient $\Psi_1(\dot{\gamma})$ as a function of shear rate. To demonstrate the quantitative capabilities of the model, we compare our predictions with nonlinear rheological data obtained for Xanthan gum, a complex semi-rigid, branched and physically associated polysaccharide that shows a very broad relaxation spectrum. Empirical rules such as the Cox-Merz rule and the Gleissle Mirror relations (see Fig. 4.1.1) have been reported to over-predict the nonlinear material functions in the case of polysaccharide gums [163, 164] and we show that this over-prediction is connected directly to the power-law exponents that characterize the shape of the material's relaxation spectrum.

Another rule relating steady shear flow and oscillatory flow, referred to by Krieger [165] as the Rutgers-Delaware rule, has been proposed by Doraiswamy et al. for materials in which the timescale of the applied deformation is much shorter than a characteristic structural recovery time [166]. This is often the case with complex materials that yield upon the application of a small deformation. These materials appear gel-like or solid-like at rest and yield or flow at large strains. We use the Fractional Kelvin Voigt Model (FKVM) that characterize the linear viscoelastic properties of solid-like power-law gels, along with a damping function proposed by Tanner and Simmons [167] to derive the Herschel-Bulkley equation for flow of a yielding material under steady shear. For this nonlinear fractional

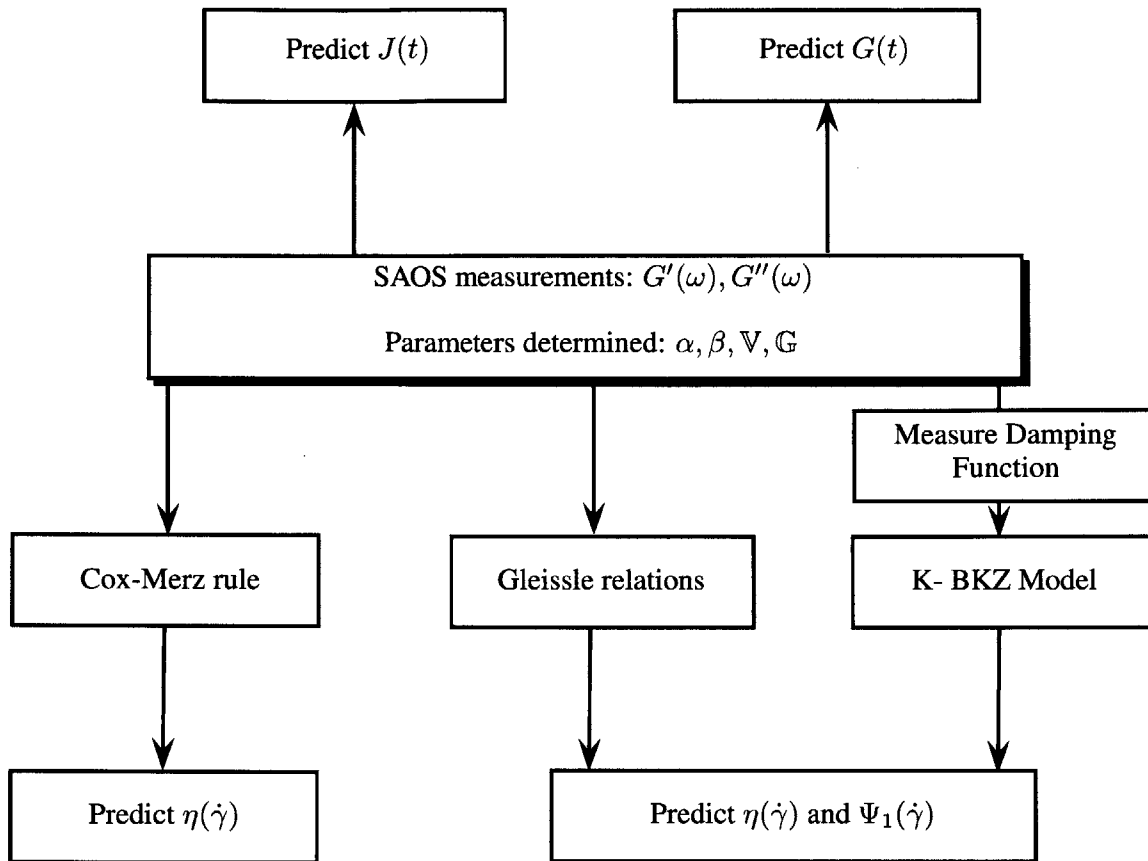


Figure 4.1.1: Flowchart showing the pathways described in this paper to arrive at viscometric material functions for multiscale materials. Beginning with a simple linear viscoelastic experiment such as Small Amplitude Oscillatory Shear (SAOS), and characterizing the power-law responses of material using a fractional constitutive model, we can make accurate predictions of other linear material functions such as the creep compliance $J(t)$ and the relaxation modulus $G(t)$. We also show in this paper that by measuring the damping function $h(\gamma)$ and using a K-BKZ framework in conjunction with the previously determined quasi-properties, nonlinear material functions such as the steady shear viscosity $\eta(\dot{\gamma})$ and the first normal stress coefficient $\Psi_1(\dot{\gamma})$ can be evaluated accurately.

gel, we also demonstrate that we can recreate exactly the Rutgers-Delaware rule proposed by Doraiswamy et al.

The remainder of this chapter is organized as follows: in the next section we present details of the preparation of the Xanthan gum solutions used in this study as prototypical power-law materials. The linear viscoelastic properties of these gums can be well characterized in compact form using the concept of quasi-properties and fractional constitutive equations. We also discuss in this section the experimental protocol and instrumentation employed for rheometric measurements. In the third section, we briefly review some of

the mathematical preliminaries of fractional calculus and springpots. The fourth section presents our experimental results and theoretical insights from the K-BKZ framework, the quantification of the shift factors that exist in the predictions of empirical relationships such as the Cox-Merz rule and the development of the Herschel-Bulkley model for yielding multiscale materials. We also derive exactly the Rutgers-Delaware rule for such materials. We next discuss the Fractional Zener Model (FZM) and show how this leads to a prediction of the flow curves of materials that are well described by the familiar inelastic Cross and Carreau models. The advantage of our approach is that in addition to the correct nonlinear flow curves, we are also able to obtain expressions for the linear viscoelastic response of materials described by the Herschel-Bulkley and Cross models. Furthermore, we also obtain predictions for the first normal stress coefficient $\Psi_1(\dot{\gamma})$ for such materials.

4.2 *Materials and Methods*

Xanthan is a highly branched high molecular weight polysaccharide produced by the *Xanthomonas campestris* bacterium [64, 168]. Both the molecular structure as well as the rheology of Xanthan gum has been extensively characterized in previous studies [169–173], amongst others. Xanthan gum finds applicability in various biological, pharmaceutical and industrial applications. In Figure 4.2.1 we present a summary of the various applications of Xanthan gum (table adapted from Ref. [68].) Due to the wide applicability of Xanthan gum, and the fact that it shows broad power-law rheological response [164], we use it as a model fluid in this chapter.

The Xanthan gum used in this study was sourced from Sigma-Aldrich (SKU: G1253) in powder form. To prepare the solutions, the specified amount of the powder was weighed using a Mettler-Toledo weighing scale (resolution 10^{-4} g) and added to deionized water at 25°C to prepare a stock solution of 1 wt.% Xanthan gum solution. The mixture was then stirred using a magnetic stirrer for 24 hours at 300 rpm. To enable complete biopolymer hydration, the solution was stored at 4°C for at least another 12 hours before being used for rheological testing ([143]). Additional solutions of 0.5 wt.% and 0.25 wt.% were prepared by careful dilution of the 1 wt.% stock solution immediately after the initial 24 hour stirring, and were also allowed to hydrate at 4°C for 12 hours.

The rheometry performed in this study was carried out using a stress controlled DHR-3 rheometer (TA Instruments, Newcastle, DE) with a 6 cm diameter 2° cone-and-plate

Application	Concentration (% w/w)	Functionality
Salad dressings	0.1–0.5	Emulsion stabilizer; suspending agent, dispersant
Dry mixes	0.05–0.2	Eases dispersion in hot or cold water
Syrups, toppings, relishes, sauces	0.05–0.2	Thickener; heat stability and uniform viscosity
Beverages (fruit and non-fat dry milk)	0.05–0.2	Stabilizer
Dairy products	0.5–0.2	Stabilizer; viscosity control of mix
Baked goods	0.1–0.4	Stabilizer; facilitates pumping
Frozen foods	0.05–0.2	Improves freeze–thaw stability
Pharmaceuticals (creams and suspensions)	0.1–1	Emulsion stabilizer; uniformity in dosage formulations
Cosmetic (denture cleaners, shampoos, lotions)	0.2–1	Thickener and stabilizer
Agriculture (additive in animal feed and pesticide formulations)	0.03–0.4	Suspension stabilizer; improved sprayability, reduced drift, increased cling and permanence
Textile printing and dyeing	0.2–0.5	Control of rheological properties of paste; preventing dye migration
Ceramic glazes	0.3–0.5	Prevents agglomeration during grinding
Slurry explosives	0.3–1.0	Thickens formulations; improves heat stability (in combination with guar gum)
Petroleum production	0.1–0.4	Lubricant or friction reduction in drill-hole
Enhanced oil recovery	0.05–0.2	Reduces water mobility by increasing viscosity and decreasing permeability

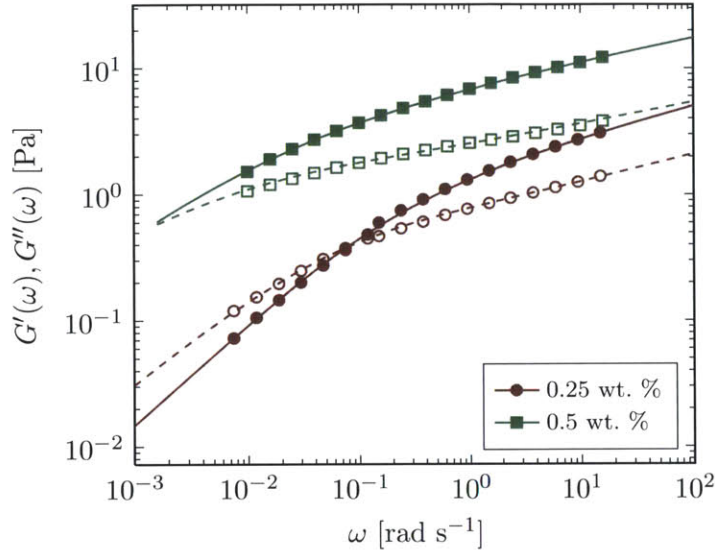
Figure 4.2.1: The various industrial applications of Xanthan gum. Reproduced from Ref. [68].

fixture. Care was taken to prevent evaporation by saturating the environment around the test fluid using a solvent trap. All experiments were performed on a Peltier plate at a constant temperature of 25°C.

4.3 Results and Discussion

4.3.1 Linear Viscoelasticity

In Fig. 4.3.1 we show the results of a frequency sweep experiment using small amplitude oscillatory shear (SAOS) on 0.25 wt.% and 0.5 wt.% Xanthan gum. The strain amplitude chosen was $\gamma_0 = 1\%$, and this amplitude was chosen from an independently performed strain amplitude sweep (not shown) to ensure tests are in the linear regime. We note that there are two distinct power-law regimes visible at low and high frequencies respectively, and there is a gradual transition from one asymptote to the other. The solid and dashed lines

**Figure 4.3.1**

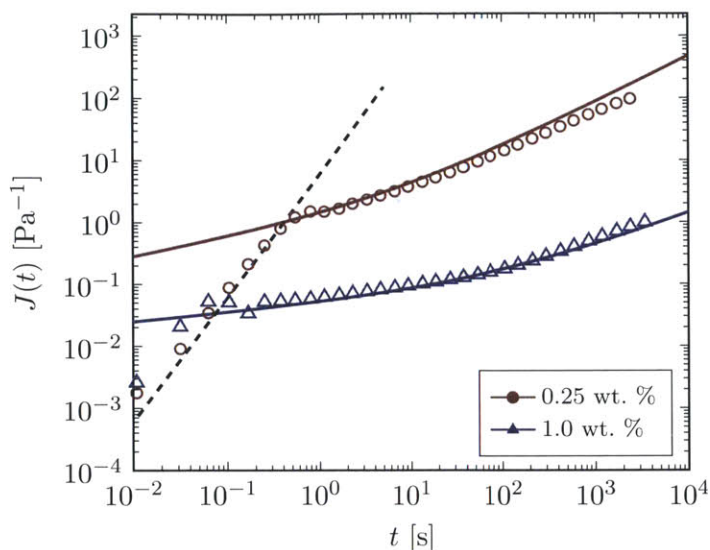
Small Amplitude Oscillatory Shear (SAOS) experiments performed on different concentrations of Xanthan gum. Data are shown by filled symbols (storage modulus) and hollow symbols (loss modulus), while the solid lines are fits to the storage modulus $G'(\omega)$ (Eq.2.3.15) and the dashed lines are fits to the loss modulus $G''(\omega)$ (Eq.2.3.16). The parameter values determined for each fluid are given in Table 1.

represent fits of the data to the predictions for $G'(\omega)$ and $G''(\omega)$ (Eqs. (2.3.15) and (2.3.16) respectively) obtained from the FMM. We also performed additional SAOS experiments on a 1 wt.% Xanthan gum solution (not shown in Fig. 4.3.1 for clarity) which are equally well described by the FMM. The values of the exponents α, β and the quasi-properties \mathbb{V}, \mathbb{G} obtained from these fits are tabulated in Tab. 4.3.1.

As the concentration of Xanthan gum is increased, the values of α and β progressively decrease, indicating transition to more gel-like behavior, with an increasingly broad spectrum of relaxation times. At the same time, an increase in Xanthan concentration leads to an increase in the quasi-properties \mathbb{V} and \mathbb{G} , implying that the magnitude of the stress increases. These constitutive parameters completely characterize the linear rheology of these viscoelastic Xanthan gum solutions and will be used to make predictions of the material response in other deformations. There exists a characteristic frequency at which the two power-law regimes transition from one to the other, and this is determined by the frequency ω_c at which $G'(\omega)$ and $G''(\omega)$ intersect. This can be found by equating Eqs. (2.3.15) and (2.3.16) and solving for the crossover frequency:

$$\omega_c = \left(\frac{\mathbb{G}}{\mathbb{V}} \left[\frac{\sin(\pi\alpha/2) - \cos(\pi\alpha/2)}{\cos(\pi\beta/2) - \sin(\pi\beta/2)} \right] \right)^{1/(\alpha-\beta)} \quad (4.3.1)$$

In Eq. (4.3.1), real solutions to ω_c exist only if $0 \leq \beta < 0.5 < \alpha \leq 1$ [93]. If these constraints are not satisfied, it means that there is no crossover between the storage and loss moduli.


Figure 4.3.2

Creep experiments performed on different concentrations of Xanthan gum (symbols) and the corresponding predictions of the linear viscoelastic creep compliance $J(t)$ (Eq. (2.3.13)). The applied stress is $\sigma_0 = 0.5$ Pa. The values of the constitutive parameters $\alpha, \beta, \mathbb{V}$ and \mathbb{G} used to make the prediction are obtained directly from the SAOS experiments (Table 1). The initial quadratic response at short times is given by $J(t) = (b/2I)t^2$ and occurs due to the coupling of the instrument inertia with viscoelasticity, and is shown as a black dashed line.

Once the linear viscoelasticity of the solutions have been characterized in this manner, we may now make predictions of the rheological response of the Xanthan gum solutions in other linear experiments.

In Fig. 4.3.2 we show the measured creep compliance data (symbols) for 0.25 wt.% and 1 wt.% Xanthan gum solutions. The lines are *a priori* predictions obtained from the FMM by substituting the corresponding model values (taken from Table 4.3.1) into Eq.(FMMCompliance). At short times the compliance increases as $J(t) \sim t^\beta$ whereas at long times the rate of creep increases, and $J(t) \sim t^\alpha$. The crossover between these regimes is gradual and depends on the values of \mathbb{V} , \mathbb{G} , α and β . Our prediction closely agrees with the measured data, and both of these power-law regimes are visible. At very short times $t \lesssim 1$ s, the measured creep compliance grows quadratically and overdamped periodic oscillations are observed. These oscillations, frequently referred to as creep ringing, arises from

Table 4.3.1: Values of the model parameters $\alpha, \beta, \mathbb{V}$ and \mathbb{G} of the FMM for different concentrations of Xanthan Gum.

Conc. [wt. %]	α	β	\mathbb{V} [Pa s $^\alpha$]	\mathbb{G} [Pa s $^\beta$]	ω_c [rad s $^{-1}$]	τ [s]
0.25	0.76	0.24	7.02	1.82	7.46×10^{-3}	13.41
0.50	0.64	0.19	71.65	7.82	1.34×10^{-3}	748.74
1.0	0.60	0.14	208.54	22.46	5.4×10^{-4}	1846.05

the coupling of instrument inertia with sample viscoelasticity [150]. The initial quadratic response in the compliance arises purely due to the inertia of the measurement system and is given by $J(t) = (b/2I)t^2$, in which b is a geometry dependent measurement system factor and I is the total inertia of the spindle and the attached fixture. Because the initial quadratic response is material independent and is only a function of the attached fixture and system inertia, the short time response of both fluids coincide. However, the crossover from the short time inertia dominated response to the power-law response of the fluid occurs when

$$\frac{1}{2} \frac{b}{I} (t^*)^2 \approx \frac{(t^*)^\beta}{G\Gamma(1+\beta)} \Rightarrow t^* \approx \left(\frac{2I/b}{G\Gamma(1+\beta)} \right)^{1/(2-\beta)} \quad (4.3.2)$$

In a similar fashion, predictions of the relaxation modulus $G(t)$ and other linear viscoelastic material functions such as the transient viscosity $\eta^+(t)$ observed during start up of steady shear flow [24] can be made; we only require the parameter set $(\alpha, \beta, \mathbb{V}$ and $\mathbb{G})$ that characterize the material. However, in each case, the material response will be independent of the magnitude of the imposed stress or strain amplitude. By contrast, experimental measurements on complex viscoelastic materials such as Xanthan gum solutions show a transition to strongly shear-rate dependent material properties [164], and we now seek to characterize this transition by generalizing the FMM to enable it to describe the rheological response to nonlinear deformations.

4.3.2 *Nonlinear Viscoelasticity and the K-BKZ Model*

When large nonlinear deformations are applied to complex fluids such as Xanthan gum, there is progressive loss of internal structure or damage to the equilibrium network in the material due to accumulated strain [174]. The material functions measured upon the application of a nonlinear strain are bounded by a linear viscoelastic envelope, and nonlinear material functions lie below this envelope. This damage or loss of internal structure is quantified by a monotonically decreasing *damping function* $h(\gamma)$, which we define below. We note that there are some polysaccharide systems that show thickening and hardening effects upon large strain deformations [71, 175]. Such systems are beyond the scope of this work, but can be described by more complex functional forms of $h(\gamma)$. In the present study we focus on responses that are bounded by a linear viscoelastic envelope.

For the case of a steady shearing deformation, we may first evaluate this envelope by

substituting into the constitutive equation for the FMM (Eq. 2.3.1) the functional form of the deformation imposed during steady shear:

$$\dot{\gamma}(t) = \dot{\gamma}_0 H(t), \quad (4.3.3)$$

where $\dot{\gamma}_0$ is the steady shear rate applied at time $t = 0$ and $H(t)$ is the Heaviside step function. We therefore arrive at

$$\sigma(t) + \frac{\mathbb{V}}{\mathbb{G}} \frac{d^{\alpha-\beta} \sigma(t)}{dt^{\alpha-\beta}} = \mathbb{V} \dot{\gamma}_0 \frac{d^{\alpha-1} H(t)}{dt^{\alpha-1}} \quad (4.3.4)$$

Taking the Laplace transform [82] of Equation 4.3.4 we obtain

$$\tilde{\sigma}(s) = \frac{\mathbb{V} \dot{\gamma}_0 s^{\alpha-2}}{1 + (\mathbb{V}/\mathbb{G}) s^{\alpha-\beta}} \quad (4.3.5)$$

In deriving the Laplace transformed stress $\tilde{\sigma}(s)$ above, we have assumed initial conditions of $\gamma(0) = 0$ and $\dot{\gamma}(0) = 0$. We invert the transformed stress using known identities [82, 176] to obtain

$$\eta^+(t) = \frac{\sigma(t)}{\dot{\gamma}_0} = \mathbb{G} t^{1-\beta} E_{\alpha-\beta, 2-\beta} \left(-\frac{\mathbb{G}}{\mathbb{V}} t^{\alpha-\beta} \right) \quad (4.3.6)$$

We note two things here: first, that the steady shear viscosity is independent of the shear rate, as expected for a linear model and second, that the shear viscosity grows as a function of time and never reaches steady state, unless $\alpha = 1$. The Mittag-Leffler function asymptotically decays as $t^{-(\alpha-\beta)}$ (see Eq. 4.3.17) for large arguments and hence $\eta^+(t) \sim t^{1-\alpha}$. This means that for the case of a dashpot with $\alpha = 1$, $\eta^+(t) \rightarrow \mathbb{V} (= \eta)$ at long times.

To be able to capture experimental observation of the shear rate dependence of the viscosity, and to be able to obtain an equilibrium steady state viscosity, we need to incorporate into our model a frame invariant finite strain measure. We follow the approach of Larson [28] who argued that the nonlinear rheology of complex multiscale materials such as polydisperse polymer melts can be described by using a separable equation of the integral K-BKZ type [24]. While Larson selected a single power-law relaxation kernel, we extend the analysis to relaxation kernels of the Mittag Leffler kind. By assuming that the temporal response and strain response are separable or factorizable, so that the stress tensor $\sigma(t)$ can

be written as ([24, 177])

$$\sigma(t) = \int_{-\infty}^t m(t-t') \left[2 \frac{\partial U}{\partial I_1} C^{-1} - 2 \frac{\partial U}{\partial I_2} C \right] dt' \quad (4.3.7)$$

in which

$$m(t-t') = \frac{\partial G(t-t')}{\partial t'} \quad (4.3.8)$$

is the memory function of the material, $U \equiv U(I_1, I_2)$ is a potential function that is related to the strain energy function of the material and $C^{-1} = (F^{-1})^T \cdot F$ is the Finger tensor [24]. For a steady shear flow, it can be shown that the Finger tensor C^{-1} can be written as [19]

$$C^{-1} = \begin{pmatrix} 1 + \gamma^2 & \gamma & 0 \\ \gamma & 1 & 0 \\ 0 & 0 & 1 \end{pmatrix} \quad (4.3.9)$$

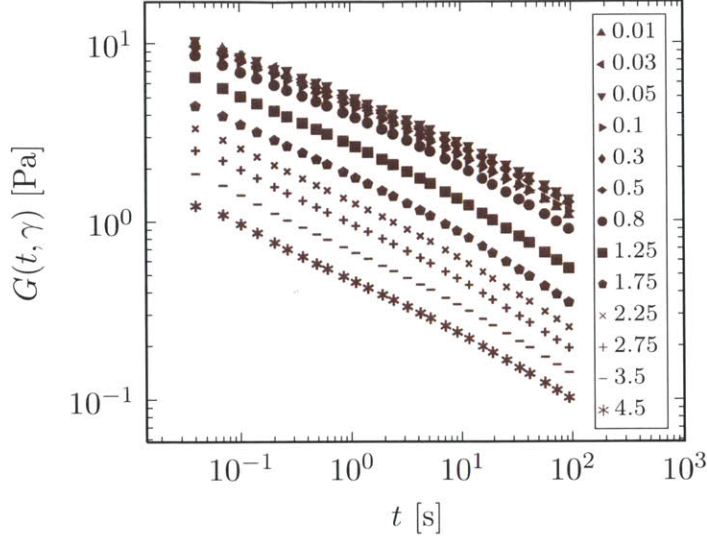
If we neglect the second term in brackets, i.e. the potential function have no dependence on the second invariant I_2 [76], then for the specific kinematics of a shear deformation, the expression for the shear stress can be written as [177]

$$\sigma(t) = \int_{-\infty}^t m(t-t') h(\gamma) \gamma(t, t') dt' \quad (4.3.10)$$

in which $\gamma(t, t') = \gamma(t') - \gamma(t)$ is the relative strain accumulated between times t and t' and $h(\gamma)$ is a damping function defined as

$$h(\gamma) = \frac{G(t, \gamma)}{G(t)}. \quad (4.3.11)$$

Many polymer kinetic theories can be rewritten in the form of the separable K-BKZ integral equations defined above, including the Rouse-Zimm theory and the Lodge network theory [24]. The challenge lies in determining a molecular basis for the memory function $m(t-t')$. In what follows we select the Mittag-Leffler relaxation kernel as the appropriate


Figure 4.3.3

Relaxation modulus $G(t)$ obtained from step strain experiments performed on a 0.5 wt.% Xanthan gum solution at different strain amplitudes. The legend box shows the strain amplitude γ_0 at which the stress relaxation test was performed. Increasing the strain amplitude causes a progressive decrease in the relaxation modulus, which can be quantified using a damping function of the form given by Eq.(4.3.11).

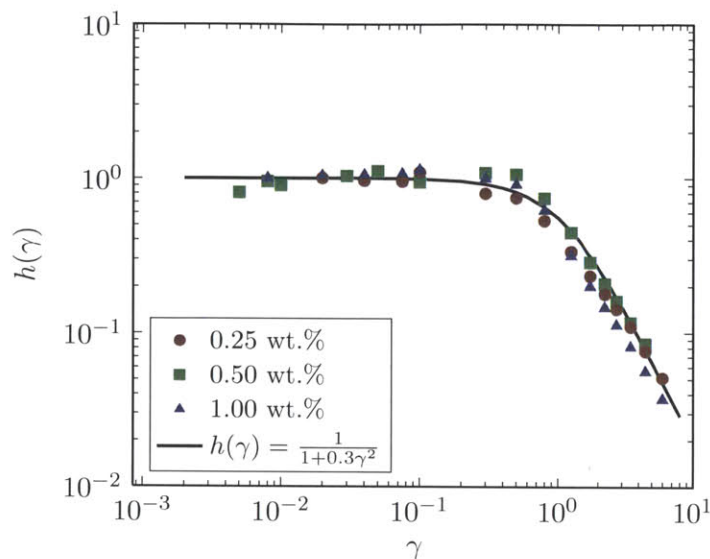
memory function for our biopolymer solutions, i.e., we set

$$m(t - t') \equiv \frac{\partial G(t - t')}{\partial t} \quad (4.3.12)$$

$$= -\mathbb{G}(t - t')^{-1-\beta} E_{\alpha-\beta, -\beta} \left(-\frac{\mathbb{G}}{\mathbb{V}} (t - t')^{\alpha-\beta} \right). \quad (4.3.13)$$

where we have used $G(t)$ from Eq. 2.3.3. Although our choice of the memory function is motivated by experimental data, and the large number of publications that have shown that complex multiscale materials exhibit relaxation of the Mittag-Leffler kind, a micro-molecular basis for this kind of relaxation process in polymeric materials has been recently proposed by Sharma and Cherayil [178].

In order to calculate the steady shear viscosity from Eq. 4.3.10, we need to determine the damping function $h(\gamma)$ for our Xanthan gum solutions. For this we performed a series of stress relaxation experiments with increasing step strain, and the results for a 0.5 wt.% solution are shown in Fig. 4.3.3. Note that here too we can detect the signature of two distinct limiting power-law regimes during relaxation, with a gradual cross over from one to the other occurring at times of order $\tau \sim (\mathbb{V}/\mathbb{G})^{1/(\alpha-\beta)}$. At small strain amplitudes ($\gamma_0 < 0.3$), the step strain experiments yield a relaxation modulus that is independent of strain amplitude, indicating a linear viscoelastic response. However, upon increasing the strain amplitude, we observe a progressive decrease in the relaxation modulus $G(t, \gamma)$. We may collapse these curves generated at different strain amplitudes onto a single master curve,

**Figure 4.3.4**

Measured values of the damping function $h(\gamma) = G(t, \gamma)/G(t)$ for different concentrations of Xanthan Gum. The damping function is independent of concentration and is well described by a function of the form $h(\gamma) = 1/(1 + 0.3\gamma^2)$.

and in the process experimentally determine the damping function $h(\gamma)$, which is given by Eq. 4.3.11. We show the measured value of the damping function $h(\gamma)$ as a function of strain amplitude γ for 0.25, 0.5 and 1.0 wt.% Xanthan gum solutions in Fig. 4.3.4. The damping functions for all concentrations of Xanthan gum tested in this study overlap on each other and fall on the same master curve. The damping function is independent of strain for small values of applied step strain; however at strains of $\gamma \approx 30\%$, $h(\gamma)$ drops sharply and approaches a power-law function of the applied strain for large γ . We have independently verified that non-linearity appears at $\gamma_0 = 30\%$ using a strain amplitude sweep under SAOS deformations. The black line in Fig. 4.3.4 indicates a fit to this master curve with a function of the form

$$h(\gamma) = \frac{1}{1 + a\gamma^2}. \quad (4.3.14)$$

and we find that $a = 0.3$ describes our data well. [174] have recently reviewed the various kinds of damping functions that arise in rheology and their role in describing non-linear rheological behavior. A damping function of the form $h(\gamma) = 1/(1 + a\gamma^b)$ where a and b are constants has been commonly observed in a number of other polymeric systems [179].

We now have all the elements required to find the steady shear viscosity $\eta(\dot{\gamma})$ using Eq. 4.3.10. We substitute Eq. 4.3.13 and Eq. 4.3.14 into Eq. 4.3.10 and also note that

$\gamma(t, t') = \gamma(t') - \gamma(t) = \dot{\gamma} \times (t - t')$ for steady shearing flow to arrive at

$$\begin{aligned} \eta(\dot{\gamma}) &\equiv \frac{\sigma(t)}{\dot{\gamma}} \\ &= -\mathbb{G} \int_0^{\infty} u^{-\beta} E_{\alpha-\beta, -\beta} \left(-\frac{\mathbb{G}}{\mathbb{V}} u^{\alpha-\beta} \right) \cdot \frac{1}{1 + 0.3(\dot{\gamma}u)^2} du \end{aligned} \quad (4.3.15)$$

in which we have made the variable transformation $u = t - t'$. The above integral for $\eta(\dot{\gamma})$ is evaluated numerically and can be shown to converge for all values of $\dot{\gamma}$. We note that to evaluate this integral for each fluid no additional fitting parameters are required, and we use the corresponding values of $\alpha, \beta, \mathbb{V}$ and \mathbb{G} from Tab. 4.3.1, which were obtained using SAOS experiments.

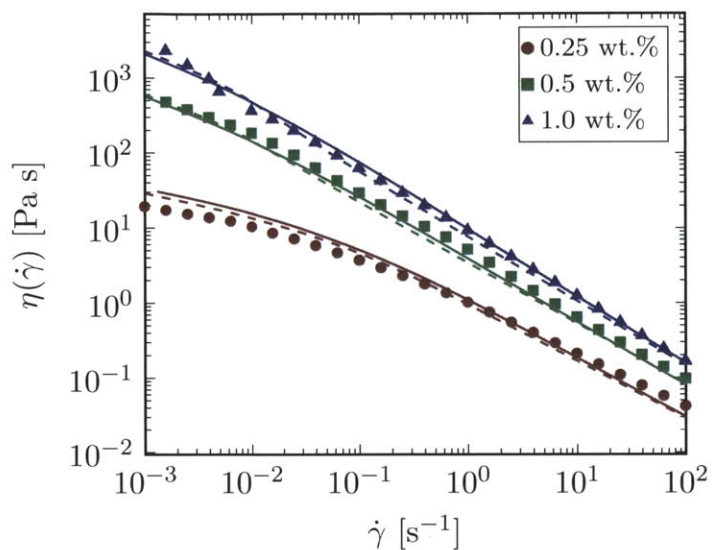
In Fig. 4.3.5a we show measured data (symbols) for the steady shear viscosity $\eta(\dot{\gamma})$ as a function of the steady shear rate $\dot{\gamma}$ for different concentrations of Xanthan gum in solution. For all concentrations tested, $\eta(\dot{\gamma})$ displays either one (1 wt. %) or two (0.25 wt.% and 0.5 wt.%) distinct power-law regions. Moreover there is no appearance of a zero shear viscosity plateau even at shear rates as low as $\dot{\gamma} = 10^{-3} \text{ s}^{-1}$, with $\eta(\dot{\gamma})$ continuing to grow as a weak power-law function of $\dot{\gamma}$ as the shear rate is progressively decreased. This asymptotic power-law behavior with the absence of a well-defined zero-shear plateau has been documented previously for Xanthan gum solutions [163, 164] as well as for other complex fluids such as liquid crystalline polymers [180] and associative polymer solutions [181]. We also show in Fig. 4.3.5a the predictions of $\eta(\dot{\gamma})$ obtained from the K-BKZ model described above (Eq. 4.3.15). The predicted material response captures the behavior of the Xanthan gum solutions very closely.

We may gain additional analytical insight into the asymptotic behavior of the flow curve by approximating the integral in Eq. 4.3.15. We begin by noting that the Mittag-Leffler function has well-defined small argument and large argument asymptotes, which we discussed in Chapter 2. We reproduce them below for convenience:

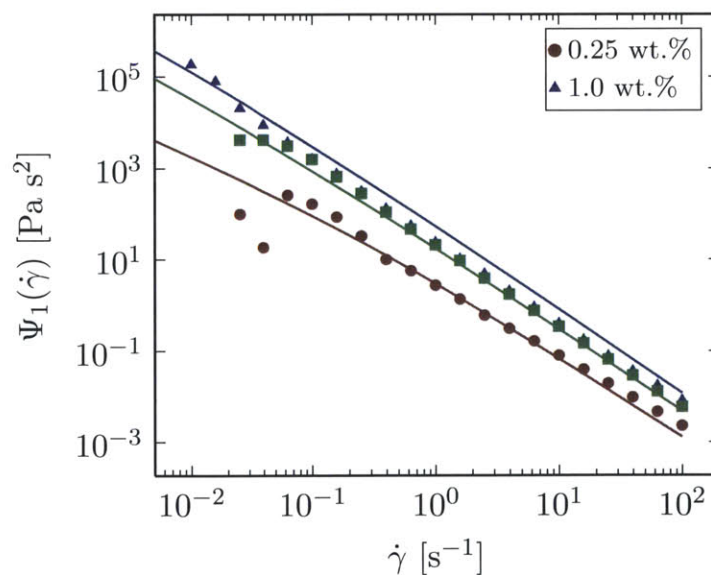
$$E_{a,b}(z) \approx \frac{1}{\Gamma(b)}; \quad z \ll 1 \quad (4.3.16)$$

$$E_{a,b}(z) \approx \frac{(-z)^{-1}}{\Gamma(b-a)}; \quad z \gg 1 \quad (4.3.17)$$

We make use of these asymptotes to evaluate Eq. 4.3.15 by approximating the Mittag-



(a)



(b)

Figure 4.3.5: Predictions of nonlinear material functions using the K-BKZ type model (lines) compared with measured data (symbols); (a) steady shear viscosity $\eta(\dot{\gamma})$, and (b) first normal stress coefficient $\Psi_1(\dot{\gamma})$. The model parameters for each fluid are determined from linear viscoelasticity and are given in Tab. I. The dashed lines in (a) show the viscosity given by the asymptotic simplification in Eq.4.3.22.

Leffler function in Eq. 4.3.15 as being a piecewise continuous function of the form

$$E_{\alpha-\beta,-\beta} \left(-\frac{\mathbb{G}}{\mathbb{V}} u^{\alpha-\beta} \right) = \frac{1}{\Gamma(-\beta)} \quad ; u < u^* \\ = \frac{(\mathbb{V}/\mathbb{G}) u^{\beta-\alpha}}{\Gamma(-\alpha)} ; u \geq u^* \quad (4.3.18)$$

where u^* is the location of the cross over from one asymptote to the other. We assume this crossover occurs when the argument of the Mittag-Leffler function $z^* = (\mathbb{V}/\mathbb{G})^{1/(\alpha-\beta)} u^* \sim 1$, i.e., $u^* = (\mathbb{V}/\mathbb{G})^{1/(\alpha-\beta)} = \tau$. Therefore we now approximate Eq. 4.3.15 as

$$\eta(\dot{\gamma}) \approx -\mathbb{G}\dot{\gamma}^{\beta-1} \left[\int_0^{\gamma^*} \gamma^{-\beta} \frac{1}{\Gamma(-\beta)} \frac{1}{1+0.3\gamma^2} d\gamma + \int_{\gamma^*}^{\infty} \gamma^{-\beta} \frac{(\mathbb{V}/\mathbb{G})\dot{\gamma}^{\alpha-\beta}\gamma^{\beta-\alpha}}{\Gamma(-\alpha)} d\gamma \right]. \quad (4.3.19)$$

In deriving the above, we have made the variable substitution $\dot{\gamma}u = \gamma$ for steady shear flow, and consequently $\gamma^* = (\mathbb{V}/\mathbb{G})^{1/(\alpha-\beta)}\dot{\gamma} = \tau\dot{\gamma}$. Note that γ^* is a product of a timescale τ and a shear rate $\dot{\gamma}$ and hence $\gamma^* = \tau\dot{\gamma}$ may be interpreted as a critical shear strain during start up of steady shear at a rate $\dot{\gamma}$, or as a Weissenberg number Wi that gives a measure of the flow strength. Upon simplifying Eq. 4.3.19 we arrive at

$$\eta(\dot{\gamma}) \approx \mathbb{G}\dot{\gamma}^{\beta-1} \frac{\beta}{\Gamma(1-\beta)} \int_0^{\gamma^*} \frac{\gamma^{-\beta}}{1+0.3\gamma^2} d\gamma + \mathbb{V}\dot{\gamma}^{\alpha-1} \frac{\alpha}{\Gamma(1-\alpha)} \int_{\gamma^*}^{\infty} \frac{\gamma^{-\alpha}}{1+0.3\gamma^2} d\gamma \quad (4.3.20)$$

where we have used the identity $\Gamma(n+1) = n\Gamma(n)$. Both the integrals obtained above can be written in terms of the hypergeometric function ${}_2F_1(a, b; c; x)$ defined as [25]

$${}_2F_1(a, b; c; z) = \frac{\Gamma(c)}{\Gamma(a)\Gamma(b)} \sum_{k=0}^{\infty} \frac{\Gamma(a+k)\Gamma(b+k)}{\Gamma(c+k)} \frac{z^k}{k!} \quad (4.3.21)$$

and we finally obtain

$$\eta(\dot{\gamma}) \approx \mathbb{G}\dot{\gamma}^{\beta-1} \frac{\beta}{\Gamma(1-\beta)} \frac{(\gamma^*)^{1-\beta}}{1-\beta} {}_2F_1 \left(1, \frac{1-\beta}{2}; \frac{3-\beta}{2}; -0.3(\gamma^*)^2 \right) + \\ \mathbb{V}\dot{\gamma}^{\alpha-1} \frac{\alpha}{\Gamma(1-\alpha)} \frac{(\gamma^*)^{-\alpha-1}}{(0.3)(1+\alpha)} {}_2F_1 \left(1, \frac{1+\alpha}{2}; \frac{3+\alpha}{2}; -\frac{1}{0.3(\gamma^*)^2} \right). \quad (4.3.22)$$

We show the predictions of this approximate analytic expression for $\eta(\dot{\gamma})$ as dashed

lines in Fig. 4.3.5a. It is observed that this analytical solution agrees very closely with the full numerical solution and hence one may avoid calculating a numerical solution to Eq. 4.3.15. For values of $\alpha \approx 1$ or $\beta \approx 0$, this approximate solution is less accurate; in Appendix C we derive an expression for $\eta(\dot{\gamma})$ to arbitrary order, and one may retain as many terms as required in the expansion depending on the accuracy needed. The utility of the analytical solution Eq. 4.3.22 is that it enables us to calculate the asymptotic behavior of $\eta(\dot{\gamma})$ as $Wi \ll 1$ and $Wi \gg 1$; in fact, it can be shown using appropriate Taylor series expansions of the hypergeometric functions that at low shear rate

$$\lim_{\dot{\gamma} \ll 1/\tau} \eta(\dot{\gamma}) \approx \left[(0.3)^{(\alpha-1)/2} \frac{(\pi\alpha/2) \sec(\pi\alpha/2)}{\Gamma(1-\alpha)} \right] \mathbb{V} \dot{\gamma}^{\alpha-1} \quad (4.3.23)$$

and at high shear rate

$$\lim_{\dot{\gamma} \gg 1/\tau} \eta(\dot{\gamma}) \approx \left[(0.3)^{(\beta-1)/2} \frac{(\pi\beta/2) \sec(\pi\beta/2)}{\Gamma(1-\beta)} \right] \mathbb{G} \dot{\gamma}^{\beta-1} \quad (4.3.24)$$

From Eq. 4.3.23, it is apparent that the existence of a constant bounded viscosity in the limit of zero shear rate thus only exists for materials in which $\alpha = 1$. The shear stress however tends to zero for all α because $\sigma = \eta\dot{\gamma} \sim \dot{\gamma}^\alpha$ for all α . This slow asymptotic divergence in the viscosity at low shear rates agrees with the experimentally observed behavior of many complex multiscale materials, some of which have been cited above.

The K-BKZ approach also enables us to make predictions of the first normal stress coefficient $\Psi_1(\dot{\gamma})$. Again, we begin with the K-BKZ framework (Eq. 4.3.7), and neglect the second term for uncrosslinked materials. We select the correct components of the Finger tensor C^{-1} (Equation 4.3.9) to calculate the normal stress difference $N_1 = \sigma_{xx} - \sigma_{yy} = \gamma^2$ and we obtain [182]

$$N_1(t) = \int_{-\infty}^t m(t-t') h(\gamma) \gamma^2(t, t') dt' \quad (4.3.25)$$

and consequently, substituting the Mittag-Leffler relaxation modulus we obtain

$$\Psi_1(\dot{\gamma}) \equiv \frac{N_1}{\dot{\gamma}^2} = -\mathbb{G} \int_0^\infty u^{1-\beta} E_{\alpha-\beta, -\beta} \left(-\frac{\mathbb{G}}{\mathbb{V}} u^{\alpha-\beta} \right) \frac{1}{1 + 0.3(\dot{\gamma}u)^2} du \quad (4.3.26)$$

In Fig. 4.3.5b we show measurements of the first normal stress coefficient $\Psi_1(\dot{\gamma})$ (symbols) for three different concentrations of Xanthan gum in solution. The solid lines show the numerical prediction of $\Psi_1(\dot{\gamma})$ evaluated using Eq. 4.3.26 and the parameters in Tab. 4.3.1. In this case too we observe that the agreement between measured data and the prediction of our model is good with no additional fitting parameters required. Similar to the approximation made above for $\eta(\dot{\gamma})$, an analytical approximation for $\Psi_1(\dot{\gamma})$ may be found, and is given by

$$\begin{aligned} \Psi_1(\dot{\gamma}) \approx & \mathbb{G}\dot{\gamma}^{\beta-2} \frac{\beta}{\Gamma(1-\beta)} \frac{(\gamma^*)^{2-\beta}}{2-\beta} {}_2F_1\left(1, \frac{2-\beta}{2}; \frac{4-\beta}{2}; -0.3(\gamma^*)^2\right) + \\ & \mathbb{V}\dot{\gamma}^{\alpha-2} \frac{\alpha}{\Gamma(1-\alpha)} \frac{(\gamma^*)^{-\alpha}}{(0.3)(\alpha)} {}_2F_1\left(1, \frac{\alpha}{2}; \frac{2+\alpha}{2}; -\frac{1}{0.3(\gamma^*)^2}\right) \end{aligned} \quad (4.3.27)$$

As before, $\gamma^* = (\mathbb{V}/\mathbb{G})^{1/(\alpha-\beta)}\dot{\gamma} = \tau\dot{\gamma}$ is a measure of the flow strength. This approximate analytical solution is nearly identical to the full numerical solution of Eq. 4.3.26, and the numerical and analytical curves overlap; therefore, we do not show the approximate solution as dashed lines for the sake of clarity. Again, with the help of the analytical solution we are able to determine the behavior of $\Psi_1(\dot{\gamma})$ for $Wi \ll 1$ given by

$$\lim_{\dot{\gamma} \ll 1/\tau} \Psi_1(\dot{\gamma}) \approx \left[(0.3)^{(\alpha-2)/2} \frac{(\pi\alpha/2)\operatorname{cosec}(\pi\alpha/2)}{\Gamma(1-\alpha)} \right] \mathbb{V}\dot{\gamma}^{\alpha-2} \quad (4.3.28)$$

and for $\gamma^* \gg 1$

$$\lim_{\dot{\gamma} \gg 1/\tau} \Psi_1(\dot{\gamma}) \approx \left[(0.3)^{(\beta-2)/2} \frac{(\pi\beta/2)\operatorname{cosec}(\pi\beta/2)}{\Gamma(1-\beta)} \right] \mathbb{V}\dot{\gamma}^{\beta-2} \quad (4.3.29)$$

i.e. $\Psi_1(\dot{\gamma}) \sim \dot{\gamma}^{\alpha-2}$ for $\gamma^* \ll 1$ and $\Psi_1(\dot{\gamma}) \sim \dot{\gamma}^{\beta-2}$ for $\gamma^* \gg 1$. We note in particular that the asymptotic behavior of $\Psi_1(\dot{\gamma})$ at low shear rates obtained above agrees with the asymptote calculated from a second order fluid expansion [24]

$$\lim_{\dot{\gamma} \ll 1/\tau} \Psi_1(\dot{\gamma}) = \lim_{\omega \ll 1/\tau} \frac{2G'(\omega)}{\omega^2} \quad (4.3.30)$$

which we can calculate with the help of Eq. 2.3.15.

In this section we have presented a theoretical constitutive framework to make predictions of the nonlinear rheological response of power-law complex fluids with broad

relaxation spectra that exhibit liquid-like behavior at long timescales. Although we discuss the examples of $\eta(\dot{\gamma})$ and $\Psi_1(\dot{\gamma})$ in this thesis, these arguments can be extended to other nonlinear deformations such as uniaxial extensional flows and LAOS. We next discuss the performance of empirical rules such as the Cox-Merz rule and the Gleissle Mirror relations that also make predictions of a material's nonlinear response (from knowledge of the linear rheology alone), and show how the very broad range of relaxation timescales that are embodied by the Mittag-Leffler function influences the validity of these approximations. We will also put these empirical rules in context by using our model to quantify the systematic deviations that these predictions can exhibit from measured data.

4.3.3 Empirical Relationships for Nonlinear Viscoelasticity

One widely known relationship that enables the prediction of the nonlinear viscometric response for complex materials from linear response is the Cox-Merz rule which states that ([24])

$$\eta(\dot{\gamma}) \cong \eta^*(\omega) \Big|_{\omega=\dot{\gamma}} \quad (4.3.31)$$

where $\eta^*(\omega)$ is the complex viscosity given by

$$\eta^*(\omega) = \frac{\sqrt{G'(\omega)^2 + G''(\omega)^2}}{\omega} \quad (4.3.32)$$

For the FMM, in which $G'(\omega)$ and $G''(\omega)$ are given by Eq. 2.3.15 and Eq. 2.3.16 respectively, we calculate $\eta^*(\omega)$ to be

$$\eta^*(\omega) = \frac{\mathbb{V}\mathbb{G}\omega^{\alpha+\beta-1}}{\sqrt{(\mathbb{V}\omega^\alpha)^2 + (\mathbb{G}\omega^\beta)^2 + 2\mathbb{V}\omega^\alpha \cdot \mathbb{G}\omega^\beta \cos\left(\frac{\pi(\alpha-\beta)}{2}\right)}} \quad (4.3.33)$$

and consequently from 4.3.31 we have

$$\eta(\dot{\gamma}) \cong \frac{\mathbb{V}\mathbb{G}\dot{\gamma}^{\alpha+\beta-1}}{\sqrt{(\mathbb{V}\dot{\gamma}^\alpha)^2 + (\mathbb{G}\dot{\gamma}^\beta)^2 + 2\mathbb{V}\dot{\gamma}^\alpha \cdot \mathbb{G}\dot{\gamma}^\beta \cos\left(\frac{\pi(\alpha-\beta)}{2}\right)}} \quad (4.3.34)$$

There also exists a less widely used empirical framework to predict nonlinear behavior from linear rheology, collectively known as the Gleissle mirror relations which state that [24, 183]

$$\eta^+(t) \approx \eta(\dot{\gamma}) \Big|_{t=1/\dot{\gamma}} \quad (4.3.35)$$

$$\Psi_1^+(t) \approx \Psi_1(\dot{\gamma}) \Big|_{t=k/\dot{\gamma}} \quad (4.3.36)$$

$$\Psi_1(\dot{\gamma}) \approx -2 \int_{\dot{\gamma}/k}^{\infty} x^{-1} \left[\frac{\partial \eta(x)}{\partial x} \right] dx \quad (4.3.37)$$

Here $\eta^+(t)$ is the transient shear viscosity upon the start-up of steady shear measured in the linear viscoelastic regime and $\Psi_1^+(t)$ is the transient first normal stress coefficient upon the start-up of steady shear, and $2 < k < 3$ is a fitting constant. Evidently, these Gleissle mirror relations allow estimation of the nonlinear material functions $\eta(\dot{\gamma})$ and $\Psi_1(\dot{\gamma})$ from their quasilinear counterparts $\eta^+(t)$ and $\Psi_1^+(t)$. The third relation Eq. 4.3.37 allows a direct calculation of $\Psi_1(\dot{\gamma})$ from $\eta(\dot{\gamma})$. For the FMM, we have already determined $\eta^+(t)$ in Eq. 4.3.6, because in deriving that expression we set $\dot{\gamma} = \dot{\gamma}_0 H(t)$, which is the imposed deformation in a start-up of steady shear flow experiment. Therefore Eq. 4.3.6 and Eq. 4.3.35 yield

$$\eta(\dot{\gamma}) \approx \mathbb{G} \left(\frac{1}{\dot{\gamma}} \right)^{1-\beta} E_{\alpha-\beta, 2-\beta} \left(-\frac{\mathbb{G}}{\mathbb{V}} \left(\frac{1}{\dot{\gamma}} \right)^{\alpha-\beta} \right) \quad (4.3.38)$$

in which $E_{a,b}(z)$ is the Mittag-Leffler function defined in Eq. 2.3.4. The argument $z = -\frac{\mathbb{G}}{\mathbb{V}} \left(\frac{1}{\dot{\gamma}} \right)^{\alpha-\beta}$ in Eq. 4.3.38 can also be written as $z = -(\tau\dot{\gamma})^{\beta-\alpha}$. It can be shown using the asymptotic forms of the Mittag-Leffler function given in Eq. 4.3.16 and Eq. 4.3.17 that Eq. 4.3.38 exhibits power-law regimes at low as well as high $\dot{\gamma}$. At low shear rates we obtain

$$\lim_{\dot{\gamma} \ll 1/\tau} \eta(\dot{\gamma}) \approx \mathbb{V} \dot{\gamma}^{\alpha-1} / \Gamma(2-\alpha), \quad (4.3.39)$$

and at high rates we find

$$\lim_{\dot{\gamma} \gg 1/\tau} \eta(\dot{\gamma}) \approx \mathbb{G} \dot{\gamma}^{\beta-1} / \Gamma(2-\beta). \quad (4.3.40)$$

These asymptotes are identical in form to those we obtained from the K-BKZ model derived above (cf. Eqs. 4.3.23 and 4.3.24) and only differ in the pre-multiplying factor.

We may now use this expression for $\eta(\dot{\gamma})$ in Eq. 4.3.37 to find $\Psi_1(\dot{\gamma})$. Making this substitution we have

$$\Psi_1(\dot{\gamma}) = -2 \int_{\dot{\gamma}/k}^{\infty} \frac{1}{x} \frac{\partial}{\partial x} \left[\mathbb{G} \left(\frac{1}{x} \right)^{1-\beta} E_{\alpha-\beta, 2-\beta} \left(-\frac{\mathbb{G}}{\mathbb{V}} \left(\frac{1}{x} \right)^{\alpha-\beta} \right) \right] dx \quad (4.3.41)$$

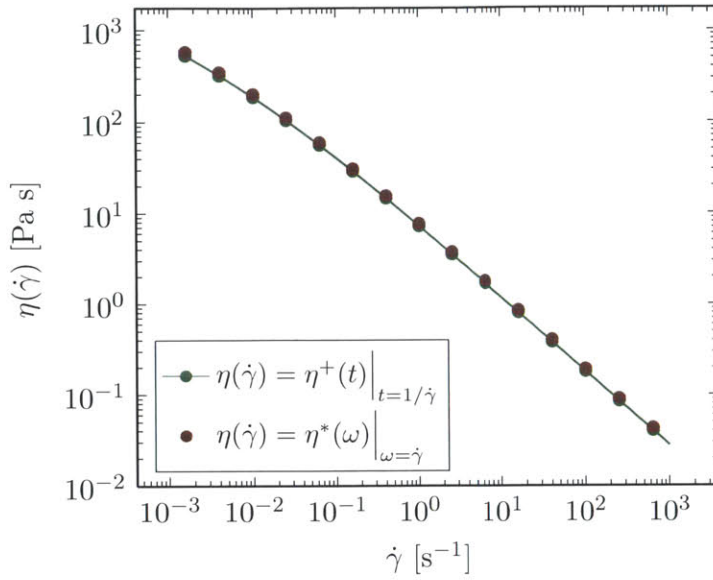
Making the variable transformation $1/x = u$ and then integrating by parts we obtain

$$\Psi_1(\dot{\gamma}) = 2\mathbb{G} \left(\frac{k}{\dot{\gamma}} \right)^{2-\beta} \left[E_{\alpha-\beta, 2-\beta} \left(-\frac{\mathbb{G}}{\mathbb{V}} \left(\frac{k}{\dot{\gamma}} \right)^{\alpha-\beta} \right) - E_{\alpha-\beta, 3-\beta} \left(-\frac{\mathbb{G}}{\mathbb{V}} \left(\frac{k}{\dot{\gamma}} \right)^{\alpha-\beta} \right) \right] \quad (4.3.42)$$

As in the case of $\eta(\dot{\gamma})$, it can be shown that the low and high shear rate asymptotes are both power-laws, and are given by $\Psi_1(\dot{\gamma}) \sim \dot{\gamma}^{\alpha-2}$ and $\Psi_1(\dot{\gamma}) \sim \dot{\gamma}^{\beta-2}$ respectively. These asymptotic power-laws agree with those of the K-BKZ model derived in Eq. 4.3.28 and Eq. 4.3.29.

In Fig. 4.3.6 we show a comparison of the prediction of $\eta(\dot{\gamma})$ from the Cox-Merz rule (Eq. 4.3.34) with the prediction of the Gleissle mirror relation (Eq. 4.3.38) for the special case of $\alpha = 0.64$, $\beta = 0.19$, $\mathbb{V} = 71.65 \text{ Pa s}^\alpha$ and $\mathbb{G} = 7.82 \text{ Pa s}^\beta$, corresponding to a 0.5 wt.% Xanthan gum solution. The two predictions agree very closely over 6 orders of magnitude in the deformation rate. We have verified for various other values of α , β , \mathbb{V} and \mathbb{G} that the two predictions are nearly equal at all shear rates. Therefore we may use either the Cox-Merz rule or the Gleissle mirror relations to arrive at an empirical prediction of the nonlinear material properties $\eta(\dot{\gamma})$ and $\Psi_1(\dot{\gamma})$ for a multiscale material with linear viscoelastic properties described by the Fractional Maxwell Model.

In Fig. 4.3.7 we show as symbols the same steady shear data measured for two different concentrations of Xanthan gum already presented in Fig. 4.3.5. The lines in Fig. 4.3.7 depict the predictions obtained from the Gleissle mirror relations (Eqs. 4.3.38 and 4.3.42). Note that although we do not show it in Fig. 4.3.7 for the sake of clarity, applying the Cox-Merz rule (Eq. 4.3.31) would give us identical predictions as the Gleissle mirror relation as explained above. We choose to show the predictions of the Gleissle mirror relations because this also provides an analytical expression for $\Psi_1(\dot{\gamma})$, however all of the conclusions in the following section apply to the Cox-Merz rule as well.

**Figure 4.3.6**

Comparison of the agreement between the Cox-Merz rule and the Gleissle mirror relations for the FMM. The predicted values of the steady shear viscosity from the two different rules virtually overlap. $\alpha = 0.64$, $\beta = 0.19$, $\mathbb{V} = 71.65 \text{ Pa s}^\alpha$, $\mathbb{G} = 7.82 \text{ Pa s}^\beta$.

We observe in Fig. 4.3.7 that the predictions of the Gleissle mirror relations correctly capture the functional form of the experimental data but exhibit a systematic offset from the measurements in both $\eta(\dot{\gamma})$ (Fig. 4.3.7a) as well as $\Psi_1(\dot{\gamma})$ (Fig. 4.3.7b). The predictions are systematically higher than the measured data. This offset between measured data and the predictions of empirical rules such as the Cox-Merz rule or Gleissle mirror relations has been observed previously in various complex fluids, especially in polysaccharide systems where it has been reported that $\eta^*(\omega)|_{\omega=\dot{\gamma}} > \eta(\dot{\gamma})$. For Xanthan gum solutions this offset has been shown to increase with increasing Xanthan concentration [164]. Using Xanthan gum and Schizophyllum solutions with varying amounts of urea [172] or DMSO [163] respectively, this offset has been shown to arise from the presence of intermolecular interactions such as hydrogen bonds. These weak physical interactions give rise to the broad power-law like characteristics we observe in the linear relaxation modulus, but are disrupted at the large strain deformations applied in steady shear.

In our K-BKZ model, we capture this structural damage accumulated during large shear deformations using the damping function. With this K-BKZ framework, it is also relatively straightforward to quantify the magnitude of this offset between the measured steady shear viscosity and the predictions of the Cox-Merz rule or Gleissle mirror relations. We define the offset factor f as

$$f \equiv \frac{\eta(\dot{\gamma})}{\eta^*(\omega)} \Big|_{\omega=\dot{\gamma}} \quad (4.3.43)$$

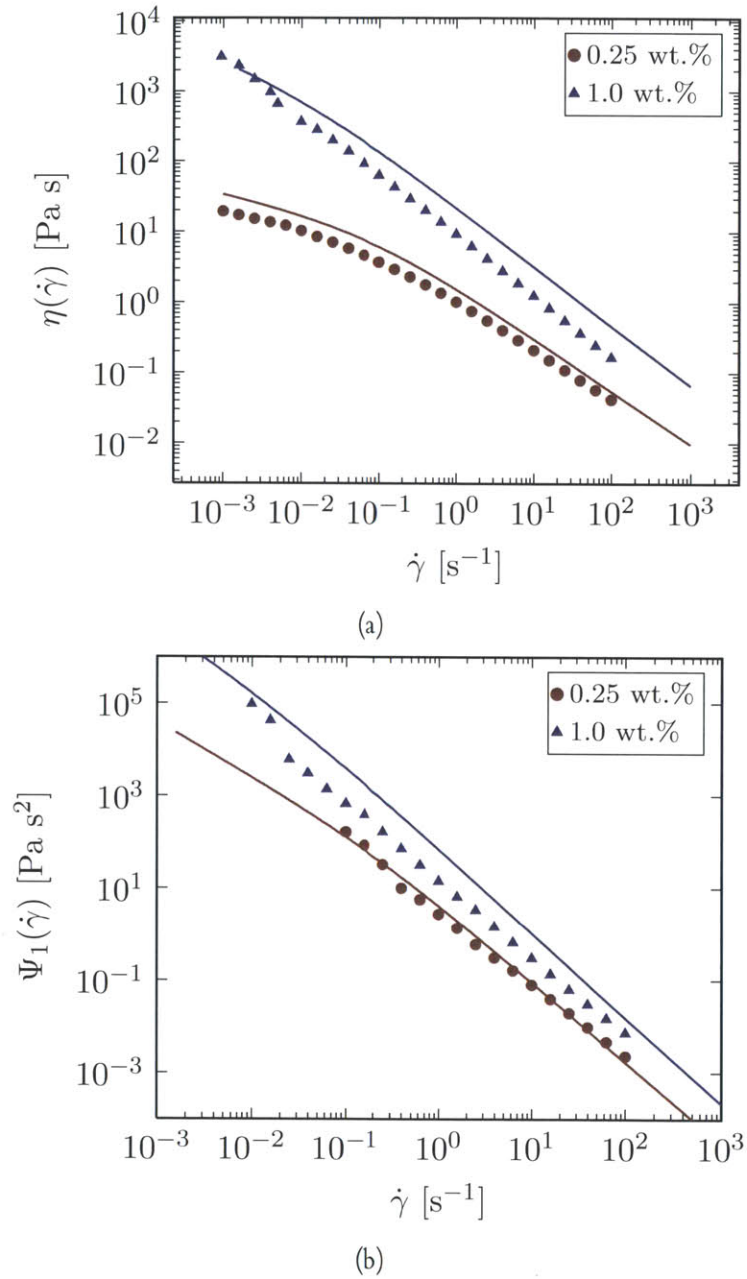


Figure 4.3.7: Predictions of the Gleissle mirror relations for the FMM (lines) compared to measured data for Xanthan gum (symbols); (a) steady shear viscosity $\eta(\dot{\gamma})$ prediction (Eq.4.3.38) and (b) first normal stress co-efficient $\Psi_1(\dot{\gamma})$ prediction (Eq.4.3.42). There is a consistent offset between the prediction and measured data, which increases with increasing concentration. Values of α , β , \mathbb{V} and \mathbb{G} used to make the model predictions were taken from Table 4.3.1.

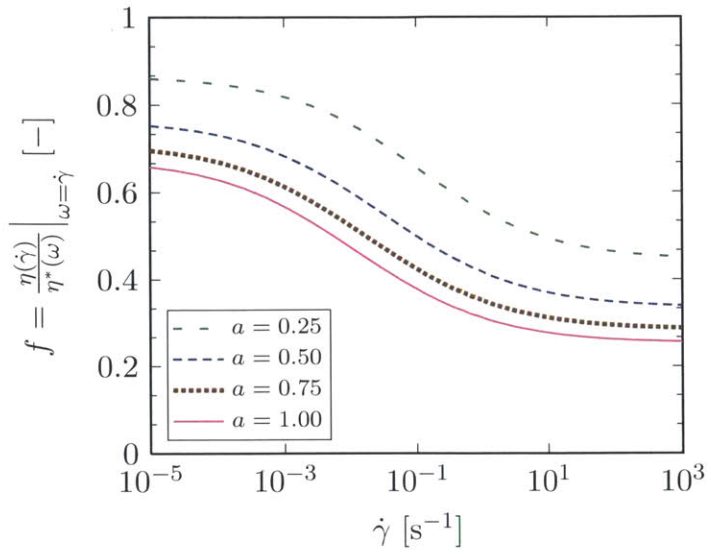


Figure 4.3.8

The offset factor f (Eq. 4.3.43) as a function of the shear rate $\dot{\gamma}$ for different values of the damping function parameter a . $0 < f < 1$ indicating that the steady shear viscosity is lower than the complex viscosity. This arises from damage accumulated at the large strains imposed during a steady shear experiment. The values of the FMM parameters are $\alpha = 0.60$, $\beta = 0.14$, $\mathbb{V} = 208.54$ Pa s $^\alpha$ and $\mathbb{G} = 22.46$ Pa s $^\beta$ corresponding to the 1 wt.% Xanthan gum solution with characteristic timescale $\tau = (\mathbb{V}/\mathbb{G})^{1/(\alpha-\beta)} = 1846$ s.

where $\eta(\dot{\gamma})$ and $\eta^*(\omega)|_{\omega=\dot{\gamma}}$ are given by Eqs. 4.3.15 and 4.3.34) respectively. We could also replace $\eta^*(\omega)|_{\omega=\dot{\gamma}}$ by $\eta(\dot{\gamma})$ obtained from the Gleissle mirror relationship (Eq. 4.3.38) because both empirical relations give nearly identical predictions of the steady shear viscosity (cf. Fig. 4.3.6). Note that as long as $0 < f < 1$, the smaller the value of f , the larger is the deviation between $\eta(\dot{\gamma})$ and $\eta^*(\omega)$. We show the value of f as a function of shear rate $\dot{\gamma}$ for various values of the strain damping coefficient a in Fig. 4.3.8. We do not compare this plot of the offset with our measured data because that would mean plotting the ratio of two measured quantities on the y -axis. Moreover, the y -axis only ranges from 0 to 1; it can be calculated that even a 5–6% error in both $\eta(\dot{\gamma})$ and $\eta^*(\omega)$, which is a reasonable assumption to make in bulk rheology, can lead to as much as a 25% error in the calculated offset. Nevertheless, from Fig. 4.3.8 we can discern various qualitative features: the introduction of the damping function leads to a systematic offset of magnitude $0.3 \leq f \leq 0.9$ between the Cox-Merz prediction and the full nonlinear model. Similar offsets were found experimentally for all the Xanthan gum concentrations tested in this study. The offset factor f also monotonically decreases as a function of $\dot{\gamma}$. We see from Fig. 4.3.7(a) that this is true for the 1 wt.%, and 0.5 wt.% (not shown for clarity); however, the trend seems to be reversed for the 0.25 wt.% solution, which we ascribe to experimental variability. The magnitude of this offset also plateaus at both low and high $\dot{\gamma}$. These plateaus indicate that approximations to the steady shear viscosity obtained from these empirical relationships will exhibit asymptotic behavior

(to within a constant factor) that is identical to the full K-BKZ model, which compares well with experimental measurements. In fact, using our analytical solution, we can show this exactly; the plateau values of the offset may be calculated from the asymptotic values of $\eta(\dot{\gamma})$ from the K-BKZ model (Eqs. 4.3.23 and 4.3.24) and those of the Gleissle mirror relations (Eqs. 4.3.39 and 4.3.40). Finally, we note that increasing the damping function parameter a decreases the magnitude of the offset factor f (i.e. it increases the disparity between $\eta(\dot{\gamma})$ and $\eta^*(\omega)|_{\omega=\dot{\gamma}}$). From 4.3.23 and 4.3.24, we observe that the plateau value of f depends on the damping function parameter a in a power-law manner, and the low shear and high shear plateau scale as $f \sim a^{(\alpha-1)/2}$ and $f \sim a^{(\beta-1)/2}$ respectively. Renardy has shown that the Cox-Merz rule is valid for materials with a broad spectrum of relaxation times to within a constant factor [162]. We have shown in this section that for complex multiscale materials with a relaxation modulus that can be well described by the Mittag-Leffler function, these constant factors can be quantified, and vary gradually with shear rate.

4.3.4 *The Delaware-Rutgers Rule for Power-Law Materials*

For other classes of complex fluids such as concentrated suspensions which exhibit a yield stress, the Cox-Merz rule is known to fail. Instead, observations show that there exists a new relationship for yield-like materials that relates dynamic and steady-shear measurements, which Krieger has suggested be called the Rutgers-Delaware rule. Doraiswamy et al. have developed a nonlinear model for such materials, and the existence of this rule is rigorously proved [166]. The rule states that dynamic measurements performed at frequency ω and shear strain amplitude γ_0 are equivalent to steady shear response performed at shear rate $\dot{\gamma}$ when $\gamma_0\omega = \dot{\gamma}$. The starting point of their model is an empirically introduced elastic Herschel-Bulkley type relationship for stress and strain. A critical strain parameter γ_c is introduced, at which transition from elastic to inelastic behavior takes place. In what follows, we show that an appropriate choice of fractional constitutive model, along with a suitable damping function can give rise to not only a constitutive equation of Herschel-Bulkley type in steady shear but also a linear viscoelastic material response and agreement with the Rutgers-Delaware rule.

We consider a model of Fractional Kelvin-Voigt type (FKVM) with a Hookean spring in parallel with a springpot such that the total stress σ is given by

$$\sigma = \sigma^s + \sigma^{sp} \quad (4.3.44)$$

with σ^s being the stress in the spring and σ^{sp} the stress in the springpot. The elastic spring, however, is nonlinear and plastically yields at a critical strain $\gamma_c = \sigma_y/G$ so that the constitutive response is

$$\sigma^s = G\gamma^s, |\gamma^s| \leq \gamma_c \quad (4.3.45)$$

$$= G\gamma_c, |\gamma^s| > \gamma_c \quad (4.3.46)$$

where G is the linear elastic modulus of the unyielded element and γ_c is a critical strain amplitude. We are now interested in determining the response of such a FKVM constitutive model under a steady shear rate $\dot{\gamma}$. To find the steady state response for the springpot, we use a K-BKZ approach as before, along with a damping function $h(\gamma)$ given by [167]

$$h(\gamma) = 1, |\gamma| \leq \gamma_c \quad (4.3.47)$$

$$= 0, |\gamma| > \gamma_c$$

The choice of this damping function is motivated by the fact that materials such as concentrated suspensions yield catastrophically [184, 185], and the elastic modulus of the material decreases sharply upon yield. We obtain from Eq. 2.2.12 and Eq. 4.3.10 and expression for the stress in the springpot σ^{sp} that is given by

$$\sigma^{sp}(\dot{\gamma}) = \int_{-\infty}^t \frac{\mathbb{V}(-\alpha)}{\Gamma(1-\alpha)} (t-t')^{-\alpha-1} h(\gamma) \dot{\gamma} dt' \quad (4.3.48)$$

Making the variable substitution $\gamma = \dot{\gamma}(t-t')$ and noting that $\dot{\gamma}$ is constant, we obtain

$$\sigma^{sp}(\dot{\gamma}) = \dot{\gamma}^\alpha \int_0^\infty \frac{\mathbb{V}\alpha}{\Gamma(1-\alpha)} \gamma^{-\alpha} h(\gamma) d\gamma \quad (4.3.49)$$

and substituting for the damping function $h(\gamma)$ from Eq. 4.3.45 and solving the integral, we finally obtain

$$\sigma^{sp}(\dot{\gamma}) = \frac{\mathbb{V}\alpha}{\Gamma(2-\alpha)} \gamma_c^{1-\alpha} \dot{\gamma}^\alpha \quad (4.3.50)$$

The total stress $\sigma = \sigma^s + \sigma^{sp}$ in steady flow is now calculated using Eq. 4.3.46 and Eq. 4.3.50

as being

$$\sigma(\dot{\gamma}) = G\gamma_c + \frac{\mathbb{V}\alpha}{\Gamma(2-\alpha)}\gamma_c^{1-\alpha}\dot{\gamma}^\alpha \quad (4.3.51)$$

or equivalently the steady shear viscosity is given by

$$\eta(\dot{\gamma}) \equiv \frac{\sigma(\dot{\gamma})}{\dot{\gamma}} = \frac{G\gamma_c}{\dot{\gamma}} + \frac{\mathbb{V}\alpha}{\Gamma(2-\alpha)}\gamma_c^{1-\alpha}\dot{\gamma}^{\alpha-1} \quad (4.3.52)$$

Note that Eq. 4.3.52 is identical to the Herschel-Bulkley type stress-strain relationship proposed by Doraiswamy et al. [166]. It is immediately seen that at low shear rates

$$\eta(\dot{\gamma}) \approx \frac{G\gamma_c}{\dot{\gamma}} = \frac{\sigma_y}{\dot{\gamma}} \quad (4.3.53)$$

and at high shear rates

$$\eta(\dot{\gamma}) \approx \frac{\mathbb{V}\alpha\gamma_c^{1-\alpha}}{\Gamma(2-\alpha)}\dot{\gamma}^{\alpha-1} = K\dot{\gamma}^{\alpha-1} \quad (4.3.54)$$

The presence of the quasi-properties \mathbb{V} and the power-law exponent α in the expression for the steady shear viscosity, which are independently determined from linear viscoelastic measurements, indicate that the linear and nonlinear rheology are interconnected through the damping function and the parameter γ_c at which the material suddenly yields.

To derive the response of this elastoviscoplastic FKVM model in oscillatory flow, we assume that a deformation profile of the form $\gamma = \gamma_0 \sin(\omega t)$ is applied, in which γ_0 is the strain amplitude. Similar to Doraiswamy et al., we also assume that the material yields upon an infinitesimally small deformation (i.e. although we are interested in small amplitude oscillations and γ_0 is small, we assume the critical strain $\gamma_c \ll \gamma_0$.) This means that the nonlinear spring saturates and yields before the oscillating strain reaches its maximum amplitude.

Because we use a FKVM type model with elements in parallel, the stresses in each element are additive and hence

$$G'(\omega) = G'^{(s)}(\omega) + G'^{(sp)}(\omega) \quad (4.3.55)$$

$$G''(\omega) = G''^{(s)}(\omega) + G''^{(sp)}(\omega) \quad (4.3.56)$$

where the superscripts s and sp stand for spring and springpot respectively, as before. We know from linear viscoelasticity theory that [19]

$$G^{(s)}(\omega) = \omega \int_0^{\infty} G(s) \sin(\omega s) ds \quad (4.3.57)$$

$$G''^{(s)}(\omega) = \omega \int_0^{\infty} G(s) \cos(\omega s) ds \quad (4.3.58)$$

Although the limits of the integral run from 0 to ∞ , we have noted that the spring yields when the strain reaches γ_c in the first quarter cycle. This happens at time t_c given by

$$t_c = \frac{1}{\omega} \sin^{-1} \left(\frac{\gamma_c}{\gamma_0} \right) \quad (4.3.59)$$

Therefore, in Eqs. 4.3.57 and 4.3.58, $G(s) = G$ for $s \leq t_c$ and $G(s) = 0$ for $s > t_c$. Consequently, the limits of the integrals in Eq. 4.3.57 and Eq. 4.3.58 span from 0 to t_c . Evaluating these integrals, we find that

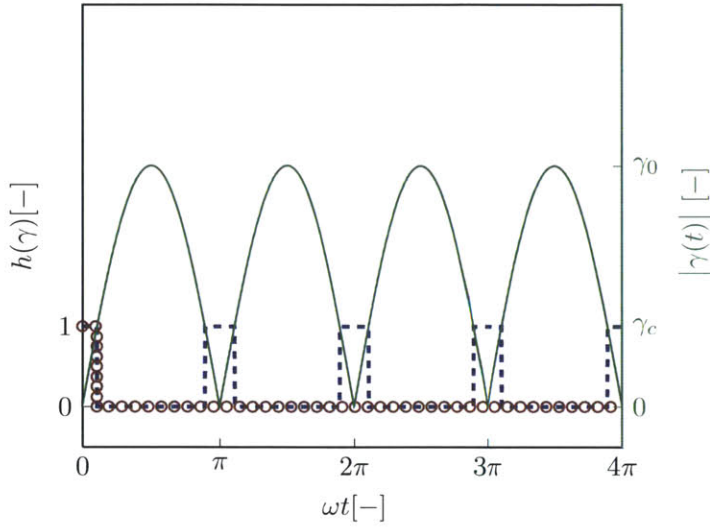
$$G^{(s)}(\omega) = G(1 - \cos \omega t_c) \approx \frac{G}{2} \left(\frac{\gamma_c}{\gamma_0} \right)^2 \quad (4.3.60)$$

$$G''^{(s)}(\omega) = G \sin \omega t_c = G \frac{\gamma_c}{\gamma_0} \quad (4.3.61)$$

In Eq. 4.3.60 we have used the fact that $\gamma_c \ll \gamma_0$ to approximate the cosine term using a Taylor series expansion.

To find $G^{(sp)}(\omega)$ and $G''^{(sp)}(\omega)$, we use the K-BKZ equation with the Tanner-Simmons damping function given in Eq. 4.3.47. Therefore in this case Eq. 4.3.10 becomes

$$\sigma^{(sp)}(t) = \frac{\mathbb{V}(-\alpha)}{\Gamma(1-\alpha)} \int_{-\infty}^t (t-t')^{-(\alpha+1)} h[\gamma(t,t')] [\gamma(t') - \gamma(t)] dt' \quad (4.3.62)$$


Figure 4.3.9

The irreversibility assumption. The green line shows $|\gamma(t)| = \gamma_0 |\sin \omega t|$. The blue dashed line is the damping function without the irreversibility assumption, and there is instant microstructural recovery of accumulated damage in the material when $\gamma < \gamma_c$. The red circles denote the damping function we use in Equation 4.3.63, which accounts for irreversibility and assumes zero recovery after the strain first exceeds the critical strain γ_c .

and making the variable transformation $u = t - t'$ we obtain

$$\sigma^{(sp)}(t) = \frac{\forall \alpha}{\Gamma(1 - \alpha)} \int_0^\infty u^{-(\alpha+1)} h[\gamma(t, t')] [\gamma(t) - \gamma(t - u)] du \quad (4.3.63)$$

In Fig. 4.3.9 we show as a green line the absolute value of an applied deformation of the form $\gamma(t) = \gamma_0 \sin(\omega t)$ for two complete cycles. The blue dashed line is a plot of $h(\gamma)$ defined in Eq. 4.3.47. Because $h(\gamma)$ depends only on the instantaneous value of the strain, whenever $|\gamma(t)| \leq \gamma_c$, $h(\gamma) = 1$, as seen in the figure. This means that any structural damage induced in the material at strains larger than γ_c is instantly undone when the strain drops below γ_c . This instantaneous recovery of material structure, however, is unphysical; in real materials there is typically a recovery time for the reversal of structural damage induced at large strains. In other words, any damage accumulated in the initial increasing portion of the sinusoidally oscillating strain will not be reversed instantaneously in the decreasing portion of the strain cycle. Wagner and Stephenson call this the irreversibility assumption, and show that for a LDPE melt, constitutive predictions of the rheological response in reversing flows are much improved by accounting for irreversibility [186]. In line with this assumption, we modify our damping function and assume that there is *zero* recovery upon the strain reaching the critical value γ_c in the first cycle. Therefore, once $h(\gamma) = 0$, it remains zero for all subsequent times. This damping function is shown by the red circles in Fig. 4.3.9, and this is the function we use in our model, given by Eq. 4.3.63.

Substituting this damping function into Eq. 4.3.63 and noting that $\gamma(t) = \gamma_0 \sin \omega t$, we obtain

$$\sigma^{(sp)}(t) = \frac{\forall \alpha \gamma_0}{\Gamma(1 - \alpha)} \int_0^{u_c} u^{-(\alpha+1)} [\sin \omega t - (\sin \omega t \cos \omega u - \cos \omega t \sin \omega u)] du \quad (4.3.64)$$

in which u_c is given by

$$u_c = \frac{1}{\omega} \sin^{-1} \left(\frac{\gamma_c}{\gamma_0} \right) \approx \frac{1}{\omega} \frac{\gamma_c}{\gamma_0} \quad (4.3.65)$$

because $\gamma_c \ll \gamma_0$. Upon simplifying and separating the in-phase and out of phase components of the stress $\sigma^{(sp)}(t)$ with respect to the applied strain $\gamma(t)$ we obtain the storage and loss moduli $G^{(sp)}(\omega)$ and $G''^{(sp)}(\omega)$ respectively as

$$G^{(sp)}(\omega) = \frac{\forall \alpha}{\Gamma(1 - \alpha)} \int_0^{u_c} u^{-(\alpha+1)} (1 - \cos \omega u) du \quad (4.3.66)$$

$$G''^{(sp)}(\omega) = \frac{\forall \alpha}{\Gamma(1 - \alpha)} \int_0^{u_c} u^{-(\alpha+1)} \sin \omega u du \quad (4.3.67)$$

To analytically solve these integrals, we note that $0 \leq u \leq u_c \ll 1$, and we approximate $1 - \cos(\omega u) \approx (\omega u)^2/2$ and $\sin(\omega u) \approx \omega u$, from appropriate Taylor series expansions. Therefore we finally obtain

$$G^{(sp)}(\omega) \approx \frac{\forall \alpha \omega^\alpha}{2(2 - \alpha)\Gamma(1 - \alpha)} \left(\frac{\gamma_c}{\gamma_0} \right)^{2-\alpha} \quad (4.3.68)$$

$$G''^{(sp)}(\omega) \approx \frac{\forall \alpha \omega^\alpha}{\Gamma(2 - \alpha)} \left(\frac{\gamma_c}{\gamma_0} \right)^{1-\alpha} \quad (4.3.69)$$

We now use Eqs. 4.3.60, 4.3.61, 4.3.68 and 4.3.69 to find the overall elastic and loss moduli

predicted by the model, and these are given by

$$G'(\omega) = \frac{G}{2} \left(\frac{\gamma_c}{\gamma_0} \right)^2 + \frac{\forall \alpha \omega^\alpha}{2(2-\alpha)\Gamma(1-\alpha)} \left(\frac{\gamma_c}{\gamma_0} \right)^{2-\alpha} \quad (4.3.70)$$

$$G''(\omega) = G \frac{\gamma_c}{\gamma_0} + \frac{\forall \alpha \omega^\alpha}{\Gamma(2-\alpha)} \left(\frac{\gamma_c}{\gamma_0} \right)^{1-\alpha} \quad (4.3.71)$$

with $\eta^*(\omega)$ given by Eq. 4.3.32 as before. From Eqs. 4.3.70 and 4.3.71, we see that

$$\frac{G'(\omega)}{G''(\omega)} \sim \frac{\gamma_c}{\gamma_0} \ll 1 \quad (4.3.72)$$

and therefore

$$\eta^*(\omega) = \frac{G''(\omega) \sqrt{1 + (G'(\omega)/G''(\omega))^2}}{\omega} \approx \frac{G''(\omega)}{\omega} \quad (4.3.73)$$

and consequently

$$\eta^*(\omega) = G \frac{\gamma_c}{\gamma_0 \omega} + \frac{\forall \alpha}{\Gamma(2-\alpha)} \gamma_c^{1-\alpha} (\gamma_0 \omega)^{\alpha-1} \quad (4.3.74)$$

Comparing this result with Eq. 4.3.52, we find that

$$\eta^*(\omega) = \eta(\dot{\gamma}) \Big|_{\dot{\gamma} = \gamma_0 \omega} \quad (4.3.75)$$

This result is identical to the Rutgers-Delaware rule. Krieger has noted in a brief correspondence that the Rutgers-Delaware rule is of a fundamentally different form to the Cox-Merz rule, and not merely an alternate form or extension of it [165]. The Rutgers-Delaware rule applies to materials that are inherently nonlinear, and for which the period of oscillation is much shorter than the structural recovery time of the material. We incorporate both these properties of the material using our choice of Tanner-Simmons damping function, detailed in Fig. 4.3.9. The inherent nonlinearity is accounted for by assuming $\gamma_c/\gamma_0 \ll 1$; i.e. the elastoplastic material always yields and flows during the imposed oscillatory deformation. The long timescale typically associated with structural recovery in such materials is captured using our damping function by assuming zero recovery after the first yielding event, as shown in Fig. 4.3.9.

We have shown above that with an appropriate choice of a fractional constitutive model,

not only can we develop a nonlinearly-elastic constitutive formulation of the familiar Herschel Bulkley model, but the resulting theoretical framework naturally gives rise to relationships such as the Rutgers-Delaware rule that relates oscillatory and steady shear rheology. We emphasize that the advantage of using a fractional constitutive model together with the K-BKZ framework is that we also obtain the linear viscoelastic response of multiscale yielding materials that exhibit a nonlinear rheological response of Herschel-Bulkley type; the linear and nonlinear properties are naturally related through the damping function.

In addition to the Herschel-Bulkley model discussed above, there are other empirical inelastic power-law models which can also be derived from first principles by an appropriate choice of fractional constitutive equation. We illustrate this process below by deriving the Cross and Carreau models starting with a Fractional Zener Model (FZM) and coupling it with a damping function using the K-BKZ framework.

4.3.5 *Fractional Zener Model (FZM) and Carreau-Type Flow Curves*

The FZM consists, in most general form, of a fractional Maxwell model branch in parallel with a single springpot [55], resulting in three mechanical elements and six model parameters (a quasi-property and a power-law exponent for each springpot). Various forms of power-law response can be obtained from this model depending on the specific values of the power-law exponents and the corresponding quasi-properties of each of the springpots. In this paper, we will consider one special case of the FZM, as shown schematically in Fig. 4.3.10, in which two of the springpots are reduced to Newtonian dashpots. We show below that this four parameter model is well suited for describing concentrated polymer solutions and other shear-thinning multiscale systems.

The dashpot in the left-hand branch of the FZM has viscosity η_s and accounts for the background solvent viscosity. One of the springpots on the FMM branch (right-hand side of the FZM) is set to be a Newtonian dashpot with viscosity $\mathbb{V} = \eta_p$ and $\alpha = 1$. This dashpot accounts for the polymer contribution to the steady shear viscosity, and the shear viscosity is bounded by $\eta_0 = \eta_p + \eta_s$ as $\dot{\gamma} \rightarrow 0$. This FZM has a characteristic relaxation time given by $\tau = (\eta_p/\mathbb{G})^{1/(1-\beta)}$. The third springpot has a power-law exponent β and a quasi-property \mathbb{G} . Therefore, this model has a total of four parameters. We call this special case

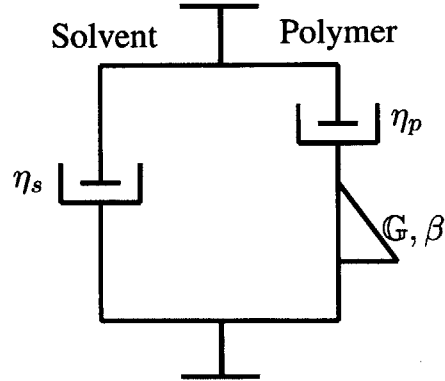


Figure 4.3.10: A special case of the Fractional Zener Model (FZM) which we refer to as the Fractional Viscoelastic Cross Model (FVCM).

of the FZM the Fractional Viscoelastic Cross Model (FVCM) and we explain this choice of nomenclature below.

The constitutive equation of the FVCM can be written as [55]

$$\sigma(t) + \frac{\eta_p}{\mathbb{G}} \frac{d^{1-\beta}}{dt^{1-\beta}} \sigma(t) = (\eta_p + \eta_s) \frac{d\gamma(t)}{dt} + \frac{\eta_p \eta_s}{\mathbb{G}} \frac{d^{2-\beta} \gamma(t)}{dt^{2-\beta}} \quad (4.3.76)$$

Using the Laplace and Fourier transform techniques outlined in Chapter 2, the linear viscometric functions may be determined as follows:

$$G'(\omega) = \frac{\eta_p^2 \mathbb{G} \omega^{\beta+2} \cos(\pi\beta/2)}{(\eta_p \omega)^2 + (\mathbb{G} \omega^\beta)^2 + 2\eta_p \mathbb{G} \omega^{\beta+1} \sin(\pi\beta/2)} \quad (4.3.77)$$

$$G''(\omega) = \eta_s \omega + \frac{\mathbb{G}^2 \eta_p \omega^{2\beta+1} + \eta_p^2 \mathbb{G} \omega^{\beta+2} \sin(\pi\beta/2)}{(\eta_p \omega)^2 + (\mathbb{G} \omega^\beta)^2 + 2\eta_p \mathbb{G} \omega^{\beta+1} \sin(\pi\beta/2)} \quad (4.3.78)$$

$$G(t) = \eta_s \delta(t) + \mathbb{G} t^{-\beta} E_{1-\beta, 1-\beta} \left(-\frac{\mathbb{G}}{\eta_p} t^{1-\beta} \right) \quad (4.3.79)$$

Because we have an expression for the relaxation modulus $G(t)$ we can use this in the K-BKZ framework as before (Eq. 4.3.7) to compute the model predictions in large straining deformations. To evaluate the integral we need to specify the form of the damping function. Here we take the same simple form as Eq. 4.3.14 which adequately describes many systems and introduces one additional model parameter.

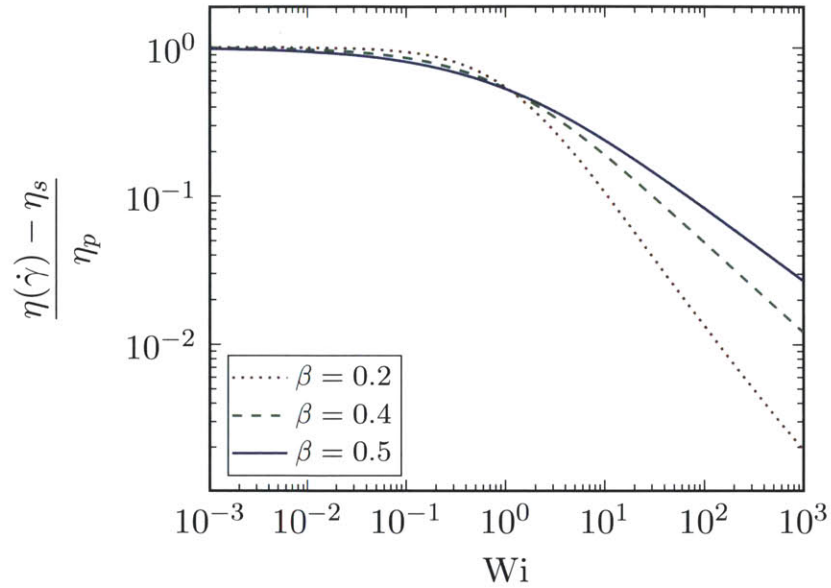
We present simulations of the steady shear viscosity predicted by the FVCM in Fig. 4.3.11. The values of η_s and η_p were chosen to be $\eta_s = 1$ Pa s and $\eta_p = 100$ Pa s. We choose to plot the predictions on dimensionless axes, with the steady shear viscosity $\eta(\dot{\gamma})$ suitably scaled by η_p and η_s and the x axis is a Weissenberg number $Wi = \tau\dot{\gamma}$, with τ being the characteristic relaxation time given above. Fig. 4.3.11(a) shows the effect of changing the exponent β of the springpot, holding all other parameters constant. Increasing β decreases the slope of the shear-thinning region; in fact, because the shear-thinning region is controlled by the Maxwell arm of the FZM (the solvent term dictates the high shear rate viscosity plateau η_s), Eq. 4.3.24 is applicable and $\eta(\dot{\gamma}) \sim \dot{\gamma}^{\beta-1}$. We also show the effect of changing the strain damping parameter a in Fig. 4.3.11(b). We observe that for $a = 0$, the damping function $h(\gamma) = 1$, and there is no shear-thinning because there is no microstructural damage accumulated in the material upon imposing large strains. For all non-zero values of a , shear-thinning is observed; as a is increased, it can be seen that at the same value of Weissenberg number Wi , the scaled viscosity is lower as expected. In this manner, the damping parameter a simply offsets each predicted curve from the next, when all other parameters are held constant.

When we consider the role of the five model parameters in this form of the FVCM, we find that the model has all the capabilities of the Cross model [19], which proposes the following expression to capture the flow curves of polymer melts:

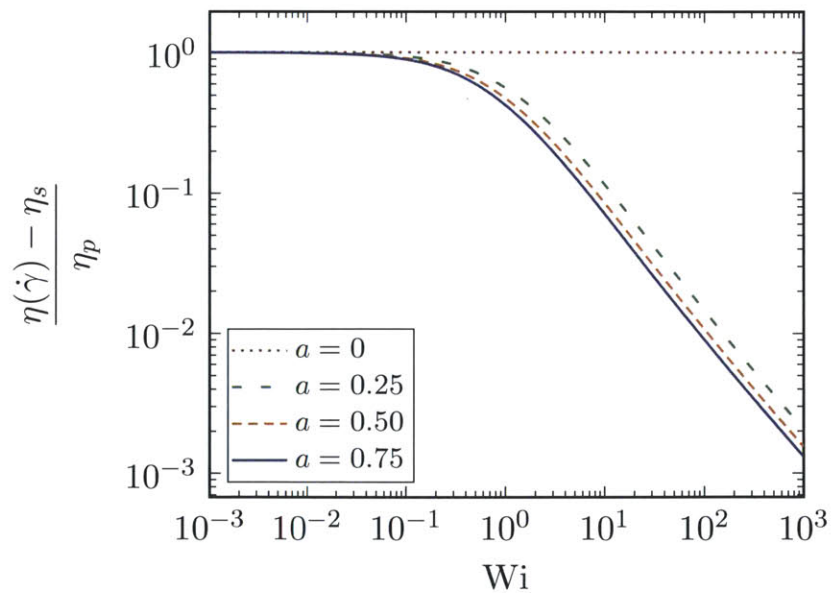
$$\eta(\dot{\gamma}) = \eta_s + \frac{\eta_p}{1 + (\dot{\gamma}/\dot{\gamma}^*)^{(1-n)}} \quad (4.3.80)$$

where $\eta(\dot{\gamma})$ is the steady shear viscosity. The parameters η_p and η_s control the zero shear and infinite shear plateau viscosities respectively, n dictates the slope of the power-law region between the two plateau regions and $\dot{\gamma}^*$ is a characteristic shear rate that determines the point of transition between the zero-shear plateau and the asymptotic power-law region. In Fig. 4.3.12 we show as a solid line the predicted steady shear viscosity $\eta(\dot{\gamma})$ obtained for the FVCM. The dashed line in the figure is the prediction of the Cross model. The model parameters used to obtain these simulations are given in the figure caption, and it is clear that the agreement between the FVCM and the Cross model is excellent.

The advantage of using the FVCM over the Cross model is three-fold: first, our approach also enables the determination of the linear viscoelastic material functions such as $G'(\omega)$ and $G''(\omega)$ (Eqs. 4.3.77 and 4.3.78 respectively) for materials that exhibit a flow curve

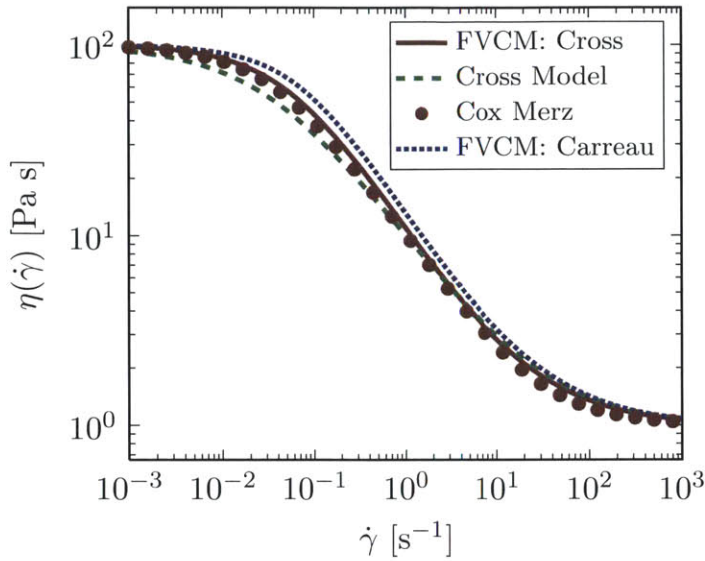


(a)



(b)

Figure 4.3.11: Simulations of the viscosity predicted by the FVCM model plotted in dimensionless form as a function of the Weissenberg number $Wi = \tau\dot{\gamma}$. (a) Effect of varying the value of the springpot exponent β , which controls the slope of the shear-thinning region. (b) Effect of varying the damping function parameter a . For $a = 0$, no shear-thinning is observed.


Figure 4.3.12

Simulations of the the steady shear viscosity $\eta(\dot{\gamma})$ as a function of shear rate $\dot{\gamma}$ obtained from the FVCM model. For all curves, $\eta_p = 100$ Pa s and $\eta_s = 1$ Pa s. The FCVM (Cross) prediction was obtained using a damping function of the form $h(\gamma) = 1/(1 + 0.1\gamma^2)$ and a springpot with $\beta = 0.3$ and $\mathbb{G} = 10$ Pa s $^\beta$, and $\tau = (\eta_p/\mathbb{G})^{1/(1-\beta)} = 26.83$ s. To generate the Cross model simulation, the same values of $(\dot{\gamma}^*)^{-1} = 26.83$ s and $n = 0.3$ were chosen.

that is captured by the Cross model. The inelastic Cross model does not have a linear viscoelastic limit at all. For example, if the shear rate $\dot{\gamma}$ were stepped up from $\dot{\gamma}_1$ to $\dot{\gamma}_2 > \dot{\gamma}_1$, the shear stress in the Cross model responds instantaneously. Second, the linear viscoelastic parameters play a role in nonlinear behavior and their relative contribution is weighted by the damping function. We illustrate this point in Fig. 4.3.12 by showing the magnitude of the complex viscosity $|\eta^*(\omega)|$ at $\omega = \dot{\gamma}$, i.e., the prediction of the steady shear viscosity obtained from the application of the Cox-Merz rule (Eq. 4.3.31) to the FVCM. Here too, we see that the magnitude of shear-thinning obtained from the linear viscoelastic properties agrees closely with the full nonlinear prediction as well as with the empirical Cross model. We also note in passing that the small offset between $\eta(\dot{\gamma})$ and $\eta^*(\omega)|_{\omega=\dot{\gamma}}$ can be quantified in terms of the damping function parameter a , as discussed previously. The third advantage of our fractional constitutive modeling approach to the Cross model is that the FVCM model also yields a prediction of the first normal stress coefficient $\Psi_1(\dot{\gamma})$ for materials such as concentrated polymer solutions that exhibit a Cross-like flow curve under steady shearing flow.

To generate the simulations of the FVCM in Fig. 4.3.12, note that we chose a damping function of the form $h(\gamma) = 1/(1 + a\gamma^2)$. In their review, Rolón-Garrido and Wagner discuss more complicated forms of the damping function [174]. Conceivably, depending on the microstructural properties of the material, the form of the damping function could be different from the one we have chosen above. We show as a dotted line in Fig. 4.3.12 the simulation of the steady shear viscosity $\eta(\dot{\gamma})$ obtained from Eq. 4.3.7 with the relaxation

kernel given by Eq. 4.3.79 and a damping function of the form $h(\gamma) = \frac{1}{[1+(0.1\gamma^2)^3]^{1/3}}$. We observe that the transition from the zero shear viscosity plateau to the power-law shear-thinning region is now ‘sharper’, displaying behavior of the kind exhibited by the empirical Carreau model [24, 187]. Hence, by controlling the damping function, we can reproduce a wide variety of steady flow curves (as commonly observed experimentally); these four linear viscoelastic parameters in the model remain unchanged and are determined from independent linear deformation histories such as SAOS.

4.4 Conclusions

There is a wealth of rheological data available in the literature on complex fluids that exhibit broad power law-like behavior in their linear viscoelastic material properties. It has been shown in previous studies that fractional constitutive equations provide an excellent framework to quantitatively describe the linear rheological properties of multiscale materials. However, there was no mechanism for extending these models to nonlinear deformations. Using the concept of quasi-properties [80], it is possible to compactly describe the linear rheology of power-law materials using an appropriate choice of fractional constitutive model. These models can be visualized as consisting of springs, dashpots and springpots in series or parallel. The resulting constitutive equations of these models are linear ODEs and can also be written in terms of linear convolution integrals with a relaxation modulus that is of Mittag-Leffler form. We have extended these linear viscoelastic models to make predictions of the nonlinear behavior of power-law materials using the K-BKZ framework. To evaluate the resulting integrals, we are required to determine the appropriate form of the material’s damping function, for which we use a series of step strain experiments with increasing strain amplitude. This introduces just one additional model parameter, and results in a nonlinear integral equation given by Eq. 4.3.7. We use this model to make accurate predictions of both $\eta(\dot{\gamma})$ and $\Psi_1(\dot{\gamma})$ for Xanthan gum solutions and provide analytical approximations for both material functions.

Evaluating empirical rules such as the Cox-Merz relationship and the Gleissle mirror relations using this constitutive framework show that a shift factor exists, and that $\eta^*(\omega)|_{\omega=\dot{\gamma}} > \eta(\dot{\gamma})$. This is because the small amplitude deformations upon which these empirical rules are based on do not account for the structural damage that is accumulated during a nonlinear deformation. Using our integral formulation, we quantify this shift fac-

tor (or offset) in terms of the linear viscoelastic as well as damping function parameters. In the limit of an exponential relaxation kernel of Maxwell-Debye form the offset is zero, but systematically increases for relaxation kernels of Mittag-Leffler form that more accurately capture the broad relaxation dynamics of complex materials such as Xanthan gum.

We also address a semi-empirical relationship that is fundamentally different from the Cox-Merz rule, but also relates steady shear and oscillatory experiments, known as the Rutgers-Delaware rule [166]. This rule applies to viscoelastoplastic materials such as concentrated suspensions exhibiting yield-like behavior beyond a critical strain. Starting with a Fractional Kelvin Voigt representation we derive from first principles a viscoelastic generalization of the elastic Herschel-Bulkley equation, which correctly follows the Rutgers-Delaware rule. Finally, we have also shown how to derive a nonlinear viscoelastic model to quantify the nonlinear rheology of shear-thinning viscoelastic materials such as concentrated polymer solutions exhibiting Cross or Carreau-type behavior in steady shear flow.

In this chapter, we have presented a framework that helps translate between the linear and nonlinear rheology of power-law multiscale materials. There are only two components that need to be determined within this framework: the fractional relaxation dynamics (specifically the memory kernel which describes the linear viscoelastic response), and the strain-dependent damping function. The extension of the fractional constitutive framework to the Cross or Carreau model detailed here opens up the possibility of accurately describing the rheological response of a large class of complex fluids in a general manner, using only a few model parameters. The resulting constitutive models provide a compact but accurate description of the linear and nonlinear viscoelastic properties of complex liquids and soft solids which should be useful for quantitative materials diagnostics, and quality control comparisons as well as for computational simulations. For geometries in which the flow field contains streamlines with complicated shapes, the stress and strain-rate fields can be calculated in the entire domain by considering the coupled system of the K-BKZ constitutive equation and the Cauchy momentum equations and solving the system as a Volterra integrals for every mesh point.

Thus far in this thesis, we have only studied shear deformations. However, as we have noted in the Introduction, extensional deformations are of immense importance in various industrial and biological applications of complex fluids. Moreover, the extensional properties of a complex fluid can be very different from its behavior in shear [61]. The next two chapters, we focus our attention on the extensional rheology of complex fluids.

5 | *Small Strain Extensional Deformations: Tacky Polymer Gels*

In the preceding chapters, we have focused on the linear and nonlinear *shear* rheology of power law complex fluids. In this chapter we begin our analysis of *extensional* deformations by analyzing the behavior of crosslinked polymer gels under small strains. These materials display the broad power law response that is typical of multiscale complex fluids [36]. The mechanical properties of Pressure Sensitive Adhesives (PSA) — which are very often crosslinked polymeric systems [188, 189] — are measured using a ‘tack’ experiment and the resultant forces are measured as a function of strain. We show how a simple three element fractional constitutive model coupled with the kinematics of a tack experiment performed on a Newtonian fluid leads to the accurate predictions of tack forces in the small strain limit. We show how our predictive model gives accurate results for the measured normal force in a tack experiment using the material parameters determined from SAOS. We next examine the inverse problem; we show how one may determine the linear viscoelastic response of the polymer gels using their tack responses alone. We establish how one may analytically derive accurate approximations for both the magnitude and temporal location of the peak force in a tack experiment. For complex fluids that flow at long timescales, we have noted that the FMM is a more appropriate constitutive model than the FKVM. Therefore we also present a complete analysis of the FMM and predict the tack response of fractional Maxwell-like materials under conditions of constant velocity as well as constant strain rate applied deformations. We derive analytic solutions for the tack force that approximate the exact numerical solution very closely. We compare our predictions with experimentally obtained tack forces for Locust Bean Gum (LBG). Finally, analogous to the FKVM case, we describe how one may achieve accurate closed-form expressions for the tack force by a careful analysis of asymptotic behaviors.

5.1 Introduction

Pressure sensitive adhesives (PSAs) are a class of adhesives that bond to a surface upon the application of even a light amount of pressure without leaving any residue on the substrate when peeled off [188, 190] i.e. the bonding does not arise from chemical or covalent interactions. We encounter them in everyday life in products such as Post-It Notes[®], stickers, packaging labels and in specialized applications such as bioelectrodes [191]. These adhesives are very often composed of chemically crosslinked polymers [192, 193] and therefore their viscoelastic properties play a major role in their tack response [189]. In a tack experiment, a probe is brought towards the surface of the adhesive and a specified contact force is applied for a specified amount of time (known as the dwell time) [194, 195]. The probe is then peeled away either at a constant velocity or constant strain rate (exponentially increasing velocity) and the resulting force vs. strain curve is measured. An example of such a curve for a typical tack experiment is shown in Figure 5.1.1. From the tack force vs. displacement curve shown, we observe two important features of a tack experiment. There exists a peak in force at small displacements (or equivalently small strains) followed by a large strain

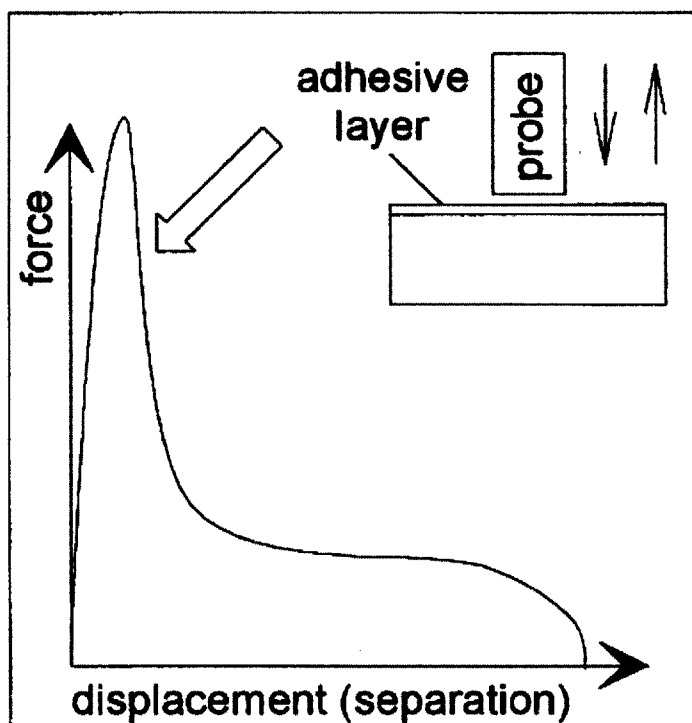


Figure 5.1.1

A diagram of a typical tack experiment showing the variation of the normal force as a function of displacement, reproduced from Ref. [196]. The tack force is also frequently plotted as a function of the strain. We observe that at small strains there is a peak in force, followed by a large strain flow regime, sometimes exhibiting strain hardening. In this Chapter, we show that this peak in the tack force arises from the lubrication flow of the polymer at small strains. The inset plot schematically shows a tack experiment.

flow regime. In this figure the tack force exhibits a plateau as a function of displacement; however in many tack experiments, nonlinear effects such as strain hardening is visible [189].

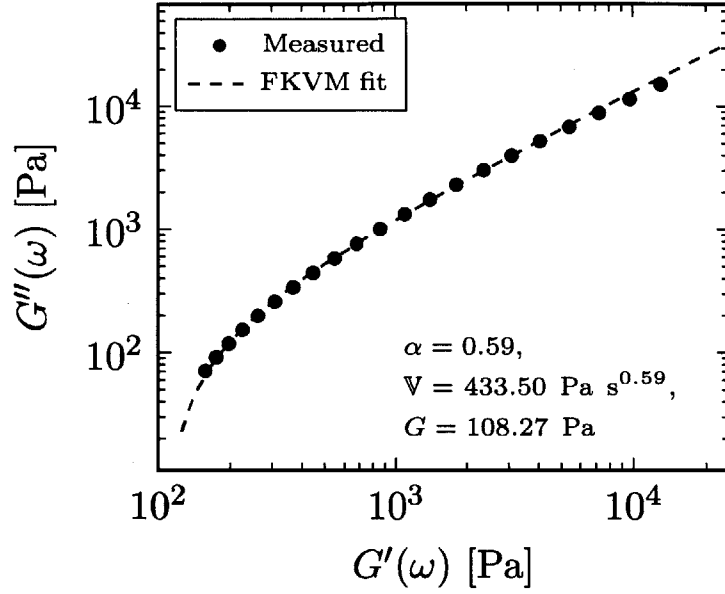
In this Chapter, we demonstrate how the peak in force in a tack experiment arises from the lubrication flow of the polymeric material at small strains. Because the value of this peak force determines the strength of the adhesive, an *a priori* prediction of the force based on the rheological characterization of the material would greatly aid in the design of pressure sensitive adhesives. We perform our analysis using data obtained by Wyatt and Grillet for a crosslinked fluoro-silicone polymeric gel [36]. We first show that a Fractional Kelvin Voigt Model (FKVM) characterizes the shear rheology over nearly five decades of frequency using just three parameters. We then couple the stress-strain relationship of the FKVM with the lubrication flow solution of a *Newtonian* fluid, and demonstrate that this leads to accurate predictions of the small strain tack force. Finally, we extend the analysis to sol-like materials that flow at long times, for which the FMM is a more accurate constitutive model.

5.2 *The Fractional Kelvin-Voigt Model*

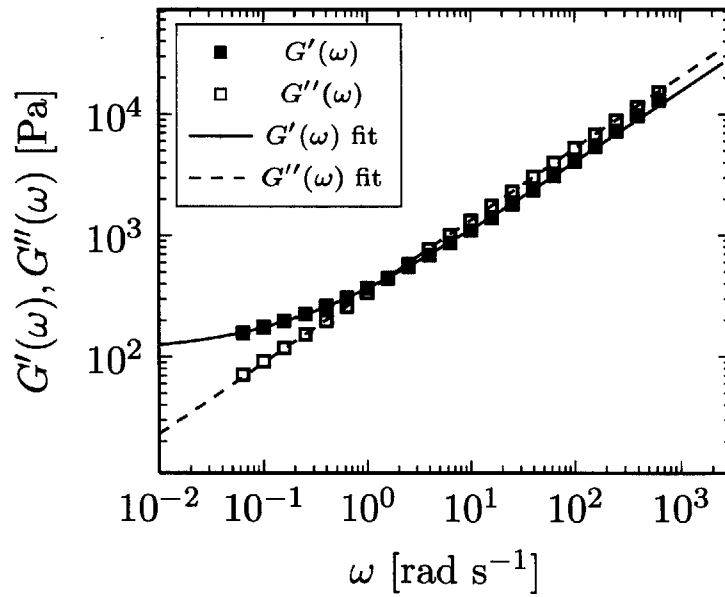
5.2.1 *SAOS Fitting and Parameter Determination*

In the analysis that follows, we will work with data from the low modulus gels reported in [36]. We first begin with the analysis of the SAOS data for these gels and fit these data to the FKVM model (equations 2.3.22 and 2.3.23). In figure 5.2.1a we show the Cole-Cole plot of the SAOS data from the low modulus gels, and figure 5.2.1b shows the same data plotted as a function of frequency. $G'(\omega)$ shows a plateau at low frequencies indicating that one of the elements may be set to a spring ($\beta = 0$).

The dashed lines show the corresponding fits of the FKVM. It is seen that the fit is excellent; the low frequency plateau modulus is captured by the spring, while the high frequency power-law response (which is dominated by the rheology of the viscous polymer sol) is closely modeled by the springpot. Note that with just three parameters G, \mathbb{V} and α , we can capture the entire dynamic range of the material response of the gels. From these fits, we obtain the values of the parameters in the FKVM that characterize the gels as $\alpha = 0.59, \beta = 0, \mathbb{V} = 433.50 \text{ Pa s}^{0.59}$ and $G = 108.27 \text{ Pa}$. We also calculate the relaxation time $t_{\text{rel}} = 1/\omega_c$ of the polymer gel using 3.3.7 to obtain $t_{\text{rel}} = 0.63\text{s}$. We show next how



(a)



(b)

Figure 5.2.1: SAOS data of the polymer gels (symbols) shown along with the FKVM fits (dashed lines). (a) Cole-Cole plot. (b) The same SAOS data plotted against angular frequency ω .

the normal force in a tack test may be predicted using just these three material parameters.

5.2.2 Determination of the Normal Force for a Probe Tack Test: Constant Velocity Applied Deformation

In this chapter, we are interested in examining the tack response of viscoelastic polymer gels. The tack response of such materials are conventionally measured using a probe tack test [189, 196, 197]. The geometry of the tack test is schematically shown in figure 5.2.2. The upper plate is pulled apart according to a specific displacement profile — notably (1) constant velocity, or (2) exponentially; the latter leads to the imposition of a constant nominal strain rate on the material being tested. The force exerted on the plates by the deforming viscoelastic material is measured as a function of time to probe both the linear and non-linear tack response of the material. We define the instantaneous aspect ratio $\Lambda = R_0/h(t)$, in which R_0 is the radius of the plates, and $h(t)$ is the separation between the bottom and top plates as a function of time.

The definition of the axes used in what follows is shown in figure 5.2.2, with gray representing the upper plate, and blue representing the deforming polymer gel. We begin the analysis with the application of the lubrication approximation to the Cauchy momentum equations retaining only the viscous and pressure terms to obtain

$$\frac{\partial p}{\partial r} = \frac{\partial \tau_{zr}}{\partial z} \quad (5.2.1)$$

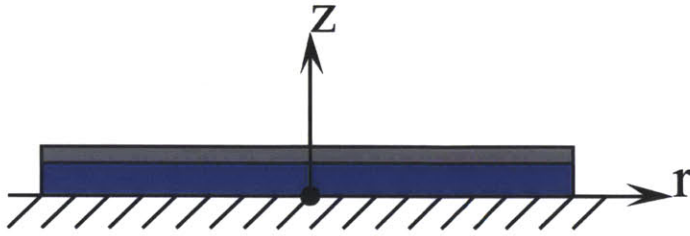
$$\frac{\partial p}{\partial z} = \frac{\partial \tau_{zz}}{\partial z} \quad (5.2.2)$$

τ_{zr} and τ_{zz} are given by the constitutive equation of the fractional Kelvin-Voigt model, (i.e)

$$\tau_{zr} = \mathbb{V} \frac{d^\alpha \gamma_{zr}}{dt^\alpha} + \mathbb{G} \frac{d^\beta \gamma_{zr}}{dt^\beta} \quad (5.2.3)$$

$$\tau_{zz} = \mathbb{V} \frac{d^\alpha \gamma_{zz}}{dt^\alpha} + \mathbb{G} \frac{d^\beta \gamma_{zz}}{dt^\beta} \quad (5.2.4)$$

The use of the lubrication approximation is justified because of the large initial aspect ratio $\Lambda_0 = R_0/h_0$ (with h_0 being the initial separation between the plates) imposed in the experiment. Due to the relatively slow withdrawal speed of the upper plate ($u_0 = 0.1$ mm/s), the aspect ratio Λ remains large enough to justify the use of the lubrication approximation

**Figure 5.2.2**

The definition of the axes used in this document. The upper plate (diameter 8 mm) is shown in gray, and the polymer gel is shown in blue. The initial aspect ratio depicted here is to scale.

across nearly three orders of magnitudes of experimental time-range. Substituting 5.2.3 and 5.2.4 into 5.2.1 and 5.2.2 respectively, we obtain

$$\frac{\partial p}{\partial r} = \frac{\partial}{\partial z} \left(\mathbb{V} \frac{d^\alpha \gamma_{zr}}{dt^\alpha} + \mathbb{G} \frac{d^\beta \gamma_{zr}}{dt^\beta} \right) \quad (5.2.5)$$

$$\frac{\partial p}{\partial z} = \frac{\partial}{\partial z} \left(\mathbb{V} \frac{d^\alpha \gamma_{zz}}{dt^\alpha} + \mathbb{G} \frac{d^\beta \gamma_{zr}}{dt^\beta} \right) \quad (5.2.6)$$

We first reformulate Equation 5.2.5 as

$$\frac{\partial p}{\partial r} = \mathbb{V} \frac{d^\alpha}{dt^\alpha} \frac{\partial \gamma_{zr}}{\partial z} + \mathbb{G} \frac{d^\alpha}{dt^\alpha} \frac{\partial \gamma_{zr}}{\partial z} \quad (5.2.7)$$

$$= \mathbb{V} \frac{d^{\alpha-1}}{dt^{\alpha-1}} \frac{\partial \dot{\gamma}_{zr}}{\partial z} + \mathbb{G} \frac{d^{\beta-1}}{dt^{\beta-1}} \frac{\partial \dot{\gamma}_{zr}}{\partial z} \quad (5.2.8)$$

$$= \mathbb{V} \frac{d^{\alpha-1}}{dt^{\alpha-1}} \frac{\partial^2 v_r(t')}{\partial z^2} + \mathbb{G} \frac{d^{\beta-1}}{dt^{\beta-1}} \frac{\partial^2 v_r(t')}{\partial z^2} \quad (5.2.9)$$

where we have used the fact that $\dot{\gamma}_{zr} = \frac{\partial v_r}{\partial z}$ (as will become evident, $\frac{\partial v_z}{\partial r} = 0$). Transforming the equation into Laplace space we get

$$\mathcal{L} \left[\frac{\partial p}{\partial r} \right] = \mathbb{V} s^{\alpha-1} \mathcal{L} \left[\frac{\partial^2 v_r(t)}{\partial z^2} \right] + \mathbb{G} s^{\beta-1} \mathcal{L} \left[\frac{\partial^2 v_r(t)}{\partial z^2} \right] \quad (5.2.10)$$

$$= \mathcal{L} \left[\frac{\partial^2 v_r(t)}{\partial z^2} \right] \cdot \left[\frac{\mathbb{G}}{s^{1-\beta}} + \frac{\mathbb{V}}{s^{1-\alpha}} \right] \quad (5.2.11)$$

and converting back into real space we get

$$\frac{\partial p}{\partial r} = \left(\frac{\mathbb{V} t^{-\alpha}}{\Gamma(1-\alpha)} + \frac{\mathbb{G} t^{-\beta}}{\Gamma(1-\beta)} \right) * \frac{\partial^2 v_r(t)}{\partial z^2} \quad (5.2.12)$$

Notice that the *product* in Laplace space is converted into a *convolution* in real space, denoted here by the symbol $*$. Moreover, the first term in the RHS of 5.2.12 is nothing but the relaxation modulus of the fractional Kelvin-Voigt model (equation 2.3.18). Therefore, we arrive at an integral akin to the Boltzmann superposition integral, except that instead of convolving the relaxation modulus with the strain rate, we now convolve it with the quantity $\frac{\partial^2 v_r(t)}{\partial z^2}$, i.e the pressure field is determined by the integral

$$\frac{\partial p}{\partial r} = \int_0^t \left(\frac{\mathbb{V}(t-t')^{-\alpha}}{\Gamma(1-\alpha)} + \frac{\mathbb{G}(t-t')^{-\beta}}{\Gamma(1-\beta)} \right) \cdot \frac{\partial^2 v_r(t')}{\partial z^2} dt' \quad (5.2.13)$$

Using an identical procedure involving 5.2.2 and $\dot{\gamma}_{zz} = 2\frac{\partial v_z}{\partial z}$, we also have

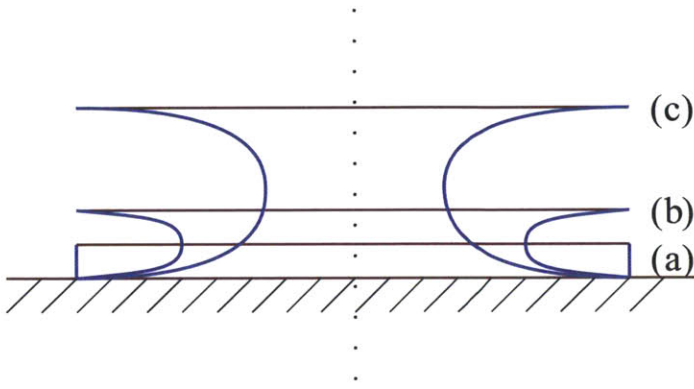
$$\frac{\partial p}{\partial z} = 2 \int_0^t \left(\frac{\mathbb{V}(t-t')^{-\alpha}}{\Gamma(1-\alpha)} + \frac{\mathbb{G}(t-t')^{-\beta}}{\Gamma(1-\beta)} \right) \cdot \frac{\partial^2 v_z(t')}{\partial z^2} dt' \quad (5.2.14)$$

To find $v_r(t)$ and $v_z(t)$, we assume that the imposed deformation on the filament is determined by the kinematics of the conditions of the tack test. The underlying motivation in this assumption is that the flow field determines the strain field and hence—through the constitutive equation—the stress field in the deforming filament. The pressure field is then found from the stress field using the Cauchy momentum equations derived above. Once the pressure field is determined, the force exerted on the plate by the deforming filament may be determined by integrating the pressure field over a cross section of the filament parallel to the surface of the plate. The FKVM yields a temporal response to various applied deformations; however, because the model is linear and the stresses are determined by linear convolution integrals, shear-thinning is absent in this model. Therefore, we may utilize the same flow field that would be realized from the result of performing a tack test on a constant viscosity Newtonian fluid and we have [198]

$$v_r(r, z, t) = -3r \left(\frac{\dot{h}(t)}{h(t)} \right) \left(\frac{z}{h(t)} \right) \left(1 - \frac{z}{h(t)} \right) \quad (5.2.15)$$

$$v_z(z, t) = \dot{h}(t) \left(\frac{z}{h(t)} \right)^2 \left(3 - \frac{2z}{h(t)} \right) \quad (5.2.16)$$

where the origin is located at the center of the bottom plate (see figure 5.2.2). We will

**Figure 5.2.3**

The profiles of the deforming filament of polymer gel at different instances of time during a tack experiment for contact force $F_c = 300\text{g}$. (a) $t = 0$ (b) $t = 5t_p$ and (c) $t = 20t_p$. Here $t_p \approx 1\text{ s}$ was determined based on the observation of the experimental data. This diagram is to scale, with the upper plate of diameter 8 mm.

henceforth denote $h(t)$ and $\dot{h}(t)$ simply by h and \dot{h} respectively for clarity of notation. For the value of $\dot{h} = u_0 = 0.1\text{ mm/s}$ used in these experiments, a diagram to scale of the profiles of the filament at different instances of time are given in figure 5.2.3. The profiles were calculated by integrating the velocity field given by equations 5.2.15 and 5.2.16 forward in time to track the location of Lagrangian particles of fixed identity that were located on the surface at $t = 0$ [198]. The quantity t_p shown in the figure is the temporal location at which the peak in force is observed. These values of t_p may be obtained from the experimental data.

From 5.2.15, we obtain

$$\frac{\partial^2 v_r(t)}{\partial z^2} = \frac{6r\dot{h}}{h^3} = \frac{6ru_0}{(h_0 + u_0 t)^3} \quad (5.2.17)$$

$$= \frac{6r}{u_0^2} \frac{1}{(h_0/u_0 + t)^3} \quad (5.2.18)$$

Substituting 5.2.18 into 5.2.13 we have

$$\frac{\partial p}{\partial r} = \frac{6r}{u_0^2} \int_0^t \left(\frac{\mathbb{V}(t-t')^{-\alpha}}{\Gamma(1-\alpha)} + \frac{\mathbb{G}(t-t')^{-\beta}}{\Gamma(1-\beta)} \right) \cdot \frac{1}{(h_0/u_0 + t')^3} dt' \quad (5.2.19)$$

$$\text{(i.e.) } \frac{\partial p}{\partial r} = \frac{6r}{u_0^2} I_3(t) \quad (5.2.20)$$

where $I_3(t)$ is a definite integral that has been defined and determined in Appendix D.

Because $I_3(t)$ is a function of time only, we have

$$p(r, z) = \frac{3r^2}{u_0^2} I_3(t) + f(z) + C(t) \quad (5.2.21)$$

To determine $f(z)$, we first take the partial derivative of 5.2.14 with respect to z , and then substitute for p from 5.2.21. From observation of the expression in 5.2.16 we see that $\frac{\partial^3 v_z(t')}{\partial z^3}$ is independent of z and is a function of time alone. We take this additional partial derivative to eliminate the variable z from the integral. This is because we are interested in the material response of the fluid element located at $z = h(t)/2$, which is a function of time. We would like to eliminate this function while carrying out the convolution integral. Therefore we substitute equation 5.2.21 into the equation

$$\frac{\partial^2 p}{\partial z^2} = 2 \int_0^t \left(\frac{\mathbb{V}(t-t')^{-\alpha}}{\Gamma(1-\alpha)} + \frac{\mathbb{G}(t-t')^{-\beta}}{\Gamma(1-\beta)} \right) \cdot \frac{\partial^3 v_z(t')}{\partial z^3} dt' \quad (5.2.22)$$

From 5.2.16 we have

$$\frac{\partial^3 v_z(t')}{\partial z^3} = -12 \frac{\dot{h}}{h^3} \quad (5.2.23)$$

Substituting this into 5.2.22 we have

$$f''(z) = 2 \int_0^t \left(\frac{\mathbb{V}(t-t')^{-\alpha}}{\Gamma(1-\alpha)} + \frac{\mathbb{G}(t-t')^{-\beta}}{\Gamma(1-\beta)} \right) \cdot \frac{-12\dot{h}}{h(t')^3} dt' \quad (5.2.24)$$

$$= -\frac{24}{u_0^2} \int_0^t \left(\frac{\mathbb{V}(t-t')^{-\alpha}}{\Gamma(1-\alpha)} + \frac{\mathbb{G}(t-t')^{-\beta}}{\Gamma(1-\beta)} \right) \cdot \frac{1}{(h_0/u_0 + t')^3} dt' \quad (5.2.25)$$

$$= -\frac{24}{u_0^2} I_3(t) \quad (5.2.26)$$

$$\Rightarrow f(z) = -\frac{12z^2}{u_0^2} I_3(t) + C_1 z \quad (5.2.27)$$

where $f'(z) = \frac{df(z)}{dz}$. Therefore, from substituting $f(z)$ into 5.2.21, we have

$$p(r, z) = \frac{3r^2}{u_0^2} I_3(t) - \frac{12z^2}{u_0^2} I_3(t) + C_1 z + C(t) \quad (5.2.28)$$

The additional partial derivative in 5.2.22 introduces an extra constant C_1 , which we may find using a suitable boundary condition. We know that τ_{zz} vanishes at the rigid surface of the plates [199]. Furthermore, we know that the pressure field variation in the z direction is symmetric. These two observations give us the boundary condition (a detailed derivation is found in Appendix D)

$$\left. \frac{\partial \tau_{zz}}{\partial z} \right|_{z=h/2} = 0 \quad (5.2.29)$$

Equations 5.2.2, 5.2.27 and 5.2.29 implies

$$C_1 = \frac{12h}{u_0^2} I_3(t) \quad (5.2.30)$$

Substituting this value of C_1 into 5.2.28, we obtain

$$p(r, z) = \frac{3r^2}{u_0^2} I_3(t) + \frac{12z(h-z)}{u_0^2} I_3(t) + C(t) \quad (5.2.31)$$

$C(t)$ can be determined by specifying the stress boundary condition at the disk edge. We use the boundary condition [199–203].

$$\sigma_{zz} = 0 \text{ at } r = R_0, z = 0, h \quad (5.2.32)$$

$$\text{(i.e.) } p = \tau_{zz} \text{ at } r = R_0, z = 0, h \quad (5.2.33)$$

where $\sigma_{zz} = -p + \tau_{zz}$ is the total axial component of the stress. Note that we may use the boundary condition either at $z = 0$ or $z = h$ to arrive at

$$C(t) = -\frac{3R_0^2}{u_0^2} I_3(t) \quad (5.2.34)$$

Substituting $C(t)$ back into 5.2.31 we obtain the pressure field in the deforming filament as

$$p(r, z) = \frac{3(r^2 - R_0^2)}{u_0^2} I_3(t) + \frac{12z(L - z)}{u_0^2} I_3(t) \quad (5.2.35)$$

We can now find the force to be exerted on the plate to balance that arising from the total stress at the midplane

$$F = \int_0^R (-p + \tau_{zz})|_{z=h/2} \cdot 2\pi r \, dr \quad (5.2.36)$$

where $R = R(t)$ is the radius of the mid-plane of the filament as a function of time. To find τ_{zz} , we substitute 5.2.35 into 5.2.2 and solve for τ_{zz} to obtain

$$\tau_{zz} = f(z) = \frac{12z(L - z)}{u_0^2} I_3(t) \quad (5.2.37)$$

Therefore,

$$-p + \tau_{zz} = \frac{3(R_0^2 - r^2)}{u_0^2} I_3(t) \quad (5.2.38)$$

and we have

$$F = \int_0^R \frac{3(R_0^2 - r^2)}{u_0^2} I_3(t) 2\pi r \, dr \quad (5.2.39)$$

$$= \frac{6\pi}{u_0^2} \left(\frac{R_0^2 R^2}{2} - \frac{R^4}{4} \right) I_3(t) \quad (5.2.40)$$

$$= \frac{3\pi R_0^4}{u_0^2} \left[\left(\frac{R}{R_0} \right)^2 - \frac{1}{2} \left(\frac{R}{R_0} \right)^4 \right] I_3(t) \quad (5.2.41)$$

We now use the result of Spiegelberg et al. [198] that relates R and h :

$$\frac{R_0}{R} = \left(\frac{h}{h_0} \right)^{3/4} \quad (5.2.42)$$

$$\Rightarrow \frac{R_0}{R} = \lambda^{3/4} \quad (5.2.43)$$

where the stretch ratio λ is defined as

$$\lambda = \frac{h}{h_0} = \frac{h_0 + u_0 t}{h_0} = 1 + \dot{\epsilon}_0 t \quad (5.2.44)$$

Here $\dot{\epsilon}_0 = u_0/h_0$ is the nominal strain rate applied. Substituting 5.2.43 into 5.2.41 we obtain

$$F = \frac{3\pi R_0^4}{u_0^2} \left(\frac{1}{\lambda^{3/2}} - \frac{1}{2\lambda^3} \right) I_3(t) \quad (5.2.45)$$

We may find the value of $I_3(t)$ by setting $n = 2$ in D.1.12; this results in an incomplete Beta function. Therefore, we ultimately arrive at an analytical expression for the force F applied by the deforming filament on the plate as

$$F = \frac{3\pi R_0^4}{h_0^2} \left(\frac{1}{\lambda^{3/2}} - \frac{1}{2\lambda^3} \right) \left[\frac{\mathbb{V}}{\Gamma(1-\alpha)} \left(\frac{u_0}{h_0} \right)^\alpha \frac{1}{\lambda^{\alpha+2}} \mathcal{B}_{1-1/\lambda}(1-\alpha, -2) + \frac{\mathbb{G}}{\Gamma(1-\beta)} \left(\frac{u_0}{h_0} \right)^\beta \frac{1}{\lambda^{\beta+2}} \mathcal{B}_{1-1/\lambda}(1-\beta, -2) \right] \quad (5.2.46)$$

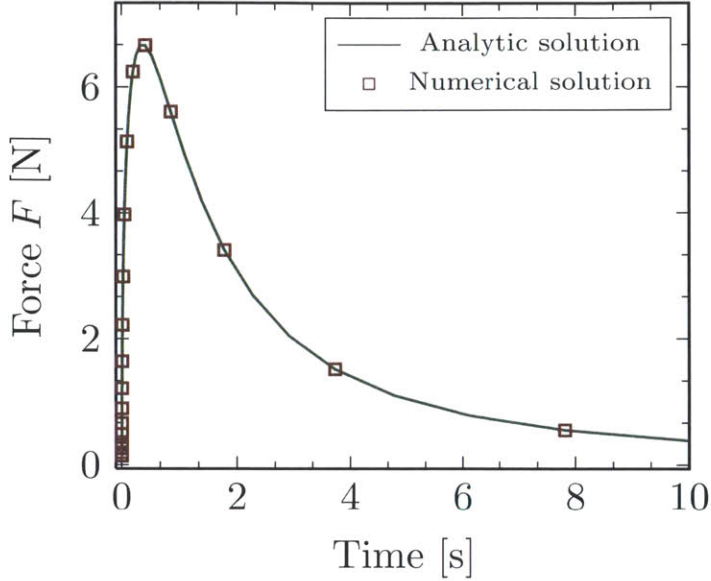
From figure 5.2.1, we see that $\beta = 0$ for our data. Therefore, upon setting $\beta = 0$ in equation 5.2.46, the second term in the brackets simplifies to

$$\frac{\mathbb{G}}{\Gamma(1-\beta)} \left(\frac{u_0}{h_0} \right)^\beta \frac{1}{\lambda^{\beta+2}} \mathcal{B}_{1-1/\lambda}(1-\beta, -2) = \frac{G}{\lambda^2} \mathcal{B}_{1-1/\lambda}(1, -2) \quad (5.2.47)$$

$$= \frac{G}{\lambda^2} \int_0^{1-1/\lambda} v^0 (1-v)^{-3} dv \quad (5.2.48)$$

$$= \frac{G}{\lambda^2} \frac{1}{2} (\lambda^2 - 1) \quad (5.2.49)$$

Substituting the equation above into 5.2.46 we obtain the force expression for the $\beta = 0$

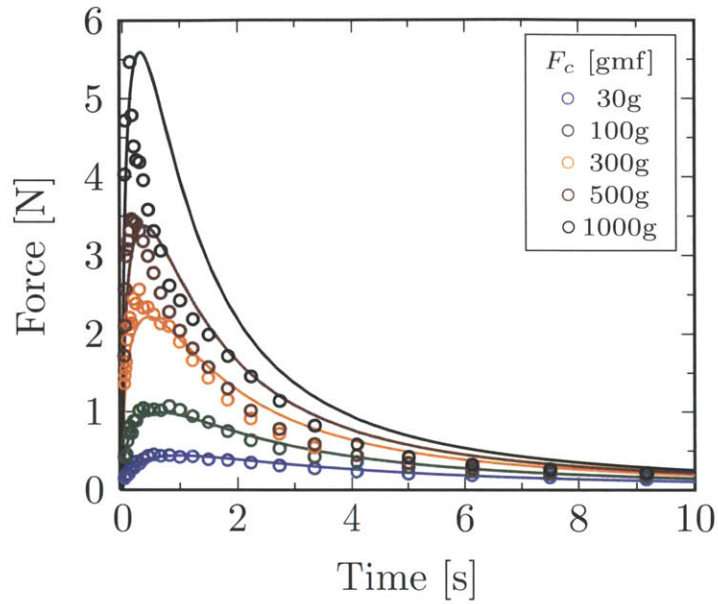
**Figure 5.2.4**

Comparison of the analytically derived solution for the tack force (equation 5.2.50 with a numerical solution obtained from solving $I_3(t)$ in 5.2.45 numerically). The numerical and analytical solutions coincide exactly. $\alpha = 0.59$, $\beta = 0$, $\mathbb{V} = 433.50 \text{ Pa s}^\alpha$, $\mathbb{G} = 108.27 \text{ Pa}$, $R_0 = 4 \text{ mm}$, $h_0 = 0.159 \text{ mm}$, $u_0 = 0.1 \text{ mm s}^{-1}$.

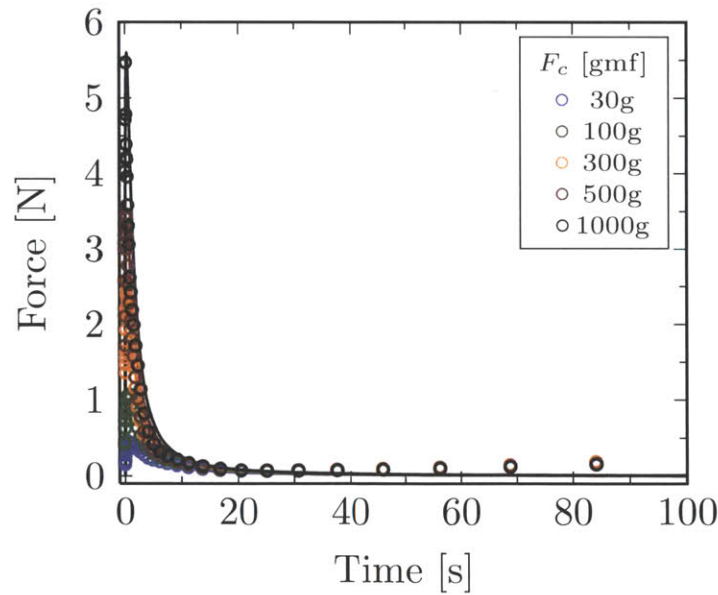
case:

$$F = \frac{3\pi R_0^4}{h_0^2} \left(\frac{1}{\lambda^{3/2}} - \frac{1}{2\lambda^3} \right) \left[\frac{G}{2} \left(1 - \frac{1}{\lambda^2} \right) + \frac{\mathbb{V}}{\Gamma(1-\alpha)} \left(\frac{u_0}{h_0} \right)^\alpha \frac{1}{\lambda^{\alpha+2}} \mathcal{B}_{1-1/\lambda}(1-\alpha, -2) \right] \quad (5.2.50)$$

To check the analytical solution in equation 5.2.50, in figure 5.2.4 we plot the analytical solution (line) against the numerical solution to 5.2.50 (symbols), (i.e.), $I_3(t)$ is numerically determined as a function of time. We observe that the solutions are exactly identical, and our analytical formulation is correct. We now plot 5.2.50 after substituting in the experimental values of R_0 , u_0 and h_0 , and the values of α , \mathbb{V} and G determined from the SAOS experiments. Note that there are no tunable fitting parameters or degrees of freedom in the force prediction. These results are shown in figures 5.2.5a and 5.2.5b respectively. However, we observe that are predictions are more accurate if the value of u_0 used in the force expression is $u_0 = 0.13 \text{ mm/s}$ instead of $u_0 = 0.10 \text{ mm/s}$. We do not capture the non-linear strain hardening implied by the upturn in the force-extension curves at very long times because the fractional Kelvin Voigt model is a linear viscoelastic model which cannot predict strain-hardening. Replacing the Hookean spring term G in our model with a neo-Hookean spring (to capture the strain-hardening resulting from large extensions of the rubbery cross-linked network) will help us to capture even better the full tack response of the material as well as the total work of adhesion measured for these soft gels.



(a) Early times $t \leq 20$ s.



(b) Long times $t > 20$ s.

Figure 5.2.5: Predictions of the tack force based on 5.2.50, with each contact force value represented by a different color. Predictions are lines and measured data are symbols. The value of h_0 for each contact force was obtained from measurements as the value of h when the force on the plate changes sign, and $u_0=0.13$ mm/s.

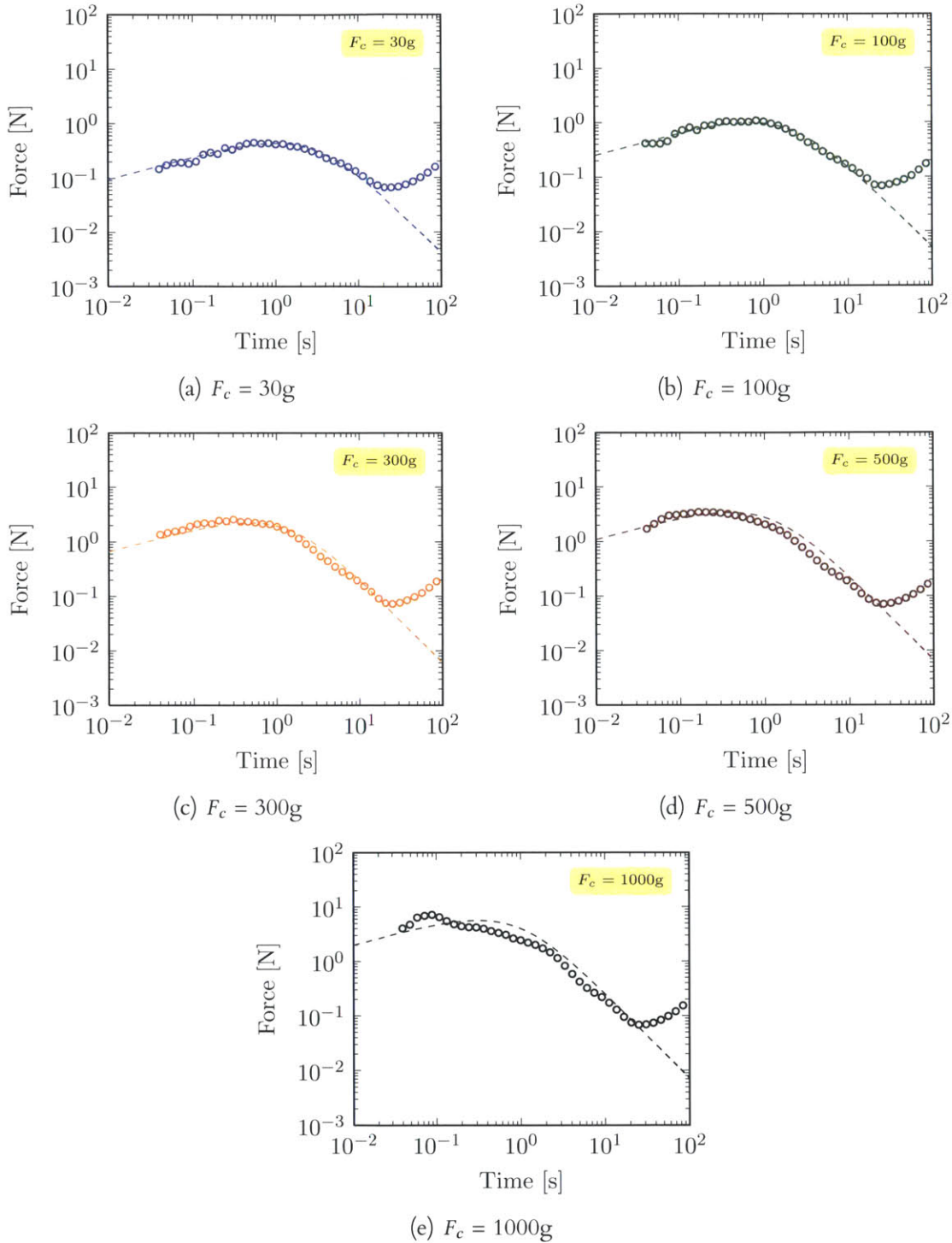


Figure 5.2.6: Prediction of the tack force based on equation 5.2.50. These are the same predictions as shown in the previous figures, but plotted here on a log-log scale to exemplify the goodness of the prediction for short times $t \leq 20$ s and small strains.

Closed form analytical solution through asymptotic analysis.

The analytical expression for the final force given in 5.2.46 readily lends itself to an asymptotic analysis, and it is possible to derive analytical expressions for the early times and long time regimes. We will show using these asymptotes how one may determine the SAOS response of the polymer gels using a tack test.

Early times

For $x \ll 1$, the incomplete beta function $\mathfrak{B}_x(a, b)$ may be approximated as [204]

$$\mathfrak{B}_x(a, b) \approx \frac{x^a}{a} + \dots \quad (5.2.51)$$

Let the stretch ratio $\lambda = 1 + \epsilon + \dots$, $\epsilon \ll 1$. Therefore 5.2.50 now becomes

$$F = \frac{3\pi R_0^4}{h_0^2} \left(\frac{1}{(1+\epsilon)^{3/2}} - \frac{1}{2(1+\epsilon)^3} \right) \times \left[\frac{\mathbb{G}}{\Gamma(1-\beta)} \left(\frac{u_0}{h_0} \right)^\beta \frac{1}{(1+\epsilon)^{\beta+2}} \mathfrak{B}_{1-1/(1+\epsilon)}(1-\beta, -2) + \frac{\mathbb{V}}{\Gamma(1-\alpha)} \left(\frac{u_0}{h_0} \right)^\alpha \frac{1}{(1+\epsilon)^{\alpha+2}} \mathfrak{B}_{1-1/(1+\epsilon)}(1-\alpha, -2) \right] \quad (5.2.52)$$

Using the binomial expansion $(1+\epsilon)^n = 1+n\epsilon$ for $\epsilon \ll 1$, and using the approximation for $\mathfrak{B}_x(a, b)$ given in 5.2.51, the expression for the force simplifies to

$$F = \frac{3\pi R_0^4}{2h_0^2} \left(\frac{\mathbb{G}}{\Gamma(1-\beta)} \left(\frac{u_0}{h_0} \right)^\beta \frac{[1-(\beta+2)\epsilon]\epsilon^{1-\beta}}{1-\beta} + \frac{\mathbb{V}}{\Gamma(1-\alpha)} \left(\frac{u_0}{h_0} \right)^\alpha \frac{[1-(\alpha+2)\epsilon]\epsilon^{1-\alpha}}{1-\alpha} \right) + \mathcal{O}(\epsilon^2) \quad (5.2.53)$$

$$\Rightarrow F \approx \frac{3\pi R_0^4}{2h_0^2} \left[\frac{\mathbb{V}}{\Gamma(1-\alpha)} \left(\frac{u_0}{h_0} \right)^\alpha \frac{\epsilon^{1-\alpha}}{1-\alpha} + \frac{\mathbb{G}}{\Gamma(1-\beta)} \left(\frac{u_0}{h_0} \right)^\beta \frac{\epsilon^{1-\beta}}{1-\beta} \right] \quad (5.2.54)$$

Furthermore, $\lambda = 1 + \frac{u_0}{h_0}t \approx 1 + \epsilon$, and we have $\epsilon = (u_0/h_0)t$. Thus 5.2.54 reduces to

$$\Rightarrow F_e \approx \frac{3\pi R_0^4 \dot{\epsilon}_0}{2h_0^2} \left[\frac{\mathbb{V}}{\Gamma(1-\alpha)} \frac{t^{1-\alpha}}{1-\alpha} + \frac{\mathbb{G}}{\Gamma(1-\beta)} \frac{t^{1-\beta}}{1-\beta} \right] \text{ for } \dot{\epsilon}_0 t \ll 1 \quad (5.2.55)$$

Therefore, with the knowledge of the experimentally imposed values of u_0 and h_0 , and the value of R_0 based on the fixture used for the tack experiment, one may, in principle, fit an equation of the form $F = At^b$ to the early times regime of the force response in a tack test to determine the material quasi-property \mathbb{V} and the power-law exponent α from the fitted co-efficients A and b respectively.

It can be shown that the short time asymptote given in 5.2.55 reduces to the correct Newtonian limit ($\alpha = 1$). To see this, we calculate

$$\lim_{\alpha \rightarrow 1} \frac{3\pi R_0^4}{2h_0^2} \left[\frac{\mathbb{V}}{\Gamma(1-\alpha)} \left(\frac{u_0}{h_0} \right) \frac{t^{1-\alpha}}{1-\alpha} \right] \quad (5.2.56)$$

$$= \lim_{\alpha \rightarrow 1} \frac{3\pi R_0^4}{2h_0^2} \left[\frac{\mathbb{V}}{(1-\alpha)\Gamma(1-\alpha)} \dot{\epsilon}_0 \right] \quad (5.2.57)$$

We know that

$$\lim_{\alpha \rightarrow 1} \frac{1}{(1-\alpha)\Gamma(1-\alpha)} = \lim_{\alpha \rightarrow 1} \frac{1}{\Gamma(2-\alpha)} = 1 \quad (5.2.58)$$

Therefore, we have

$$F_{\text{Newtonian}} \Big|_{\lambda \ll 1} = \frac{3\pi R_0^4}{2h_0^2} \eta \dot{\epsilon}_0 \quad (5.2.59)$$

where the quasi-property \mathbb{V} is nothing but the viscosity η when $\alpha = 1$. This is the correct Newtonian limit for the initial force during a tack test [198].

Long times

We can also determine the long time asymptotic response of the force expression derived in 5.2.46, for the case $\lambda \gg 1$. We first consider 5.2.46 which we write not in terms of the incomplete beta function $\mathcal{B}_x(a, b)$ but in terms of the definite integral (cf. equations 5.2.20

and 5.2.45)

$$F = \frac{3\pi R_0^4}{u_0^2} \left(\frac{1}{\lambda^{3/2}} - \frac{1}{2\lambda^3} \right) \int_0^t \left(\frac{\mathbb{V}(t-t')^{-\alpha}}{\Gamma(1-\alpha)} + \frac{\mathbb{G}(t-t')^{-\beta}}{\Gamma(1-\beta)} \right) \cdot \frac{1}{(h_0/u_0 + t')^3} dt' \quad (5.2.60)$$

We use the notation in the appendix to write this as

$$F = \frac{3\pi R_0^4}{u_0^2} \left(\frac{1}{\lambda^{3/2}} - \frac{1}{2\lambda^3} \right) \left(\frac{\mathbb{V}}{\Gamma(1-\alpha)} I_{n\alpha} + \frac{\mathbb{G}}{\Gamma(1-\beta)} I_{n\beta} \right) \quad (5.2.61)$$

where

$$I_{n\alpha} = \int_0^t \frac{(t-t')^{-\alpha}}{(h_0/u_0 + t')^3} dt' \quad (5.2.62)$$

and $I_{n\beta}$ is determined from $I_{n\alpha}$ using the transformations $\alpha \rightarrow \beta$, $\mathbb{V} \rightarrow \mathbb{G}$. The term $(h_0/u_0 + t')^{-3}$ becomes small for large values of t' and the contribution of the integrand to the total integral becomes smaller as the dummy variable t' increases. Therefore, we expand the term $(t-t')^{-\alpha}$ using a Taylor series and retain only the $\mathcal{O}(t'^0)$ term. This approximation is similar to the Laplace's Method discussed in [205]. We now have $(t-t')^{-\alpha} = t^{-\alpha} + \mathcal{O}(t')$ and $I_{n\alpha}$ simplifies to

$$I_{n\alpha} \approx t^{-\alpha} \int_0^t \frac{dt'}{(h_0/u_0 + t')^3} \quad (5.2.63)$$

$$= \left(\frac{u_0}{h_0} \right)^2 \left(1 - \frac{1}{(1 + \dot{\epsilon}_0 t)^2} \right) \frac{t^{-\alpha}}{2} = \left(\frac{u_0}{h_0} \right)^2 \left(1 - \frac{1}{\lambda^2} \right) \frac{t^{-\alpha}}{2} \quad (5.2.64)$$

where $\lambda = 1 + \dot{\epsilon}_0 t$ is the stretch ratio. In an identical fashion, we obtain

$$I_{n\beta} \approx \left(\frac{u_0}{h_0} \right)^2 \left(1 - \frac{1}{\lambda^2} \right) \frac{t^{-\beta}}{2} \quad (5.2.65)$$

Substituting 5.2.64 and 5.2.65 into 5.2.61, we obtain

$$F = \frac{3\pi R_0^4}{2h_0^2} \left(\frac{1}{\lambda^{3/2}} - \frac{1}{2\lambda^3} \right) \left(\frac{\mathbb{V}}{\Gamma(1-\alpha)} t^{-\alpha} + \frac{\mathbb{G}}{\Gamma(1-\beta)} t^{-\beta} \right) \left(1 - \frac{1}{\lambda^2} \right) \quad (5.2.66)$$

which upon further simplification yields

$$F_l \approx \frac{3\pi R_0^4}{2h_0^2 \lambda^{3/2}} \left(\frac{\mathbb{V} t^{-\alpha}}{\Gamma(1-\alpha)} + \frac{\mathbb{G} t^{-\beta}}{\Gamma(1-\beta)} \right) \text{ for } \lambda \gg 1 \quad (5.2.67)$$

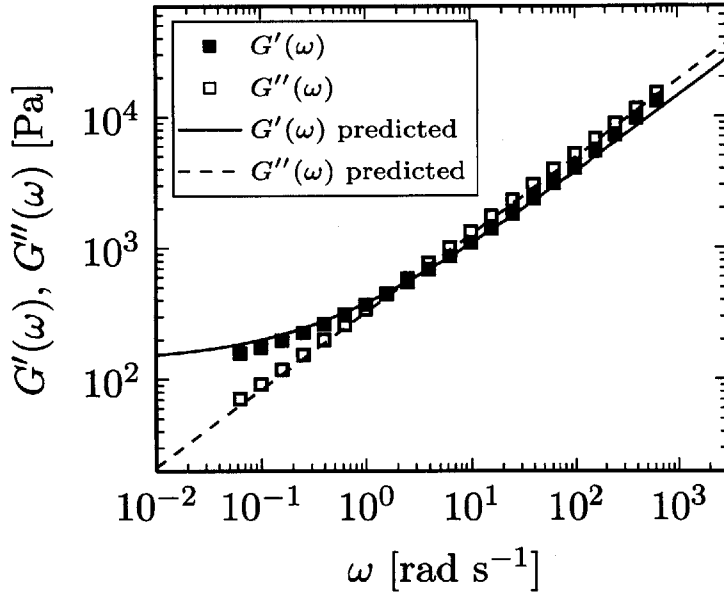
Similar to the early time asymptote case, because we know R_0, u_0 and h_0 , we may determine the material parameter G from the tack test ($\beta = 0$). We note that the ‘long time’ asymptotic analysis only applies to the regime of the experiment where no non-linear strain hardening is present. [206].

We have shown in this subsection that on simply performing a tack test, and subsequently fitting 5.2.55 and 5.2.67 to early times and long times (non-strain hardening regime) we can determine the material parameters α, \mathbb{V} and G that characterize the polymer gel. We can then use these parameters to predict the behavior of the gel to other linear deformations, for example SAOS. We substitute the values of α, \mathbb{V} and G found from the tack response asymptotes into equations 2.3.22 and 2.3.23 to determine $G'(\omega)$ and $G''(\omega)$ respectively. For example, we show in figure 5.2.7 the prediction for the SAOS response (lines) of the polymer gel based on extracting α, \mathbb{V} and G from the tack response under a contact force of $F_c = 300\text{g}$. The measured SAOS response is shown as symbols, and it is seen the prediction quantitatively follows the measured data.

Maximum force location and magnitude

In the preceding two subsections, we have determined the early and long time asymptotes F_e (equation 5.2.55) and F_l (equation 5.2.67) respectively. We now seek to find the location and the magnitude of the peak force in the tack experiment. We will make use of the asymptotes determined above as follows.

We first approximate the analytically derived force F in a tack test (equation 5.2.50) by constructing a composite force F_{comp} that has a similar asymptotic form as the exact analytic


Figure 5.2.7

The prediction of the SAOS response (equations 2.3.22 and 2.3.23) of the low modulus polymer gel based on the values of α , ν and G determined from the short and long time asymptotes of the tack experiment (equations 5.2.55 and 5.2.67).

solution (given by equation 5.2.50):

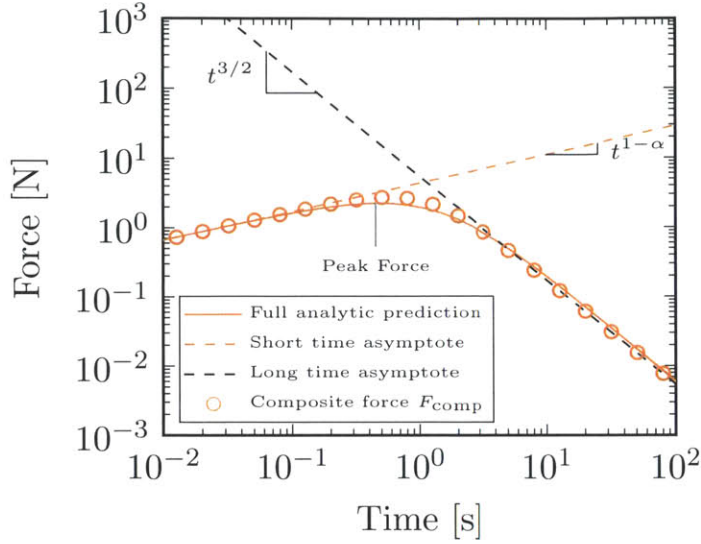
$$\frac{1}{F_{\text{comp}}} = \frac{1}{F_e} + \frac{1}{F_l} \quad (5.2.68)$$

This choice is motivated by the fact that the above equation reduces to the right limits at early and long times, namely, $F_{\text{comp}} = F_e$ and $F_{\text{comp}} = F_l$ for $t/t_p \ll 1$ and $t/t_p \gg 1$ respectively, with t_p being the time at which the maximum force F_p occurs. F_{comp} represents the step responses of the (linearly independent) spring and spring-pot terms as acting in parallel. Substituting 5.2.55 and 5.2.67 into 5.2.68 we get

$$\frac{1}{F_{\text{comp}}} = \frac{(\dot{\epsilon}_0 t)^{3/2}}{\Pi G} + \frac{(1-\alpha)\Gamma(1-\alpha)t^{\alpha-1}}{\Pi \nu \dot{\epsilon}_0} \quad (5.2.69)$$

where $\Pi = 3\pi R_0^4/2h_0^2$ is a constant geometric factor for tack tests, and $\dot{\epsilon}_0 = u_0/h_0$. We now wish to maximize F_{comp} , or equivalently, minimize $1/F_{\text{comp}}$. Therefore, we seek to determine the value of t_p such that

$$\left. \frac{d}{dt} \left(\frac{1}{F_{\text{comp}}} \right) \right|_{t=t_p} = 0 \quad (5.2.70)$$


Figure 5.2.8

Comparison of the composite force F_{comp} given by equation 5.2.69 (symbols) against the full analytic solution given by equation 5.2.50 (solid line). The short and long time asymptotes are represented as dashed lines. The peak force F_p and its temporal location t_p are labeled.

Substituting 5.2.69 in 5.2.70 and evaluating gives

$$\Rightarrow \frac{3}{2} \mathbb{V} \dot{\epsilon}_0^{5/2} t_p^{1/2} = (1 - \alpha)^2 G \Gamma(1 - \alpha) t_p^{\alpha-2} \quad (5.2.71)$$

$$\Rightarrow t_p = \left(\frac{2(1 - \alpha)^2 G \Gamma(1 - \alpha)}{3 \mathbb{V} \dot{\epsilon}_0^{5/2}} \right)^{2/(2-2\alpha)} \quad (5.2.72)$$

Substituting the value of t_p into 5.2.69 and solving for F_{comp} we determine the peak force F_p as

$$F_p = \frac{3 \Pi \mathbb{V} \dot{\epsilon}_0}{(1 - \alpha)(3 - 2\alpha) \Gamma(1 - \alpha)} \left(\frac{2(1 - \alpha)^2 G \Gamma(1 - \alpha)}{3 \mathbb{V} \dot{\epsilon}_0^{5/2}} \right)^{\frac{2(1-\alpha)}{5-2\alpha}} \quad (5.2.73)$$

To aid in understanding the short and long time asymptotes and the resulting composite function, in figure 5.2.8 we compare these quantities to the full analytical solution for the force F in a tack test (equation 5.2.50) performed with a contact force of $F_c = 300\text{g}$. The short and long time asymptotes are shown as red and blue dashed lines respectively. The composite function (symbols) is compared against these asymptotes. Also shown is the full analytical solution obtained from 5.2.50 (orange lines).

In figures 5.2.9a and 5.2.9b, we show the predictions of the peak force (equation 5.2.73)

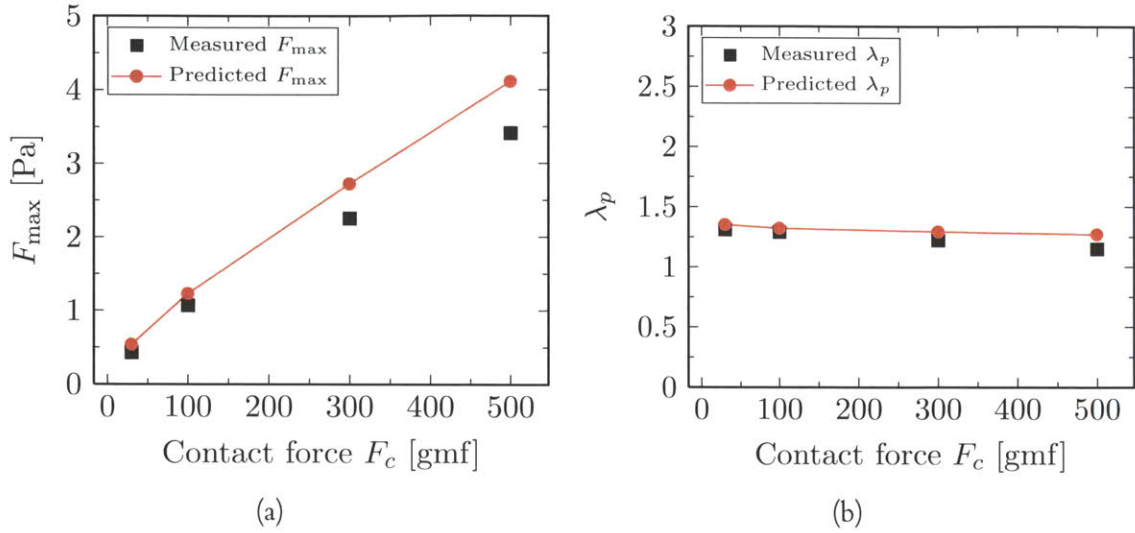


Figure 5.2.9: Prediction of the magnitude (equation 5.2.73) and location of the peak force (equation 5.2.72) as determined by the composite function constructed from the asymptotic analysis. Measured data (■) is for the low modulus gels ($\alpha = 0.59$, $\mathbb{V} = 433.50 \text{ Pa s}^{0.59}$ and $G = 108.27 \text{ Pa}$.) taken from N.B. Wyatt, A.M. Grillet, L.G. Hughes, *Macromolecules*, submitted, 2012.

and the stretch ratio λ_p at which the peak occurs respectively, where $\lambda_p = 1 + \frac{u_0}{h_0} t_p$, with t_p given by equation 5.2.72. It can be seen that the predicted magnitude of the peak force and its location are very close to the experimentally determined values.

In summary, using the framework of the fractional Kelvin-Voigt model, not only can we predict the tack response of the polymeric gel, as shown in figure 5.2.5, but we can also predict the SAOS response of the gel once a tack test has been performed by employing the asymptotic analysis described above. The ability of the framework to describe the rheology of polymer gel and make predictions of the gel response upon the imposition of other linear deformations strongly emphasizes the suitability of the FKVM to model these tacky weakly cross-linked gels.

5.2.3 Determination of the normal force for a constant strain rate applied deformation

In this section, we examine the response of a material characterized by the FKVM described above under the conditions of a displacement imposing a constant strain rate. It is straightforward to prove that such a displacement profile is of the form $h(t) = h_0 e^{\dot{\epsilon}_0 t}$, where $\dot{\epsilon}_0$ is

the nominal strain rate. The lubrication model still holds and equations 5.2.13 and 5.2.14 describe the evolution of stresses in the deforming filament. However, the term $\frac{\partial^2 v_r(t')}{\partial z^2}$ in 5.2.13 is now given by

$$\frac{\partial^2 v_r(t')}{\partial z^2} = \frac{6rh(t')}{h^3(t')} = \frac{\dot{\epsilon}_0 e^{-2\dot{\epsilon}_0 t'}}{h_0^2} \quad (5.2.74)$$

and hence from 5.2.13

$$\frac{\partial p}{\partial r} = 6r \int_0^t \left(\frac{\mathbb{G}(t-t')^{-\beta}}{\Gamma(1-\beta)} + \frac{\mathbb{V}(t-t')^{-\alpha}}{\Gamma(1-\alpha)} \right) \cdot \frac{\dot{\epsilon}_0 e^{-2\dot{\epsilon}_0 t'}}{h_0^2} dt' \quad (5.2.75)$$

$$\Rightarrow \frac{\partial p}{\partial r} = 6r \frac{\dot{\epsilon}_0}{h_0^2} Q(t) \quad (5.2.76)$$

in which

$$Q(t) = \int_0^t \left(\frac{\mathbb{G}(t-t')^{-\beta}}{\Gamma(1-\beta)} + \frac{\mathbb{V}(t-t')^{-\alpha}}{\Gamma(1-\alpha)} \right) \cdot e^{-2\dot{\epsilon}_0 t'} dt' \quad (5.2.77)$$

Note that 5.2.76 and 5.2.20 are of the same form, with $\dot{\epsilon}_0 Q(t)/h_0^2$ in 5.2.76 replacing $I_3(t)/u_0^2$ in 5.2.20. Therefore, the derivation of the final force expression follows an identical sequence of steps as those in equations 5.2.21 to 5.2.45, and the force F exerted by the deforming fractional Kelvin Voigt material under constant strain rate conditions is given by

$$F = \frac{3\pi R_0^4 \dot{\epsilon}_0}{h_0^2} \left(\frac{1}{\lambda^{3/2}} - \frac{1}{2\lambda^3} \right) [Q_\alpha(t) + Q_\beta(t)] \quad (5.2.78)$$

in which

$$Q_\alpha(t) = \frac{\mathbb{V}}{\Gamma(1-\alpha)} \int_0^t (t-t')^{-\alpha} \cdot e^{-2\dot{\epsilon}_0 t'} dt' \quad (5.2.79)$$

and $Q_\beta(t)$ may be found from $Q_\alpha(t)$ by making the transformations $\alpha \rightarrow \beta$ and $\mathbb{V} \rightarrow \mathbb{G}$.

To find an analytic closed-form for $Q_\alpha(t)$, we Laplace transform both sides of equation 5.2.79. This is motivated by the observation that the $Q_\alpha(t)$ is nothing but the con-

volution of the functions $t^{-\alpha}$ and $\exp(-2\dot{\epsilon}_0 t)$. This convolution transforms to a product in Laplace space and therefore we obtain

$$\mathcal{L}[Q_\alpha(t)] = \mathcal{L}[t^{-\alpha}] \times \mathcal{L}[e^{-2\dot{\epsilon}_0 t}] \quad (5.2.80)$$

$$= \frac{\Gamma(1-\alpha)}{s^{1-\alpha}} \cdot \frac{1}{s+2\dot{\epsilon}_0} \quad (5.2.81)$$

$$= \Gamma(1-\alpha) \cdot \frac{s^{\alpha-1}}{s+2\dot{\epsilon}_0} \quad (5.2.82)$$

Note that we have used the identity $\mathcal{L}[t^\alpha] = \Gamma(\alpha+1)/s^{\alpha+1}$. We know that [82]

$$\mathcal{L}^{-1} \left[\frac{k!s^{a-b}}{(s+\mu)^k} \right] = t^{ak+b-1} E_{a,b}^{(k)}(-\mu t^a) \quad (5.2.83)$$

where $E_{a,b}(t)$ is the Mittag-Leffler function defined as [82]

$$E_{a,b}(z) = \sum_{k=0}^{\infty} \frac{z^k}{\Gamma(ak+b)} \quad (5.2.84)$$

in which $\Gamma(x)$ is the Gamma function defined in the usual manner [25], and the notation (k) denotes the derivative to the k -th order. Inspecting 5.2.82 and 5.2.83 simultaneously, we set in 5.2.83 $a \rightarrow 1$, $b \rightarrow 2-\alpha$, $\mu \rightarrow 2\dot{\epsilon}_0$ and $k = 0$ to obtain

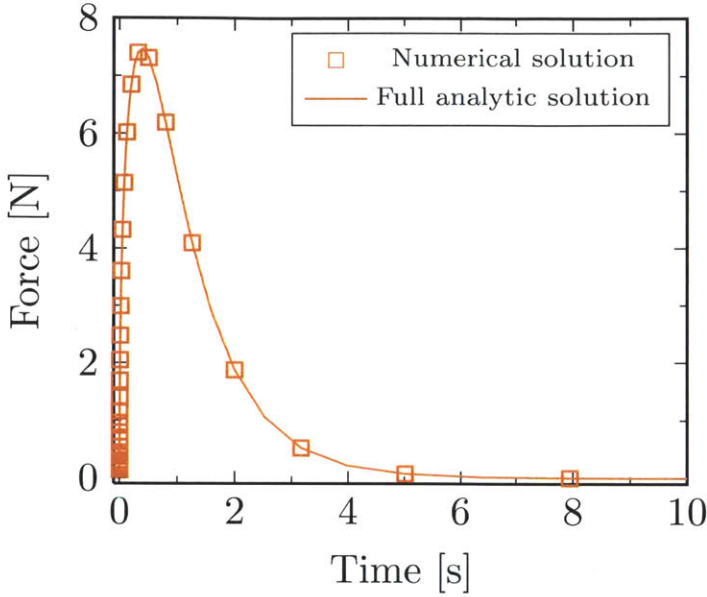
$$\mathcal{L}^{-1} \left[\Gamma(1-\alpha) \frac{s^{\alpha-1}}{s+2\dot{\epsilon}_0} \right] = \Gamma(1-\alpha) t^{1-\alpha} E_{1,2-\alpha}(-2\dot{\epsilon}_0 t) \quad (5.2.85)$$

and hence we have

$$Q_\alpha(t) = \mathbb{V} t^{1-\alpha} E_{1,2-\alpha}(-2\dot{\epsilon}_0 t) \quad (5.2.86)$$

and similarly

$$Q_\beta(t) = \mathbb{G} t^{1-\beta} E_{1,2-\beta}(-2\dot{\epsilon}_0 t) \quad (5.2.87)$$


Figure 5.2.10

Comparison of the analytically derived solution for the tack force (equation 5.2.88) and the solution from solving $Q(t)$ (cf. 5.2.78 and 5.2.79) numerically. It is observed that the analytical and numerical solutions coincide exactly. $\alpha = 0.59$, $\mathbb{V} = 433.50 \text{ Pa s}^{0.59}$, $G = 108.27 \text{ Pa}$, $R_0 = 4 \text{ mm}$, $u_0 = 0.1 \text{ mm/s}$ and $h_0 = 0.159 \text{ mm}$.

Substituting 5.2.86 and 5.2.87 into 5.2.78, we finally obtain

$$F = \frac{3\pi R_0^4 \dot{\epsilon}_0}{h_0^2} \left(\frac{1}{\lambda^{3/2}} - \frac{1}{2\lambda^3} \right) \left[\mathbb{G}t^{1-\beta} E_{1,2-\beta}(-2\dot{\epsilon}_0 t) + \mathbb{V}t^{1-\alpha} E_{1,2-\alpha}(-2\dot{\epsilon}_0 t) \right] \quad (5.2.88)$$

For the viscoelastic materials of interest in this study, we have $\beta = 0$; we therefore substitute $\beta = 0$ in equation 5.2.88 and we have

$$F = \frac{3\pi R_0^4 \dot{\epsilon}_0}{h_0^2} \left(\frac{1}{\lambda^{3/2}} - \frac{1}{2\lambda^3} \right) \left[Gt^1 E_{1,2}(-2\dot{\epsilon}_0 t) + \mathbb{V}t^{1-\alpha} E_{1,2-\alpha}(-2\dot{\epsilon}_0 t) \right] \quad (5.2.89)$$

$$= \frac{3\pi R_0^4 \dot{\epsilon}_0}{h_0^2} \left(\frac{1}{\lambda^{3/2}} - \frac{1}{2\lambda^3} \right) \left[\frac{G}{2\dot{\epsilon}_0} (1 - e^{-2\dot{\epsilon}_0 t}) + \mathbb{V}t^{1-\alpha} E_{1,2-\alpha}(-2\dot{\epsilon}_0 t) \right] \quad (5.2.90)$$

In figure 5.2.10 we compare the analytical solution 5.2.88 to the solution arrived at by solving equation 5.2.78 numerically ((i.e) we solve $Q(t)$ numerically). It can be seen that the analytical solution coincides exactly with the numerical solution.

Closed-form analytic solution through the analysis of asymptotes

We first examine the short time asymptote of equation 5.2.88. In this limit, $e^{2\dot{\epsilon}_0 t'} \approx 1$ in $Q_\alpha(t)$ (cf. equation 5.2.79) and therefore we have

$$Q_\alpha(t) \approx \frac{\mathbb{V}}{\Gamma(1-\alpha)} \int_0^t (t-t')^{-\alpha} dt' \quad (5.2.91)$$

$$\Rightarrow Q_\alpha(t) \approx \frac{\mathbb{V}}{\Gamma(1-\alpha)} \frac{t^{1-\alpha}}{1-\alpha} \quad (5.2.92)$$

and

$$Q_\beta(t) \approx \frac{\mathbb{G}}{\Gamma(1-\beta)} \frac{t^{1-\beta}}{1-\beta} \quad (5.2.93)$$

Substituting this expression for the early time approximation for $Q_\alpha(t)$ and $Q_\beta(t)$ into equation 5.2.78 we obtain

$$F_e(t) = \frac{3\pi R_0^4 \dot{\epsilon}_0}{h_0^2} \left(\frac{1}{\lambda^{3/2}} - \frac{1}{2\lambda^3} \right) \left[\frac{\mathbb{G}}{\Gamma(1-\beta)} \frac{t^{1-\beta}}{1-\beta} + \frac{\mathbb{V}}{\Gamma(1-\alpha)} \frac{t^{1-\alpha}}{1-\alpha} \right] \quad (5.2.94)$$

We also show in section 5.2.2 that $(\lambda^{-3/2} - (1/2)\lambda^{-3}) \approx 1/2$ for early times. Therefore the expression for the early time asymptote for the tack force $F_e(t)$ exerted by a fractional Kelvin-Voigt material under a constant strain rate displacement is given by

$$F_e(t) = \frac{3\pi R_0^4 \dot{\epsilon}_0}{2h_0^2} \left(\frac{\mathbb{V}}{\Gamma(1-\alpha)} \frac{t^{1-\alpha}}{1-\alpha} + \frac{\mathbb{G}}{\Gamma(1-\beta)} \frac{t^{1-\beta}}{1-\beta} \right) \text{ for } \dot{\epsilon}_0 t \ll 1 \quad (5.2.95)$$

Note that this asymptote for the tack force at early times is exactly identical to the asymptote obtained for the constant velocity displacement introduced earlier. This is not surprising because at early times $h_0 \exp(\dot{\epsilon}_0 t) \approx h_0(1 + \dot{\epsilon}_0 t)$, with $\dot{\epsilon}_0 = u_0/h_0$. Therefore, the applied deformation profiles are identical.

We now derive the asymptote for the tack force at long times. Consider again equation 5.2.88. We show in the appendix that at long times,

$$\mathbb{V} t^{1-\alpha} E_{1,2-\alpha}(-2\dot{\epsilon}_0 t) \approx \frac{1}{2\dot{\epsilon}_0} \frac{\mathbb{V} t^{-\alpha}}{\Gamma(1-\alpha)} \quad (5.2.96)$$

and hence—in this limit— equation 5.2.88 reduces to

$$F_l = \frac{3\pi R_0^4}{h_0^2} \dot{\epsilon}_0 \left(\frac{1}{\lambda^{3/2}} - \frac{1}{2\lambda^3} \right) \left[\frac{1}{2\dot{\epsilon}_0} \frac{\mathbb{V}t^{-\alpha}}{\Gamma(1-\alpha)} + \frac{1}{2\dot{\epsilon}_0} \frac{\mathbb{G}t^{-\beta}}{\Gamma(1-\beta)} \right] \quad (5.2.97)$$

Which upon simplification yields

$$F_l = \frac{3\pi R_0^4}{2h_0^2} \left(\frac{1}{\lambda^{3/2}} - \frac{1}{2\lambda^3} \right) \left[\frac{\mathbb{V}t^{-\alpha}}{\Gamma(1-\alpha)} + \frac{\mathbb{G}t^{-\beta}}{\Gamma(1-\beta)} \right] \quad (5.2.98)$$

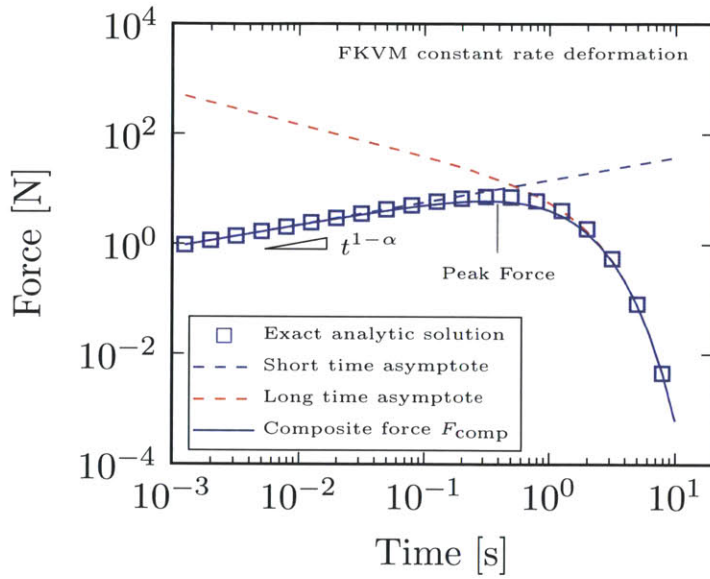
In our case, we have $\beta = 0$. We also observe that at long times $\lambda^{-3/2} - (1/2)\lambda^{-3} \approx \lambda^{-3/2} = \exp[-(3/2)\dot{\epsilon}_0 t]$. Therefore we obtain for the tack force F_l exerted by a fractional Kelvin-Voigt material undergoing a constant strain rate deformation (with $\beta = 0$)

$$F_l = \frac{3\pi R_0^4}{2h_0^2} e^{-(3/2)\dot{\epsilon}_0 t} \left(G + \frac{\mathbb{V}}{\Gamma(1-\alpha)} t^{-\alpha} \right) \text{ for } \dot{\epsilon}_0 t \gg 1 \quad (5.2.99)$$

As before, we may substitute 5.2.95 and 5.2.99 into 5.2.68 to arrive at an analytic closed-form approximate solution for the tack force, whose expression does not contain the Mittag-Leffler function. Making these substitutions, and after some algebra we get

$$F_c = \frac{3\pi R_0^4}{2h_0^2} \frac{\mathbb{V}}{\Gamma(1-\alpha)} \left(\frac{\dot{\epsilon}_0 t^{1-\alpha} [\mathbb{G}\Gamma(1-\alpha) + \mathbb{V}t^{-\alpha}]}{(1-\alpha) [\mathbb{G}\Gamma(1-\alpha) + \mathbb{V}t^{-\alpha}] + e^{(3/2)\dot{\epsilon}_0 t} \dot{\epsilon}_0 \mathbb{V}t^{1-\alpha}} \right) \quad (5.2.100)$$

We now compare in figure 5.2.11 the exact analytical solution for the tack force (equation 5.2.88) with the approximate composite force expression derived above (equation 5.2.100). It can be seen that the composite force obtained from the asymptotic analysis is a very good approximate to the exact analytical solution.


Figure 5.2.11

The composite force obtained from equation 5.2.100 (solid line) compared against the exact analytic solution for the force derived in equation 5.2.88 (symbols). Also shown are the short time (blue dashed line) and long time asymptotes (red dashed line) determined by equations 5.2.95 and 5.2.99 respectively. The composite force is seen to approximate the exact analytic solution excellently. $\alpha = 0.59$, $\mathbb{V} = 433.50 \text{ Pa s}^{0.59}$, $G = 108.27 \text{ Pa}$, $R_0 = 4 \text{ mm}$, $u_0 = 0.1 \text{ mm/s}$ and $h_0 = 0.159 \text{ mm}$.

5.3 The Fractional Maxwell Model

5.3.1 Determination of the normal force for a constant strain rate applied deformation

Consider the rearranged form of the Laplace transform of the constitutive equation 2.3.1

$$\tilde{\tau}(s) = \frac{\mathbb{V}s^{\alpha-1}\tilde{\dot{\gamma}}_{zr}}{1 + \frac{\mathbb{V}}{G}s^{\alpha-\beta}} \quad (5.3.1)$$

Coupling 5.3.1 with the Laplace transform of 5.2.2 have

$$\begin{aligned} \mathcal{L}\left[\frac{\partial p}{\partial r}\right] &= \frac{\partial}{\partial z}\mathcal{L}[\tau_{zr}] \\ &= \frac{\mathbb{V}s^{\alpha-1}}{1 + \frac{\mathbb{V}}{G}s^{\alpha-\beta}} \cdot \frac{\partial}{\partial z}\tilde{\dot{\gamma}}_{zr} \end{aligned} \quad (5.3.2)$$

and upon taking the inverse Laplace transform and invoking the fact that $\dot{\gamma}_{zr} = \frac{\partial v_r}{\partial z}$ we finally arrive at

$$\frac{\partial p}{\partial r} = \mathcal{L}^{-1} \left[\frac{\mathbb{V}s^{\alpha-1}}{1 + \frac{\mathbb{V}}{\mathbb{G}}s^{\alpha-\beta}} \right] * \frac{\partial^2 v_r}{\partial z^2} \quad (5.3.3)$$

in which the symbol $*$ stands for Laplace convolution as before, defined as

$$f(t) * g(t) = \int_0^t f(t-t')g(t') dt' = \int_0^t f(t')g(t-t') dt' \quad (5.3.4)$$

where $f(t)$ and $g(t)$ are arbitrary functions. It is trivially demonstrated by substituting $\gamma(t) = \gamma_0 H(t)$ (with $H(t)$ denoting the Heaviside step function) in the constitutive equation 2.3.1 that the term in brackets in 5.3.3 is nothing but the Laplace transform of the relaxation modulus $G(t)$ for the fractional Maxwell model. Therefore, we write out the convolution integral explicitly after substituting 2.3.3 into 5.3.3 to obtain

$$\frac{\partial p}{\partial r} = \int_0^t \mathbb{G}(t-t')^{-\beta} E_{\alpha-\beta, 1-\beta} \left(-\frac{\mathbb{G}}{\mathbb{V}}(t-t')^{\alpha-\beta} \right) \cdot \frac{\partial^2 v_r(t')}{\partial z^2} dt'. \quad (5.3.5)$$

We know from 5.2.17 that

$$\frac{\partial^2 v_r(t')}{\partial z^2} = \frac{6r\dot{h}(t')}{h^3(t')}. \quad (5.3.6)$$

Therefore, we have

$$\frac{\partial p}{\partial r} = 6r\mathbb{G}J(t) \quad (5.3.7)$$

where

$$J(t) = \int_0^t (t-t')^{-\beta} E_{\alpha-\beta, 1-\beta} \left(-\frac{\mathbb{G}}{\mathbb{V}}(t-t')^{\alpha-\beta} \right) \frac{\dot{h}(t')}{h^3(t')} dt' \quad (5.3.8)$$

Integrating 5.3.7 with respect to r we obtain

$$p(r, z) = 3r^2 J(t) + f(z) + C(t) \quad (5.3.9)$$

To find $f(z)$, we follow an identical procedure as presented for the FKVM and we arrive at (cf. equations 5.2.21 - 5.2.31)

$$p(r, z) = 3r^2 \mathbb{G} J(t) + 12\mathbb{G} J(t) z(h - z) + C(t). \quad (5.3.10)$$

We apply the same boundary condition as in the FKVM case and $C(t)$ is determined to be (cf. equation 5.2.33)

$$C(t) = -3R_0^2 \mathbb{G} J(t) \quad (5.3.11)$$

and we finally have for the pressure $p(r, z)$ on the plate

$$p(r, z) = 3(r^2 - R_0^2) \mathbb{G} J(t) + 12\mathbb{G} J(t) z(h - z) \quad (5.3.12)$$

and integrating as before the total stress $-p + \tau_{zz}$ at the mid-plane over the entire area of the mid-plane filament we arrive at the total force on the plate during a tack test for the fractional Maxwell model

$$F = 3\pi R_0^4 \mathbb{G} \left(\frac{1}{\lambda^{3/2}} - \frac{1}{2\lambda^3} \right) J(t) \quad (5.3.13)$$

To determine the full expression for the force, we will need to calculate the integral $J(t)$. An examination of its definition in 5.3.8 informs us that we need to know the exact displacement profile applied during the tack test to determine $J(t)$. In what follows, we will examine two cases: (1) constant strain rate displacement, and (2) constant velocity displacement.

To achieve a constant strain rate we apply a displacement profile of the form $h(t) =$

$h_0 \exp[\dot{\epsilon}_0 t]$. Therefore, $J(t)$ now becomes

$$J(t) = \int_0^t (t-t')^{-\beta} E_{\alpha-\beta,1-\beta} \left(-\frac{\mathbb{G}}{\mathbb{V}} (t-t')^{\alpha-\beta} \right) \frac{\dot{h}(t')}{h^3(t')} dt' \quad (5.3.14)$$

$$= \int_0^t (t-t')^{-\beta} E_{\alpha-\beta,1-\beta} \left(-\frac{\mathbb{G}}{\mathbb{V}} (t-t')^{\alpha-\beta} \right) \frac{h_0 \dot{\epsilon}_0 e^{\dot{\epsilon}_0 t'}}{h_0^3 e^{3\dot{\epsilon}_0 t'}} dt' \quad (5.3.15)$$

$$\Rightarrow J(t) = \frac{\dot{\epsilon}_0}{h_0^2} \int_0^t (t-t')^{-\beta} E_{\alpha-\beta,1-\beta} \left(-\frac{\mathbb{G}}{\mathbb{V}} (t-t')^{\alpha-\beta} \right) e^{-2\dot{\epsilon}_0 t'} dt' \quad (5.3.16)$$

An exact closed-form analytic solution to this integral 5.3.16 is not readily available and we seek to find an approximate analytic solution. Consider

$$j_1(t') = \left[(t-t')^{-\beta} E_{\alpha-\beta,1-\beta} \left(-\frac{\mathbb{G}}{\mathbb{V}} (t-t')^{\alpha-\beta} \right) \right] e^{-2\dot{\epsilon}_0 t'} \quad (5.3.17)$$

$$= j_2(t') e^{-2\dot{\epsilon}_0 t'} \quad (5.3.18)$$

in which

$$j_2(t') = (t-t')^{-\beta} E_{\alpha-\beta,1-\beta} \left(-\frac{\mathbb{G}}{\mathbb{V}} (t-t')^{\alpha-\beta} \right) \quad (5.3.19)$$

The contribution of the integrand to the total integral is negligible for large enough values of the dummy variable t' , because the $\exp[-2\dot{\epsilon}_0 t']$ term becomes very small. Observing that the dominant contribution to the integral comes from around the point $t' = 0$, we expand $j_2(t')$ using its Taylor series to obtain

$$j_2(t') = j_2(0) + \mathcal{O}(t) \quad (5.3.20)$$

Thus we have

$$j_2(t') \approx t^{-\beta} E_{\alpha-\beta,1-\beta} \left(-\frac{\mathbb{G}}{\mathbb{V}} t^{\alpha-\beta} \right) \quad (5.3.21)$$

Substituting this result into 5.3.16 we obtain

$$J_1(t) = \frac{\dot{\epsilon}_0}{h_0^2} t^{-\beta} E_{\alpha-\beta, 1-\beta} \left(-\frac{\mathbb{G}}{\mathbb{V}} t^{\alpha-\beta} \right) \int_0^t e^{-2\dot{\epsilon}_0 t'} dt' \quad (5.3.22)$$

$$= \frac{1}{2h_0^2} t^{-\beta} E_{\alpha-\beta, 1-\beta} \left(-\frac{\mathbb{G}}{\mathbb{V}} t^{\alpha-\beta} \right) (1 - e^{-2\dot{\epsilon}_0 t}) \quad (5.3.23)$$

We now replace $J(t)$ with $J_1(t)$ in 5.3.13 to obtain

$$F = 3\pi R_0^4 \mathbb{G} \left(\frac{1}{\lambda^{3/2}} - \frac{1}{2\lambda^3} \right) J_1(t) \quad (5.3.24)$$

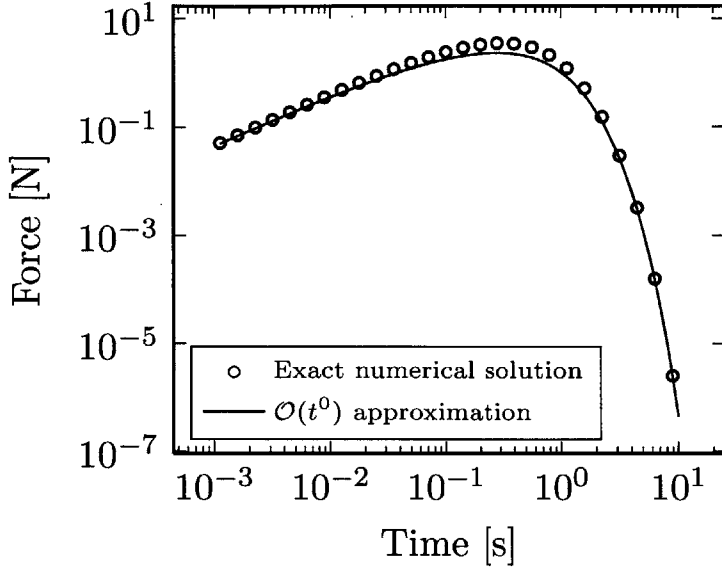
$$\Rightarrow F = \frac{3\pi R_0^4 \mathbb{G}}{2h_0^2} \left(\frac{1}{\lambda^{3/2}} - \frac{1}{2\lambda^3} \right) t^{-\beta} E_{\alpha-\beta, 1-\beta} \left(-\frac{\mathbb{G}}{\mathbb{V}} t^{\alpha-\beta} \right) (1 - e^{-2\dot{\epsilon}_0 t}) \quad (5.3.25)$$

In figure 5.3.1, we show the exact numerical solution for the force (equation 5.3.13) which we obtain by solving $J(t)$ (given by equation 5.3.16) numerically at select instances of time (symbols). We compare this numerical solution to the approximate analytical solution derived in equation 5.3.25, obtained by retaining only $\mathcal{O}(t^0)$ terms. For the purposes of illustration, we choose $\alpha = 0.59, \beta = 0, \mathbb{V} = 100 \text{ Pa s}^\alpha$ and $\mathbb{G} = 400 \text{ Pa}$. It can be seen that the approximate agrees very well with the exact solution involving the Mittag-Leffler function; we hence achieve a good compromise between accuracy and simplicity through the use of this method. Even better approximations could be achieved if $\mathcal{O}(t')$ and higher terms are retained in the Taylor series.

Closed-form analytic solution through the analysis of asymptotes

We first seek to derive the early time asymptote for the force. Consider again 5.3.16

$$J(t) = \frac{\dot{\epsilon}_0}{h_0^2} \int_0^t (t-t')^{-\beta} E_{\alpha-\beta, 1-\beta} \left(-\frac{\mathbb{G}}{\mathbb{V}} (t-t')^{\alpha-\beta} \right) e^{-2\dot{\epsilon}_0 t'} dt' \quad (5.3.26)$$


Figure 5.3.1

Comparison of the numerically determined value of the force given by equations 5.3.13 and 5.3.16 (symbols) against the approximate analytical solution given by equation 5.3.25 (line). The parameters were chosen to be $\alpha = 0.59$, $\beta = 0$, $\mathbb{V} = 100 \text{ Pa s}^\alpha$ and $\mathbb{G} = 400 \text{ Pa}$. For the purposes of illustration, $R_0 = 4 \text{ mm}$, $u_0 = 0.1 \text{ mm/s}$ and $h_0 = 0.1 \text{ mm}$.

Setting $t - t' = u$ we have

$$J_1(t) = \frac{\dot{\epsilon}_0}{h_0^2} e^{-2\dot{\epsilon}_0 t} \int_0^t u^{-\beta} E_{\alpha-\beta, 1-\beta} \left(-\frac{\mathbb{G}}{\mathbb{V}} (t-t')^{\alpha-\beta} \right) e^{2\dot{\epsilon}_0 u} du \quad (5.3.27)$$

For small t (and hence small u), from equation 5.2.84

$$E_{\alpha-\beta, 1-\beta} \left(-\frac{\mathbb{G}}{\mathbb{V}} (t-t')^{\alpha-\beta} \right) = \frac{1}{\Gamma(1-\beta)} + \mathcal{O} \left((t-t')^{\alpha-\beta} \right) \quad (5.3.28)$$

and hence the integral above can be simplified as

$$J_1(t) \approx \frac{\dot{\epsilon}_0}{h_0^2} e^{-2\dot{\epsilon}_0 t} \frac{1}{\Gamma(1-\beta)} \int_0^t u^{-\beta} e^{2\dot{\epsilon}_0 u} du \quad (5.3.29)$$

Furthermore, we observe that $\exp[2\dot{\epsilon}_0 u] \approx 1$ for small values of t . Therefore, we find that at early times

$$J_1(t) \Big|_e = \frac{\dot{\epsilon}_0}{h_0^2} \frac{1}{\Gamma(1-\beta)} \frac{t^{1-\beta}}{1-\beta} \quad (5.3.30)$$

and the expression for the force at early times reduces to

$$F_e = 3\pi R_0^4 \left(\frac{1}{\lambda^{3/2}} - \frac{1}{2\lambda^3} \right) \frac{\dot{\epsilon}_0}{h_0^2} \frac{\mathbb{G}}{\Gamma(1-\beta)} \frac{t^{1-\beta}}{1-\beta} \quad (5.3.31)$$

We show in section 5.2.2 that $\frac{1}{\lambda^{3/2}} - \frac{1}{2\lambda^3} \rightarrow 1/2$ as $\lambda \rightarrow 1$. This simplification gives us the final expression for the early time asymptote for the force in a tack test of a fractional Maxwell material undergoing constant rate deformation as

$$F_e = \frac{3\pi R_0^4 \dot{\epsilon}_0}{2h_0^2} \frac{\mathbb{G}}{\Gamma(1-\beta)} \frac{t^{1-\beta}}{1-\beta} \text{ for } \dot{\epsilon}_0 t \ll 1 \quad (5.3.32)$$

We now seek to find the expression for the long time asymptote of the force. We begin with $J_1(t)$ reproduced here for clarity (cf. equation 5.3.23):

$$J_1(t) = \frac{1}{2h_0^2} t^{-\beta} E_{\alpha-\beta, 1-\beta} \left(-\frac{\mathbb{G}}{\mathbb{V}} t^{\alpha-\beta} \right) (1 - e^{-2\dot{\epsilon}_0 t}) \quad (5.3.33)$$

In the Appendix, it is proved that for long times

$$t^{-\beta} E_{\alpha-\beta, 1-\beta} \left(-\frac{\mathbb{G}}{\mathbb{V}} t^{\alpha-\beta} \right) \approx \frac{\mathbb{V}}{\mathbb{G}} \frac{t^{-\alpha}}{\Gamma(1-\alpha)} \quad (5.3.34)$$

Therefore,

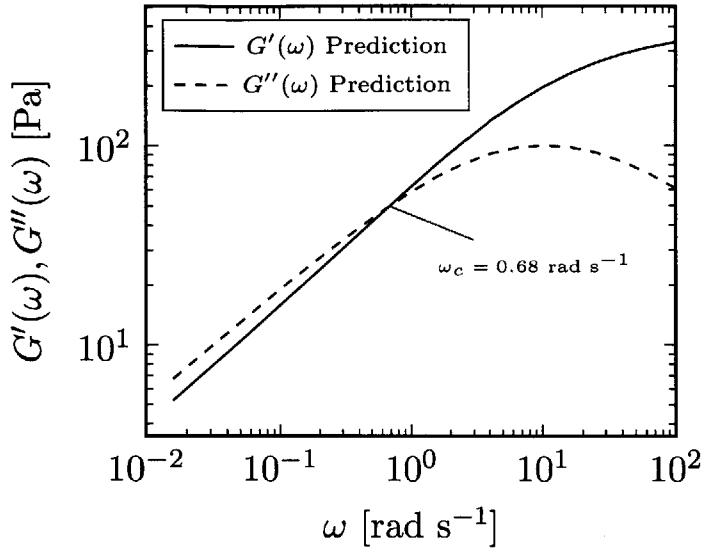
$$\Rightarrow J_1(t) \Big|_l = \frac{1}{2h_0^2} \frac{\mathbb{V}}{\mathbb{G}} \frac{t^{-\alpha}}{\Gamma(1-\alpha)} (1 - e^{-2\dot{\epsilon}_0 t}) \quad (5.3.35)$$

Consequently, the force at long times is given by

$$F_l \approx \frac{3\pi R_0^4}{2h_0^2} \left(\frac{1}{\lambda^{3/2}} - \frac{1}{2\lambda^3} \right) \frac{\mathbb{V} t^{-\alpha}}{\Gamma(1-\alpha)} (1 - \lambda^{-2}) \quad (5.3.36)$$

where $\lambda = \exp(\dot{\epsilon}_0 t)$.

As before, one may determine the model parameters $\alpha, \beta, \mathbb{V}$ and \mathbb{G} by fitting a power law equation of the form $F = At^b$ to the short and long time asymptotes respectively; the short time asymptote yields the values of β and \mathbb{G} , while the long time asymptote yields the values of α and \mathbb{V} . These parameters can then be substituted into equations 2.3.15


Figure 5.3.2

An example of predicting the SAOS response of a fractional Maxwell-like viscoelastic material from the asymptotic analysis of a tack experiment performed on the material. Here, the values of the parameters used are $\alpha = 0.59$, $\beta = 0$, $\mathbb{V} = 100 \text{ Pa s}^\alpha$, $\mathbb{G} = 400 \text{ Pa}$. For the purposes of illustration, $R_0 = 4 \text{ mm}$, $u_0 = 0.1 \text{ mm s}^{-1}$ and $h_0 = 0.1 \text{ mm}$.

and 2.3.16 to find $G'(\omega)$ and $G''(\omega)$ respectively. In this manner we can make a prediction of the SAOS response of the material purely from the analysis of a tack experiment. We present an example of such a prediction in figure 5.3.2.

The composite force F_{comp} is defined by 5.2.68 and we have from equations 5.3.32 and 5.3.36

$$\frac{1}{F_{\text{comp}}} = \frac{2h_0^2}{3\pi R_0^4} \left[\frac{\Gamma(2-\beta)}{\dot{\epsilon}_0 t^{1-\beta} \mathbb{G} t^{1-\beta}} + \frac{\lambda^{3/2} \Gamma(1-\alpha) t^{-\alpha}}{\mathbb{V}} \right] \quad (5.3.37)$$

and upon some algebra and simplification we obtain

$$F_{\text{comp}} = \frac{3\pi R_0^4}{2h_0^2} \left[\frac{\dot{\epsilon}_0 t^{1-\beta}}{\frac{1}{\mathbb{G}} \Gamma(2-\beta) + \frac{1}{\mathbb{V}} \lambda^{3/2} \dot{\epsilon}_0 \Gamma(1-\alpha) t^{\alpha-\beta+1}} \right] \quad (5.3.38)$$

In figure 5.3.3 we plot the exact value of the tack force $F(t)$ as symbols—determined by numerically solving 5.3.13—and compare it to F_{comp} constructed in equation 5.3.38. The individual short and long time asymptotes are shown as dashed lines. It is observed that F_{comp} very closely approximates the exact numerical solution.

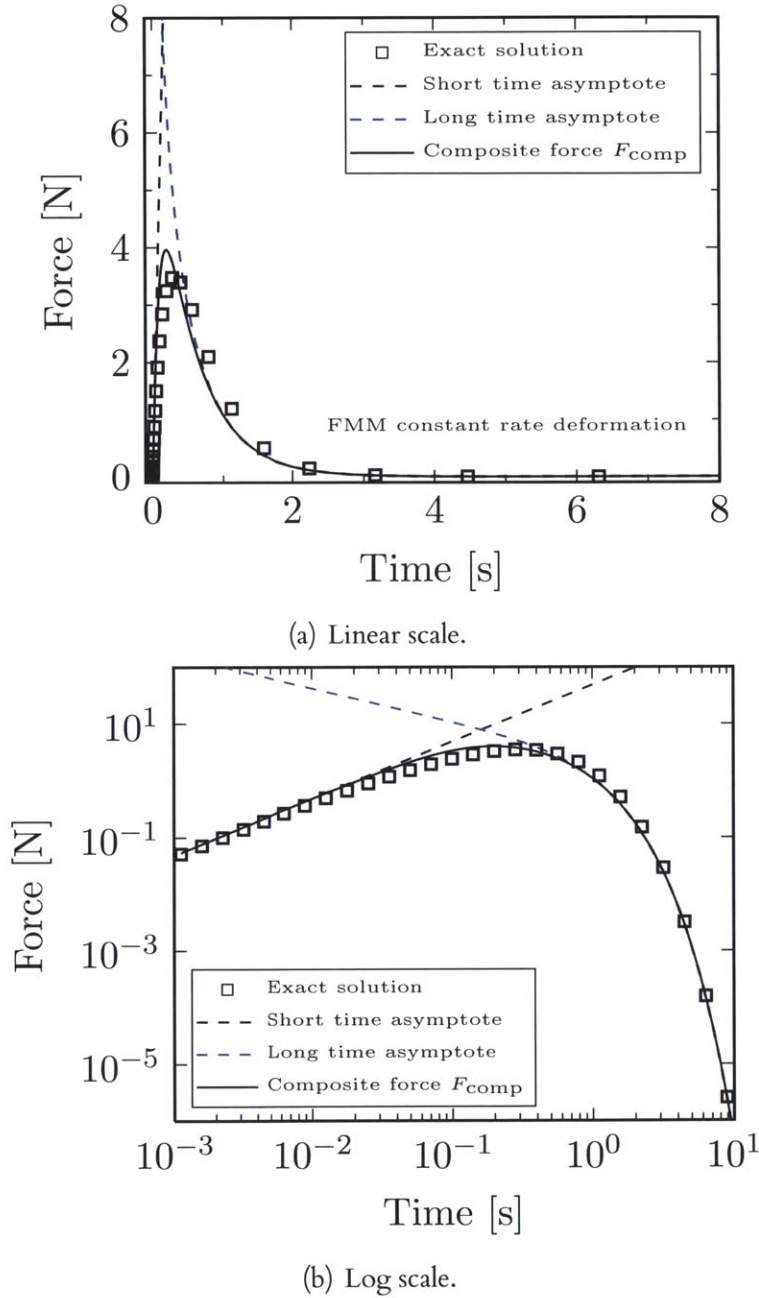


Figure 5.3.3: The composite force determined in equation 5.3.38 (solid line) compared to the exact numerical solution for the tack force as given by equation 5.3.13 (symbols). Also shown here are the short time (black dashed line) and long time (blue dashed line) asymptotes, determined in equations 5.3.32 and 5.3.36 respectively. Note that the approximate composite force is a good approximation to the exact numerically determined solution. The parameters were chosen to be $\alpha = 0.59$, $\beta = 0$, $\mathbb{V} = 100 \text{ Pa s}^\alpha$ and $\mathbb{G} = 400 \text{ Pa}$. For the purposes of illustration, $R_0 = 4 \text{ mm}$, $u_0 = 0.1 \text{ mm s}^{-1}$ and $h_0 = 0.1 \text{ mm}$.

5.3.2 Determination of the normal force for a constant velocity applied deformation

For the case of the top plate withdrawn at constant velocity, the height $h(t)$ of the fluid sample in the gap between the plates is given by $h(t) = h_0 + u_0 t$, in which h_0 is the initial gap height, and u_0 is the velocity of pull off. Substituting this displacement profile into 5.3.8 we obtain

$$K(t) = \int_0^t (t-t')^{-\beta} E_{\alpha-\beta,1-\beta} \left(-\frac{\mathbb{G}}{\mathbb{V}} (t-t')^{\alpha-\beta} \right) \frac{u_0}{(h_0 + u_0 t')^3} dt' \quad (5.3.39)$$

The kinematic arguments of the preceding section still hold and the tack force is given by

$$F = 3\pi R_0^4 \mathbb{G} \left(\frac{1}{\lambda^{3/2}} - \frac{1}{2\lambda^3} \right) K(t) \quad (5.3.40)$$

To find an approximate analytic solution we expand the relaxation modulus term in the integrand using a Taylor series and approximate it by retaining only the $\mathcal{O}(t^0)$ determined in equation 5.3.21 and define

$$K_1(t) = t^{-\beta} E_{\alpha-\beta,1-\beta} \left(-\frac{\mathbb{G}}{\mathbb{V}} t^{\alpha-\beta} \right) \int_0^t \frac{u_0}{(h_0 + u_0 t')^3} dt' \quad (5.3.41)$$

$$= \frac{1}{2h_0^2} t^{-\beta} E_{\alpha-\beta,1-\beta} \left(-\frac{\mathbb{G}}{\mathbb{V}} t^{\alpha-\beta} \right) \left(1 - \frac{1}{(1 + \dot{\epsilon}_0 t)^2} \right) \quad (5.3.42)$$

Replacing $K(t)$ with $K_1(t)$ in equation 5.3.40 we obtain the approximate analytic solution to the tack force for a fractional Maxwell-like material undergoing a constant velocity deformation as

$$F = \frac{3\pi R_0^4 \mathbb{G}}{2h_0^2} \left(\frac{1}{\lambda^{3/2}} - \frac{1}{2\lambda^3} \right) t^{-\beta} E_{\alpha-\beta,1-\beta} \left(-\frac{\mathbb{G}}{\mathbb{V}} t^{\alpha-\beta} \right) \left(1 - \frac{1}{\lambda^2} \right) \quad (5.3.43)$$

In figure 5.3.4 we show the exact numerical value of the force determined as a function of time (cf. equations 5.3.39 and 5.3.40) and compare it to the approximate analytic solution derived in equation 5.3.43. It can be seen that the analytical solution is a good

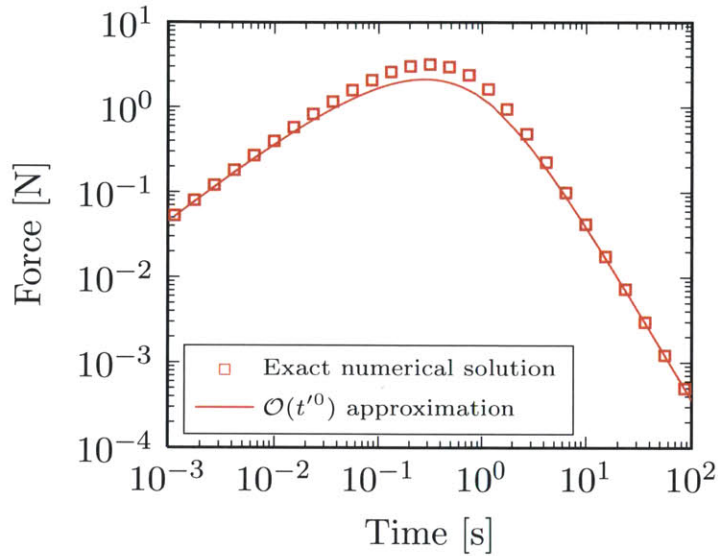


Figure 5.3.4

Comparison of the numerically determined value of the force given by equation 5.3.40 (symbols) against the approximate analytic solution determined in equation 5.3.43 (line). The analytical solution is a good approximation to the exact numerically determined force. $\alpha = 0.59, \beta = 0, \mathbb{V} = 100 \text{ Pa s}^\alpha$ and $\mathbb{G} = 400 \text{ Pa}$.

approximation to the exact numerically determined solution. Again, the accuracy of the analytical solution may be increased by retaining $\mathcal{O}(t')$ and higher terms.

Closed-form analytic solution through the analysis of asymptotes

We begin the asymptotic analysis with the consideration of equation 5.3.39. For small t , we use equation 5.3.28 to write $K(t)$ as

$$K(t) \approx \frac{1}{\Gamma(1 - \beta)} \frac{1}{u_0^2} \int_0^t \frac{(t - t')^{-\beta}}{(h_0/u_0 + t')^3} dt' \tag{5.3.44}$$

From equation D.1.9 of the Appendix, we know that

$$\int_0^t \frac{(t - t')^{-\beta}}{(h_0/u_0 + t')^3} dt' = \left(\frac{u_0}{h_0}\right)^{\beta+2} \cdot \frac{1}{\lambda^{\alpha+2}} \mathcal{B}_{1-1/\lambda}(1 - \beta, -2) \tag{5.3.45}$$

and therefore

$$K(t) \approx \frac{1}{u_0^2 \Gamma(1 - \beta)} \left(\frac{u_0}{h_0}\right)^{\beta+2} \cdot \frac{1}{\lambda^{\alpha+2}} \mathcal{B}_{1-1/\lambda}(1 - \beta, -2) \tag{5.3.46}$$

This expression is identical to one found in section 5.2.2 and we follow the procedure there to arrive at

$$F_e \approx \frac{3\pi R_0^4 \dot{\epsilon}_0}{2h_0^2} \frac{\mathbb{G}}{\Gamma(1-\beta)} \frac{t^{1-\beta}}{1-\beta} \text{ for } \dot{\epsilon}_0 t \ll 1 \quad (5.3.47)$$

where $\dot{\epsilon}_0 = u_0/h_0$ is the nominal strain rate.

To find the long time asymptote, we consider again equation 5.3.43 and use the result given in 5.3.34 and we have

$$F_l = \frac{3\pi R_0^4}{2h_0^2} \frac{1}{\lambda^{3/2}} \frac{\mathbb{V}t^{-\alpha}}{\Gamma(1-\alpha)} \left(1 - \frac{1}{\lambda^2}\right) \quad (5.3.48)$$

We construct the composite force using 5.2.68 so that it has the right asymptotic limits and we have

$$\frac{1}{F_{\text{comp}}} = \frac{2h_0^2}{3\pi R_0^4} \left(\frac{\Gamma(2-\beta)}{\dot{\epsilon}_0 \mathbb{G} t^{1-\beta}} + \frac{\Gamma(1-\alpha)\lambda^{7/2}}{\mathbb{V}t^{-\alpha}(\lambda^2-1)} \right) \quad (5.3.49)$$

which, after some algebra, reduces to

$$F_{\text{comp}} = \frac{3\pi R_0^4}{2h_0^2} \left(\frac{\dot{\epsilon}_0(\lambda^2-1)}{\frac{1}{\mathbb{V}}\Gamma(1-\alpha)\dot{\epsilon}_0\lambda^{7/2}t^\alpha + \frac{1}{\mathbb{G}}\Gamma(2-\beta)(\lambda^2-1)t^{\beta-1}} \right) \quad (5.3.50)$$

We show in figure 5.3.5 the values of the exact numerically determined force (equation 5.3.40) and compare it to the force constructed from the asymptotic analysis (equation 5.3.50). We observe that the expression obtained from the asymptotic analysis is excellent. As this expression for the tack force does not contain the Mittag-Leffler function, it is easier to work with.

5.3.3 Experimental verification of analytical results

In order to verify the theoretical predictions derived above, in this section we present experimental results of tack experiments performed on a 2 wt.% sample of Locust Bean Gum (LBG). LBG is widely used as a thickening additive in the food industry. While its shear rheology has been reported in the literature [207, 208], the extensional properties of galac-

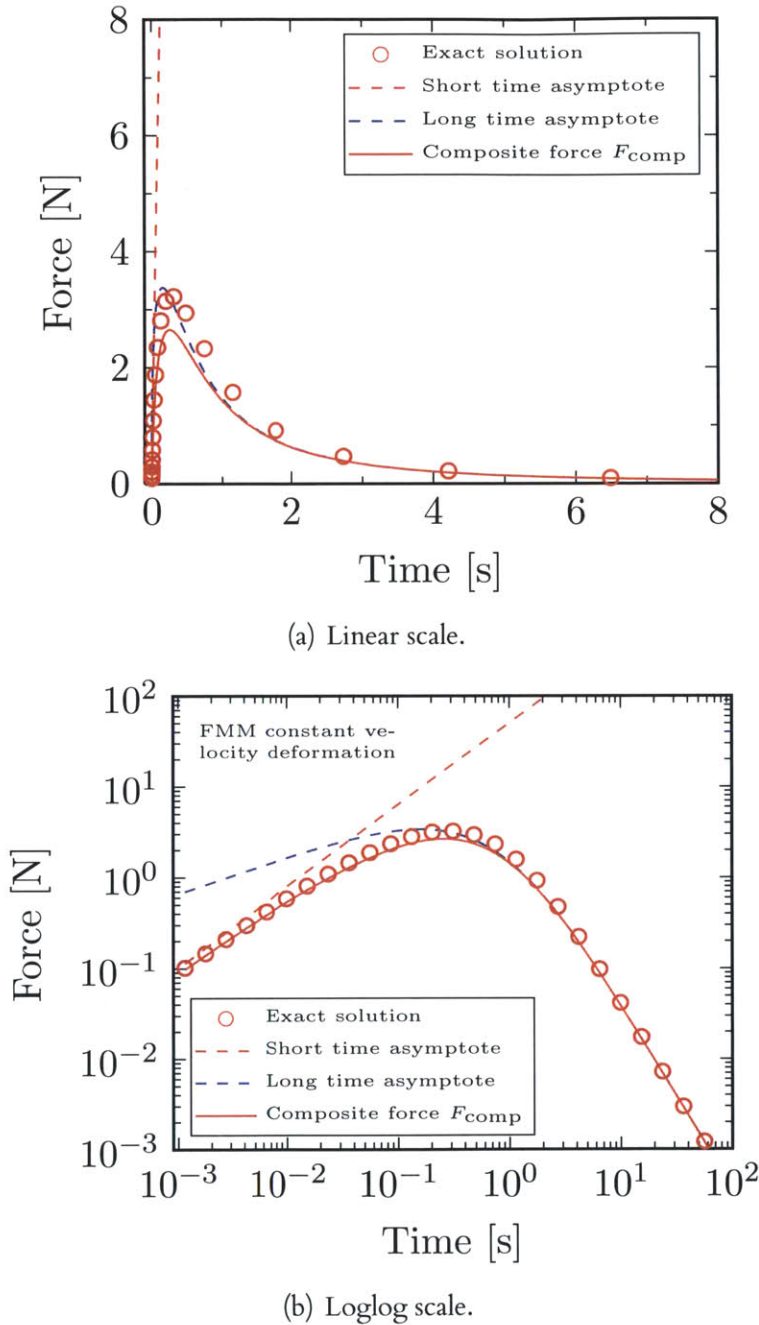


Figure 5.3.5: The composite force determined by equation 5.3.50 (solid line) compared to the numerically determined exact solution for the tack force given in equation 5.3.40 (symbols). Also shown here are the short time (red dashed line) and long time (blue dashed line) asymptotes derived in equations 5.3.47 and 5.3.48 respectively. It is observed that the composite force is a very good approximation to the exact value of the tack force. The parameters were chosen to be $\alpha = 0.59$, $\beta = 0$, $\mathbb{V} = 100 \text{ Pa s}^\alpha$ and $\mathbb{G} = 400 \text{ Pa}$, with $R_0 = 4 \text{ mm}$, $u_0 = 0.1 \text{ mm s}^{-1}$, and $h_0 = 0.1 \text{ mm}$ for purposes of illustration.

tomannan solutions is still relatively poorly understood [209]. Employing tack tests to study extensional properties of these solutions is an accurate and convenient technique. In this section we present an application of the analysis derived above to determine the tack response of LBG from the material parameters obtained from shear rheology experiments.

In figure 5.3.6a we show the results of a small amplitude oscillatory shear experiment performed on a 2 wt.% LBG sample. It is observed that the LBG sample responds linearly at least up till a strain amplitude of 10%. In fact, the material begins to yield only at around a strain amplitude of 100% (not shown in this figure). A strain amplitude of 5% was chosen for frequency sweep experiments.

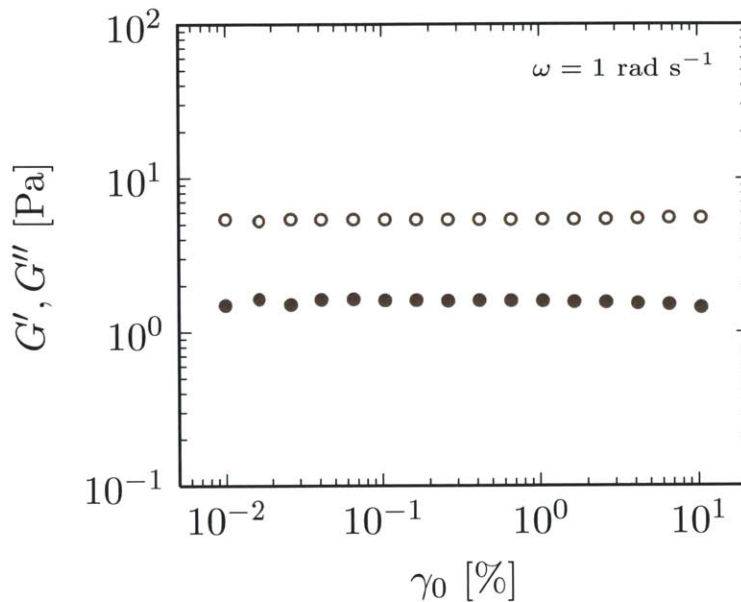
The frequency sweep response of LBG is shown in figure 5.3.6b. From the figure, it can be observed that the material exhibits power-law behavior. To model this power-law behavior, we employ the fractional Maxwell model framework discussed previously and fit equations 2.3.15 and 2.3.16 to the measured $G'(\omega)$ and $G''(\omega)$ data respectively. These fits are shown as lines in the figure. It can be observed that the fits are excellent and the power-law behavior of the material can be captured adequately using just four parameters $\alpha = 0.85$, $\beta = 0.22$, $\mathbb{V} = 11.15 \text{ Pa s}^\alpha$, $\mathbb{G} = 72.81 \text{ Pa s}^\beta$. We also determine the crossover frequency ω_c using equation 3.3.7 to be $\omega_c = 0.68 \text{ rad s}^{-1}$.

In figure 5.3.7 we show the flow curve of LBG to examine its non-linear rheology. It can be seen that LBG is shear-thinning at high shear rates, and the flow curve approaches a zero-shear plateau at low shear rates. We also superimpose on the steady shear data the complex viscosity η^* plotted as a function of the excitation frequency ω . In accordance with the empirical Cox-Merz rule, which states that [24]

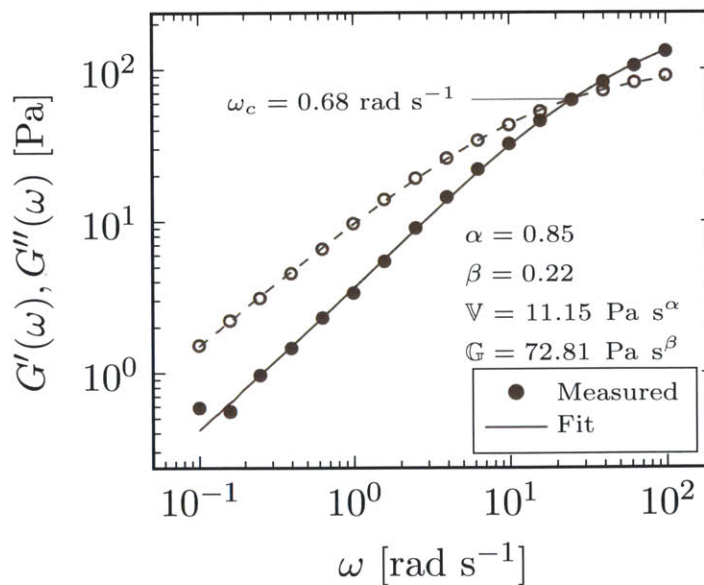
$$\eta(\dot{\gamma}) = |\eta^*(\omega)|_{\omega=\dot{\gamma}} \quad (5.3.51)$$

there is good overlap between the curves; however we note that at higher $\dot{\gamma}$, $\eta^*(\dot{\gamma}) > \eta(\dot{\gamma})$. This is typical of systems where hydrogen bonding interactions play an important role in its rheology [210]. This suggests that hydrogen bonding interactions might be present in this system.

With the shear rheology established, and the parameters α , β , \mathbb{V} and \mathbb{G} that characterize the material having been determined, we now invoke the tack analysis above to make predictions of the tack response of LBG. In figure 5.3.8, snapshots of a tack experiment performed on 2 wt.% LBG solutions is presented as a time series. The horizontal green line represents the edge of the top plate, whose radius is $R_0 = 4 \text{ mm}$. We scale the time of

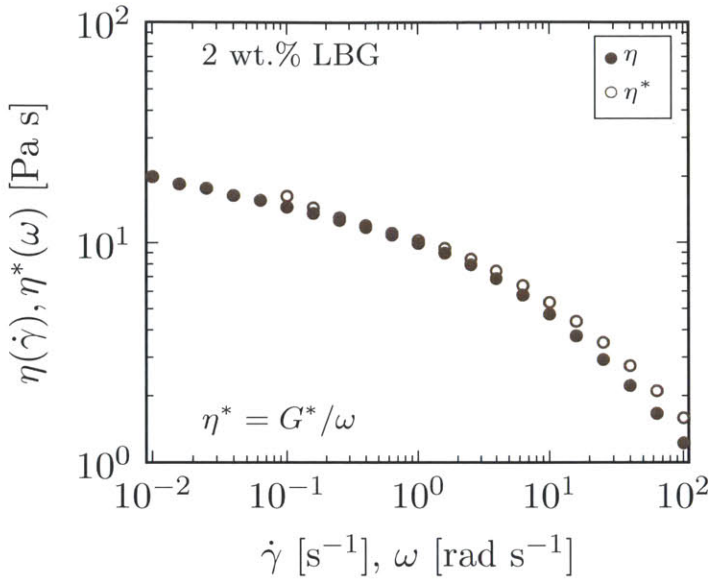


(a) Strain sweep



(b) Frequency sweep

Figure 5.3.6: SAOS measurements performed on 2 wt.% LBG solutions. (a) The material responds linearly at least until a strain amplitude of 10%. (b) Frequency sweep at a strain amplitude of $\gamma_0 = 5\%$. Also shown are the FMM fits (equations 2.3.15 and 2.3.16) and the corresponding fit parameters.


Figure 5.3.7

Steady shear viscosity $\eta(\dot{\gamma})$ of 2 wt.% LBG. The fluid approaches a zero-shear plateau at low shear rates and is shear-thinning at high shear rates. The complex modulus $\eta^*(\omega)$ agrees well with $\eta(\dot{\gamma})$ at $\omega = \dot{\gamma}$, as suggested by the empirical Cox-Merz rule. Deviations to the rule are seen at higher rates.

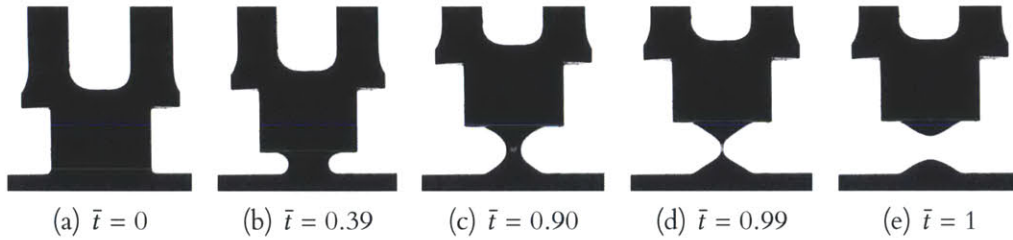
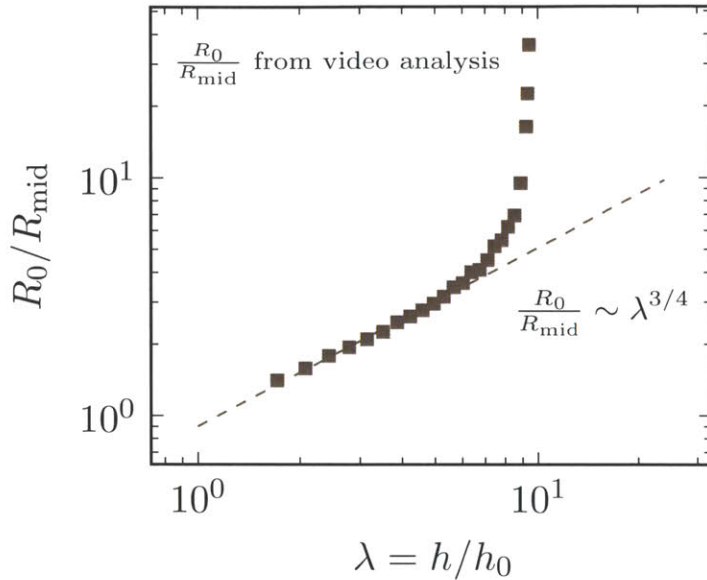


Figure 5.3.8: A time-sequence of snapshots of a tack experiment performed on 2 wt.% LBG solutions using a plate of radius $R_0 = 4$ mm. The profile of the fluid filament close to breakup indicates the existence of an elasto-capillary balance of forces. Image analysis of the video gives us the true velocity of the upper plate $u_0|_{\text{true}} = 0.539$ mm s⁻¹, and the mid-plane radius R_{mid} as a function of time. $u_0|_{\text{imposed}} = 0.5$ mm s⁻¹, $h_0 = 0.5$ mm, $t_b = 7.9$ s.

the snapshot by the breakup time t_b to define a dimensionless time $\bar{t} = t/t_b$. t_b is determined from image analysis to be $t_b \approx 7.9$ s.

A number of important observations can be made from this sequence of snapshots. Firstly, we may experimentally verify our assumption that the kinematics of a tack experiment performed on viscoelastic fluids is the same as a tack experiment performed on a purely viscous fluid, (i.e.) equations 5.2.15 and 5.2.16 apply for the viscoelastic case. In figure 5.3.9 we plot the radius of the mid-plane of the fluid filament R_{mid} against the stretch ratio λ . We also show the equation of our assumption (equation 5.2.43) about the kinematics on this plot.

It can be seen that the experimentally measured radius profile agrees very well with our

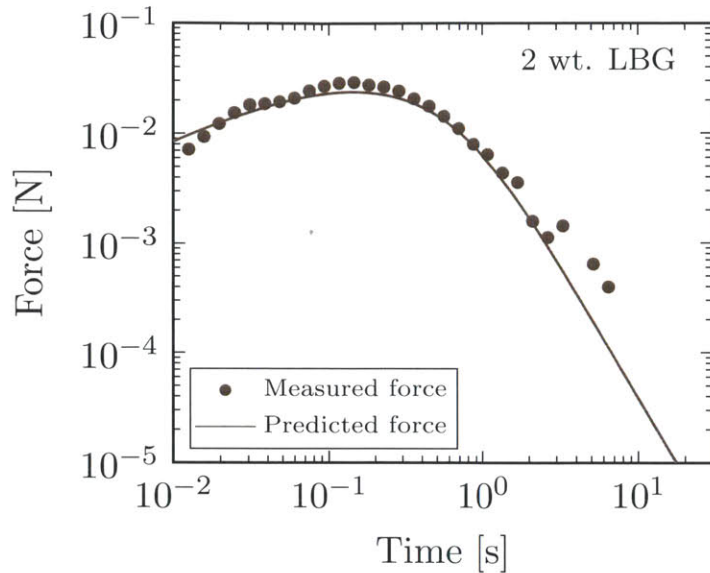
**Figure 5.3.9**

The reciprocal of the experimentally measured mid-plane radius R_{mid} (suitably scaled with the initial radius R_0) obtained from video analysis plotted against the stretch ratio λ . It is observed that except near breakup, assumptions made about the kinematics of the fluid filament (equation 5.2.43) agree closely with experiment.

assumption about the kinematics, except very close to the breakup of the filament. This may be attributed to the fact that elastic effects play a much stronger role near breakup, and the breakup may be modeled as a balance between elastic forces and capillary forces [211]. The appearance of this so-called elasto-capillary balance is clearly seen in figure 5.3.8d by the uniform cylindrical liquid bridge. This force balance may be exploited to measure the extensional viscosity of the fluid in a Capillary Breakup Extensional Rheometry (CaBER) experiment [209].

A further measurement we perform from the videos of the tack test is a direct calculation of the velocity of the top plate. Although we impose $u_0 = 0.5 \text{ mm s}^{-1}$ while setting up the experiment, the actual velocity of the plate was measured to be $u_0 = 0.539 \text{ mm s}^{-1}$.

The force exerted on the top plate as a function of time during a tack experiment is shown in figure 5.3.10 as symbols, and the prediction obtained from equation 5.3.40 is shown as a solid line. It is observed that the prediction agrees very well with the measured data. Note that this prediction has been achieved by using the parameters $\alpha, \beta, \mathbb{V}$ and \mathbb{G} determined from an independent SAOS experiment (cf. figure 5.3.6b)—we do not fit equation 5.3.40 to the data. The small deviation of the measured force from the prediction towards the end of the experiment may be attributed to the additional elastic stresses present in the filament which retards the breakup, and our assumptions about Newtonian kinematics breaks down.

**Figure 5.3.10**

The measured tack force exerted by a 2 wt.% LBG solution (symbols) compared to the corresponding analytical prediction derived in equation 5.3.40 (line). It is observed that the prediction agrees very closely with the experimental data. The deviation of the measured force from the data close to breakup is due to additional elastic stresses retarding the breakup leading to a change in the kinematics of the flow.

5.4 Conclusions

In this Chapter, we have analyzed the tack response of a chemically crosslinked fluoro-silicone gel. These materials are frequently used as pressure sensitive adhesives, which have immense industrial and practical importance. We have demonstrated that beginning with a characterization of the gel, by performing a linear rheological experiment such as SAOS and subsequently fitting an appropriate fractional constitutive model, we obtain accurate predictions of the normal force generated upon performing a tack experiment on these gels. Our approach involves applying the lubrication approximation to the Cauchy momentum equations (which is justified because we are interested in the small extensional strain limit), and subsequently coupling them with an appropriate fractional constitutive equation (either FMM or FKVM, depending on the nature of the material). To calculate the strain and strain rate fields, we use the result obtained for a tack experiment performed on a Newtonian fluid. As shown in this chapter, FCEs are able to predict the rheological response of multiscale power-law complex fluids under small extensional deformations. We next focus on the more challenging problem of large extensional deformations applied to such complex materials.

6 | *Large Strain Extensional Deformations: Polysaccharide Systems*

In this chapter, we experimentally determine the extensional rheology of two polysaccharide systems that exhibit power law rheology, namely Mamaku gum [71] and Hyaluronic acid [212, 213]. The former is a plant extract that exhibits shear thickening behavior, and hence has potential applications as a food thickener and as a treatment for dysphagia. On the other hand, Hyaluronic acid (HA) is known to be an important component of synovial fluid [70], which is the chief component of the lubricant in healthy mammalian joints. In this chapter, we measure and characterize the extensional rheology of these fluids in detail using various extensional rheometry devices such as the Capillary Breakup Extensional Rheometer (CaBER), the filament stretching extensional rheometer (FiSER) and an Optimized Shape Cross-slot Extensional Rheometry (OSCER) device.

6.1 Mamaku Gum

Mamaku gum is a polysaccharide extracted from the fronds of the black tree fern found in New Zealand. The cooked pith has traditionally been used for various medicinal purposes and as a food source by the native tribes of New Zealand. It has potential applications as a thickener in the food industry and as a palliative for patients with dysphagia. Studies on the shear rheology of Mamaku gum have revealed that the gum exhibits shear thickening at a critical shear rate due to a transition from intra- to inter-molecular chain interactions upon shear induced chain elongation. In this paper we demonstrate that these interactions are primarily due to hydrogen bonding. We perform extensional rheology on mixtures of Mamaku gum and urea (a known disruptor of hydrogen bonds) to quantify the nature

of these interactions. Capillary Breakup Extensional Rheometry (CaBER) performed on the pure Mamaku gum solutions yield plateau values of the Trouton ratio as high as $\sim 10^4$, showing that the viscoelasticity of the gum in uniaxial elongation is much higher than in shear. For all Mamaku concentrations tested, the extensional viscosity decreases upon increasing urea concentration. Furthermore, the relaxation time decreases exponentially with increasing urea concentration. This exponential relationship is independent of the Mamaku concentration, and is identical to the relationships between urea concentration and characteristic timescales measured in nonlinear shear rheology. We show using the sticky reptation model for polymers with multiple sticker groups along the backbone how such a relationship is consistent with a linear decrease in the free energy for hydrogen bond dissociation. We then demonstrate that a time-concentration superposition principle can be used to collapse the viscoelastic properties of the Mamaku-gum urea mixtures.

6.1.1 Introduction

Polysaccharides play critical roles in a number of industrial and biological applications [64]. They provide structural reinforcement in plants and animals [214–216], are the chief component of the lubricating synovial fluid found in mammalian joints [63, 217], are the main source of energy in foods [218], and are found in various biological slimes and mucus [219, 220]. Furthermore, the widespread availability, biocompatibility, biodegradability and the ability of polysaccharides to form swollen gels has stimulated much research in using them in controlled drug release systems [221, 222]. Perhaps one of the most important applications of polysaccharides is in the foods industry. Precise control of the organoleptic characteristics of foodstuffs such as texture, thickness, chewiness, tackiness and mouth-feel is crucial for the shelf-life, consumer perception and overall quality of the food [64]. Polysaccharides such as Xanthan gum, Guar gum and Locust Bean gum have enjoyed particular success in this area [164].

Recently, a new plant polysaccharide called Mamaku gum, obtained from the fronds of the black tree fern, has been discovered and its shear rheology has been characterized [71, 72]. The Maori tribes of New Zealand have used Mamaku gum for treating boils, burns, wounds, rashes and diarrhea [73]. A large number of plant mucins and gums exhibit such healing and curative properties [223]. Plant gums such as Mamaku also control the rate of flow of food through the digestive tract due to their ability to swell and retain water. This leads to longer transit times in the digestive tract, higher nutrient uptake [64] and also

provides bulk to ingested foods, thus helping in smoother peristalsis and healthier bowel movements [224]. In Table 6.1.1, we list various natural and synthetic polysaccharides currently used as additives to food products for thickening and other purposes. Given these myriad uses of polysaccharide containing mixtures, and indeed polysaccharides themselves, an extensive rheological study of Mamaku gum and the understanding of the nature of inter- and intra-molecular interactions will aid in promoting commercial scale applications of Mamaku gum in food thickeners and as a digestive emollient.

It has been shown in previous viscometric studies [71] that in steady simple shear flow, Mamaku gum exhibits shear-thickening behavior, i.e., the steady shear viscosity $\eta(\dot{\gamma})$ increases as a function of shear rate $\dot{\gamma}$ for a certain range of shear rates. This is an exceptional occurrence for polysaccharide solutions [64], which very frequently display shear-thinning, i.e., $\eta(\dot{\gamma})$ decreases as a function of shear rate $\dot{\gamma}$. This shear-thickening behavior arises from the appearance of increased inter-molecular interactions at a critical shear rate. Matia-Merino et al. have shown that the shear thickening behavior of Mamaku gum exhibits very low sensitivity to changes in salt composition as well as salt concentration [73]. In Figures 6.1.1a and 6.1.1b, we re-plot the data from Ref. [73] demonstrating the relative insensitivity of Mamaku gum solutions to changes in the concentration of salt in the solution. The rheology of Mamaku gum is also unchanged over a wide range of pH values; from Figure 6.1.2 we see that the zero shear viscosity η_0 of the Mamaku gum solutions remains nearly constant for a wide range of pH values (pH 2-9). At very alkaline pH values, the change observed in the shear viscosity could possibly arise from structural changes in the polysaccharide induced in highly alkaline environments [73].

The rheology of Xanthan gum, which is currently one of the most widely used food thickeners, is sensitive to both salt content as well as pH [226]. This presents the possibility of using Mamaku gum as a rheology modifier for foods with low pH in which other frequently used modifiers are ineffective. Moreover, the unique shear-thickening behavior of the gum (as opposed to a majority of other food thickeners which are shear-thinning) may itself have potential applications. For example, thickening agents are added to foods as a treatment for dysphagia [227, 228]; this retards the process of bolus swallowing and hence provides more time for muscular control of the swallowing process [67]. With this application in mind, it is important to understand the rheology and the nature of the supramolecular interactions present in Mamaku gum that lead to the shear-thickening behavior. The peristaltic swallowing and digestive processes involves extensional deformations [65], and

Polysaccharide	Applications
Agar	Ice creams, milk shakes, cakes, cookies, jams, processed cheese.
Alginates	Puddings, mousse, tomato ketchup, soups, mayonnaise, juice.
Carrageenan	Cheese, desserts, whipped cream, pet foods, syrups, salad dressings, milk thickening applications.
Cellulose Derivatives	Beverages, meat analogues, breads and other baked foods. Also used in encapsulation and coating film applications, to prevent food oxidation.
Gelatin	Beverages, yogurt, low-fat spreads, canned meat products
Gellan Gum	Drinking jellies such as in sports drinks, jams, fruit yogurts.
Gum Tragacanth	Emulsifier—especially in the presence of gum Arabic, thickener for beverages, used in pharmaceuticals such as creams and lotions.
Inulin	Provides improved mouthfeel in fat-free products: acts as a fat replacement, foam stabilizer.
Pullulan	Confectionaries, processed meat, instant beverages, forms films and is used as an oxygen barrier, binding agent due to its strong adhesive properties
Starch	Thickening and gelling agent for soups and sauces
Xanthan Gum	One of the most widely employed thickeners in the food industry. Used in dressings and sauces, baked products and instant beverages. Exhibits synergistic effects with other polysaccharides and forms strong gels, for example with guar gum and locust bean gum.

Table 6.1.1: The various uses of polysaccharides in the food industry. Most frequently they are used as thickeners and gelling agents. Thickening is important not only to provide better texture and mouthfeel to foods, but also to help patients suffering from dysphagia. More information on molecular structure and applications of polysaccharides in foods can be found in Ref. [225].

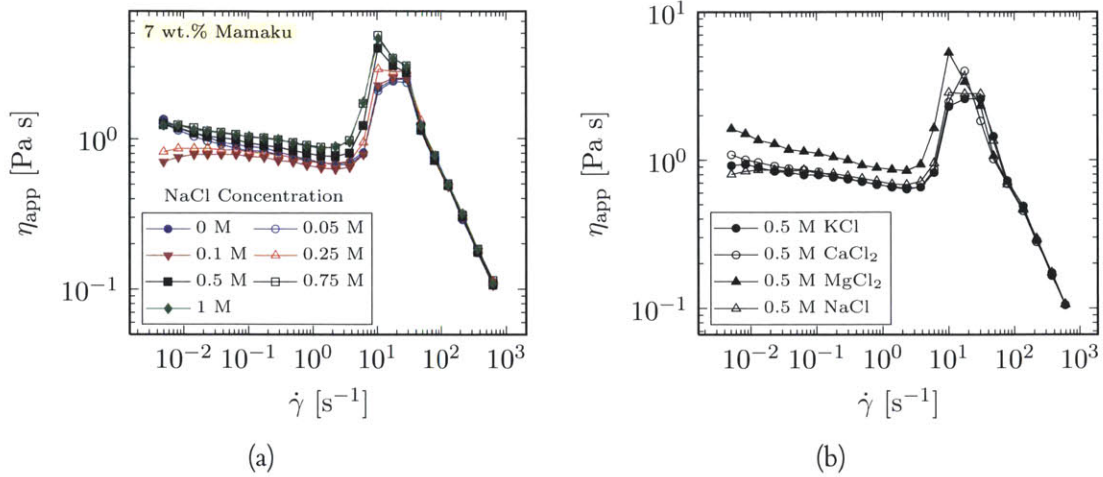


Figure 6.1.1: Effect of changing the salt environment of Mamaku gum solutions. (a) Adding different concentrations of NaCl does not drastically influence the shear viscosity of Mamaku gum solutions. (b) Varying the salt composition only minimally influences the steady shear viscosity of Mamaku gum solutions. Data from Ref. [73].

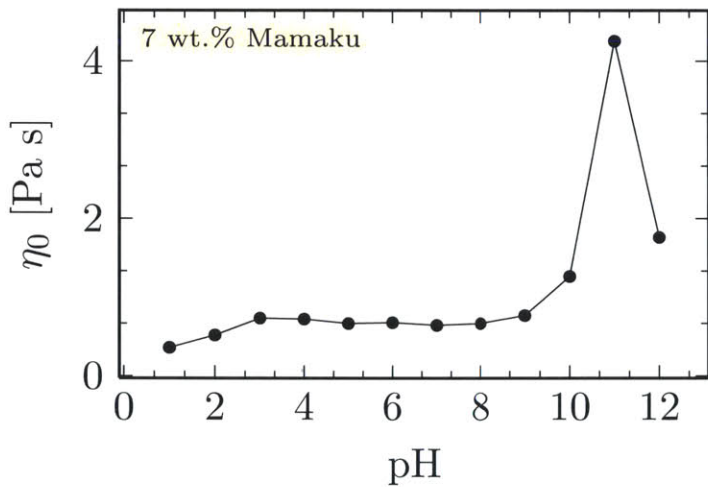


Figure 6.1.2
Zero shear viscosity η_0 of a 7 wt. % Mamaku gum solution as a function of pH. Changing the pH leaves η_0 relatively unchanged, except at very alkaline pH. This could be due to structural changes induced in the polysaccharide chains at very alkaline pH. Data from Ref. [73].

fluid elements are intermittently stretched or elongated as the food bolus moves from the mouth and through the digestive tract. Moreover, the stress response of complex fluids to extensional flows is a more sensitive probe of the composition, morphology and structure of the fluid [61, 229, 230], than a shearing deformation of comparable strength. Therefore, use of polysaccharides such as Mamaku gum as a digestive emollient requires a characterization of their viscoelastic response under extensional deformation. However, a brief review of the literature indicates that such data is relatively sparse for polysaccharide solutions and

self-associating polymeric fluids in general.

In this paper, we use a combination of nonlinear shear rheology, and Capillary Breakup Extensional Rheometry (CaBER) [231] to probe the nature of the intermolecular interactions in Mamaku gum. We validate the hypothesis that hydrogen bonding interactions lead to the unusual viscoelastic response of Mamaku gum, using mixtures of Mamaku gum and urea. The remainder of the paper is organized as follows. The next section details the extraction and preparation of the fluids and describes the various experimental techniques used. In the third section we describe and interpret the experimental results. We comprehensively characterize the extensional rheology of Mamaku gum using CaBER measurements and extract relaxation times and extensional viscosities of both pure Mamaku gum solutions as well as Mamaku-urea mixtures. Urea is known to be an effective disrupter of hydrogen bonding in proteins [30] and polysaccharides [232]. We document the rheological changes induced upon the addition of urea to Mamaku gum, and demonstrate that the source of the unusual nonlinear rheology of the solution arises from intra-molecular hydrogen bonds. We demonstrate the existence of a quantitative ‘concentration-temperature superposition’ and interpret the underlying physics of this superposition principle in terms of the lifetime of hydrogen bond formation and the changes induced in the activation energy landscape upon the addition of urea.

6.1.2 *Experimental*

Materials

The freeze-dried aqueous extract of Mamaku gum was obtained from the stem pith of the fronds of the New Zealand black tree fern (*Cyathea medullaris*) in Palmerston North, New Zealand, in August 2011 according to the procedure outlined by Goh et al. [71] The freeze-dried extract was prepared by hydrating in deionized water overnight under gentle stirring at 25°C. Solutions that were not used immediately were stored under refrigeration at 4°C. In all cases, experiments were performed with solutions less than 72 hours old.

Methods

The shear rheology presented in this paper was performed using a TA Instruments (New Castle, DE, USA) stress-controlled ARG2 rheometer using a 40 mm, 2° cone-and-plate fixture. For all experiments, the temperature was held fixed at 25°C using a Peltier plate.

Extensional rheology was performed using a Capillary Breakup Extensional Rheometer (CaBER). The CaBER device consists of two parallel plates of diameter D_0 separated by an initial gap of length L_0 . The test fluid is loaded between this gap and the top plate is pulled apart rapidly ($t_{\text{open}} \approx 50$ ms) using a stepper motor to a final gap L_f to impose an extensional deformation on the fluid sample and form a liquid bridge between the plates. The resultant filament then thins under the action of viscous, elastic and capillary forces, and the mid-plane diameter of the fluid $D_{\text{mid}}(t)$ varies as a function of time [231]. In our CaBER setup, this diameter is measured using a laser micrometer (resolution $5 \mu\text{m}$), and is also independently monitored using a macro lens with a focal length of 100 mm attached to a DSLR camera. For sufficiently viscous Newtonian fluids, in the absence of inertial or gravitational effects, the mid-plane diameter $D(t)$ decays linearly with time until eventual breakup [233]. However, in the present study, there is a point in the thinning process of the filament at which the capillary pressure arising from surface tension is balanced purely by the stress arising from fluid elasticity. Such a balance of stresses is known as an elasto-capillary balance [211].

The Hencky strain $\varepsilon(t)$ experienced by the fluid element at the mid-plane of the thinning filament is given by

$$\varepsilon(t) = 2 \ln \left(\frac{D_0}{D(t)} \right) \quad (6.1.1)$$

Under the conditions of elasto-capillary balance, Entov and Hinch[211] have shown that the mid-plane diameter $D(t)$ decays exponentially, and is given by

$$\frac{D(t)}{D_0} = \left(\frac{GD_0}{2\sigma} \right)^{1/3} \exp[-t/(3\tau)] \quad (6.1.2)$$

in which G and τ are the modulus and relaxation time, respectively, of the longest relaxation mode of the fluid, and σ is the surface tension. Therefore, the CaBER experiment yields a measure of the characteristic relaxation time τ of the fluid in elongation. Note that the strain rate imposed on the fluid filament in a CaBER device is chosen by the fluid according to the balance of elastic and capillary forces, and cannot be independently controlled in the experiment. The strain rate $\dot{\varepsilon}(t)$ in the *elasto-capillary regime* can be calculated from

equations 6.1.1 and 6.1.2 and is given by

$$\dot{\epsilon}(t) = \frac{2}{3\tau} \quad (6.1.3)$$

which is a constant. In our experiments, $D_0 = 6$ mm, $L_0 = 2$ mm and $L_f = 7$ mm, and the step from L_0 to L_f is performed over a controlled time step of 50 ms. The transient extensional viscosity may then be calculated as [231]

$$\eta_E^+ = -\frac{\sigma}{dD_{\text{mid}}(t)/dt} \quad (6.1.4)$$

Note that in a CaBER measurement, we do not independently measure the tensile stress difference; instead, we obtain it from balancing the elastic stress difference and the capillary pressure arising from surface tension in the thinning filament. The surface tension of the fluids was measured independently with a platinum Wilhelmy plate (Kruss K-10 tensiometer).

6.1.3 Results and Discussion

Shear Rheology

We begin with a discussion of the shear rheology of the Mamaku gum solutions. In figure 6.1.3a we show the zero shear rate viscosity of Mamaku gum as a function of concentration, which has been replotted from Goh et al. [71]. The dilute and the semidilute regimes are clearly demarcated by the two different power-laws ($\eta_0 \sim c^{1.25}$ and $\eta_0 \sim c^{4.64}$ respectively). The concentration at which the two power-laws intersect gives us a coil overlap concentration $c^* \approx 2.2$ wt.%. The two distinct power-laws observed in the scaling of zero shear viscosity with concentration has also been widely observed in a number of synthetic polymers [20]. The change in the scaling occurs from increased interactions between polymer molecules upon coil overlap. However, in the semidilute regime, instead of $\eta_0 \sim c^{3.4}$ expected from scaling arguments [234], we observe a higher power law exponent of $\eta_0 \sim c^{4.64}$. This exponent is also higher than what has been observed in the majority of polysaccharide solutions with the notable exception of Xanthan gum [169] — in this case the semidilute regime exhibits a scaling of $\eta_0 \sim c^{4.2}$. This anomalous scaling has been attributed to the presence of intermolecular interactions in addition to those arising due to

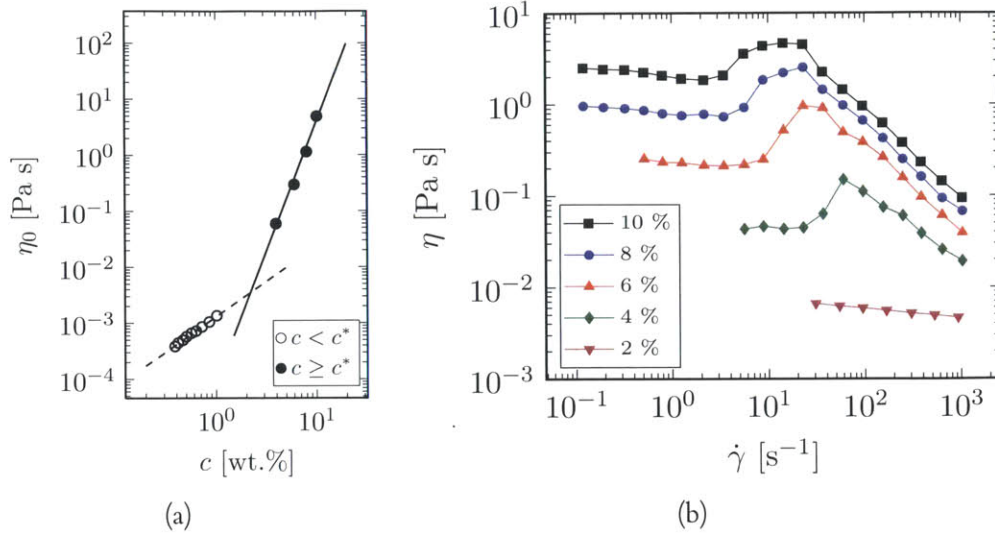


Figure 6.1.3: (a) The zero shear viscosity η_0 of Mamaku gum solutions as a function of concentration showing the different power law scalings characteristic of the dilute and semidilute regimes. In the semidilute regime, $\eta_0 \sim c^{4.464}$. (b) The shear rheology of different concentrations of Mamaku gum in the absence of urea, reproduced with permission from Goh et al.[71] For Mamaku gum, $c^* \approx 2.2$ wt. %. At some critical shear rate $\dot{\gamma}_p$, which depends on the Mamaku gum concentration, a shear thickening regime appears for $c > c^*$, followed by strong shear thinning.

physical entanglements of overlapping coils [235, 236]. In this paper, it is our goal to explore the nature of these additional intermolecular interactions in Mamaku gum solutions, using the amplified molecular deformation resulting from extensional flow.

These intermolecular interactions are even more dramatically visible at higher shear rates. In Figure 6.1.3(b), we replot the nonlinear shear rheology results of Goh et al. [71]. For all concentrations larger than $c^* \approx 2.2$ wt.%, pronounced shear thickening is present in the flow curve over a certain range of shear rates $\dot{\gamma}$. Such shear thickening has been observed in many associative polymer solutions, suspensions and worm-like micelles [237], but has rarely been observed in polysaccharide biopolymers [175, 238]. The proposed mechanism of shear thickening in Mamaku gum is the conversion of *intra*-molecular interactions to *inter*-molecular interactions; upon the imposition of high shear rates (compared to the characteristic relaxation time of the polymer), the polymer chains are partially elongated due to the extensional component of the shear deformation which exposes additional unravel ‘sticker’ groups that locally interact between different molecules [71]. These physical crosslinks thus formed lead to increase in the effective hydrodynamic size of the polymer chains, thus leading to an increase in viscosity [239]. The strong shear-thinning observed

at higher shear rates occurs when the stress in the fluid exceeds the value needed to break the intermolecular associations, and the associated chains are then pulled apart. This is effectively a constant stress process, and this can be validated by plotting the shear stress $\sigma(\dot{\gamma})$ as a function of shear rate $\dot{\gamma}$ (see supporting information). Previous studies have eliminated the possibility that the interactions that lead to the shear-thickening behavior arise from electrostatic or hydrophobic effects [73]. Intra- and intermolecular hydrogen bonding is present in many polysaccharide systems [173, 240] making it a likely candidate for the origin of the observed physical entanglements.

To test this hypothesis we measure the rheology of Mamaku gum solutions with different concentrations of urea added. Urea is known to be a strong disruptor of macromolecular hydrogen bonds [241], in the sense that it competes for the hydrogen bonding sites, and prevents Mamaku–Mamaku intermolecular hydrogen bonding. In figure 6.1.4, we show the effect that the addition of urea has on the shear rheology of Mamaku gum. There are three changes induced in the shear rheology of the solutions upon the progressive increase in urea concentration: (1) The zero-shear viscosity η_0 drops, (2) the shear rate $\dot{\gamma}_p$ at which the peak viscosity is observed is shifted out to larger shear rates and (3) the peak viscosity η_p drops. This shows that the intermolecular interactions in Mamaku gum are strongly decreased in the presence of urea, and it is hydrogen bonding that leads to the shear-thickening behavior seen in these solutions. Defining a time constant $\tau_p = 1/\dot{\gamma}_p$ yields a characteristic timescale for the lifetimes of the hydrogen bond associations between

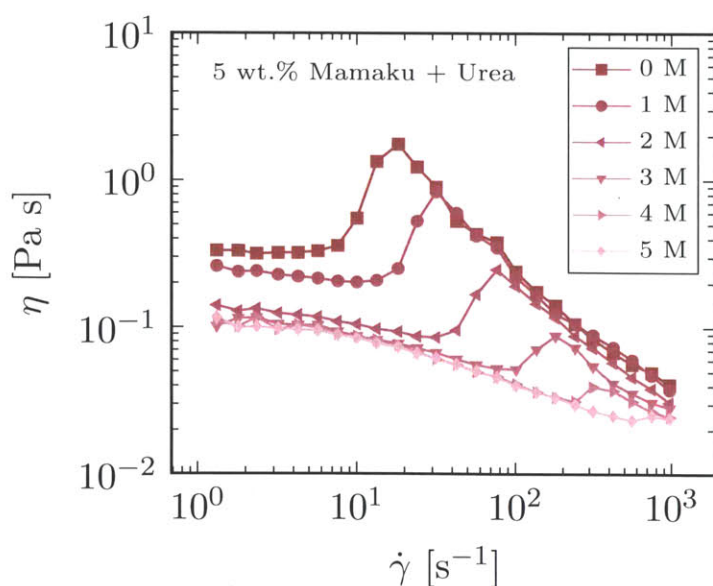


Figure 6.1.4

Effect of the addition of urea on the viscosity of a 5 wt.% Mamaku gum solution. Upon the addition of urea, three changes are observed, namely, the zero shear viscosity plateau drops, the onset of shear thickening is pushed to higher shear rates, and the extent of shear thickening also drops.

Mamaku gum molecules in solution. In figure 6.1.5 we plot the value of τ_p as a function of the urea concentration c on a log-linear scale. We observe that the characteristic timescale τ_p decreases exponentially with urea concentration as $\tau_p \sim \exp(-mc)$ where m is a constant. Linear regression gives us

$$\tau_p = \tau_p^0 e^{-c/1.25}. \quad (6.1.5)$$

where c is the molar concentration of urea ($M_0 = 60.06$ g/mol) and τ_p^0 is the characteristic timescale for the onset of shear-thickening with no urea addition.

Moreover, when we plot the peak shear viscosity η_p as a function of urea concentration c (also shown in Figure 6.1.5), we observe that η_p varies with c in an identical exponential fashion, i.e. $\eta_p = \eta_p^0 e^{-c/1.25}$. The stress σ_p at which this peak viscosity occurs is given by

$$\sigma_p = \eta_p \dot{\gamma}_p \quad (6.1.6)$$

$$= \eta_p^0 e^{-c/1.25} \cdot \dot{\gamma}_p^0 e^{c/1.25} = \eta_p^0 \dot{\gamma}_p^0 \quad (6.1.7)$$

in which η_p^0 and $\dot{\gamma}_p^0$ are the peak viscosity and the value of the shear rate at which the peak viscosity is attained for the Mamaku gum solution with zero added urea ($c = 0$). This quantity σ_p is independent of urea concentration, indicating that shear thinning appears at a constant value of stress.

Our measurements give $\sigma_p \approx 28$ Pa. These observations suggest that the addition of urea does not change the average number of association junctions per chain, or the strength of each hydrogen bond, but only modifies the average lifetimes of the associations. We explore

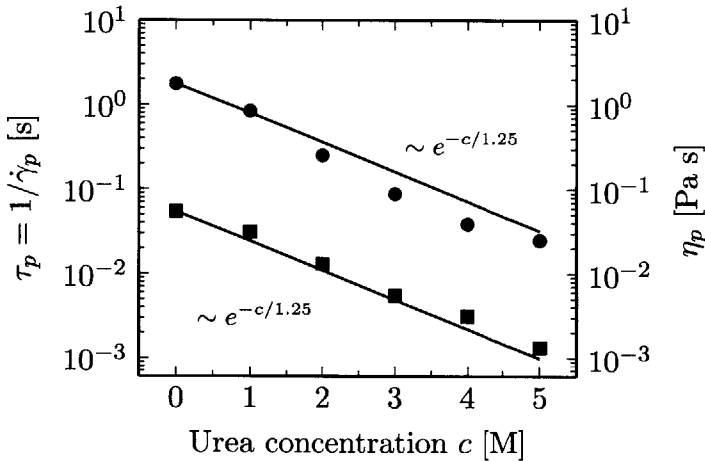


Figure 6.1.5

Dependence of the characteristic timescale τ_p (squares) and the peak viscosity η_p (circles) on the concentration of added urea for a 5 wt. % Mamaku gum solution. An identical exponential dependence (differing only by a constant pre-factor) is observed in the variation of η_p as well as τ_p with urea concentration. We measure the same exponential sensitivities for 2.5 wt. % and 5.0 wt. % Mamaku gum solutions.

this hypothesis further with the help of the extensional rheology experiments described below.

Capillary Breakup Extensional Rheometry

Because shear thickening behavior can arise from the partial extension of polymer chains leading to increased intermolecular interactions [71, 239], we directly study the behavior of Mamaku gum solutions in extensional flow. We use the CaBER device to quantitatively measure the changes in the extensional rheology of Mamaku gum upon increasing the urea concentration. Although limited in number, CaBER experiments performed on other polysaccharide systems, such as cellulose/ionic liquid solutions [242], Sundew plant mucilage [243] and Schizophyllan solutions [244], have revealed that capillary breakup rheometry is an accurate technique for quantifying the elongational properties of these fluids. Moreover, the potential application of Mamaku gum solutions as a food thickener necessitates an understanding of its elongational properties; the biomechanics of swallowing is such that a food bolus encounters a squeeze flow [245], whose kinematics has elongational deformation components.

In figure 6.1.6, we show images of CaBER experiments as a function of time for both 2.5 wt.% (top row) and 5 wt.% (bottom row) Mamaku gum solutions. We have scaled time by the breakup time t_b of the fluid filament for each concentration (the values of t/t_b are given in the figure caption). The shape of the liquid bridge helps us determine the onset of the elasto-capillary regime, in which equations 6.1.2 – 6.1.4 hold. At very early times $t/t_b \ll 1$, the liquid bridge has just been formed and inertial stresses generated during the step deformation are dominant. Immediately following this inertial regime there is a viscocapillary regime, where capillary forces are balanced by the viscosity of the fluid. In this regime, the midplane diameter of the fluid filament decreases linearly with time and is given by [233]

$$D(t) = D_0 - \frac{2x - 1}{6} \frac{\sigma}{\eta_0} t \quad (6.1.8)$$

where $x = 0.7127$ for the viscocapillary similarity solution [233]. The linear viscous thinning regime is followed by an exponential elasto-capillary regime in which the filament diameter decays as $D \sim \exp(-t/3\tau)$. Because the fluid filament formed after the step deformation in a CaBER device experiences the deformation kinematics of a uniaxial elon-

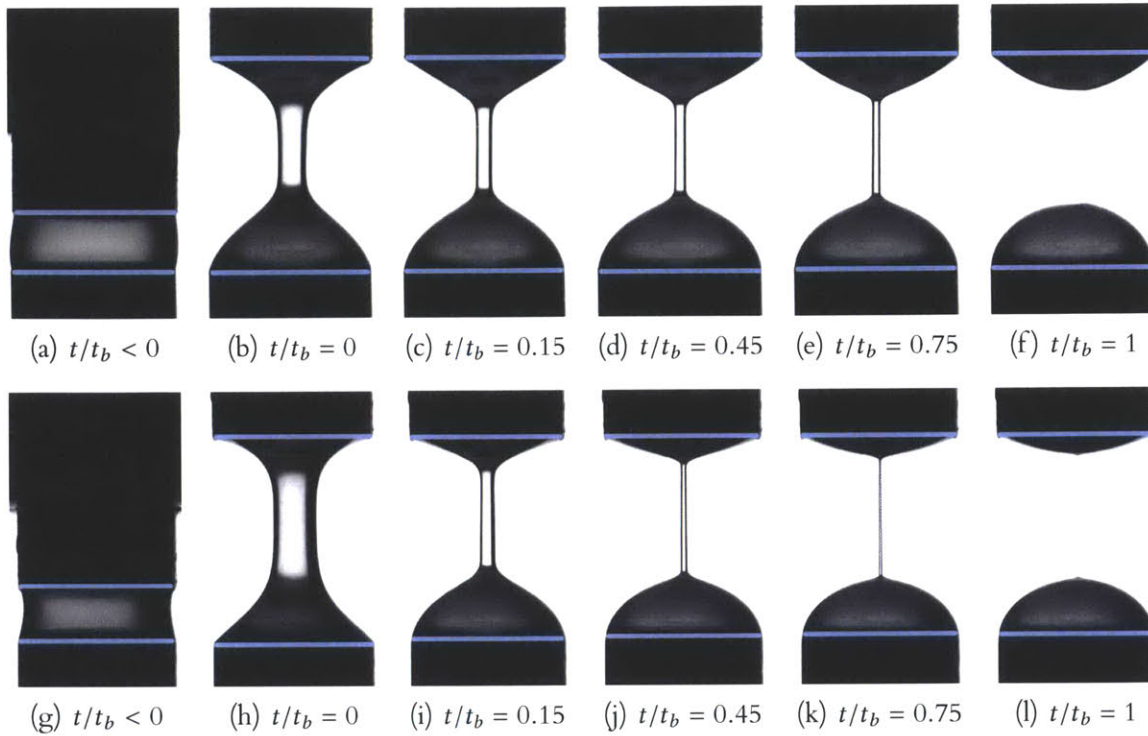


Figure 6.1.6: Snapshots of CaBER experiments for 2.5 wt. % (top row) and 5.0 wt. % (bottom row) Mamaku gum solutions. In both cases, it can be seen that the onset of the elasto-capillary regime, characterized by a uniform cylindrical fluid filament, occurs at around $t/t_b \approx 0.15$. For the 2.5 wt.% solution, the break-up time $t_b = 0.80$ s, while for the 5 wt.% solution, $t_b = 55.30$ s. The initial gap is $L_0 = 2$ mm, the final gap $L_f = 8$ mm, and the plate diameter $D_0 = 6$ mm. This yields an initial aspect ratio of $\Lambda_0 = 0.33$ and a final aspect ratio of $\Lambda_f = 1.33$.

gational flow, the polymeric chains of Mamaku gum are constantly accumulating strain, and elastic stresses in the filament increase with time. At one particular instant of time, the elastic stress contribution exceeds that of the viscous stresses, and the capillary forces are predominantly balanced by the elastic stresses [231]; the breakup dynamics now enters the elasto-capillary regime which is characterized by the formation of a uniform cylindrical liquid bridge of constant diameter between two filament ‘feet’ attached at each endplate. In this regime, the evolution of the diameter as a function of time is given by equation 6.1.2. From figure 6.1.6, we see that for both the 2.5 wt% and 5 wt. % solutions, the elasto-capillary regime is established for $t/t_b \gtrsim 0.15$. Anna and McKinley[231] have discussed that during a CaBER experiment, the diameter evolution as a function of time can gener-

ally be fit by a function of the form

$$D(t) = ae^{-bt} - ct + d \quad (6.1.9)$$

where a , b , c and d are constants, and this functional form captures both the early time viscous regime as well as the subsequent elasto-capillary regime. The coefficient b is related to the relaxation time of the fluid, and the value of c is related to the steady state extensional viscosity plateau at large Hencky strains.

We show the midplane diameter of the liquid bridge $D_{\text{mid}}(t)$ as a function of time for 2.5 wt.%, 5.0 wt.% and 7.0 wt.% Mamaku gum solutions respectively. As the Mamaku gum concentration is increased, breakup of the fluid filament occurs at larger times; we measure the breakup time t_b as being 0.80 s, 55.3 s and 89.2 s for the 2.5 wt.%, 5.0 wt.% and 7.0 wt.% solutions respectively. From the $D_{\text{mid}}(t)$ vs. t data, we can now use equation 6.1.2 in the elasto-capillary regime of the experiment to determine the relaxation time of the fluids, and these are $\tau = 0.16$ s, $\tau = 4.55$ s and $\tau = 6.28$ s for the 2.5 wt.%, 5.0 wt.% and 7.0 wt.% solutions respectively. We can also use the $D_{\text{mid}}(t)$ vs. t data to calculate the transient extensional viscosities η_E^+ of the Mamaku gum solutions using equation 6.1.4. In figure 6.1.8a, we show the variation of η_E^+ as a function of the Hencky strain at the filament midplane $\epsilon_H(t)$; the latter was calculated using equation 6.1.1. To find the derivative of the midplane diameter $dD(t)/dt$, rather than fitting a function of the form given in equation 6.1.9, we

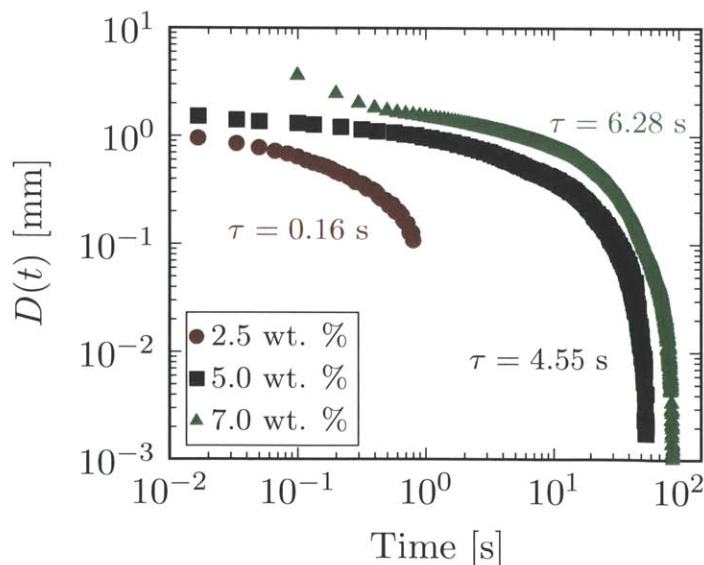


Figure 6.1.7

Diameter of the fluid filament as a function of time for CaBER experiments performed on different concentrations of Mamaku gum. The relaxation times shown in the figure is determined by fitting equation 6.1.2 to the elasto-capillary regime of the experiment. The relaxation time τ increases with increasing Mamaku concentration.

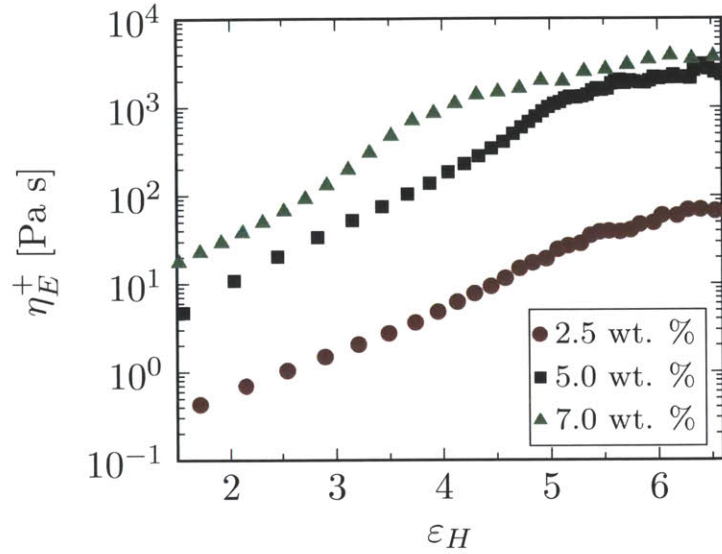
directly differentiate the measured data for the diameter (shown in figure 6.1.7) and apply a minimal amount of smoothing (3 point moving average). The surface tensions for the 2.5 wt. %, 5.0 wt.% and 7.0 wt.% was measured to be $\sigma = 44.6$ mN m, $\sigma = 33.7$ mN m and $\sigma = 33.5$ mN m respectively. We observe that at large values of Hencky strain ε_H , the transient extensional viscosity η_E^+ for the 5.0 wt.% and 7.0 wt.% solutions are both of the order $\mathcal{O}(10^3 \text{ Pa s})$.

For the semidilute Mamaku gum solutions used in this study, the coil overlap parameter ranges between $1.27 < c/c^* < 3.18$, based on the value of $c^* = 2.2$ wt. % determined by Goh et al.[71] The measured value of the steady extensional viscosity are an order of magnitude higher than the steady state extensional viscosities of other polysaccharide systems with the same values of c/c^* used in this study, for example, hydroxypropyl guar gum solutions[246] and sodium hyaluronate[213]. This indicates that intermolecular interactions during extension are significantly higher for Mamaku gum as compared to many other polysaccharide systems. We have already noted from Figure 6.1.3 that the shear viscosities of the Mamaku gum solutions increase as the concentration is increased. In the elasto-capillary regime, the flow field in the CaBER device is well described by uniaxial elongational kinematics and hence is shear-free. Therefore, to separate out the effect of increasing shear viscosity with concentration (cf. Figure 6.1.3), we define the Trouton ratio Tr as

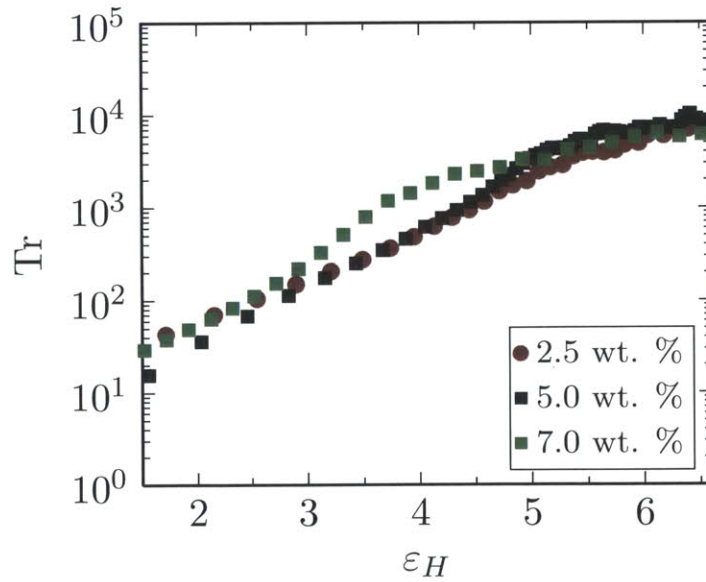
$$\text{Tr} = \frac{\eta_E^+}{\eta_0} \quad (6.1.10)$$

in which η_E^+ is the transient extensional viscosity of the fluid, and η_0 is the zero shear viscosity. For a Newtonian fluid[177], the Trouton ratio is a constant, and $\text{Tr} = 3$. We show the values of the Trouton ratio Tr for Mamaku gum solutions in Figure 6.1.8b. We observe that the Trouton ratio remains relatively unchanged upon changing the Mamaku gum concentration, indicating that increasing the concentration of Mamaku gum affects the shear properties of the gum more than the form of the extensional response.

Having characterized the extensional rheology of urea-free Mamaku gum solutions, we next study the changes induced in the rheological response of Mamaku gum solutions when hydrogen bonding interactions are suppressed, by studying Mamaku-Urea mixtures in the CaBER device. In figure 6.1.9a we show the transient extensional viscosity η_E^+ of 2.5 wt. % Mamaku gum solutions with various molar concentrations of urea added. Figure 6.1.9b shows the corresponding values of η_E^+ for 5 wt.% Mamaku gum solution with added urea of



(a)



(b)

Figure 6.1.8: (a) Transient extensional viscosity of different concentrations of Mamaku gum calculated using equation 6.1.4. (b) Trouton ratio $Tr = \eta_E^+/\eta_0$ for the same concentrations of Mamaku gum shown in (a). Whereas the extensional viscosity increases with increasing Mamaku gum concentration c , the Trouton ratio is nearly independent of c .

varying molar concentrations. We observe the expected trend of a decrease in $\eta^+ a_E$ and Tr with increasing urea concentration in both cases, indicating that once again the addition of urea interferes with the intermolecular hydrogen bonds formed by Mamaku gum in solution.

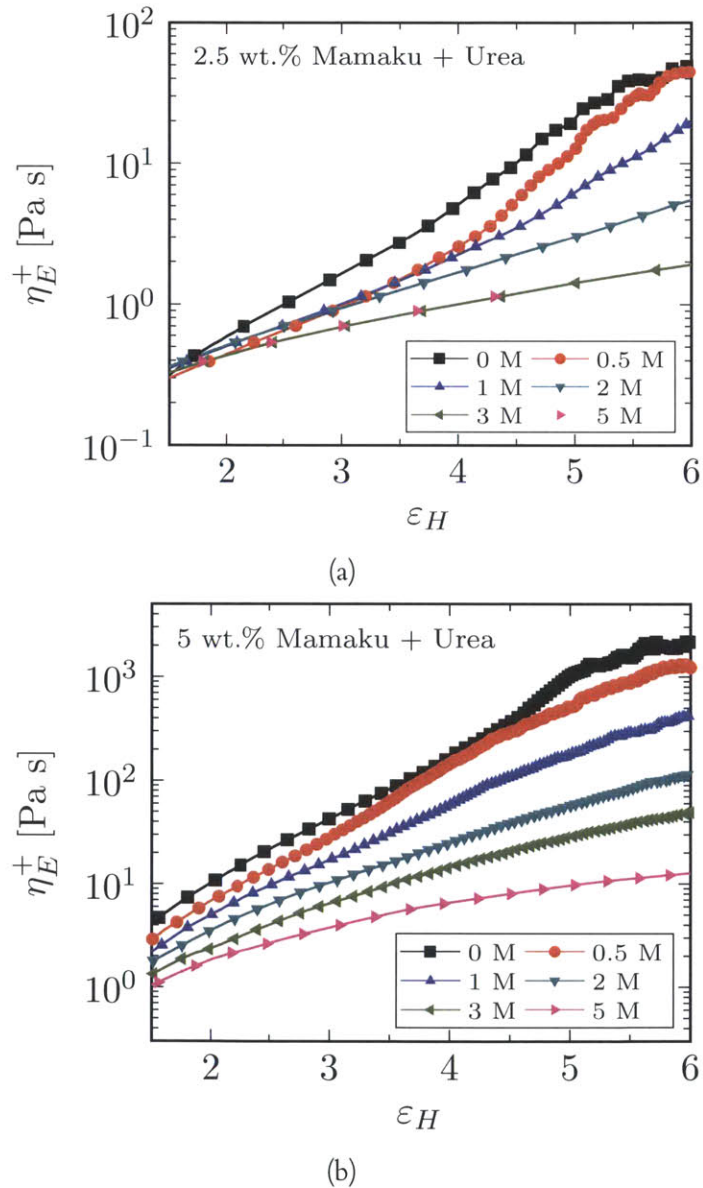
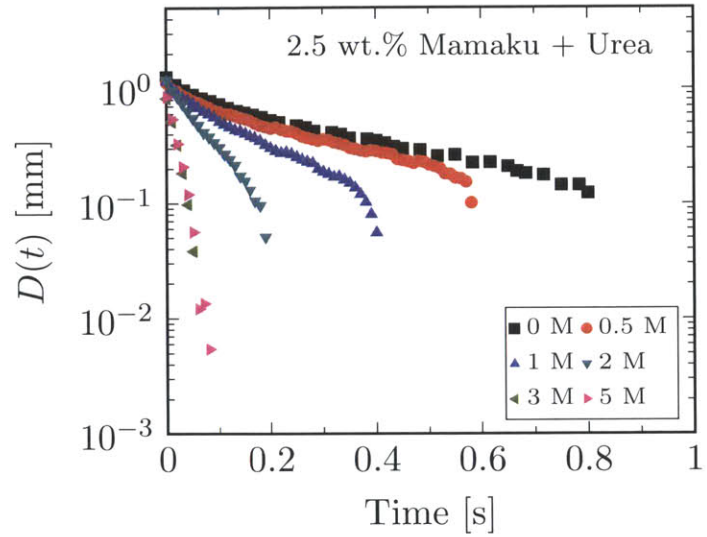


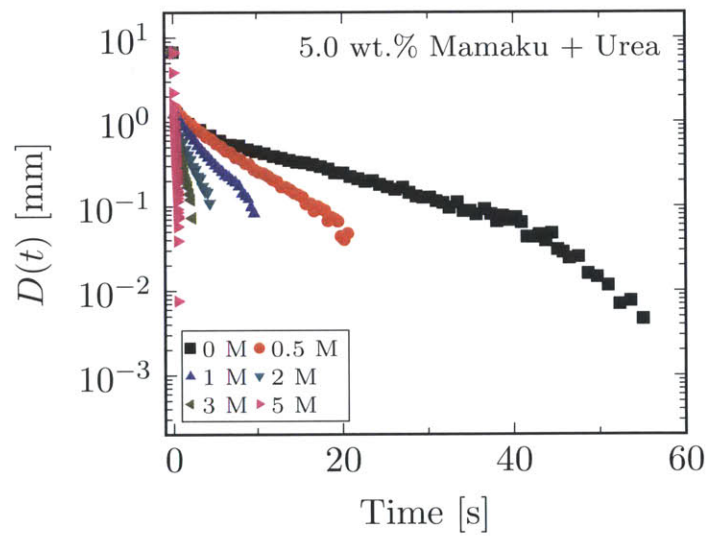
Figure 6.1.9: The transient extensional viscosity η_E^+ of 2.5 wt. % (a) and 5.0 wt. % (b) Mamaku gum solutions measured in a CaBER device. In both solutions, η_E^+ drops by nearly two orders of magnitude when the urea concentration is increased from 0 M to 5 M.

The breakup dynamics of the Mamaku gum solutions in the presence of urea can be directly observed by studying the evolution of the midplane diameter $D(t)$ as a function of time t . We show these curves for 2.5 wt. % and 5 wt. % solutions with varying concentrations of added urea in Figures 6.1.10a and 6.1.10b respectively. We immediately observe that for both concentrations of Mamaku gum solutions, the breakup time t_b strongly decreases with increasing urea concentration. This indicates that the elastic stresses generated in the fluid filament formed upon imposition of the step extensional deformation are greatly reduced in comparison to the capillary stresses. This is again a consequence of the Mamaku macromolecules in solution preferentially forming hydrogen bonds with urea molecules rather than intermolecular Mamaku–Mamaku hydrogen bonds. The data also allows us to conjecture that a concentration of 0.5 M of added urea is enough to disrupt all the hydrogen bonding sites along the chain when it is coiled, but not as it stretches out; there is an upturn in the transient extensional viscosity η_E^+ for $\epsilon_H > 4$. This possibly arises from new sites for hydrogen bonding that are exposed during the unraveling process.

From the curves showing the evolution in midplane diameter with time, we can also calculate the characteristic relaxation time for each specific Mamaku–Urea mixture from the midplane diameter vs. time curves by fitting an exponential of the form given by equation 6.1.2 in the elasto–capillary regime. We show the values of the relaxation times thus extracted on a log–linear scale in Figure 6.1.11 as a function of the urea concentration in the mixture. Although we do not show the individual time traces in this paper, we have also performed CaBER experiments on 7.0 wt.% Mamaku gum solutions with the same concentrations of urea added as in the 2.5 wt.% and 5.0 wt.% solutions. The relaxation times of these solutions are also shown in Figure 6.1.11. Note that the relaxation time is a function of the concentrations of two different components present in the mixture: the Mamaku gum concentration as well as the urea concentration present in the mixture, i.e., $\tau \equiv \tau(c_{\text{Mamaku}}, c_{\text{urea}})$. In figure 6.1.11 the relaxation time of each Mamaku–urea mixture has been non-dimensionalized by the value of the relaxation time $\tau^0 = \tau(c_{\text{Mamaku}}, 0)$ obtained for the Mamaku gum solution of concentration c_{Mamaku} with zero added urea ($c_{\text{urea}} = 0$). We denote this non-dimensionalized relaxation time by the notation $\bar{\tau} = \tau(c_{\text{Mamaku}}, c_{\text{urea}})/\tau^0$. Moreover, we scale the horizontal axis by 5 M, which is the maximum urea concentration used in the mixtures, and hence, the lower and upper bounds of the abscissa are 0 and 1 respectively. We find that for all the Mamaku concentrations tested in this study (2.5, 5.0 and 7.0 wt.%), the relaxation time varies exponentially with

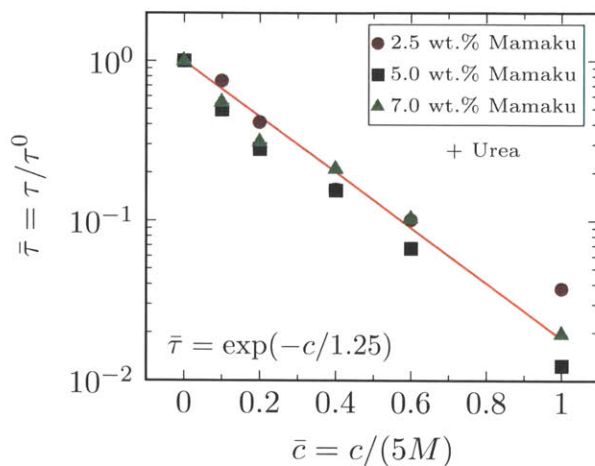


(a)



(b)

Figure 6.1.10: The diameter $D(t)$ as a function of time t of 2.5 wt. % (a) and 5.0 wt. % (b) Mamaku gum solutions measured during CaBER experiments, plotted on a log-linear scale. Increasing the urea concentration leads to earlier breakup and a drop in viscoelasticity. The magnitude of the slope of the $D(t)$ vs. t curves is inversely related to the relaxation time τ ; for both Mamaku concentrations, the relaxation time decreases upon increasing urea concentration.

**Figure 6.1.11**

(a) The normalized relaxation time $\bar{\tau} = \tau/\tau^0$ for Mamaku/urea mixtures calculated from CaBER experiments, where τ^0 is the relaxation time of the pure Mamaku solution (0 M urea). The relaxation times fall onto a master curve given by $\bar{\tau} = \exp(-0.8c)$, independent of the Mamaku concentration. (b) An identical exponential dependence is observed in the variation of the peak shear viscosity with urea concentration, as well as the reciprocal of the critical shear rate at which the peak shear viscosity is observed, shown here for a 5 wt.% solution of Mamaku.

increasing Mamaku concentration (i.e. we observe linear decay on a log-linear scale), and $\bar{\tau} = \exp[-0.8c]$. Comparing this result with what we obtain from figure 6.1.5, we find that this exponential form is identical to that obtained for the dependence of the characteristic shear thickening timescale τ_p on the concentration of urea. Equation 6.1.5). The presence of the identical exponential forms across Mamaku gum concentrations in both shear and extensional rheology experiments suggests a common origin which can be rationalized by examining the influence that the addition of urea has on the lifetime of the intermolecular hydrogen bond associations present in Mamaku gum.

The rheological response and strong shear-thickening behavior of Mamaku gum is reminiscent of other physically crosslinked networks that form temporary, reversible associations [20]. These associations may arise from a number of physical mechanisms, for example hydrophobic interactions [247], ion complexation [239] and, most relevant to this study, hydrogen bonding [248]. Leibler et al. have developed a theory for soft reversible networks called sticky reptation [249], which applies to networks formed by linear chains with multiple temporary cross-links along the chain (For example the modified polybutadienes studied by Freitas and Stadler [250]). The relaxation time of a system that relaxes through sticky reptation is given by [20, 249]

$$\tau \approx \left(\frac{N}{N_e}\right)^{1.5} \frac{2S^2\tau_d}{1 - 9/p + 12/p^2} \quad (6.1.11)$$

in which N is the number of monomers per chain, N_e is the number of monomers in an

entanglement segment, S is the number of stickers per chain and p is the average fraction of stickers that are associated at any given time. The timescale τ_d is the average time a sticker spends in the associated state, and is given by [20, 251]

$$\tau_d = \omega_0^{-1} e^{\Delta G/k_B T} \quad (6.1.12)$$

in which ΔG is the free energy barrier for disassociation, k_B is Boltzmann's constant, T is the absolute temperature and ω_0 is a vibration frequency that determines the average number of times per second the sticker tries to climb the energy barrier for dissociation as a result of thermal fluctuations [251]. Substituting Equation 6.1.12 into Equation 6.1.11, we obtain

$$\tau \approx \omega_0^{-1} \left(\frac{N}{N_e} \right)^{1.5} \frac{2S^2}{1 - 9/p + 12/p^2} e^{\Delta G/k_B T} \quad (6.1.13)$$

It is evident from the above equation that the relaxation timescale τ of a particular system depends exponentially on the free energy for disassociation ΔG , all other parameters being held constant. Our experimental observations in Figure 6.1.11 show that the relaxation time τ decreases exponentially with increasing concentration of urea. This is only possible if adding urea to the Mamaku gum solutions modifies the free energy ΔG in such a way that

$$\Delta G = \Delta G^0 - mc \quad (6.1.14)$$

Here ΔG^0 is the free energy for disassociation in the absence of any urea, c is the concentration of urea added and m is a constant. Substituting Equation 6.1.14 into Equation 6.1.13 we obtain

$$\tau = \tau^0 e^{-mc/k_B T} \quad (6.1.15)$$

where τ^0 is the relaxation time of the hydrogen bonded temporary network in the absence of urea and is given by

$$\tau^0 = \omega_0^{-1} \left(\frac{N}{N_e} \right)^{1.5} \frac{2S^2}{1 - 9/p + 12/p^2} e^{\Delta G^0/k_B T} \quad (6.1.16)$$

The linear dependence of the free energy ΔG on the urea concentration c given in Equa-

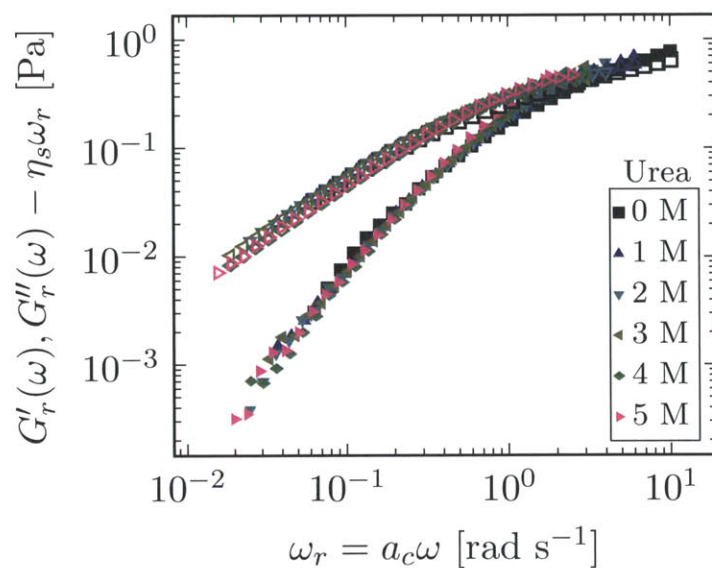
tion 6.1.14 has been experimentally observed in the context of protein solutions. Greene and Pace have observed that adding denaturants such as urea or guanidine hydrochloride (GmHCl) to various protein solutions results in a linear decrease of the free energy for denaturation with denaturant concentration [252]. Similar observations have been made by many other studies of protein denaturation [253–255]. In fact, the denaturation energies ΔG^0 for protein solutions are routinely found by linearly interpolating the ΔG vs c curve to zero denaturant concentration [256]. Our results show that this linear relationship holds at least for the Mamaku gum polysaccharide, and possibly for other polysaccharide systems as well. From our experimental result of $\tau = \tau^0 e^{-0.8c}$, we calculate a value of $m = 471.9 \text{ cal/mol} \cdot \text{M}$ ($m = 1982 \text{ J/mol} \cdot \text{M}$), where units of M stand for molarity of urea in Molar. The m value quantifies the strength of the interaction of a hydrogen bond-disruptor such as urea with the Mamaku gum polysaccharide; the larger the m value, the stronger the interaction between the bond-breaker and the polysaccharide, and the more pronounced is the ability of the bond-disruptor to decrease the free energy barrier for disassociation. The value of m will vary not only with the specific chemical used, but also the polysaccharide system [253]. Myers et al. have listed the m values of various proteins-denaturant combinations, and the m values for urea range from $250 \text{ cal/mol} \cdot \text{M}$ to as high as $7800 \text{ cal/mol} \cdot \text{M}$ [253].

Note that our experimental observation of an exponential dependence of τ on urea concentration c indicates that the addition of urea does not modify the other network parameters such as the number of stickers per chain S or the average fraction of stickers that are associated at any given time p ; it is only the dissociation lifetime τ_d that is modified through the variation in the free energy barrier for disassociation. This implies that there are no fundamental structural changes induced in the Mamaku gum polysaccharide upon the addition of urea, such as in the number of stickers per chain S or the average fraction p of stickers that are associated at any given moment. This presents the possibility of a *time-concentration* superposition principle. Time-temperature superposition is widely used in rheology to measure the relaxation spectra of polymeric systems at frequencies that are experimentally inaccessible [257]. It has been observed that for complex fluids that obey time-temperature superposition, small amplitude oscillatory shear experiments may be performed at different temperatures and then shifted along the frequency axis using a shift factor a_T to obtain a master curve of the relaxation spectrum of the fluid over many decades of frequency. Such fluids are said to be thermorheologically simple, and time-temperature

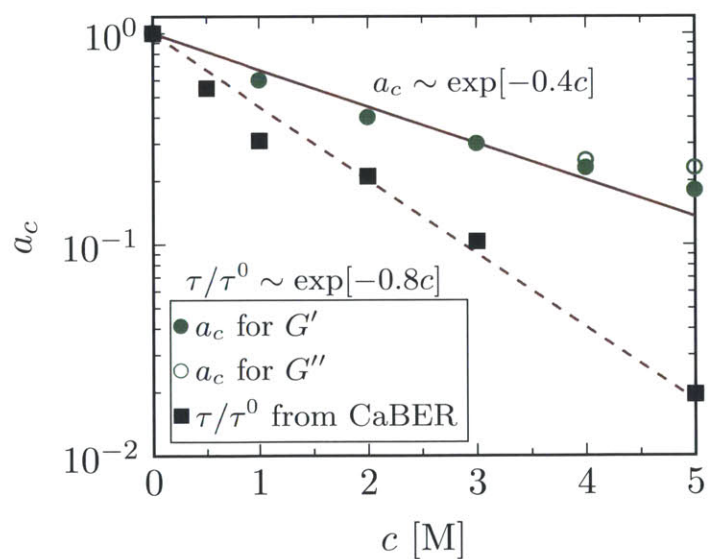
superposition holds for polymeric systems that do not undergo structural changes upon a change in temperature [257]. As discussed above, we observe no structural changes in Mamaku gum polysaccharide molecules upon the addition of urea, and we expect a time-concentration superposition principle to exist in this case.

In figure 6.1.12(a) we show the values of the reduced storage and loss moduli, $G'_r(\omega)$ and $G''_r(\omega)$ respectively, of a 5 wt. % Mamaku gum solution with a range of different molar concentrations of added urea. We have shifted these curves along the frequency axis using a shift factor a_c to construct a reduced frequency $\omega_r = a_c\omega$. The subscript c denotes that this shift factor is a function of the urea concentration c . We note that the values of $G'(\omega)$ for each of the different Mamaku gum-urea mixtures fall on a master curve over nearly three decades of frequency. Again, this confirms the fact that there are no major structural changes introduced upon the addition of urea, and it is only the timescale of hydrogen bond association and dissociation that is altered. Figure 6.1.12(b) shows the values of the shift factors a_c used to construct the master curve as a function of the urea concentration c . The concentration shift factor a_c varies exponentially, with $a_c \sim e^{-0.4c}$. The coefficient 0.4 in the exponential yields a urea sensitivity of $m = 235.9 \text{ cal/mol} \cdot \text{M}$ ($m = 991 \text{ J/mol} \cdot \text{M}$). This value is lower than the value $m = 471.9 \text{ cal/mol} \cdot \text{M}$ we obtained previously from nonlinear shear and extensional rheology experiments. The latter is shown as black squares in Figure 6.1.12.

The differing urea sensitivities between linear and nonlinear deformations (which we quantify in terms of the magnitude of the shift factors) indicates that the Mamaku gum solutions are *rheologically* complex. The complexity can be explained in terms of the increased chain extension of Mamaku gum solutions under a nonlinear flow. In the case of proteins, the sensitivity to denaturants has been found to be larger for proteins that are in more extended or unfolded conformations[253], and this effect has been studied by controlling the amount of unfolding of the protein molecule by varying the pH[258, 259]. Previous rheological studies have shown that Mamaku gum solutions are relatively insensitive to change in pH [73]. However a steady shear flow at high shear rates or extensional flows such as that produced in the CaBER device can elongate the Mamaku gum polysaccharide chains and this appears to lead to much larger required shifts as compared to those found from a linear viscoelastic experiment. Upon the imposition of a nonlinear deformation (say steady shearing flow at a shear rate $\dot{\gamma} \approx \dot{\gamma}_p$), the elongated chain now has additional exposed sites for hydrogen bonding (i.e.) the value of S in Equation 6.1.13 is modified. The



(a)



(b)

Figure 6.1.12: (a) The values of $G'_r(\omega)$ (solid symbols) and $G''_r(\omega)$ (hollow symbols) measured in an SAOS experiment for a 5 wt. % Mamaku gum solution with different concentrations of added urea. The curves have been shifted along the frequency axis using a shift factor a_c to generate a master curve. (b) The values of the shift factor a_c as a function of urea concentration required to generate the master curves of $G'_r(\omega)$ and $G''_r(\omega)$. There is an exponential relationship between a_c and urea concentration c . However, the dependence of the shift factor on urea concentration is stronger in the nonlinear experiments (black squares) as compared to the linear SAOS experiments.

hydrogen bonding at these additional exposed sites are also influenced by the addition of urea. In fact, the shift factor obtained from nonlinear rheology is almost exactly a factor of 2 larger than linear rheology. This suggests that nonlinear effects arise from pairwise interactions. Detailed investigation of the microstructural origins of the different sensitivities in weak and strong flows requires further experimental and computational studies, for example, kinetic theory simulations.

6.1.4 Filament Stretching Extensional Rheometry

One drawback of the CaBER device is that over the duration of the experiment, not only does the Hencky strain ϵ_H imposed on the fluid sample increase as a function of time, but the strain rate $\dot{\epsilon}$ imposed on the fluid sample also varies with time. The latter is a consequence of the thinning fluid filament choosing its own breakup dynamics according to the balance of viscous, elastic and capillary forces in a CaBER experiment ([260]).

In a FiSER experiment, a test fluid is placed between two parallel plates of diameter D_0 initially separated by a gap L_0 [61]. The plates are then pulled apart from each other to yield a time-varying gap $L(t)$. The strain rate $\dot{\epsilon}$ at the midplane of the resultant fluid filament is given by

$$\dot{\epsilon} = -\frac{2}{D(t)} \frac{dD(t)}{dt} = \frac{1}{L(t)} \frac{dL(t)}{dt} \quad (6.1.17)$$

From Equation 6.1.17, it can be shown that in order to obtain a constant strain rate, the gap $L(t)$ should be varied in an exponential fashion, i.e. $L(t) = L_0 \exp(\dot{\epsilon}t)$ (by contrast, the gap in a CaBER experiment is varied instantaneously, closely approximated by a step-function). As $L(t)$ is varied, the midplane diameter $D(t)$ as well as the normal force $F(t)$ exerted by the stretching fluid filament are continuously measured. These quantities can subsequently be used to calculate the extensional modulus $G_E^+(\epsilon_H, t)$ which is given by

$$G_E^+(\epsilon_H, t) = \frac{\sigma_{11} - \sigma_{22}}{\epsilon_H} = \frac{F(t)}{\pi R^2(t) \epsilon_H} \quad (6.1.18)$$

where $R(t) = D(t)/2$ is the instantaneous midplane radius, and σ_{11} and σ_{22} are the axial and radial components, respectively, of the stress tensor. We show a schematic figure of our FiSER device in Figure 6.1.13

In Figure 6.1.14, we show snapshots of FiSER experiments performed on two Mamaku-

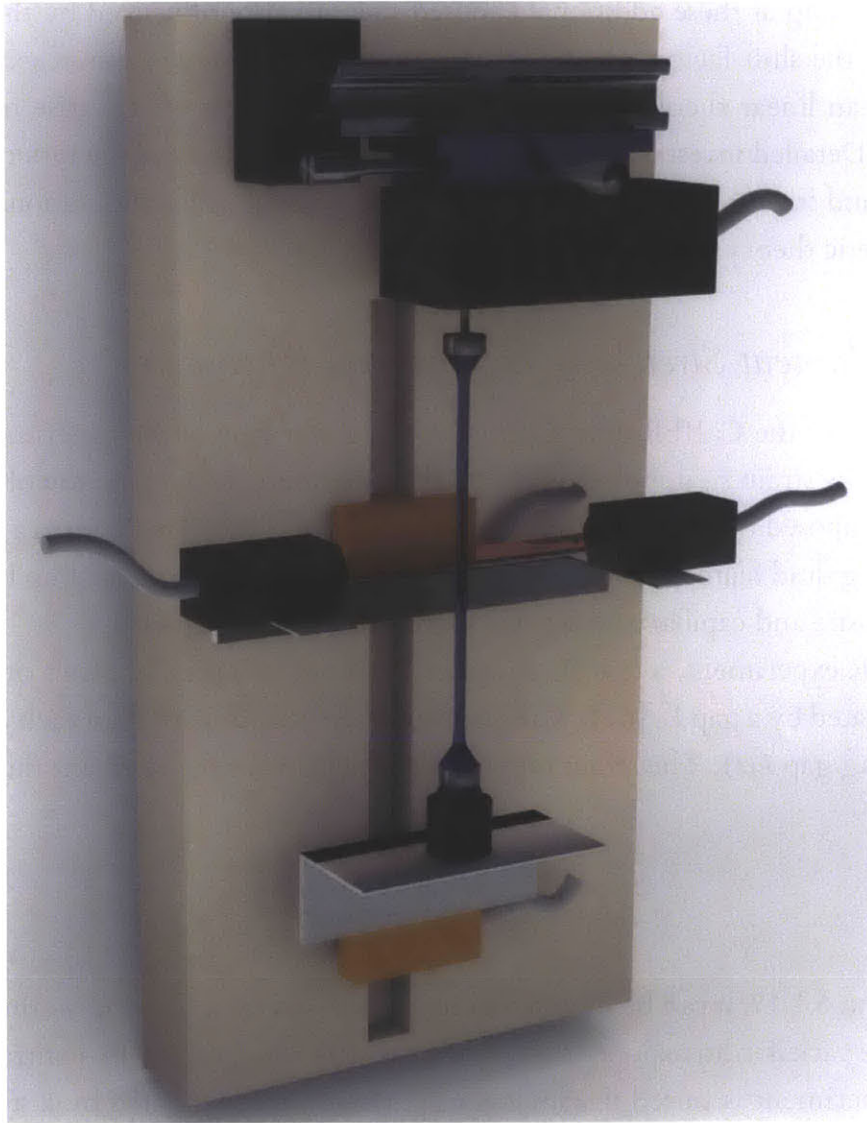


Figure 6.1.13: A schematic figure of the FiSER device. In a FiSER experiment, a fluid filament is set up between two parallel plates (shown in blue) and the bottom plate is then pulled apart in an exponential manner, to obtain a desired strain rate. A laser sheet (shown in red) continuously measures the midplane diameter of the filament and a force transducer measures the normal force during the stretch.

urea mixtures (5 wt.% Mamaku gum with 0M urea and 3M urea). Each row corresponds to a single Mamaku-urea mixture, and each column corresponds to a fixed value of Hencky strain ε_H at the midplane of the fluid filament, whose values are given as column headers. The scalebar is the same length as the diameter of the plates ($D_0 = 6$ mm). We observe that

at a fixed value of Hencky strain ϵ_H , the stretch ratio $\lambda = L(t)/L_0$ is much smaller in the case of the solution with 3M added area as opposed to the urea-free solution. This indicates that the breakup of the filament occurs much earlier in the 3M urea solution. This is direct consequence of the decreased elasticity of the Mamaku gum solution upon the addition of urea; the higher elasticity of the pure Mamaku gum solution retards filament breakup and hence we are able to reach much larger stretch ratios λ before breakup in this case.

To study the viscoelasticity of the Mamaku gum solutions as a function of strain rate in a quantitative manner, we perform FiSER experiments at various values of Weissenberg number $Wi = \lambda \dot{\epsilon}$ for the three different Mamaku-urea mixtures. The results of these experiments are shown in Figure 6.1.15. Figures 6.1.15(a),(c) and (e) show the normal stress difference $\sigma_{11} - \sigma_{22}$ as a function of Hencky strain ϵ_H imposed on the fluid filament for the different Mamaku-urea mixture (the particular composition of the mixture is given in each graph). In all cases, the fluid is strain-hardening, and the normal stress difference increases

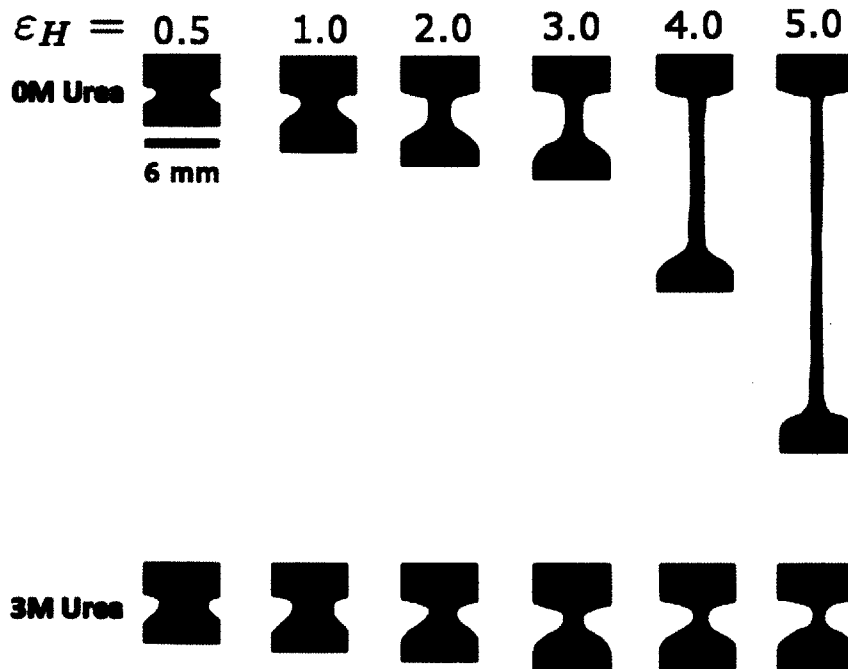


Figure 6.1.14: Snapshots of the fluid filament during a FiSER experiment. The top row of images is of a 5 wt. % Mamaku gum solution, while the bottom row corresponds to a 5 wt. % Mamau gum solution with urea added at a concentration of 3 M. The Hencky strains ϵ_H at which the images were taken are given at the top of the figure. Upon the addition of urea, the viscoelasticity of the polysaccharide gum is dramatically decreased, and the breakup of the fluid filament occurs at much smaller stretch ratios compared to the urea-free solutions.

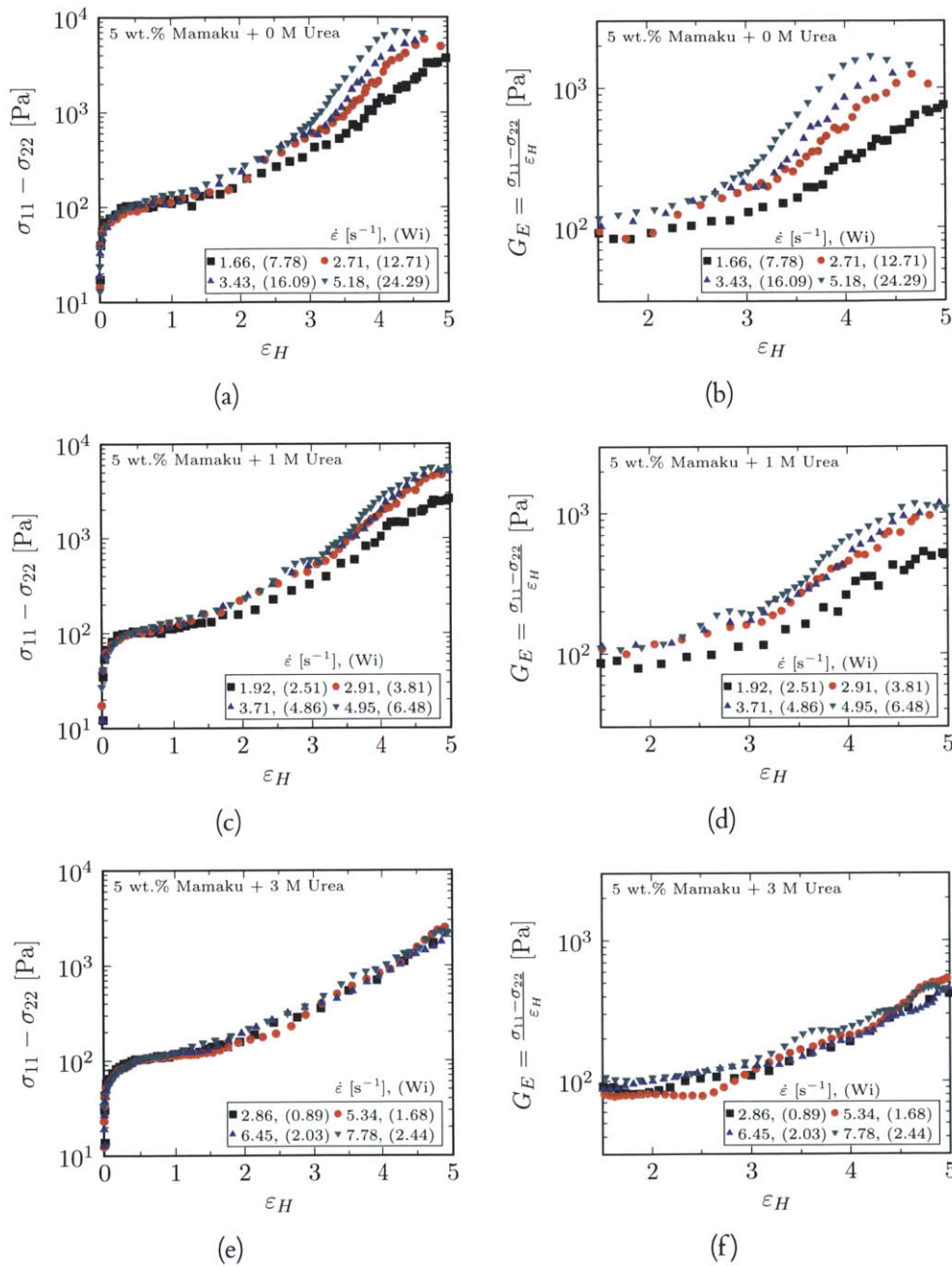


Figure 6.1.15: Stress vs. Hencky strain ((a),(c),(e)) and modulus vs. Hencky strain ((b),(d),(f)) obtained from filament stretching experiments for different Mamaku/urea mixtures. In all cases, the Mamaku/urea mixtures are strain hardening. The stress is strain-rate independent for small strains, and shows rate dependency as the Hencky strain increases. The stress (and correspondingly the modulus) increase with increasing nominal strain rate for the 0 M urea and 1 M urea mixtures. However, no clear trend is observed for the 3 M urea mixture. This is because the relaxation time of the 3 M urea solutions is so low ($\lambda = 0.31$ s.) that the maximum experimentally imposable Weissenberg number is not high enough to exhibit any rate dependence.

with increasing Hencky strain. However, it is evident from the figures that upon increasing the urea concentration, the amount of strain hardening is decreased. We only observe a weak dependence of the first normal stress on the strain rate $\dot{\epsilon}$.

In Figures 6.1.15(b), (d) and (f), we show the modulus G_E^+ as a function of Hencky strain ϵ_H . In these figures, the changes induced in the viscoelasticity of the Mamaku gum solutions upon the addition of urea are clearly apparent; comparing Figures 6.1.15(b) and (f), we observe that the modulus G_E^+ decreases by nearly an order of magnitude with increasing urea, again indicating that the interactions in Mamaku gum predominantly arise from hydrogen bonding. Whereas we note that there is some strain rate dependence of the modulus G_E^+ from the solutions with no added urea, G_E^+ is practically independent of strain rate for the mixtures with 3 M urea.

The FiSER results presented in this section complement the results obtain from the CaBER device presented in the main manuscript. The addition of urea to Mamaku gum dramatically decreases the viscoelasticity of the gum solutions, demonstrating that the intermolecular associations are predominantly arise from hydrogen bonding.

6.1.5 Conclusions

The steady shear flow curves of Mamaku gum solutions exhibit a pronounced shear-thickening response, which is very unusual for polysaccharide systems [64]. At a critical shear rate $\dot{\gamma}_p$, the shear-thickening ceases and there is an onset of extreme shear-thinning, which occurs at an approximately constant shear stress σ_p for all experimentally imposed shear-rates $\dot{\gamma} > \dot{\gamma}_p$. In this paper, we have explored the origin and consequence of this shear thickening behavior; through a combination of shear and extensional rheology experiments performed on Mamaku gum-urea mixtures, we have determined the source of the shear-thickening to be intermolecular hydrogen bonding.

Nonlinear steady shear experiments reveal that increasing the amount of urea in the mixture (while holding the Mamaku gum concentration a constant), both the zero shear viscosity η_0 as well as the peak viscosity in the shear-thickening regime η_p progressively decrease. The reciprocal of the shear rate $\dot{\gamma}_p$ at which the peak viscosity appears, provides a characteristic timescale of the fluid in nonlinear deformation, also become smaller; in fact both η_p and $\tau_p = \dot{\gamma}_p^{-1}$ decrease exponentially with increasing urea concentration.

Transient extensional rheometry performed using a CaBER device demonstrate that the relaxation time in extension also follows an exponentially decreasing relationship with

increasing urea concentration. Moreover, this exponential dependence on relaxation time with urea concentration is identical to that obtained from nonlinear shear experiments. We interpret this in terms of the modification of the free-energy barrier for hydrogen bond dissociation, leading to an exponential relationship between the dissociation timescale of hydrogen bonds with urea concentration. Our experiments are consistent with the expected relaxation dynamics of Mamaku gum-urea mixtures predicted by the sticky reptation theory for reversible networks of polymers with multiple associative groups along the backbone. We show that this leads to the concept of a time-concentration superposition principle, akin to the more familiar time-temperature superposition used for concentrated polymer solutions or polymer melts. However we find that the linear and nonlinear rheology of the Mamaku gum-urea mixtures shift by different extents upon addition of urea. By analogy with other polymeric systems which are described as thermorheologically complex, we may refer to Mamaku gum solutions as *urheologically* complex.

This rheological study improves our understanding of Mamaku gum solutions in particular and shear thickening polysaccharides in general. Mamaku gum has traditionally been used as a food source by the native Maori tribes of New Zealand [71]. The shear thickening properties and the pH insensitivity make it an excellent potential food thickener to aid patients with dysphagia. The ability to independently control the linear and nonlinear rheological characteristics via the different sensitivities to hydrogen bond disruptors offers an additional level of formulation control. Additional controlled trials on the safety and the efficacy of Mamaku gum, as well as the behavior of the gum in mammalian digestive tracts would greatly help towards realizing this possibility.

6.2 Hyaluronic Acid

We utilize a recently developed microfluidic device, the Optimized Shape Crossslot Extensional Rheometer (OSCER), to study the elongational flow behavior and rheological properties of hyaluronic acid (HA) solutions representative of the synovial fluid (SF) found in the knee joint. The OSCER geometry is a stagnation point device that imposes a planar extensional flow with a homogenous extension rate over a significant length of the inlet and outlet channel axes. Due to the compressive nature of the flow generated along the inlet channels, and the planar elongational flow along the outlet channels, the flow field in the OSCER device can also be considered as representative of the flow field that arises between

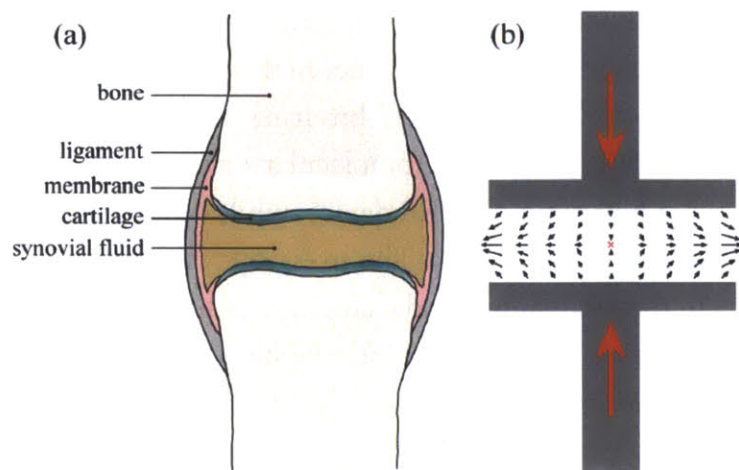
compressing articular cartilage layers of the knee joints during running or jumping movements. We show this by modeling the flow field in a joint as a squeeze flow of a power law fluid, and analyze the resulting kinematics in detail. Full-field birefringence microscopy measurements demonstrate a high degree of localized macromolecular orientation along streamlines passing close to the stagnation point of the OSCER device, while micro-particle image velocimetry is used to quantify the flow kinematics. The stress-optical rule is used to assess the local extensional viscosity in the elongating fluid elements as a function of the measured deformation rate. The large limiting values of the dimensionless Trouton ratio, $Tr \sim \mathcal{O}(50)$, demonstrate that these fluids are highly extensional-thickening, providing a clear mechanism for the load-dampening properties of SF. The results also indicate the potential for utilizing the OSCER in screening of physiological SF samples, which will lead to improved understanding of, and therapies for, disease progression in arthritis sufferers.

6.2.1 Introduction

Hyaluronic acid (HA) is a naturally occurring linear polysaccharide composed of D-glucuronic acid and N-acetyl-D-glucosamine disaccharide units linked by alternating $\beta 1 \rightarrow 3$ and $\beta 1 \rightarrow 4$ glycosidic bonds [217, 261].

Hyaluronic acid is found abundantly in many biological systems and occurs in particularly high concentrations in the vitreous humour of the eyes, umbilical cord, cockerel comb, and the synovial fluid (SF) of the joints [70]. In healthy human synovial fluid, a broad range of values for the concentration of HA has been measured, ranging generally between around 0.05 and 0.4 wt. %, with 0.3 wt. % being typical [262–264]. The molecular weight of HA in healthy SF can be extremely high and has been reported as reaching more than 7 MDa [265]. The high concentration and molecular weight of the HA in SF confer strong viscoelastic properties to the fluid [266, 267]. Synovial fluid is highly viscous (on the order of 10's to 100's of Pa s) and is strongly shear thinning [213, 268]; a property which contributes to the highly effective lubrication of joints undergoing flexion. Synovial fluid is also highly elastic and it has been suggested that this may be the key to the shock-absorbing properties of SF that protects joints from sudden high-load impacts [269, 270].

Compression of the synovial fluid in the joint cavities (e.g., between the femur and tibia in the knee, when running or landing after a jump) can be considered (in a simplified sense) essentially as a squeeze flow between two compressing disks or plates (see Figure 6.2.1).

**Figure 6.2.1**

(a) Schematic drawing of a synovial joint highlighting the important anatomic features. (b) Simplified picture of the squeeze flow in a synovial joint undergoing a compressive deformation (such as occurs in the knees during locomotion). The black arrows indicate the flow of the synovial fluid being squeezed outwards orthogonal to the compression axis, resulting in a biaxial extensional flow at the mid-plane between joint surfaces and a stagnation point at the center of symmetry (marked by the red 'x').

In general, with a no-slip boundary condition at the plates, squeezing flows generate a complex time-varying and inhomogeneous flow field composed of strong shear near the surfaces of the plates and a biaxial extensional flow with a stagnation point at the mid-plane between the plates [203, 271]. At the stagnation point, the fluid velocity is zero, so the residence time of material elements in the flow can be (in principle) infinite. Under such circumstances, flexible macromolecules are expected to unravel and stretch to a considerable fraction of their contour length provided the extension rate $\dot{\epsilon}$ exceeds the reciprocal of the longest macromolecular relaxation time $1/\tau$. This condition defines a critical value for the dimensionless flow strength or Weissenberg number, $Wi = \tau \dot{\epsilon} \approx 1$, above which macromolecules will stretch [272]. This behavior has been demonstrated experimentally in many systems including direct observations of chain unraveling in fluorescently labeled DNA [273, 274] and measurements of flow-induced birefringence in synthetic and biological polymer solutions [62, 275]. Simulations of squeezing flows using a Finitely Extensible Non-linear Elastic (FENE) dumbbell-type model predict significant macromolecular stretching between the compressing plates for “fast squeezing”; i.e., when the timescale for the squeezing is much less than the relaxation time of the dumbbell or macromolecule [276].

If perfect slip is allowed at the solid surfaces of the plates, the squeezing flow generates a homogeneous biaxial extensional flow field with no contribution from shear [203]. Slip can be introduced into experimental squeeze flow apparatus through the introduc-

tion of thin layers of an immiscible low-viscosity lubricant at the plates, such that (ideally) shearing deformation is confined within the lubricating layer while the bulk fluid contained between the plates undergoes an homogeneous biaxial extension. Such lubricated squeezing devices have been demonstrated as effective biaxial extensional rheometers for relatively high-viscosity fluid samples such as polymer melts [277, 278]. For the flow of shear-thinning fluids in squeeze flows, shear localization at the plate surfaces has a similar effect to partial slip at the surfaces. Effectively the fluid self-lubricates, resulting in a more plug-like flow in the bulk and an increased dominance of extensional effects over shearing contributions to the flow in the region of the mid-plane between the plates. In the next section, we describe the kinematics of a power-law fluid undergoing a squeeze flow and quantify the extensional component of the deformation using a flow-type parameter.

We note that in a real joint the bounding surfaces (i.e., the cartilage) are in fact charged, porous and compressible [279, 280] and several mechanisms of joint lubrication have been suggested based on these physical properties of cartilage and their interaction with the synovial fluid. These include squeeze-film lubrication [279], weeping lubrication [281–283], boundary lubrication mediated by surface adsorbed lubricin proteins [284], and electrostatic binding of an HA network to the cartilage [280]. While our simple picture of the compressing joint (as illustrated in Figure 6.2.1 and explored in further detail in the next section) does not incorporate any of these additional complexities, we believe the basic squeeze flow description nevertheless captures many of the characteristics of the mixed extensional and shearing kinematics. Lubrication analysis of squeeze flow using a power-law constitutive model to represent the shear-thinning SF, clearly shows that for typical values of the geometric aspect ratio and shear-thinning exponent the flow field contains a significant region of extension-dominated flow. Based on this simplified scenario, we argue that in joints undergoing compressive deformations, shear-thinning of the synovial fluid at small gaps actually augments the importance of the extensional flow field between the two approaching cartilage surfaces.

Due to the very small gaps ($\sim \mathcal{O}(100 \mu\text{m})$) between the articular cartilage layers and the short time scales involved in sudden joint impacts, only small deformations are required to generate high values of the extensional strain rate $\dot{\epsilon}$, which is estimated to range between 1 and 1000 s^{-1} in the knee [285]. On the other hand, the high molecular weight of HA and the high viscosity of synovial fluid means the relaxation time τ of the HA in SF can be very long ($0.1 \leq \tau \leq 1$) s [213]. Hence, it is highly likely that biologically rele-

vant deformation rates generated within joints can result in high Weissenberg numbers for the HA macromolecules contained in the synovial fluid, and therefore induce significant stretching of the HA [269, 270]. The stretching of macromolecules in solution can result in orders of magnitude increases in elastic stresses and the corresponding measure of the transient extensional viscosity [286–288]. This provides a possible mechanism for energy dissipation during shock loading and the prevention of contact between cartilage layers in compressing joints [270].

In patients with osteo- and rheumatoid arthritis, the properties of synovial fluid become degraded, with both the concentration and molecular weight of the HA being significantly altered [262, 264, 265, 289–291] and the viscoelasticity significantly reduced. Monitoring the concentration and molecular weight of HA in SF (or alternatively the co-related viscoelastic properties of SF) therefore has potential as a marker for diagnosis of such joint diseases [289]. An important application of commercially produced HA (normally isolated from cockerel combs or produced by bacterial fermentation) is in visco-supplementation of arthritic joints in order to enhance the properties of the diseased and degraded SF [70, 292, 293]. A full characterization and understanding of the rheological properties of HA in solution is therefore vital for the optimization of the fluids used for this form of therapy. While such rheological studies are numerous for simple shearing flows that are relevant to joint flexion [213, 294–297], detailed studies of extensional flows of HA solutions that could be relevant to SF function during joint compression remain scarce [213, 269, 270, 298].

In a recent study, Bingöl et al. [213] performed comprehensive experiments on HA solutions in a physiological phosphate buffered saline (PBS) using both steady shear in a cone-and-plate rheometer and uniaxial extensional flow in a capillary thinning (CaBER) device. Hyaluronic acid solutions of two molecular weights (1.7 and 4.6 MDa) and a range of concentrations spanning $0.09\text{wt. } \% \leq c \leq 0.88\text{wt. } \%$ were tested, along with “mode” synovial fluid systems consisting of HA mixtures with bovine serum albumin (BSA) and c-globulin. It has been suggested that complexes formed between HA and the proteins present in SF could play an important role in influencing SF rheological properties [299]. However, Bingöl et al. found no significant differences between the shear and extensional rheological properties of HA solutions with and without the proteins present, and concluded that it is the HA alone that is predominantly responsible for the functional properties of SF. In addition to HA solutions, Bingöl et al. also examined samples of real human SF in shear and extensional flow. They found that a 4.6 MDa HA at a concentration of $c = 0.3$

wt. % in PBS had shear and extensional rheological properties that compared well with the physiological SF samples.

A potential limitation of the work of Bingöl et al. is the use of a capillary thinning rheometer to study the extensional properties of HA solutions. In the CaBER device it is not possible to impose a controlled deformation rate to a fluid sample; the fluid simply drains, necks down, and eventually breaks up according to its own timescale, determined by a balance between viscous, capillary and elastic stresses [211]. Also, since the CaBER is a free-surface instrument, hydrophobic molecules can be drawn to the air-liquid interface in the device, modifying the interfacial rheology and potentially affecting measurements by stabilizing the eventual breakup of the fluid filament [54, 300].

Recently, Haward et al. presented a novel microfluidic device for performing extensional rheometry of polymer solutions [74]. The Optimized Shape Cross-slot Extensional Rheometer (or OSCER) is similar to a cross-slot device, but has a shape that has been numerically optimized in order to generate a large region of homogenous planar extensional flow. This device allows fluid extensional rheological properties to be measured as a function of the flow strength in a clean and enclosed environment, with no additional complicating effects resulting from the presence of a free surface and while using small volumes of fluid (≈ 10 ml). In this chapter, we examine viscoelastic fluids consisting of semidilute, shear-thinning solutions of semiflexible HA macromolecules and also of HA/protein mixtures similar to those studied by Bingöl et al. [213]. The OSCER device enables us to determine fluid relaxation times and planar extensional viscosity behavior as a function of the deformation rate, which is not possible in the CaBER device employed by Bingöl et al. Our aim is to characterize the extensional properties of HA in solution and to assess whether or not the stretching of HA in synovial fluid can play a significant role in joint protection. This type of study may lead to improved formulation of prosthetic fluids with properties better matched to real SF. If we can demonstrate a direct connection between HA concentration and molecular weight and the extensional flow behavior of a given fluid, then our methods may also offer a technique for tracking changes in the synovial fluid HA characteristics during the progression of joint disease and thus potentially to a novel disease diagnostic technique.

6.2.2 *Modeling the Squeeze flow of HA in Joints*

In this subsection, we discuss the changes in the kinematics of a shear-thinning fluid during squeeze flow between parallel circular plates of radius R and gap separation $h(t)$. The flow field in squeezing flow of a Newtonian fluid has a stagnation point on the axis of symmetry and is characterized by a biaxial extension in the midplane between the plates, however the majority of the volume of fluid contained between the plates is predominantly subjected to shear. We show that the presence of shear-thinning in the fluid rheological properties modifies the kinematics of squeezing flow and thus changes the relative balance of the extensional components to the shearing components in the flow field. We consider the simplified case of a power-law fluid (i.e. a fluid with no zero-shear-rate viscosity plateau at low shear rates and no normal stresses in a shear flow), and quantify the relative importance of extension with respect to shear using a flow type parameter. The flow of the lubricating synovial fluid in mammalian joints under applied deformations such as running or jumping is well modeled as a squeeze flow. Real synovial fluid is significantly shear-thinning and hence knowledge of the extensional viscosity of these fluids as well as an understanding of its behavior under squeezing deformations are important in analyzing the function and efficacy of synovial fluid in mammalian joints.

Background

Consider a power-law fluid in which the shear viscosity η is given by

$$\eta = m\dot{\gamma}^{n-1} \quad (6.2.1)$$

where $\dot{\gamma}$ is the shear rate, m is a constant referred to as the consistency index and n is a positive constant known as the power-law index. For $n = 1$, Equation 6.2.1 represents a non-shear-thinning Newtonian fluid. For $0 < n < 1$ the power-law index describes the extent of shear-thinning in the fluid viscosity; as $n \rightarrow 0$ shear-thinning becomes increasingly important. For $n > 1$ the fluid is shear-thickening. Bird et al. [24] give expressions for the velocity field of such a power-law fluid under squeezing flow, which we present

here in a suitably non-dimensional form:

$$\bar{v}_r = \frac{v_r}{-\dot{h}} = \bar{r} \left[\frac{2n+1}{2(n+1)} (1 - |\bar{z}|^{1+1/n}) \right] \quad (6.2.2)$$

$$\bar{v}_z = \frac{v_z}{-\dot{h}} = \frac{2n+1}{n+1} \left[\frac{n}{2n+1} (|\bar{z}|^{2+1/n}) - |\bar{z}| \right] \quad (6.2.3)$$

in which v_r and v_z are the radial and axial components of the velocity vector, respectively and $z = z/h$ and $r = r/h$. Here r is the radial coordinate measured from the symmetry axis, z is the axial coordinate measured from the mid plane, h is the distance from the mid plane to either plate, and \dot{h} is the velocity of the top plate (relative velocity between the plates is $2\dot{h}$). The radial coordinate varies between 0 and R , where R is the radius of both the top and the bottom plates.

With these calculated velocity profiles, we now determine the rate of deformation tensor D and the vorticity tensor Ω , defined respectively as

$$D = \frac{1}{2} (\nabla \vec{v} + \nabla \vec{v}^T) \quad (6.2.4)$$

$$\Omega = \frac{1}{2} (\nabla \vec{v} - \nabla \vec{v}^T) \quad (6.2.5)$$

to obtain

$$D = \begin{pmatrix} -\frac{\dot{h}}{h} \frac{2n+1}{2(n+1)} (1 - |\bar{z}|^{1+1/n}) & 0 & \frac{\dot{h}}{h} \frac{2n+1}{4n} |\bar{z}|^{1/n} \bar{r} \\ 0 & -\frac{\dot{h}}{h} \frac{2n+1}{2(n+1)} (1 - |\bar{z}|^{1+1/n}) & 0 \\ \frac{\dot{h}}{h} \frac{2n+1}{4n} |\bar{z}|^{1/n} \bar{r} & 0 & \frac{\dot{h}}{h} \frac{2n+1}{n+1} (1 - |\bar{z}|^{1+1/n}) \end{pmatrix} \quad (6.2.6)$$

and

$$\Omega = \begin{pmatrix} 0 & 0 & \frac{\dot{h}}{h} \frac{2n+1}{4n} |\bar{z}|^{1/n} \bar{r} \\ 0 & 0 & 0 \\ \frac{\dot{h}}{h} \frac{2n+1}{4n} |\bar{z}|^{1/n} \bar{r} & 0 & 0 \end{pmatrix} \quad (6.2.7)$$

To describe the nature of the flow field, in terms of shear and extensional contributions, we define the flow type parameter as [301]

$$\psi(\bar{r}, \bar{z}) = \frac{|\mathbf{D}| - |\boldsymbol{\Omega}|}{|\mathbf{D}| + |\boldsymbol{\Omega}|} \quad (6.2.8)$$

where $|\mathbf{D}|$ and $|\boldsymbol{\Omega}|$ represent the magnitudes of the rate of deformation and vorticity tensors respectively, defined by

$$|\mathbf{D}| = \sqrt{\frac{1}{2}(\mathbf{D} : \mathbf{D}^T)} = \sqrt{\frac{1}{2} \sum_i \sum_j D_{ij}^2} \quad (6.2.9)$$

$$|\boldsymbol{\Omega}| = \sqrt{\frac{1}{2}(\boldsymbol{\Omega} : \boldsymbol{\Omega}^T)} = \sqrt{\frac{1}{2} \sum_i \sum_j \Omega_{ij}^2} \quad (6.2.10)$$

$$(6.2.11)$$

It is straightforward to show that $\psi = -1, 0, 1$, respectively corresponding to the limits in which the flow is pure rotation, simple shear or pure extension. Calculating ψ for our flow kinematics, we find that

$$\psi(\bar{r}, \bar{z}) = \frac{\sqrt{\bar{r}^2 |\bar{z}|^{2/n} + 12 \left(\frac{n}{n+1}\right)^2 (1 - |\bar{z}^{1+1/n})^2 - \bar{r} |\bar{z}|^{1/n}}}{\sqrt{\bar{r}^2 |\bar{z}|^{2/n} + 12 \left(\frac{n}{n+1}\right)^2 (1 - |\bar{z}^{1+1/n})^2 + \bar{r} |\bar{z}|^{1/n}}} \quad (6.2.12)$$

Results

In Figures 6.2.2 and 6.2.3 we show the velocity field as a function of spatial location between the plates for various values of the power-law exponent n . In Figure 6.2.2 the ratio of plate diameter to the total gap between the plates is given by $R/h = 10$. In Figure 6.2.3 $R/h = 100$, which is thought to be a physiologically relevant ratio of length scales [285]. In all cases we observe a stagnation point on the midpoint of the compression axis (i.e. $r = 0$, $z = 0$) and fluid accelerates continuously along the radial direction generating a biaxial extensional flow.

We observe that the velocity field for shear-thinning fluids in squeeze flows becomes

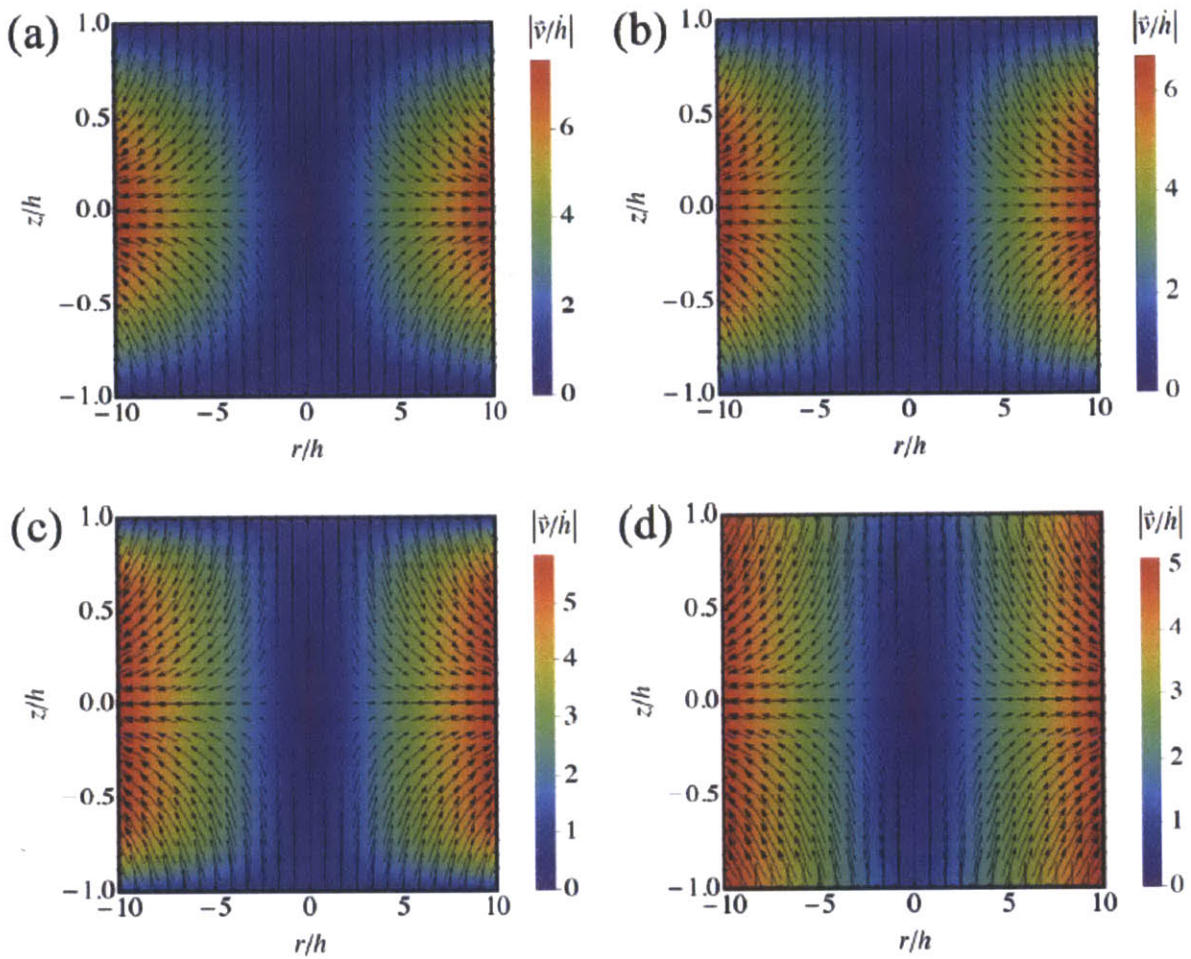


Figure 6.2.2: Flow velocity magnitudes and direction for shear-thinning power-law fluids in a squeeze flow with $R/h = 10$. The power-law exponents are: (a) $n = 1$, (b) $n = 0.5$, (c) $n = 0.2$, and (d) $n \rightarrow 0$.

increasingly plug-like with increasing shear-thinning (i.e. decreasing n). In fact, the flow reduces to one of pure biaxial extension for $n = 0$. This is also clearly seen from Figures 6.2.4 and 6.2.5, where we show line plots of v_r at fixed values of r at different values of n . It can be seen that the width of the plug-like region increases with decreasing n , eventually leading to a plug-like velocity profile everywhere for $n = 0$.

We plot the value of the flow type parameter ψ as a function of the spatial position for different values of n in Figures 6.2.6 and 6.2.6. It can be seen that even for a Newtonian fluid ($n = 1$, Figure 6.2.6(a)), the compression axis (i.e. the $r = 0$ axis) and, more importantly, the midplane between the compressing plates (i.e. the $z = 0$ plane) are dominated

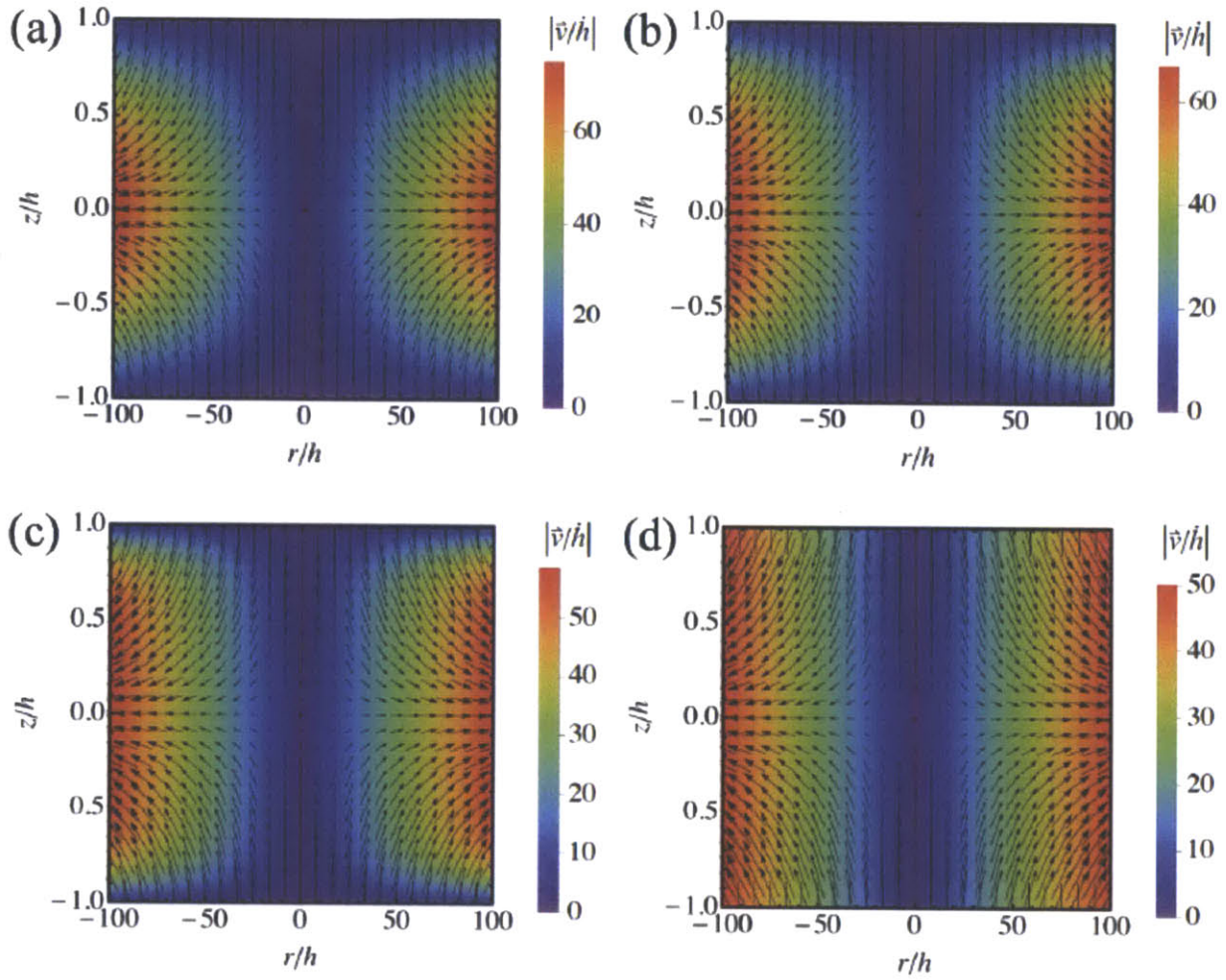


Figure 6.2.3: Flow velocity magnitudes and direction for shear-thinning power-law fluids in a squeeze flow with $R/h = 100$. The power-law exponents are: (a) $n = 1$, (b) $n = 0.5$, (c) $n = 0.2$, and (d) $n \rightarrow 0$.

by a shear-free biaxial extensional flow. Decreasing the value of n (Figure 6.2.6(b-d)), i.e. increasing the extent of shear-thinning, results in a significantly enlarged region of pure biaxial extension centered on the midplane. For a fluid with power-law exponent $n \rightarrow 0$, the entire gap between the plates is characterized by homogeneous biaxial extension, with no component of simple shear (Figure 6.2.6(d)).

Increasing the aspect ratio of the geometry from $R/h = 10$ (Figure 6.2.6) to $R/h = 100$ (Fig 6.2.7), the result remains qualitatively similar, though for a given value of n the width of the central, extension-dominated region becomes slightly reduced. Nevertheless, at this physiologically relevant aspect ratio and at physiologically relevant values of $n = 0.5$ and

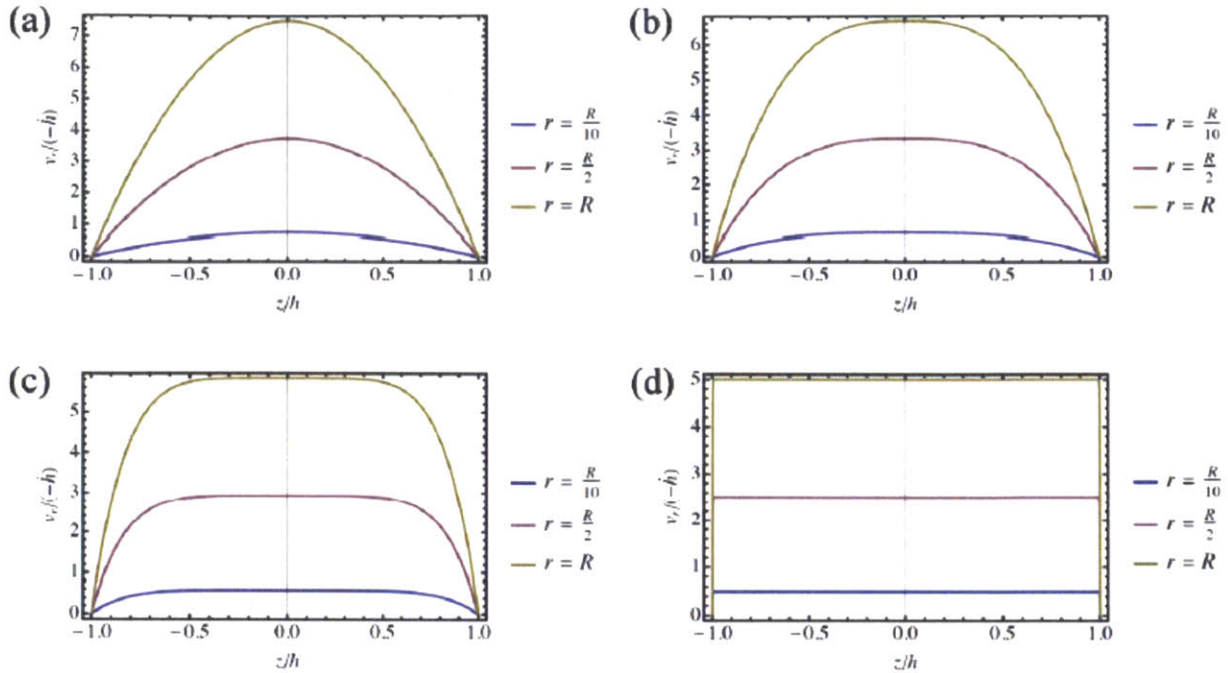


Figure 6.2.4: Velocity as a function of non-dimensional height in the channel z at fixed values of radius r and for $R/h = 10$. The power-law exponent is: (a) $n = 1$, (b) $n = 0.5$, (c) $n = 0.2$, and (d) $n \rightarrow 0$.

$n = 0.2$ [213], we can observe a significant region of pure biaxial extensional flow between the plates.

We have shown here that the presence of shear-thinning can significantly alter the flow kinematics of the squeeze flow problem. Upon calculating the flow type parameter, we find that shear-thinning locally enhances the dominance of extensional deformations near the midplane between two compressing plates. Paradoxically, as the power-law exponent n is decreased, shear-thinning becomes less important and the flow field as a whole becomes increasingly dominated by extension. This demonstrates that the shear-thinning of synovial fluid in mammalian joints, may in fact enhance the importance of the extensional flow generated during when joints are suddenly compressed (such as occurs in the knees during running and jumping, for example). We note also that any slip that may occur at the surfaces during squeeze flow will also further increase the relative dominance of the extensional components in the flow field [302]. In the joints we speculate that partial slip could occur due to “weeping” of low viscosity fluid from the porous cartilage matrix [281, 282]. Thus we believe that characterizing and understanding the extensional rheology properties of synovial fluid may be an invaluable component in finally elucidating its full range

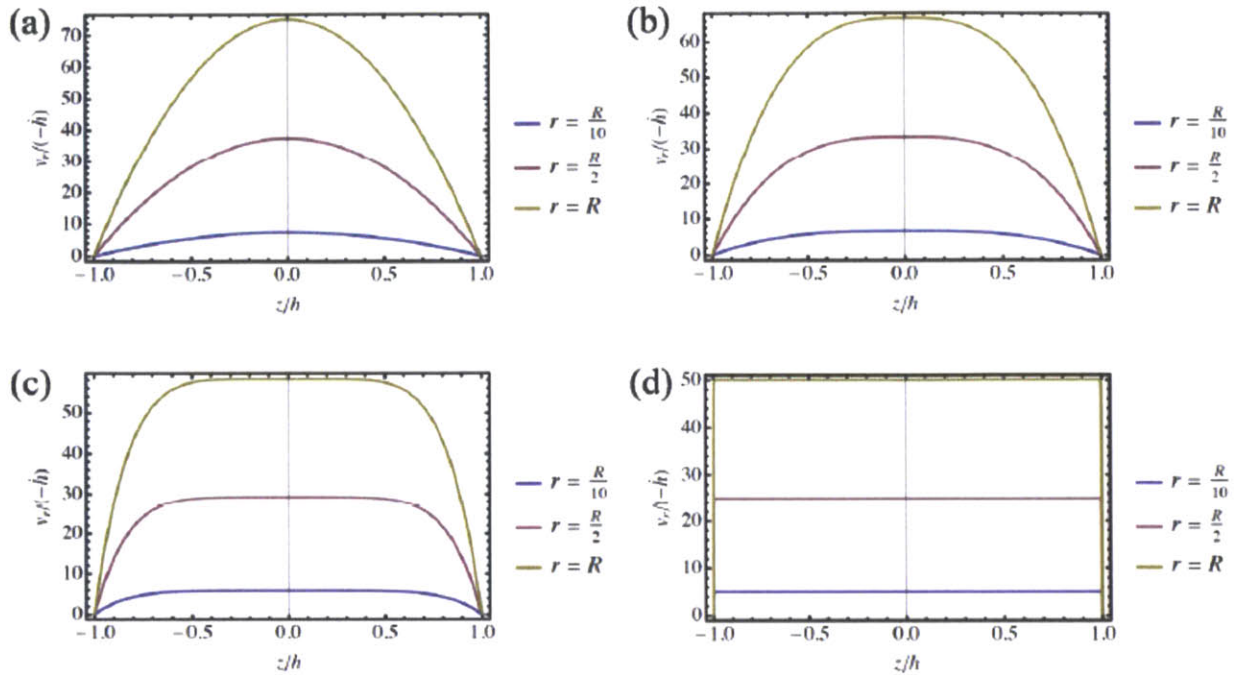


Figure 6.2.5: Velocity as a function of non-dimensional height in the channel z at fixed values of radius r and for $R/h = 100$. The power-law exponent is: (a) $n = 1$, (b) $n = 0.5$, (c) $n = 0.2$, and (d) $n \rightarrow 0$. As n decreases the velocity field becomes increasingly independent of z and approaches plug-like flow.

of physiological functions. We next describe our model tests fluids and determine their shear rheology. We then proceed to measurements of their extensional rheology using a microfluidic cross-slot device.

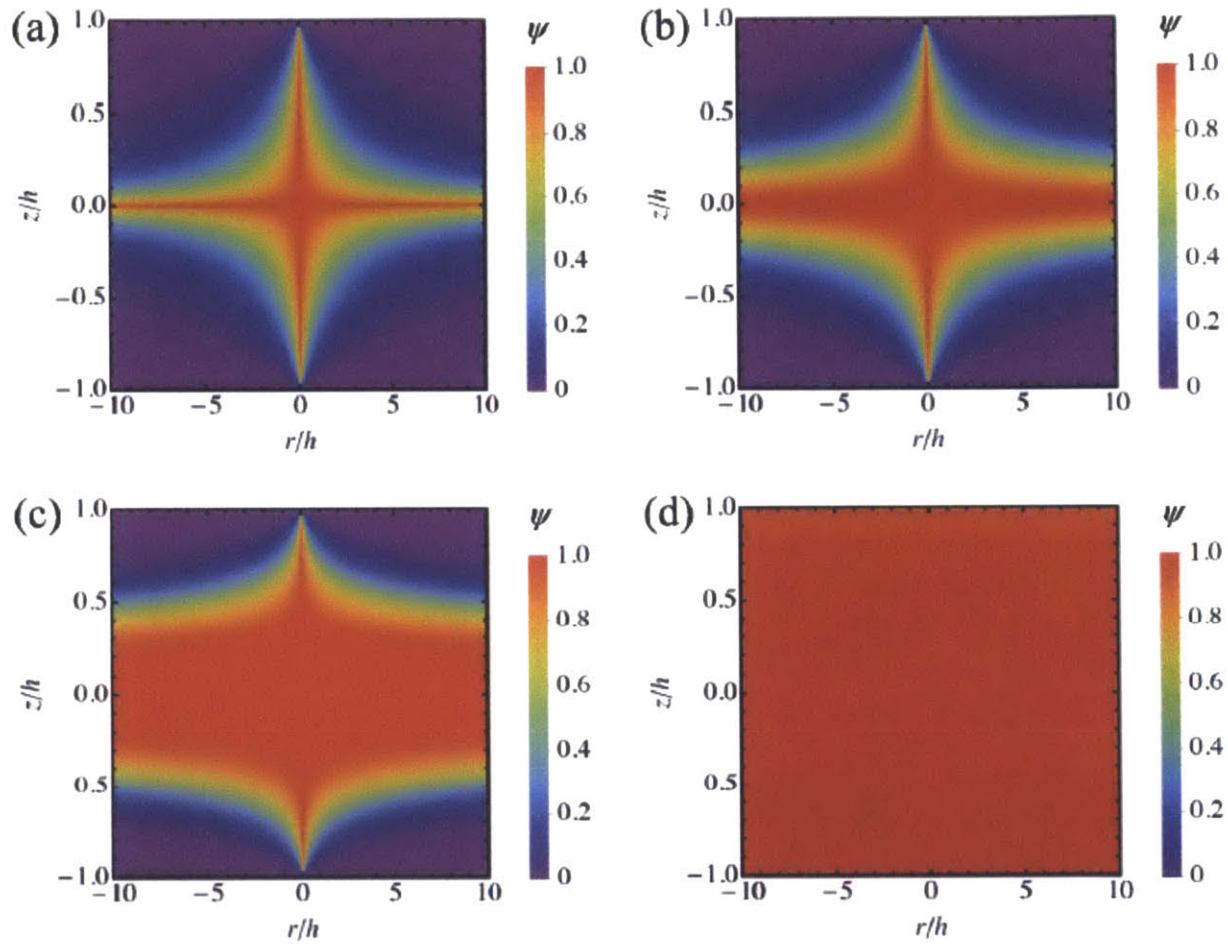


Figure 6.2.6: The flow type parameter ψ as a function of spatial position for $R/h = 10$ and (a) $n = 1$, (b) $n = 0.5$, (c) $n = 0.2$, and (d) $n \rightarrow 0$. $\psi = 1$ corresponds to pure extensional flow, while $\psi = 0$ corresponds to simple shear flow.

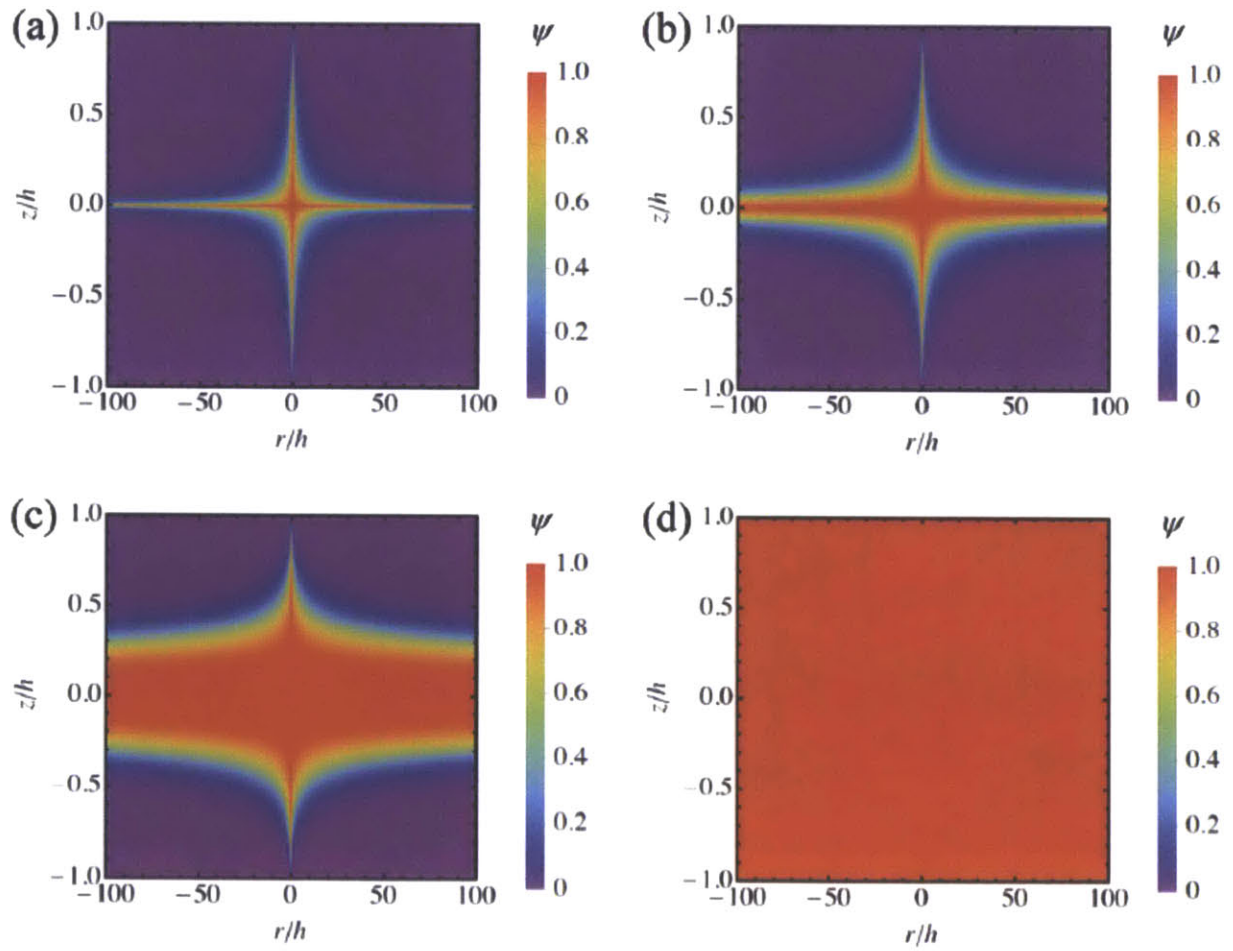


Figure 6.2.7: The flow type parameter ψ as a function of spatial position for $R/h = 100$ and (a) $n = 1$, (b) $n = 0.5$, (c) $n = 0.2$, and (d) $n \rightarrow 0$.

6.2.3 Test Fluids and their Rheological Characterization

The high molecular weight (MW = 1.6 MDa, as specified by the supplier) HA sample used in this study was obtained from Sigma Aldrich and was produced by fermentation of *Streptococcus equi*. For convenience we refer to it as HA1.6 in the remainder of the thesis. HA solutions were prepared at concentrations of 0.1 wt. % and 0.3 wt. % in a physiological phosphate buffered saline (PBS, 0.01 M, pH 7.4, obtained from Sigma Aldrich). We also prepared a model synovial fluid formed from a solution of 0.3 wt. % HA combined with 1.1 wt. % BSA, and 0.7 wt. % γ -globulin [299]. Light scattering experiments indicate an overlap concentration of $c^* \approx 0.05 \text{ wt. \%}$ for this HA molecule in PBS solution, suggesting that our solutions are in the semidilute regime [296, 303].

All of the test solutions were prepared by weighing the HA and protein powders into a glass container and adding the appropriate volume of PBS solution. In order to avoid mechanical degradation of the HA during dissolution, magnetic stirring was avoided; instead occasional gentle manual agitation was applied to the containing vessel until the solution appeared completely transparent and homogenous. This typically took around 36 h. Following complete dissolution of the sample in the PBS, the fluid was tested without delay (i.e., within the subsequent 12 h) to determine the rheological and extensional flow properties.

Test solutions were characterized by steady shear experiments in an AR-G2 stress-controlled rheometer with a 40mm diameter 2° cone-and-plate fixture. To access higher shear rates ($100 \text{ s}^{-1} < \dot{\gamma} < 10000 \text{ s}^{-1}$) a microfluidic shear rheometer was used (m-VROC, Rheosense Inc, CA) [304]. The results of the experiments are presented in Figure 6.2.8.

In the absence of added protein, the steady shear rheology presented in Figure 6.2.8 is highly comparable with that of previous authors using microbial HA solutions of comparable molecular weight and concentration under equivalent solvent conditions [213, 295, 296]. For example, Krause et al. [295] report that a solution with 0.3 wt. % of a hyaluronic acid of MW = 1.5 MDa has a zero shear-rate viscosity of $\eta_0 \approx 0.07 \text{ Pa s}$, which commences to shear thin at a characteristic shear rate of $\dot{\gamma}^* \approx 50 \text{ s}^{-1}$ and to reach a viscosity of $\eta \approx 0.01 \text{ Pa s}$ at a shear rate of $\dot{\gamma} \approx 1000 \text{ s}^{-1}$. The fluids used in the present work also display a zero-shear-rate viscosity plateau and are shear-thinning. Increasing the HA concentration from 0.1 wt. % to 0.3 wt. % results in a significant increase in η_0 and in a more pronounced shear-thinning behavior. At 0.3 wt. %, the viscosity drops by almost an order of magnitude over two decades in shear rate. Addition of 1.1 wt. % BSA and 0.7 wt. % γ -globulin

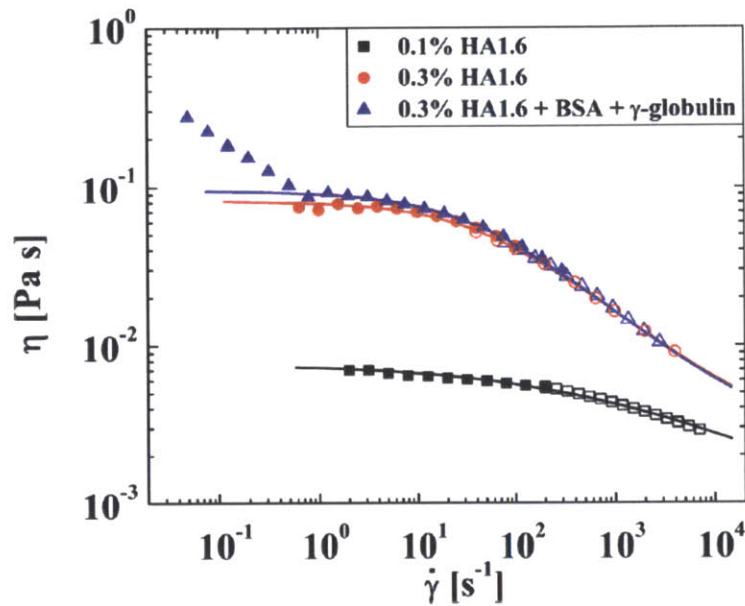


Figure 6.2.8

Steady shear viscosity of HA/PBS solutions measured using an AR-G2 stress-controlled cone-and-plate rheometer (closed symbols) and an m-VROC microfluidic rheometer (open symbols). The viscosity is well-described by a Carreau-Yasuda model (solid lines), except for the fluid containing BSA and γ -globulin at low shear rates.

to the 0.3 wt. % HA solution, appears to have little effect on the fluid rheology except at low shear rates, where an additional region of strong shear-thinning is observed. Such behavior was also reported by Oates et al. [305] using a concentric cylinder geometry and was attributed to complexation between the HA and protein resulting in the formation of a weak gel. However, Bingöl et al. observed no such phenomenon in a 60mm diameter 1° cone-and-plate geometry. The fact that the observation of this phenomenon depends on the flow geometry employed suggests that it may be due to an interfacial, as opposed to a bulk, property of the fluid [54, 306]. In general, the fluid steady shear viscosity is well described by the Carreau-Yasuda model [24]

$$\eta = \eta_{\infty} + \frac{\eta_0 - \eta_{\infty}}{[1 + (\dot{\gamma}/\dot{\gamma}^*)^a]^{(1-n)/a}} \quad (6.2.13)$$

where η_{∞} is the infinite-shear-rate viscosity, η_0 is the zero-shear-rate viscosity, $\dot{\gamma}^*$ is the characteristic shear rate for the onset of shear-thinning, n is the “power-law exponent”, and a is a dimensionless fitting parameter that influences the sharpness of the transition from a constant shear viscosity at low shear rates to the power-law region. The values of these parameters determined for all the test fluids are provided in Table 6.2.1.

We have discussed in Chapter 4 how it is possible to derive the Carreau-like steady shear behavior given in Equation 6.2.13 starting from fractional constitutive model. The parameters $\dot{\gamma}^*$ and n can be directly mapped to quasiproperties and power law exponents of the

Table 6.2.1: Parameters used to fit the Carreau-Yasuda model to the steady shear rheology data.

HA1.6 conc. (wt. %)	η_0 [Pa s]	η_∞ [Pa s]	$\dot{\gamma}^*$ [s^{-1}]	n	a
0.1	0.0073	0.001	200	0.68	0.60
0.3	0.082	0.002	50	0.45	0.75
0.3 + BSA + γ -globulin	0.097	0.0021	45	0.42	0.72

FVCM. By measuring the linear viscoelastic spectrum of the HA solutions, followed by a measurement of the Damping function in nonlinear step-strain experiments, we can predict the nonlinear steady shear behavior of the HA and HA simulant solutions. Furthermore, the value of n is directly related to the springpot exponent β used in the fractional model. However, in this chapter we are interested in the extensional rheology of HA; therefore, we simply perform a fit to the empirical Carreau model.

The power-law exponents n shown in Table 6.2.1 indicate the highly shear-thinning nature of the HA-based test fluids at shear rates $\dot{\gamma} > \dot{\gamma}^*$. However, it should be noted that the steady shear rheology of fluids, with higher HA concentrations or MW, and also of real synovial fluid, can be significantly more shear-thinning than this, with $n \approx 0.2$ or 0.3 (and sometimes even less) [213].

6.2.4 Extensional Flow Apparatus

We refer to the microfluidic device used to generate the extensional flow field as the Optimized Shape Cross-slot Extensional Rheometer (OSCER). The OSCER geometry operates on principles similar to traditional cross-slots (i.e., with opposed inlets and outlets to generate a free stagnation point [62, 273]) but has an optimized shape that achieves a homogeneous strain rate along a significant portion of the inlet and outlet channel axes [74, 307]. A 3D drawing and a photograph of the actual flow geometry are provided in Figure 6.2.9.

The OSCER geometry is precision micro-machined in stainless steel using the technique of wire electrical discharge machining (EDM). It has initially parallel channels far upstream and far downstream of the stagnation point, with a characteristic dimension of $H = 100 \mu\text{m}$, and a uniform depth of $d = 2100 \mu\text{m}$, providing a high aspect ratio of $\alpha = 10.5$ and hence a good approximation to a 2D flow. The geometry is optimized over the central 3 mm ($30H$) section of the device, i.e., $\pm 15H$ either side of the stagnation point in both the

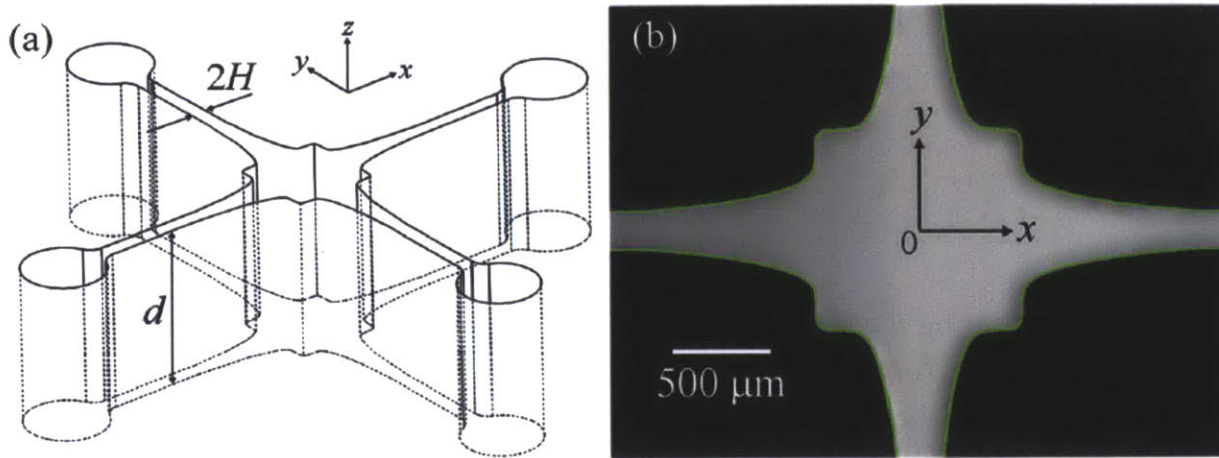


Figure 6.2.9: (a) 3D view of the OSCER geometry showing the upstream and downstream characteristic channel dimension H and the uniform depth d . (b) Light micrograph of the actual OSCER geometry. The inflow is along the y - and the outflow along the x -direction. At the center of the geometry there is a stagnation point, here marked as the origin of coordinates. The superimposed green line represents the prescribed profile determined from numerical optimization.

x - and y directions. The extensional deformation rate (or strain rate, $\dot{\epsilon}$) has been shown to be nominally constant over this optimized region in both Newtonian fluids and viscoelastic polymer solutions [74].

Experiments are conducted at controlled total volume flow rates, Q , using a Harvard PHD-Ultra syringe pump to drive the flow from a single syringe into both opposing inlets of the OSCER device. We define the superficial flow velocity U as the average flow velocity in the upstream and downstream parallel sections of channel: $U = Q/(4Hd)$. The homogenous strain rate $\dot{\epsilon}$ on the flow axes depends on the imposed flow velocity and is measured experimentally using micro-particle image velocimetry (μ -PIV). For details on the techniques used for streakline visualization and strain rate measurement through μ -PIV, see Ref. [63].

6.2.5 Flow Induced Birefringence Measurement

The spatial distribution of flow-induced birefringence in the central region of the OSCER device is measured using an ABRIO birefringence imaging system (CRi Inc., MA). Briefly, the cross-slot flow cell is placed on the imaging stage of an inverted microscope (Nikon Eclipse TE 2000-S) and the mid-plane of the flow cell is brought into focus using a 4×0.13 NA objective lens. Circularly polarized monochromatic light (wavelength 546 nm) is

passed first through the sample, then through a liquid crystal compensator optic and finally onto a CCD array. The CCD camera records five individual frames with the liquid crystal compensator configured in a specific polarization state for each frame. Data processing algorithms described by Shribak and Oldenbourg [308] combine the five individual frames into a single full-field map of retardation and orientation angle. The system can measure the retardation (R) to a nominal resolution of approximately 0.02 nm and has an excellent spatial resolution (projected pixel size approximately 2 μm with a 4 \times objective lens). Assuming 2D flow, the relationship between retardation and birefringence is given by

$$R = d\Delta n \quad (6.2.14)$$

where d is the depth of the flow cell and Δn is the birefringence.

The birefringence intensity measured along the stagnation point streamline of the OSCER device is used to determine the local extensional viscosity of the fluid η_E using the stress-optical rule (SOR). The SOR states that, for a range of microstructural deformations, the magnitude of the birefringence Δn is directly proportional to the principal stress difference in the fluid $\Delta\sigma = \sigma_{xx} - \sigma_{yy}$, i.e.,

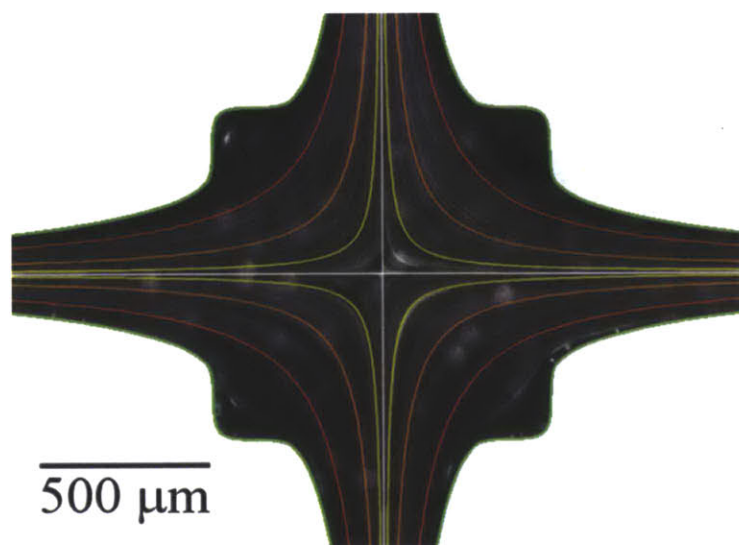
$$\Delta n = C\Delta\sigma \quad (6.2.15)$$

where the constant of proportionality C is called the stress-optical coefficient. For solutions of 1.5 MDa HA in PBS over a concentration range of 0.22wt. % $\leq c \leq$ 0.88wt. %, the stress-optical coefficient has been determined rheo-optically to be $C = 1.82 \times 10^{-8} \text{ Pa}^{-1}$ [296]. The apparent extensional viscosity follows directly from

$$\eta_E = \frac{\Delta\sigma}{\dot{\epsilon}} = \frac{\Delta n}{C\dot{\epsilon}} \quad (6.2.16)$$

6.2.6 Results and Discussion

In Figure 6.2.10, we show streak imaging performed with a Newtonian fluid consisting of 66 wt. % glycerol in water. The fluid viscosity is approximately 13 mPa s and the volume flow rate is $Q = 0.5 \text{ ml min}^{-1}$, equivalent to $U = 0.01 \text{ ms}^{-1}$. Superimposed in color on the streak image is a family of hyperbolic streamlines (defined by $y = k/x$, for a range of k values) expected for an ideal homogeneous extensional flow, and it is clear

**Figure 6.2.10**

Streak imaging showing the nature of the flow field in the OSCER with a Newtonian fluid at $U = 0.01 \text{ m s}^{-1}$, with superimposed colored hyperbolae for comparison. The superimposed white lines indicate the symmetry axes of the geometry, which coincide at the stagnation point. Flow enters through the top and bottom channels and exits through the left- and right-hand channels.

that in the central region of the device the experimental streamlines broadly follow these hyperbolae. Superimposed in white are the x and y axes of symmetry, which clearly bisect at the hyperbolic singularity (the stagnation point) at the center of the OSCER geometry.

In Figure 6.2.11 we show the measured value of flow induced birefringence in the cross-slot device for HA1.6 and synovial fluid simulants. We observe the formation of a localized birefringent strand along the outflowing stagnation point streamline. The progressive development and strengthening of this strand with increasing values of the flow rate through the OSCER device is visible in Figure 6.2.11. At the flow rates (or strain rates) at which the birefringence first becomes measurable, the birefringence microscopy images in Figure 6.2.11 indicate that significant macromolecular stretching and orientation takes place only along streamlines that pass close to the stagnation point, where the residence times in the high velocity gradient are maximal. The intensity of the birefringence along the x -axis can be seen to be almost constant, which is a result of the homogenous strain rate along the x -axis and provides a clear visual demonstration of the strong extensional flow field generated in the OSCER device. The intensities of the birefringent strands shown in Figure 6.2.11 increase as the imposed strain rate are incrementally increased. The fluids with the higher concentration of HA (Figures 6.2.11(b) and 6.2.11(c)) are significantly more birefringent than the low concentration fluid (Figure 6.2.11(a)), as expected. Additionally, for a given strain rate, we observe little qualitative difference between the behavior of the two 0.3 wt. % HA1.6 fluids with and without added protein.

In addition, as the flow rate is incremented, not only the extensional strain rate in the

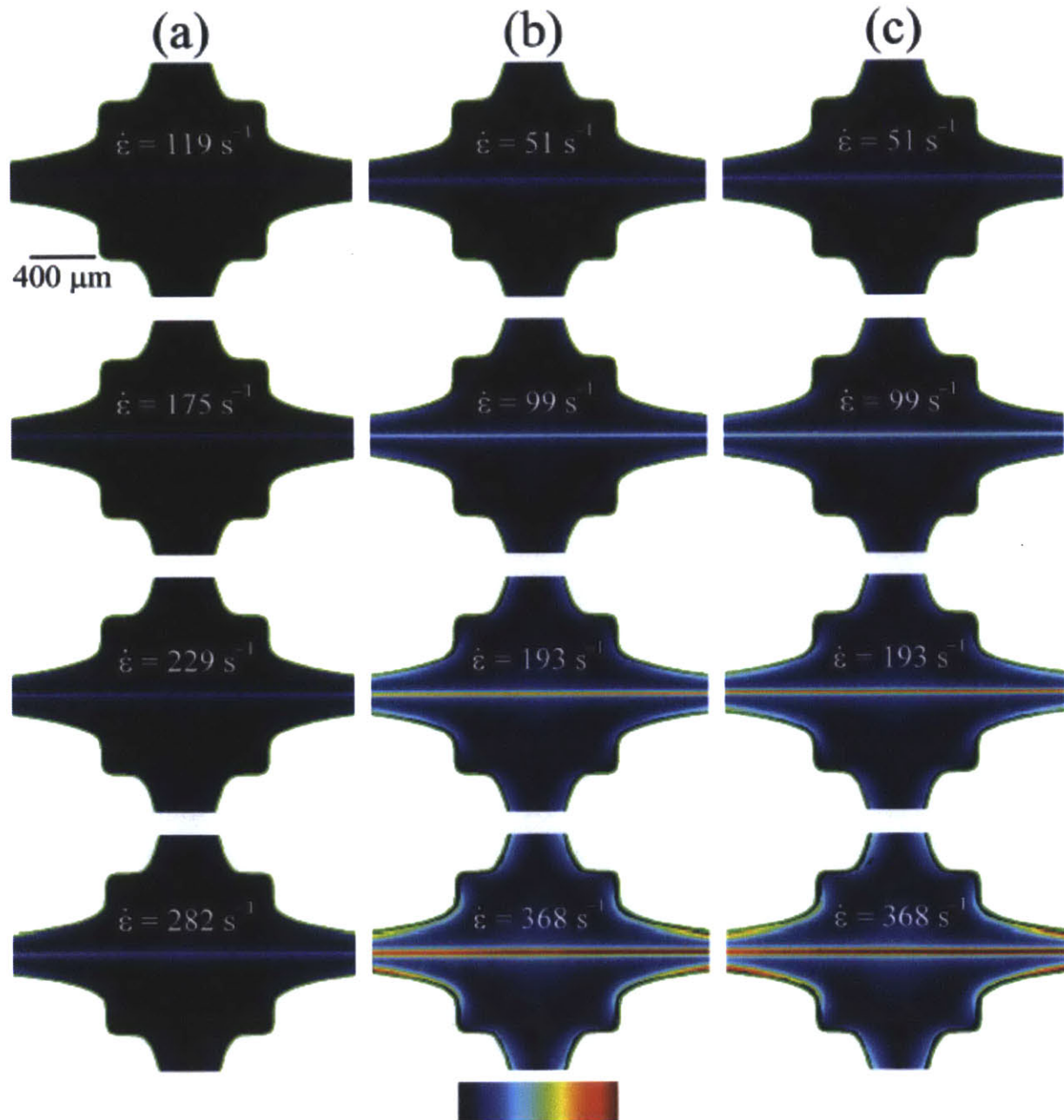


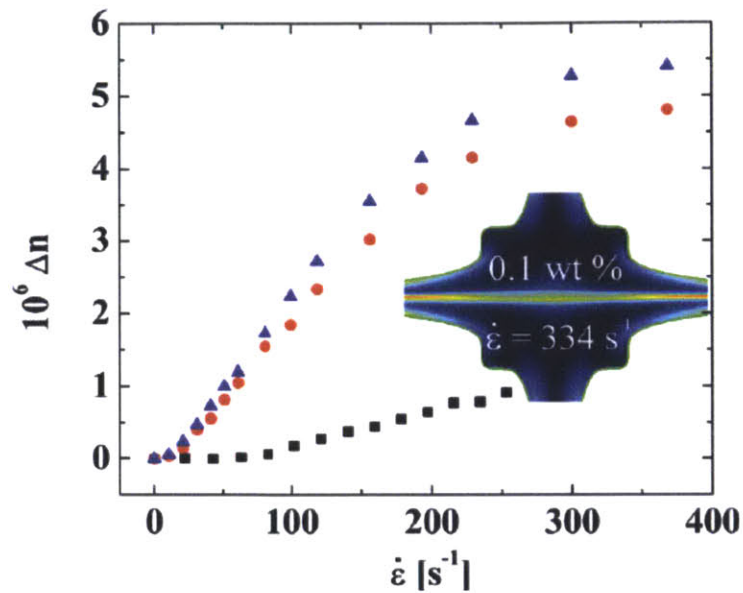
Figure 6.2.11: Flow induced birefringence measured over a range of extension rates in solutions of HA1.6: (a) 0.1 wt. %, (b) 0.3 wt. %, (c) 0.3 wt. % + BSA + γ -globulin. The color scale bar represents retardation in the range of $R = 0 - 10$ nm.

OSCER device but also the shear rate near the curved non-slip walls of the device is increased. Here, the flow field is not purely extensional in character, and shear stresses as well as the first normal stress difference contribute to the total principal stress difference in the fluid. As this occurs, the more concentrated HA solutions (Figures 6.2.11(b) and Figure 6.2.11(c)) display a clear increase in the birefringence (or equivalently the principal stress difference) along the walls of the flow geometry. However, it should be noted that the magnitude of the stress difference along the channel walls is never as great as that observed along the channel center-plane. Note that at higher flow rates the more dilute HA solution (Figure 6.2.11(a)) also displays such stress boundary layers at the channel walls, however, in this case, the intensity of the birefringence is very low indeed and is difficult to observe.

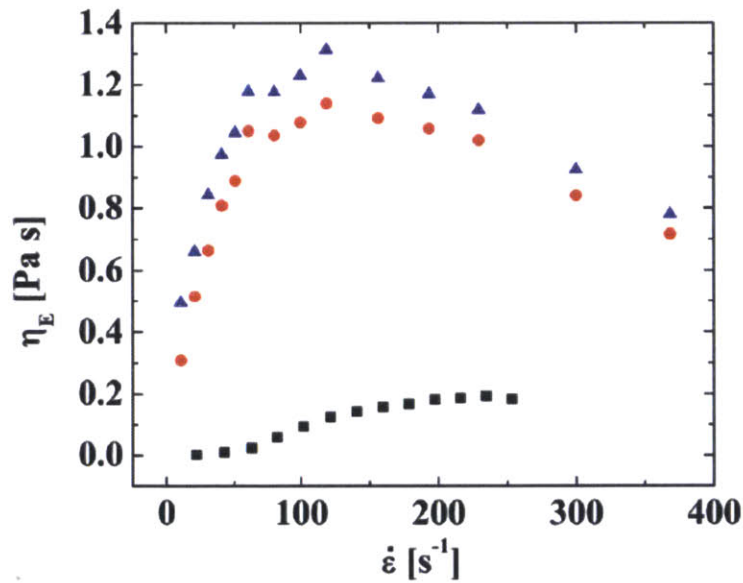
By measuring the birefringence on the x-axis (averaging along sections of strands close to the stagnation point), we obtain the birefringence Δn as a function of the strain rate for the three HA1.6 solutions, as shown in Figure 6.2.12(a). In the two 0.3 wt. % HA1.6 fluids, with and without added protein, we observe an initial increase in the birefringence at a strain rate of $\dot{\epsilon} \approx 10 \text{ s}^{-1}$, up to similar plateau values of $\Delta n \approx 5 \times 10^{-6}$ at strain rates of $\dot{\epsilon} \approx 370 \text{ s}^{-1}$. In the 0.1 wt. % HA1.6 solution the initial increase in Δn occurs at a higher value of $\dot{\epsilon} \approx 80 \text{ s}^{-1}$, and we are not able to reach a plateau value of birefringence due to the onset of an inertio-elastic instability that distorts the birefringent strand (as shown by the inset birefringence field image in Figure 6.2.12(a) captured at $\dot{\epsilon} \approx 334 \text{ s}^{-1}$).

Using the stress-optical rule to convert from birefringence to an extensional viscosity (Equations 6.2.15 and 6.2.16), we obtain the extensional viscosity versus strain rate curves shown in Figure 6.2.12(b). In the 0.1 wt. % HA1.6 solution, the extensional viscosity increases at a strain rate of approximately 50 s^{-1} and rises to a plateau value of around 0.2 Pa s . In the more concentrated HA1.6 solutions, the extensional viscosity begins to increase even from the lowest applied strain rates and rises very rapidly to a maximum value of $\eta_E \approx 1.2 \text{ Pa s}$ for $\dot{\epsilon} \approx 120 \text{ s}^{-1}$, before gradually thinning with further increases in the strain rate.

In this section, we have demonstrated the application of a recently developed numerically optimized microfluidic cross-slot (OSCER) device to test the extensional response of biologically-relevant hyaluronic acid solutions. Analogous formulations of fluids are used for visco-supplementation of the degraded synovial fluid in patients with joint disease, especially in the articular cavity of the knees. Our microfluidic device provides a good model of the flow field within the knee joint as it undergoes compressional and extensional de-



(a)



(b)

Figure 6.2.12: (a) Measured birefringence Δn as a function of the strain rate $\dot{\epsilon}$ for HA1.6 solutions in the OSCER. In the 0.1 wt. % solution the experiment is curtailed at lower $\dot{\epsilon}$ due to the onset of an inertio-elastic instability that distorts the birefringent strand (as illustrated by the inserted image for $U = 0.36$ m s⁻¹). (c) Extensional viscosity η_E as a function of $\dot{\epsilon}$, determined from birefringence measurements using the stress-optical rule.

formations (e.g., during running and jumping activities), in which the synovial fluid is squeezed at high deformation rates (and thus at $Wi \gg 1$). Our analysis demonstrates that for a highly shear-thinning fluid such as HA, the kinematics of a squeeze flow involved large extensional components. Our birefringence observations and measurements with semidilute HA solutions clearly demonstrate that these high molecular weight polysaccharides stretch significantly under such conditions of high flow strength, resulting in a significant increase in the extensional viscosity and in the corresponding dimensionless Trouton ratio. This is likely to represent an important functional aspect of synovial fluid, which allows it to resist compression under high loading rates at short time scales, thus preventing damaging contact from occurring between articular cartilage layers.

7 | *Conclusions*

A diverse range of complex fluids exhibit relaxation spectra that contain broad power laws, including physically and chemically cross-linked gels, soft glasses, emulsions, colloidal dispersions, polymer solutions and melts. The physical origin of the multiple timescale (or multiscale) power law behavior depends on the specific class of material. For example, a polymer melt may exhibit multiscale relaxation due to high polydispersity. On the other hand, a chemically crosslinked gel with dangling chain ends exhibits multiscale power law behavior due to the nature of the retraction of these dangling ends during the relaxation process. We have discussed these and some of the other major physical origins of multiscale rheological response in Chapter 1. Due to the diverse classes of materials encompassed by multiscale complex fluids, they are frequently encountered in industrial, biological, pharmaceutical and engineering applications. It is therefore important to possess modeling frameworks to predict the rheological response of these materials.

The fractional constitutive equations presented in this thesis overcome the difficulties associated with modeling a broad spectrum using a sum of exponentials, or Prony series, which introduces a large number of material parameters. Depending on the nature of spectrum, it may also be necessary to make arbitrary choices to determine the modal parameters. This is a fact that has been noted by other researchers, such as Tschogel and Scott Blair. There have been many subsequent studies that have successfully fit fractional linear viscoelastic models to the broad power law spectra exhibited by multiscale materials.

In Chapter 3, we have provided further evidence that fractional models are compact and accurate frameworks to quantitatively describe the broad relaxation spectra of multiscale materials. Furthermore, we have demonstrated that once a material has been characterized, the constitutive framework can be used to make predictions of material response under complex applied kinematics. We take the example of a viscoelastic air-solution interface formed by a globular protein solution (BSA), and analyze the case of a creep experiment

in which there is appreciable inertia contributed by the instrument. We show that we can predict the short time inertio-elastic oscillations arising from the coupling between inertia and viscoelasticity, as well as the long time power law creep response. Making such a prediction using a Prony series would not be possible without the introduction of a large number of material parameters, and would be cumbersome and impractical.

The literature on modeling the rheology of multiscale complex fluids shows that models for predicting the nonlinear behavior of these fluids is relatively scarce. However, nonlinear effects such as shear thinning in the viscosity can be very important in industrial and biological applications of multiscale complex fluids. In Chapter 4 we extended the fractional constitutive framework to nonlinear deformations using a K-BKZ type integral constitutive model, which includes the proper frame-invariant strain measure (the Finger tensor). We demonstrate that by characterizing the power law relaxation spectrum of the fluids in a linear experiment (say SAOS) and determining a damping function from a single set of nonlinear step-strain experiments, we are able to make accurate predictions of nonlinear response such as shear thinning and positive first normal stress coefficients. In particular, we demonstrate the following:

- The power law exponents and quasi-properties suggest a direct relationship between linear and nonlinear rheology. We demonstrate this by deriving analytical expressions for predictions of steady shear viscosity and first normal stress coefficients and analyzing the resulting asymptotic behavior,
- We quantified offsets that exist between measured data and empirical rules employed for nonlinear rheology, such as the Cox-Merz rule. For materials that yield upon an infinitesimally small deformation, we derived the exact result of the so-called Rutgers-Delaware rule,
- Many empirical proposed models such as the power law fluid model, the Herschel-Bulkley model, and the Cross and Carreau models can be derived from a fractional rheological model containing at most four parameters and an appropriate fluid dependent damping function,
- We have derived expressions for the linear viscoelastic behavior of complex fluids that exhibit Herschel-Bulkley, Cross and Carreau like behavior under a steady shear flow. In addition, we also derive expressions for the first normal stress coefficients for these complex fluids. Such explicit expressions do not currently exist in the literature.

In Chapter 5, we demonstrated using a chemically crosslinked polymeric gel that fractional constitutive equations can make predictions of material response in small strain extensional deformations. The tack response of pressure sensitive adhesives, which are often formulated from chemically crosslinked polymeric gels, is an important design parameter; we demonstrated that by coupling the appropriate fractional constitutive equation with the Newtonian (non-shear-thinning) kinematics of a tack experiment, accurate predictions of the tack force in the small strain lubrication limit can be obtained. We have also derived expressions for the tack response of complex fluids displaying sol-like material response.

The large strain extensional rheology of complex fluids is important in various industrial applications, such as fiber spinning and spin coating, as well as in biologically relevant fluids such as saliva and lubricating synovial fluid. Many physiologically relevant complex fluids are complex polysaccharides. Their microstructure possesses interactions arising from hydrogen bonding or ionic effects, which results in the broad power law relaxation spectra characteristic of multiscale materials. Given the industrial and biological importance of polysaccharide solutions, and the need for an understanding of their extensional rheology for these applications, in Chapter 6 we have explored the extensional rheology of two polysaccharide solutions: the shear-thickening Mamaku gum, and the shear-thinning Hyaluronic Acid (HA). For this purpose, we employed experimental techniques such as CaBER, FiSER and OSCER. We demonstrated that for Mamaku gum, whose shear-thickening behavior is a rare occurrence for polysaccharides, the interactions arise from hydrogen bonding, and their rheology can be finely tuned with a hydrogen bond breaker such as urea. Furthermore, we demonstrated the existence of a time-concentration superposition principle that arises from the nature of interactions between urea and the lifetimes of hydrogen bond dissociation. This detailed understanding of the microstructural relaxation process that exist in Mamaku gum could potentially lead to new formulations of food thickeners and treatments for dysphagia. Additionally, the extensional rheology measurements of HA solutions on the optimized microfluidic cross-slot device could also lead to potential diagnostic techniques for patients with osteo-arthritis.

In this thesis we have examined in detail the modeling of broad power law spectra exhibited by multiscale complex fluid under shear deformations in both the linear and non-linear regime. However, for the case of extensional deformations we only model the small strain behavior, and a majority of our results in the large strain extensional deformation case are experimentally determined. One important area of future work would be to ex-

tend the fractional constitutive framework here to large strain extensional deformation. We have shown in this thesis that the Finger tensor is an excellent finite strain measure in large strain *shear* deformations. We hypothesize that the only modification required in the framework to predict rheological response under large extensional strains is to suitably calculate the Finger tensor in the model for large applied elongational kinematics. However, we note that large strain extensional deformations could introduce new physics in the problem (such as finite extensibility effects) and it may require us to make suitable modifications to the underlying general K-KBKZ framework (the damping function that is measured in extension is different from the shear damping function [28]).

Yet another potential area of research is to develop the framework for shear-thickening fluids, for example the Mamaku gum solutions described in this thesis. In our K-BKZ framework, the damping function $h(\gamma)$ is derived from a more general strain energy function W , which quantifies the change in internal energy of the complex fluid as a function of applied deformation. We may imagine experimentally determining a *thickening* function for shear-thickening fluids, i.e. these complex fluids do not possess a linear viscoelastic envelope. We may then use the K-BKZ approach to predict the steady shear viscosity of such fluids, leading to a prediction of the shear thickening behavior.

In this thesis, we have demonstrated that for some experimentally measured power-law rheological responses—for example that of a soft glass, or a cross-linked network with dangling chain ends—the quasi-properties and power-law exponents can be directly linked to physical parameters that have a microstructural origin. In general, however, mapping an observed power-law rheological response to microstructural parameters is still not well understood, and is an active area of current research [146, 309]. The difficulty arises due to the many-to-one nature of power-law rheology. As we discuss in Chapter 1, there are various physical mechanisms that can lead to broad, scale-free rheological response, each mechanism with its own microstructural basis. It is also possible that in complex environments such as cells, there are multiple physical origins of power law behavior. Recently Kim et al. [310] have studied a model system of actin filaments and actin crosslinking proteins (ACPs). Using a Brownian dynamics approach, they showed that in this same system, there are different underlying microstructural properties that lead to power-law behavior depending on the applied pre-strain. These properties include the bending stiffness of the ACPs and actin filaments at low and moderate pre-strain, and the extensional stiffness of the ACPs and actin filaments at large strains. They find that at very low pre-strains

(and no ACP) transverse thermal fluctuations of the actin filaments lead to a power-law dependence of the linear viscoelastic moduli on frequency ($G' \sim \omega^{0.75}$). However, upon the addition of ACPs, the power-law dependence of the viscoelastic moduli on frequency is much weaker. Such a weak dependence of $G'(\omega)$ and $G''(\omega)$ on ω has been observed in other rheological studies of cells and cell-like environments [311, 312] and has been attributed to a crowded glassy environment existing within the cytoskeleton. Kroy and Glaser [313] have successfully modeled these power-law responses from a microstructural standpoint by proposing the so-called glassy wormlike chain model, which begins with the wormlike chain model and ‘stretches’ the relaxation spectrum in an exponential fashion [314]. In this model, the power-law exponent is dependent on an *interaction strength* ϵ which is ultimately phenomenological, and difficult to predict from first-principles [315]. This is akin to the SGR model, which also predicts power-law spectrum response through the introduction of a phenomenological athermal noise temperature x , whose origin remains poorly understood. The above discussion shows that a general microstructural basis connecting power-law exponents and the corresponding quasi-properties remains elusive. The development of such theories, along with the fractional constitutive equations presented in this thesis, will be a powerful framework that is not only predictive, but also provides microstructural insight from bulk rheology.

This thesis has demonstrated how a wide variety of theoretically and empirically proposed rheological models can be derived from a fractional constitutive framework. In this sense, our framework resembles a universal or ‘umbrella’ framework, which, in the appropriate limits of the model parameters, reduces to more familiar rheological constitutive equations used for power law behavior. The proposals outlined above to extend the framework to shear-thickening fluids and large strain extensional deformations would further establish the conclusions of this thesis, and expand the applicability of these compact models for multiscale complex fluids, that we have already shown to be very versatile.

A | *List of Useful Formulas Related to the Fractional Calculus*

In this Appendix, we list important and useful mathematical definitions and results relating to the fractional calculus and fractional constitutive equations. More details may be found in Refs. [82, 83, 85, 176].

A.1 Definitions and Properties of Fractional Derivatives

In this section we list the different definitions of the fractional derivative. We predominantly use the Caputo derivative in this thesis, which we also denote by the notation d^α/dt^α .

Caputo Derivative

$${}^C D_t^\alpha f(t) \equiv \frac{d^\alpha f(t)}{dt^\alpha} = \frac{1}{\Gamma(n-\alpha)} \int_a^t (t-t')^{n-\alpha-1} f^{(n)}(t') dt'; \quad n-1 \leq \alpha < n \text{ and } n \in \mathbb{Z} \quad (\text{A.1.1})$$

Riemann-Liouville Derivative

$${}^{RL} D_t^\alpha f(t) = \frac{1}{\Gamma(n-\alpha)} \frac{d^n}{dt^n} \int_a^t (t-t')^{n-\alpha-1} f(t') dt'; \quad n-1 \leq \alpha < n \text{ and } n \in \mathbb{Z} \quad (\text{A.1.2})$$

Grünwald-Letnikov Derivative

$${}^aGLD_t^\alpha f(t) = \lim_{\substack{h \rightarrow 0 \\ nh=t-a}} = h^{-\alpha} \sum_{r=0}^n (-1)^r \binom{\alpha}{r} f(t-rh) \quad (\text{A.1.3})$$

where

$$\binom{\alpha}{r} = \frac{\alpha(\alpha-1)(\alpha-2)\cdots(\alpha-k+1)}{k(k-1)(k-2)\cdots 1} \quad (\text{A.1.4})$$

are the binomial coefficients.

Properties of Caputo Derivatives

- Linearity:

$$\frac{d^\alpha [af(t) + g(t)]}{dt^\alpha} = a \frac{d^\alpha f(t)}{dt^\alpha} + \frac{d^\alpha g(t)}{dt^\alpha} \quad (\text{A.1.5})$$

where a is a constant.

- Leibniz's rule (Product rule):

$$\frac{d^\alpha [f(t)g(t)]}{dt^\alpha} = \sum_{r=0}^{\infty} \binom{\alpha}{r} g^{(r)}(t) \frac{d^{\alpha-r} f(t)}{dt^{\alpha-r}} \quad (\text{A.1.6})$$

- Composition rule: If $0 \leq m < \alpha < m+1$ and $0 \leq n < \beta < n+1$ and $f(t)$ satisfies the conditions

$$f^{(k)}(0) = 0, \quad k = 0, 1, \dots, r-1 \quad (\text{A.1.7})$$

where $r = \max(n, m)$ then

$$\frac{d^\beta}{dt^\beta} \left(\frac{d^\alpha f(t)}{dt^\alpha} \right) = \frac{d^\alpha}{dt^\alpha} \left(\frac{d^\beta f(t)}{dt^\beta} \right) = \frac{d^{\alpha+\beta} f(t)}{dt^{\alpha+\beta}} \quad (\text{A.1.8})$$

A.2 Frequently Encountered Special Functions

Dirac Delta Function

$$\delta(t) = \begin{cases} \infty, & \text{if } x = 0 \\ 0, & \text{if } x \neq 0 \end{cases}, \quad \text{and} \quad \int_{-\infty}^{\infty} \delta(x) dx = 1 \quad (\text{A.2.1})$$

Heaviside Step Function

$$H(t) = \begin{cases} 1, & \text{if } x \geq 0 \\ 0, & \text{if } x < 0 \end{cases} \quad (\text{A.2.2})$$

Gamma Function

$$\Gamma(z) = \int_0^{\infty} t^{z-1} e^{-t} dt \quad (\text{A.2.3})$$

Mittag-Leffler Function

- Definition:

$$E_{a,b}(z) = \sum_{k=0}^{\infty} \frac{z^k}{\Gamma(ak + b)} \quad (\text{A.2.4})$$

- Special cases of the Mittag-Leffler Function:

$$E_{1,1}(z) = e^z \quad (\text{A.2.5})$$

$$E_{2,1}(z) = \cosh(z) \quad (\text{A.2.6})$$

$$E_{2,2}(z^2) = \frac{\sinh(z)}{z} \quad (\text{A.2.7})$$

- Derivatives of the Mittag-Leffler function:

$$\frac{\partial^n}{\partial t^n} [E_{a,b}(t)] = n! t^{-n} E_{a,an+1}^{n+1}(t) \quad (\text{A.2.8})$$

$$\frac{\partial^n}{\partial t^n} [t^{ak+b-1} E_{a,b}^{(k)}(\lambda t^a)] = t^{ak+b-n-1} E_{a,b-n}^{(k)}(\lambda t^a) \quad (\text{A.2.9})$$

- Asymptotic expansions of the Mittag-Leffler function:

$$E_{a,b}(-z) \approx \sum_{k=0}^N \frac{z^k}{\Gamma(ak+b)} + O(z^{N+1}); z \ll 1 \quad (\text{A.2.10})$$

$$E_{a,b}(-z) \approx \sum_{k=1}^N \frac{z^{-k}}{\Gamma(b-ak)} + O(z^{-(N+1)}); z \gg 1 \quad (\text{A.2.11})$$

Hypergeometric Function

$${}_2F_1(a, b; c; z) = \frac{\Gamma(c)}{\Gamma(a)\Gamma(b)} \sum_{k=0}^{\infty} \frac{\Gamma(a+k)\Gamma(b+k)}{\Gamma(c+k)} \frac{z^k}{k!} \quad (\text{A.2.12})$$

A.3 Laplace and Fourier Transforms of Fractional Derivatives

- Definition of the Laplace transform:

$$\mathcal{L}\{f(t)\} = \tilde{f}(s) = \int_0^{\infty} f(t) e^{-st} dt \quad (\text{A.3.1})$$

- Definition of the Fourier transform:

$$\mathcal{F}\{f(t)\} = \tilde{f}(\omega) = \int_{-\infty}^{\infty} f(t) e^{-i\omega t} dt \quad (\text{A.3.2})$$

- Properties:

$$\mathcal{L} \left\{ \frac{d^\alpha f(t)}{dt^\alpha} \right\} = s^\alpha \tilde{f}(s) - \sum_{k=0}^{n-1} s^{\alpha-k-1} f^{(k)}(0), \quad n-1 < \alpha \leq n \quad (\text{A.3.3})$$

$$\mathcal{F} \left\{ \frac{d^\alpha f(t)}{dt^\alpha} \right\} = (i\omega)^\alpha \tilde{f}(\omega) \quad (\text{A.3.4})$$

- A useful Laplace transform result:

$$\mathcal{L}^{-1} \left\{ \frac{k!s^{a-b}}{(s^a \mp \lambda)^{k+1}} \right\} = t^{ak+b-1} \frac{d^k}{d(\pm \lambda t^a)^k} [E_{a,b}(\pm \lambda t^a)] \quad (\text{A.3.5})$$

A.4 Constitutive Equations and their Linear Viscometric Functions

Hookean Solid Model

- Constitutive equation:

$$\sigma(t) = G_0 \gamma(t) \quad (\text{A.4.1})$$

- Relaxation modulus:

$$G(t) = G_0 H(t) \quad (\text{A.4.2})$$

- Creep compliance:

$$J(t) = \frac{1}{G_0} H(t) \quad (\text{A.4.3})$$

- Storage and loss moduli:

$$G'(\omega) = G_0 \quad (\text{A.4.4})$$

$$G''(\omega) = 0 \quad (\text{A.4.5})$$

Newtonian Liquid Model

- Constitutive equation:

$$\sigma(t) = \eta_0 \dot{\gamma}(t) \quad (\text{A.4.6})$$

- Relaxation modulus:

$$G(t) = \eta_0 \delta(t) \quad (\text{A.4.7})$$

- Creep compliance:

$$J(t) = \frac{t}{\eta_0} \quad (\text{A.4.8})$$

- Storage and loss moduli:

$$G'(\omega) = 0 \quad (\text{A.4.9})$$

$$G''(\omega) = \eta_0 \omega \quad (\text{A.4.10})$$

Linear Maxwell Model

- Constitutive equation:

$$\sigma(t) + \frac{\eta_0}{G_0} \frac{d\sigma(t)}{dt} = \eta_0 \frac{d\gamma(t)}{dt} \quad (\text{A.4.11})$$

- Relaxation modulus:

$$G(t) = \eta_0 e^{-t/\tau} \quad (\text{A.4.12})$$

- Creep compliance:

$$J(t) = \frac{1}{G_0} + \frac{t}{\eta_0} \quad (\text{A.4.13})$$

- Storage and loss moduli:

$$G'(\omega) = G_0 \frac{(\tau\omega)^2}{1 + (\tau\omega)^2} \quad (\text{A.4.14})$$

$$G''(\omega) = G_0 \frac{\tau\omega}{1 + (\tau\omega)^2} \quad (\text{A.4.15})$$

where $\tau = \eta_0/G_0$ is the relaxation time.

Linear Kelvin-Voigt Model

- Constitutive equation:

$$\sigma(t) = G_0\gamma(t) + \eta_0 \frac{d\gamma(t)}{dt} \quad (\text{A.4.16})$$

- Relaxation modulus:

$$G(t) = G_0H(t) + \eta_0\delta(t) \quad (\text{A.4.17})$$

- Creep compliance:

$$J(t) = \frac{1}{G_0}(1 - e^{-t/\tau}) \quad (\text{A.4.18})$$

- Storage and loss moduli:

$$G'(\omega) = G_0 \quad (\text{A.4.19})$$

$$G''(\omega) = \eta_0\omega \quad (\text{A.4.20})$$

Springpot Model

- Constitutive equation:

$$\sigma(t) = \mathbb{V} \frac{d^\alpha \gamma(t)}{dt^\alpha} \quad (\text{A.4.21})$$

- Relaxation modulus:

$$G(t) = \frac{\mathbb{V} t^{-\alpha}}{\Gamma(1-\alpha)} \quad (\text{A.4.22})$$

- Creep compliance:

$$J(t) = \frac{1}{\mathbb{V}} \frac{t^\alpha}{\Gamma(1+\alpha)} \quad (\text{A.4.23})$$

- Storage and loss moduli:

$$G'(\omega) = \mathbb{V} \omega^\alpha \cos(\pi\alpha/2) \quad (\text{A.4.24})$$

$$G''(\omega) = \mathbb{V} \omega^\alpha \sin(\pi\alpha/2) \quad (\text{A.4.25})$$

Fractional Maxwell Model

- Constitutive equation:

$$\sigma(t) + \frac{\mathbb{V}}{\mathbb{G}} \frac{d^{\alpha-\beta} \sigma(t)}{dt^{\alpha-\beta}} = \mathbb{V} \frac{d^\alpha \gamma(t)}{dt^\alpha} \quad (\text{A.4.26})$$

- Relaxation modulus:

$$G(t) = \mathbb{G} t^{-\beta} E_{\alpha-\beta, 1-\beta} \left(- \left(\frac{t}{\tau} \right)^{\alpha-\beta} \right) \quad (\text{A.4.27})$$

- Creep compliance:

$$J(t) = \left(\frac{1}{\mathbb{V}} \frac{t^\alpha}{\Gamma(1+\alpha)} + \frac{1}{\mathbb{G}} \frac{t^\beta}{\Gamma(1+\beta)} \right) \quad (\text{A.4.28})$$

- Storage and loss moduli:

$$G'(\omega) = \mathbb{V}\tau^{-\alpha} \frac{(\omega\tau)^\alpha \cos(\pi\alpha/2) + (\omega\tau)^{2\alpha-\beta} \cos(\pi\beta/2)}{(\omega\tau)^{2(\alpha-\beta)} + 2(\omega\tau)^{\alpha-\beta} \cos(\pi(\alpha-\beta)/2) + 1} \quad (\text{A.4.29})$$

$$G''(\omega) = \mathbb{V}\tau^{-\alpha} \frac{(\omega\tau)^\alpha \sin(\pi\alpha/2) + (\omega\tau)^{2\alpha-\beta} \sin(\pi\beta/2)}{(\omega\tau)^{2(\alpha-\beta)} + 2(\omega\tau)^{\alpha-\beta} \cos(\pi(\alpha-\beta)/2) + 1} \quad (\text{A.4.30})$$

where $\tau = (\mathbb{V}/\mathbb{G})^{1/(\alpha-\beta)}$ is a characteristic timescale.

Fractional Kelvin-Voigt Model

- Constitutive equation:

$$\sigma(t) = \mathbb{V} \frac{d^\alpha \gamma(t)}{dt^\alpha} + \mathbb{G} \frac{d^\beta \gamma(t)}{dt^\beta} \quad (\text{A.4.31})$$

- Relaxation modulus:

$$G(t) = \frac{\mathbb{V}t^{-\alpha}}{\Gamma(1-\alpha)} + \frac{\mathbb{G}t^{-\beta}}{\Gamma(1-\beta)} \quad (\text{A.4.32})$$

- Creep compliance:

$$J(t) = \frac{t^\alpha}{\mathbb{V}} E_{\alpha-\beta, 1+\alpha} \left(- \left(\frac{t}{\tau} \right)^{\alpha-\beta} \right) \quad (\text{A.4.33})$$

- Storage and loss moduli:

$$G'(\omega) = \mathbb{V}\omega^\alpha \cos(\pi\alpha/2) + \mathbb{G}\omega^\beta \cos(\pi\beta/2) \quad (\text{A.4.34})$$

$$G''(\omega) = \mathbb{V}\omega^\alpha \sin(\pi\alpha/2) + \mathbb{G}\omega^\beta \sin(\pi\beta/2) \quad (\text{A.4.35})$$

where $\tau = (\mathbb{V}/\mathbb{G})^{1/(\alpha-\beta)}$ is a characteristic timescale.

Fractional Viscoelastic Cross Model

- Constitutive equation:

$$\sigma(t) + \frac{\eta_p}{\mathbb{G}} \frac{d^{1-\beta}}{dt^{1-\beta}} \sigma(t) = (\eta_p + \eta_s) \frac{d\gamma(t)}{dt} + \frac{\eta_p \eta_s}{\mathbb{G}} \frac{d^{2-\beta} \gamma(t)}{dt^{2-\beta}} \quad (\text{A.4.36})$$

- Relaxation modulus:

$$G(t) = \eta_s \delta(t) + \mathbb{G} t^{-\beta} E_{1-\beta, 1-\beta} \left(-\frac{\mathbb{G}}{\eta_p} t^{1-\beta} \right) \quad (\text{A.4.37})$$

- Creep compliance:

$$J(t) = \frac{\mathbb{G} t^{2-\beta}}{\eta_p \eta_s} E_{1-\beta, 3-\beta} \left(-\frac{\mathbb{G}(\eta_p + \eta_s)}{\eta_p \eta_s} t^{1-\beta} \right) + \frac{t}{\eta_s} E_{1-\beta, 2} \left(-\frac{\mathbb{G}(\eta_p + \eta_s)}{\eta_p \eta_s} t^{1-\beta} \right) \quad (\text{A.4.38})$$

- Storage and loss moduli:

$$G'(\omega) = \frac{\eta_p^2 \mathbb{G} \omega^{\beta+2} \cos(\pi\beta/2)}{(\eta_p \omega)^2 + (\mathbb{G} \omega^\beta)^2 + 2\eta_p \mathbb{G} \omega^{\beta+1} \sin(\pi\beta/2)} \quad (\text{A.4.39})$$

$$G''(\omega) = \eta_s \omega + \frac{\mathbb{G}^2 \eta_p \omega^{2\beta+1} + \eta_p^2 \mathbb{G} \omega^{\beta+2} \sin(\pi\beta/2)}{(\eta_p \omega)^2 + (\mathbb{G} \omega^\beta)^2 + 2\eta_p \mathbb{G} \omega^{\beta+1} \sin(\pi\beta/2)} \quad (\text{A.4.40})$$

B | *Supplementary Information to Chapter 3*

In this Appendix we provide arguments on the thermodynamic inconsistency of Scott-Blair's higher-order Nutting equation, additional details of the short and long time creep response of the fractional Maxwell model when the moment of inertia of the device is included (see Equation 4.8 of the main text.). We also provide a vectorial interpretation of the concept of quasi-properties promulgated by Blair et al. [80], and show an equivalence to the SGR model of Sollich et al. [32] for a special choice of the density distribution of energy states in the model.

B.1 Thermodynamic inconsistency of the higher-order Nutting equation

[80] attempted to model measurements of anomalous stress relaxation in a range of materials using a higher-order Nutting equation of the form

$$\gamma = \sigma^\beta (At^{k'} + Bt^{k'-1} + Ct^{k'-2} \dots) \quad (\text{B.1.1})$$

with $A \gg B, C, \dots$. The same study presents extensive experiments on materials that exhibit complex relaxation dynamics, such as 'highly anomalous' butyl rubber and Scott-Blair notes that most materials tested in their study are modeled well by the use of a single term or in some cases two terms. The unmodified one term Nutting equation, with $B = C \dots = 0$ is equivalent to a constitutive model involving a single spring-pot. Again it is difficult to use an empirical expression of this form to describe the material response to predict other modes of deformation except in special cases.

For example, in a creep experiment we impose a step stress $\sigma(t)$ given by

$$\sigma(t) = \sigma_0 H(t) \quad (\text{B.1.2})$$

where $H(t)$ is the Heaviside step function and σ_0 is the magnitude of the step in stress. Substituting this into equation B.1.1, rearranging the terms and Laplace inverting the resulting expression, it can be shown that Scott-Blair's higher order Nutting equation is equivalent to a constitutive equation of the form

$$\frac{d^{k'} \gamma(t)}{dt^{k'}} = a\sigma(t) + b \frac{d\sigma(t)}{dt} + c \frac{d^2\sigma(t)}{dt^2} + \dots \quad (\text{B.1.3})$$

where a, b, c, \dots are material constants. The terms containing higher order derivatives of stress, which Nutting [120] proposed on an empirical basis render the model thermodynamically inconsistent: In Refs. [55, 316] and [102] we find general arguments from rational mechanics showing that the order of the derivative operator on the stress must be smaller than the order of the derivative operator on the strain for thermodynamic admissibility, and this condition is violated in equation B.1.3. This difficulty arises because the addition of extra terms in equation B.1.1 is *ad hoc* and the resulting constitutive model lacks a corresponding mechanical analogue.

B.2 Confidence interval estimate discussion

An interesting observation upon the calculation of the confidence intervals is that for the acacia gum solutions, we find that $\alpha = 0.8 \pm 0.2$, $\beta = 0.124 \pm 0.003$, $\mathbb{V} = 3 \pm 2 \text{Pa s}^{0.8}$, $\mathbb{G} = 0.027 \pm 0.003 \text{Pa s}^{0.124}$. Hence, for the parameters α and \mathbb{V} the 95% confidence interval half-width is comparable to the mean value, while for the parameters β and \mathbb{G} the error estimate is relatively small. This result can be rationalized as follows. A close observation of the frequency sweep data for the acacia gum solution reveals that $G'(\omega)$ and $G''(\omega)$ nearly have a constant slope with changing frequency on a log-log plot, for the range of frequencies measured in this experiment (cf. figure 4a of the main paper). This data would be well fit by a single spring-pot (or equivalently, Winter's gel equation). However, the 'flattening out' of $G''(\omega)$ at lower frequencies and the corresponding downturn in $G'(\omega)$ warrants the use of another spring-pot. Table 1 of the paper shows that the spring-pot with the larger

exponent, i.e. α , determines the limit of the low frequency response. However the long durations required to complete measurements at such low frequencies, and the consequent solvent evaporation, mean that it is very challenging to measure data at frequencies lower than $\omega = 0.01$ rad/s. Therefore there is a corresponding large uncertainty in the value of the exponent α and the corresponding quasi-property \mathbb{V} , because the fit was performed over a range of experimental frequencies not very sensitive to α and \mathbb{V} . However, this does not influence the fit to the data at the frequencies measured in the experiment and the uncertainty in β and \mathbb{G} is relatively low. The mean values of α and \mathbb{V} were subsequently used to predict the oscillatory creep-ringing profile (Figure 6(b) in the paper). The excellent prediction obtained is encouraging, and although the 95% confidence interval on these parameters is large, the measured material response is accurately predicted.

B.3 Asymptotic analysis of the interfacial creep compliance $J_s(t)$

B.3.1 Small t limit

We first investigate the compliance at early times. Laplace transforming equation (4.14) of the main paper, we have

$$\tilde{\gamma}(s) = \frac{\sigma_s^0}{s} \left(\frac{1 + \frac{\mathbb{V}_s}{\mathbb{G}_s} s^{\alpha-\beta}}{\mathbb{V}_s s^\alpha + As^2 + A \frac{\mathbb{V}_s}{\mathbb{G}_s} s^{2+(\alpha-\beta)}} \right) \quad (\text{B.3.1})$$

$$= \frac{\sigma_s^0/s}{\mathbb{V}_s s^\alpha + As^2 + A \frac{\mathbb{V}_s}{\mathbb{G}_s} s^{2+(\alpha-\beta)}} + \frac{\frac{\mathbb{V}_s}{\mathbb{G}_s} \sigma_s^0 s^{\alpha-\beta-1}}{\mathbb{V}_s s^\alpha + As^2 + A \frac{\mathbb{V}_s}{\mathbb{G}_s} s^{2+(\alpha-\beta)}} \quad (\text{B.3.2})$$

$$\Rightarrow \tilde{\gamma}(s) = \tilde{\gamma}_1(s) + \tilde{\gamma}_2(s) \quad (\text{B.3.3})$$

We first direct our attention to the first term $\tilde{\gamma}_1(s)$. The early times limits corresponds to the large s limit, and therefore, we factor out the highest power of s to obtain

$$\tilde{\gamma}_1(s) = \frac{\sigma_s^0}{s^{\alpha+1}[\mathbb{V}_s + As^{2-\alpha} + A\frac{\mathbb{V}_s}{\mathbb{G}_s}s^{2-\beta}]} \quad (\text{B.3.4})$$

$$= \frac{\sigma_s^0}{A\frac{\mathbb{V}_s}{\mathbb{G}_s}s^{3+\alpha-\beta} \left(1 + \frac{\mathbb{V}_s + As^{2-\alpha}}{A\frac{\mathbb{V}_s}{\mathbb{G}_s}s^{2-\beta}}\right)} \quad (\text{B.3.5})$$

We expand the above equation using the binomial theorem to get

$$\tilde{\gamma}_1(s) = \frac{\sigma_s^0}{A\frac{\mathbb{V}_s}{\mathbb{G}_s}s^{3+\alpha-\beta}} \sum_{k=0}^{\infty} (-1)^k \left(\frac{\mathbb{V}_s + As^{2-\alpha}}{A\frac{\mathbb{V}_s}{\mathbb{G}_s}s^{2-\beta}} \right)^k \quad (\text{B.3.6})$$

The term between parentheses in equation B.3.6 can also be expanded using the binomial theorem as follows.

$$\left(\frac{\mathbb{V}_s + As^{2-\alpha}}{A\frac{\mathbb{V}_s}{\mathbb{G}_s}s^{2-\beta}} \right)^k = \left(\frac{\mathbb{G}_s}{A} \right)^k \left(\frac{1 + \frac{A}{\mathbb{V}_s}s^{2-\alpha}}{s^{2-\beta}} \right)^k \quad (\text{B.3.7})$$

$$= \left(\frac{\mathbb{G}_s}{A} \right)^k \frac{1}{(s^{2-\beta})^k} \left(1 + \frac{A}{\mathbb{V}_s}s^{2-\alpha} \right)^k \quad (\text{B.3.8})$$

$$= \left(\frac{\mathbb{G}_s}{A} \right)^k \frac{1}{(s^{2-\beta})^k} \sum_{j=0}^k \binom{k}{j} \left(\frac{A}{\mathbb{V}_s}s^{2-\alpha} \right)^j \quad (\text{B.3.9})$$

Substituting equation B.3.9 into B.3.6, we get the double sum

$$\tilde{\gamma}_1(s) = \frac{\sigma_s^0}{A\frac{\mathbb{V}_s}{\mathbb{G}_s}s^{3+\alpha-\beta}} \sum_{k=0}^{\infty} (-1)^k \left(\frac{\mathbb{G}_s}{A} \right)^k \frac{1}{s^{k(2-\beta)}} \sum_{j=0}^k \binom{k}{j} \left(\frac{A}{\mathbb{V}_s}s^{2-\alpha} \right)^j \quad (\text{B.3.10})$$

which can be simplified to yield

$$\tilde{\gamma}_1(s) = \left(\frac{\mathbb{G}_s}{A\mathbb{V}_s}\right) \sigma_s^0 \sum_{k=0}^{\infty} (-1)^k \left(\frac{\mathbb{G}_s}{A}\right)^k \sum_{j=0}^k \binom{k}{j} \left(\frac{A}{\mathbb{V}_s}\right)^j \frac{1}{s^{\alpha(1+j)-\beta(k+1)+3+2k-2j}} \quad (\text{B.3.11})$$

We can now invert this expression term by term to obtain

$$\gamma_1(t) = \left(\frac{\mathbb{G}_s}{A\mathbb{V}_s}\right) \sigma_s^0 \sum_{k=0}^{\infty} (-1)^k \left(\frac{\mathbb{G}_s}{A}\right)^k \sum_{j=0}^k \binom{k}{j} \left(\frac{A}{\mathbb{V}_s}\right)^j \frac{t^{\alpha(j+1)-\beta(k+1)-2j+2k+2}}{\Gamma(\alpha(j+1) - \beta(k+1) - 2j + 2k + 3)} \quad (\text{B.3.12})$$

We follow a very similar procedure for the second term of equation B.3.3, which is shown below for clarity:

$$\tilde{\gamma}_2(s) = \frac{\frac{\mathbb{V}_s}{\mathbb{G}_s} \sigma_s^0 s^{\alpha-\beta-1}}{\mathbb{V}_s s^\alpha + As^2 + A\frac{\mathbb{V}_s}{\mathbb{G}_s} s^{2+(\alpha-\beta)}} \quad (\text{B.3.13})$$

$$= \frac{\sigma_s^0}{As^3 \left(1 + \frac{\mathbb{V}_s s^\alpha + As^2}{A\frac{\mathbb{V}_s}{\mathbb{G}_s} s^{2+(\alpha-\beta)}}\right)} \quad (\text{B.3.14})$$

$$= \frac{\sigma_s^0}{As^3} \sum_{k=0}^{\infty} (-1)^k \left(\frac{\mathbb{V}_s s^\alpha + As^2}{A\frac{\mathbb{V}_s}{\mathbb{G}_s} s^{2+(\alpha-\beta)}}\right)^k \quad (\text{B.3.15})$$

The term between parentheses in equation B.3.15 can be expanded using a similar procedure:

$$\left(\frac{\mathbb{V}_s s^\alpha + A s^2}{A \frac{\mathbb{V}_s}{\mathbb{G}_s} s^{2+\alpha-\beta}} \right)^k = \left(\frac{\mathbb{G}_s}{A \mathbb{V}_s} \right)^k \left(\frac{\mathbb{V}_s s^\alpha + A s^2}{s^{2+\alpha-\beta}} \right)^k \quad (\text{B.3.16})$$

$$= \left(\frac{\mathbb{G}_s}{A} \right)^k \left(\frac{s^\alpha + \frac{A}{\mathbb{V}_s} s^2}{s^{2+\alpha-\beta}} \right)^k \quad (\text{B.3.17})$$

$$= \left(\frac{\mathbb{G}_s}{A} \right)^k \frac{1}{s^{k(2-\beta)}} \left(1 + \left(\frac{A}{\mathbb{V}_s} \right) s^{2-\alpha} \right)^k \quad (\text{B.3.18})$$

$$= \left(\frac{\mathbb{G}_s}{A} \right)^k \frac{1}{s^{k(2-\beta)}} \sum_{j=0}^k \binom{k}{j} \left(\frac{A}{\mathbb{V}_s} s^{2-\alpha} \right)^j \quad (\text{B.3.19})$$

Combining equations B.3.15 and B.3.19, we obtain

$$\tilde{\gamma}_2(s) = \frac{\sigma_s^0}{A s^3} \sum_{k=0}^{\infty} (-1)^k \left(\frac{\mathbb{G}_s}{A} \right)^k \frac{1}{s^{k(2-\beta)}} \sum_{j=0}^k \binom{k}{j} \left(\frac{A}{\mathbb{V}_s} s^{2-\alpha} \right)^j \quad (\text{B.3.20})$$

which upon simplification results in

$$\tilde{\gamma}_2(s) = \frac{\sigma_s^0}{A} \sum_{k=0}^{\infty} (-1)^k \left(\frac{\mathbb{G}_s}{A} \right)^k \sum_{j=0}^k \binom{k}{j} \left(\frac{A}{\mathbb{V}_s} \right)^j \frac{1}{s^{\alpha j - \beta k + 2(k-j) + 3}} \quad (\text{B.3.21})$$

Laplace inverting the above term-by-term, we arrive at

$$\tilde{\gamma}_2(t) = \frac{\sigma_s^0}{A} \sum_{k=0}^{\infty} (-1)^k \left(\frac{\mathbb{G}_s}{A} \right)^k \sum_{j=0}^k \binom{k}{j} \left(\frac{A}{\mathbb{V}_s} \right)^j \frac{t^{\alpha j - \beta k + 2(k-j) + 2}}{\Gamma(\alpha j - \beta k + 2(k-j) + 3)} \quad (\text{B.3.22})$$

Adding equations B.3.12 and B.3.22 and after some algebra and simplification, we obtain the strain response of the FMM for early times following the imposition of a step stress as

$$\gamma(t) = \sigma_s^0 \left(\sum_{k=0}^{\infty} \sum_{j=0}^k (-1)^k \left(\frac{\mathbb{G}_s}{A} \right)^{k+1} \binom{k}{j} \left(\frac{A}{\mathbb{V}_s} \right)^j \left[\frac{1}{\mathbb{V}_s} \frac{t^p}{\Gamma(p+1)} + \frac{1}{\mathbb{G}_s} \frac{t^q}{\Gamma(q+1)} \right] \right) \quad (\text{B.3.23})$$

where

$$p = 2 + \alpha - \beta + k(2 - \beta) - j(2 - \alpha) \quad (\text{B.3.24})$$

$$q = p - (\alpha - \beta) \quad (\text{B.3.25})$$

The leading order term is obtained by setting $k = j = 0$ in equation B.3.23. Moreover, $\alpha > \beta$ and hence $p > q$. Therefore, we can ignore the t^q term obtained from setting $k = j = 0$ for early times and we finally have

$$\gamma(t) \approx \frac{\sigma_s^0}{A} \left(\frac{t^2}{\Gamma(3)} \right) = \frac{1}{2} \left(\frac{\sigma_s^0}{A} \right) t^2 \quad (\text{B.3.26})$$

The strain response at short times is thus quadratic, as one would expect from the equation of motion, and is consistent with it.

B.3.2 Large t limit

We now consider the creep response at long times. Consider again the Laplace transformed constitutive equation (equation B.3.3) which we write as $\tilde{\gamma}(s) = \tilde{\gamma}_1(s) + \tilde{\gamma}_2(s)$. Let us first direct our attention to the quantity $\tilde{\gamma}_1(s)$. We have

$$\tilde{\gamma}_1(s) = \frac{\sigma_s^0}{\mathbb{V}_s s^{1+\alpha} \left(1 + \frac{A}{\mathbb{V}_s} s^{2-\alpha} + \frac{A}{\mathbb{G}_s} s^{2-\beta} \right)} \quad (\text{B.3.27})$$

$$= \frac{\sigma_s^0}{\mathbb{V}_s s^{1+\alpha}} \sum_{k=0}^{\infty} (-1)^k \left(\frac{A}{\mathbb{V}_s} s^{2-\alpha} + \frac{A}{\mathbb{G}_s} s^{2-\beta} \right)^k \quad (\text{B.3.28})$$

Factoring out the term $\left(\frac{A}{V_s}s^{2-\alpha}\right)^k$ from the term between parentheses, we obtain

$$\tilde{\gamma}_1(s) = \frac{\sigma_s^0}{V_s s^{1+\alpha}} \sum_{k=0}^{\infty} (-1)^k \left(\frac{A}{V_s}s^{2-\alpha}\right)^k \left(1 + \frac{V_s}{G_s}s^{\alpha-\beta}\right)^k \quad (\text{B.3.29})$$

We also know that

$$\left(1 + \frac{V_s}{G_s}s^{\alpha-\beta}\right)^k = \sum_{j=0}^k \binom{k}{j} \left(\frac{V_s}{G_s}\right)^j s^{j(\alpha-\beta)} \quad (\text{B.3.30})$$

Combining equation B.3.29 and B.3.30, we arrive at

$$\tilde{\gamma}_1(s) = \frac{\sigma_s^0}{V_s s^{1+\alpha}} \sum_{k=0}^{\infty} (-1)^k \left(\frac{A}{V_s}s^{2-\alpha}\right)^k \sum_{j=0}^k \binom{k}{j} \left(\frac{V_s}{G_s}\right)^j s^{j(\alpha-\beta)} \quad (\text{B.3.31})$$

$$= \frac{\sigma_s^0}{V_s} \sum_{k=0}^{\infty} (-1)^k \left(\frac{A}{V_s}\right)^k \sum_{j=0}^k \binom{k}{j} \left(\frac{V_s}{G_s}\right)^j \frac{1}{s^{\alpha+1-k(2-\alpha)-j(\alpha-\beta)}} \quad (\text{B.3.32})$$

Using a procedure identical to that described above, it may be shown that

$$\tilde{\gamma}_2(s) = \frac{\sigma_s^0}{G_s} \sum_{k=0}^{\infty} (-1)^k \left(\frac{A}{V_s}\right)^k \sum_{j=0}^k \binom{k}{j} \left(\frac{V_s}{G_s}\right)^j \frac{1}{s^{1+\beta-k(2-\alpha)-j(\alpha-\beta)}} \quad (\text{B.3.33})$$

Adding equations B.3.32 and B.3.33 and Laplace inverting the resulting expression term by term, we obtain

$$\gamma(t) = \sigma_s^0 \sum_{k=0}^{\infty} (-1)^k \left(\frac{A}{V_s}\right)^k \sum_{j=0}^k \binom{k}{j} \left(\frac{V_s}{G_s}\right)^j \left[\frac{1}{V_s} \frac{t^u}{\Gamma(u+1)} + \frac{1}{G_s} \frac{t^v}{\Gamma(v+1)} \right] \quad (\text{B.3.34})$$

where

$$u = \alpha - k(2 - \alpha) - j(\alpha - \beta) \quad (\text{B.3.35})$$

$$v = u - (\alpha - \beta) \quad (\text{B.3.36})$$

To leading order, the behavior of the stress response will correspond to the term in the expansion obtained upon setting $k = j = 0$. Therefore,

$$\gamma(t \rightarrow \infty) = \sigma_s^0 \left(\frac{t^\alpha}{\mathbb{V}_s \Gamma(\alpha + 1)} + \frac{t^\beta}{\mathbb{G}_s \Gamma(\beta + 1)} \right) \quad (\text{B.3.37})$$

It may also be shown that for $\alpha = 1$ and $\beta = 0$, the expression in equation B.3.34 exactly reduces to

$$J_s(t) = \frac{t}{\eta} - \left(\frac{A}{\eta^2} - \frac{1}{G} \right) \quad (\text{B.3.38})$$

where $\eta = \mathbb{V}_s$ and $G = \mathbb{G}_s$ for the case $\alpha = 1$, $\beta = 0$. This is the correct limit in the linear Maxwell model.

B.4 Fractional calculus and the Soft Glassy Rheology (SGR) model

We now examine the soft glassy rheology (SGR) model and search for a relationship between the SGR model and the spring-pot. The motivation behind this exploration is the observation that both these models are extremely well suited to capturing power-law-like rheological behaviour.

The state of a macroscopic sample is characterized by a probability distribution $P(l, E; t)$ whose evolution as a function of time is given by [32]

$$\frac{\partial}{\partial t} P = -\dot{\gamma} \frac{\partial}{\partial l} P - \Gamma_0 \exp \left[-\left(E - \frac{1}{2} k l^2 \right) / x \right] P + \Gamma(t) \rho(E) \delta(l) \quad (\text{B.4.1})$$

where $\dot{\gamma}$ is the macroscopic strain rate, l is the local strain variable in a representative mesoscopic region, k is an elastic constant, E is the maximal yield energy of each mesoscopic region, $\rho(E)$ is the prior distribution of yield energy (density of states), x is the effective “noise temperature”, Γ_0 is an “attempt frequency”, and $\Gamma(t) = \Gamma_0 \langle \exp[-(E - \frac{1}{2} k l^2) / x] \rangle_P$ describes the relaxation of regions to new local equilibrium positions after yielding. [18] then

considers the functions

$$G_0(z) = \int dE P_0(E) \exp(-ze^{-E/x}) \quad (\text{B.4.2})$$

$$G_\rho(z) = \int dE \rho(E) \exp(-ze^{-E/x}) \quad (\text{B.4.3})$$

which describe the purely noise-induced decay of the stress. Furthermore, he takes $\rho(E)$ to be of the form $\rho(E) = \exp\{-E[1 + f(E)]\}$ with $f(E) \rightarrow 0$ for $E \rightarrow \infty$. In what follows, $f \equiv 0$, but all power-laws reported below are valid for any $f(E)$ (i.e. general $\rho(E)$) up to 'sub-power-law factors' such as logarithms; see Appendix B of Ref. [18] for details. Substituting this form for $\rho(E)$ into equation B.4.3, we obtain a Laplace integral which we expand asymptotically to obtain [205]

$$G_\rho(z) = \frac{1}{2} \left\{ \sqrt{2\pi x} \left(\frac{x}{e} \right)^x \right\} z^{-x} \quad (\text{B.4.4})$$

Now, [18] assumes $P_0(E) = P_{\text{eq}}(E) = \Gamma_{\text{eq}} \exp(E/x)\rho(E)$ and correspondingly, $G_0(z) = G_{\text{eq}}(z)$ and it is observed that $G_\rho(z) = -\Gamma_{\text{eq}}^{-1} G'_{\text{eq}}(z)$. This gives us

$$G_{\text{eq}}(z) = \Gamma_{\text{eq}} \sqrt{\frac{\pi x}{2(x-1)^2}} \left(\frac{x}{e} \right)^x z^{-(x-1)} \quad (\text{B.4.5})$$

In the linear regime, the constitutive equation of the SGR model reduces to

$$\sigma(t) = \int_0^t dt' \dot{\gamma}(t') G_{\text{eq}}(t-t') \quad (\text{B.4.6})$$

Substituting equation B.4.5 into equation B.4.6 and inspecting the result we obtain

$$\begin{aligned} \sigma(t) &= \Gamma_{\text{eq}} (\alpha-1)! \sqrt{\frac{\pi(\alpha+1)}{2\alpha^2}} \left(\frac{\alpha+1}{e} \right)^{\alpha+1} \frac{d^\alpha \gamma(t)}{dt^\alpha} \\ &= \Gamma_{\text{eq}} \xi(\alpha) \frac{d^\alpha \gamma(t)}{dt^\alpha} \\ &= \mathbb{V} \frac{d^\alpha \gamma(t)}{dt^\alpha} \end{aligned} \quad (\text{B.4.7})$$

where $\alpha = x - 1$,

$$\xi(\alpha) = (\alpha - 1)! \sqrt{\frac{\pi(\alpha + 1)}{2\alpha^2}} \left(\frac{\alpha + 1}{e}\right)^{\alpha+1} \quad (\text{B.4.8})$$

and $\mathbb{V} = \Gamma_{\text{eq}}\xi(\alpha)$. Therefore, in the limit of large z (or long times compared to the reciprocal of the attempt frequency $1/\Gamma_0$), the constitutive equation of the SGR model reduces to that of a single spring-pot with the fractional exponent α related to the effective noise temperature x through $\alpha = x - 1$ and the quasi-property \mathbb{V} related to the equilibrium attempt frequency Γ_{eq} through $\mathbb{V} = \Gamma_{\text{eq}}\xi(\alpha)$ for general $\rho(E)$ up to sub-power-law factors.

B.5 Creep ringing and the linear Jeffreys model

In figure B.5.1 we show a creep experiment performed on 50 mg/ml BSA solutions with significant inertial effects as well as the best fit prediction of the Maxwell-Jeffreys model [26] with an added inertial mass. The damped oscillatory ringing arising from the interaction of the fluid viscoelasticity with instrument inertial effects can be observed at short times, and power-law creep behaviour is seen in the experimental data at long times. The solid black line shows the best fit to a linear Jeffreys model performed on the full temporal span of the creep data ($0.02 \leq t \leq 60$ s). Although the long time ($t \geq 1$ s) fit is acceptable, the fit to the inertio-elastic ringing regime is poor. Moreover, the best fit increasingly deviates at longer times. On the other hand, a fit performed only to the creep-ringing regime ($0 \leq t \leq 1$ s), shown by the black dashed line, predicts the material response poorly at long times.

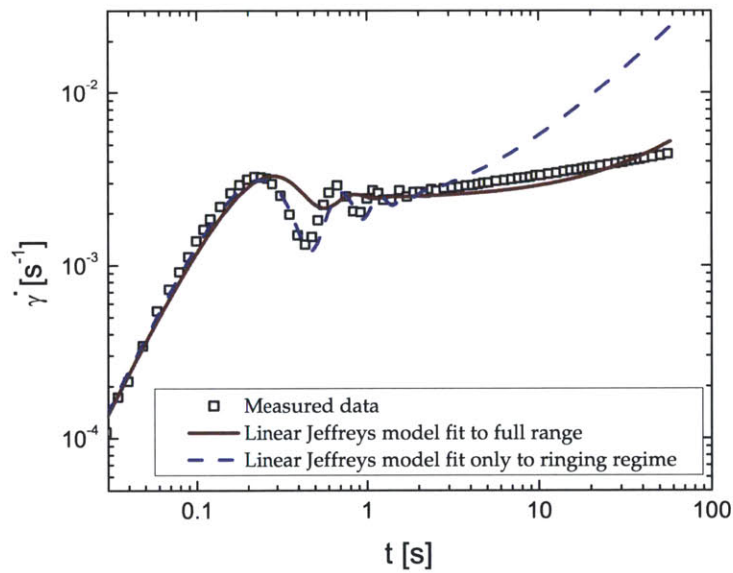


Figure B.5.1: Interfacial creep data obtained with a 50 mg/ml BSA solution. A viscously damped inertio-elastic ringing is present at early times and a power-law behaviour is exhibited at long times. The solid line shows the linear Maxwell fit to the entire time range of the experiment, and the dashed line shows the linear Maxwell fit only to the ringing regime. Neither fit performs adequately at capturing both the ringing phenomenon as well as the long-time power-law behaviour.

C | *Supplementary Information to Chapter 4*

In Chapter 4, we provide analytical expressions for $\eta(\dot{\gamma})$ and $\Psi_1(\dot{\gamma})$ (Eqs. 4.3.22 and 4.3.27 respectively). However, the solution presented is the lowest order term of a more general higher order solution. For most experimental values of the exponents α and β , including for the fluids discussed in the main manuscript, a single term expansion is fine. But for $\alpha \rightarrow 1$ and/or $\beta \rightarrow 0$, higher order descriptions are needed. In this appendix we provide the derivation of the full analytical solution. However for the particular values of $\alpha = 1$ and $\beta = 0$, the Mittag-Leffler kernel reduces to an exponential, and hence does not have a power-law asymptote at long times. In this case, the integral must be solved explicitly with an exponential relaxation kernel. For all other values of $0 < \beta < \alpha < 1$, the analysis below holds.

We begin with the expression for the steady shear viscosity $\eta(\dot{\gamma})$ given by Eq. 4.3.15 as follows:

$$\eta(\dot{\gamma}) = -\mathbb{G} \int_0^{\infty} u^{-\beta} E_{\alpha-\beta, -\beta} \left(-\frac{\mathbb{G}}{\mathbb{V}} u^{\alpha-\beta} \right) \cdot \frac{1}{1 + a(\dot{\gamma}u)^2} du \quad (\text{C.0.1})$$

Note that in Eq. 4.3.15 we set the damping function constant $a = 0.3$ on account of this being the appropriate experimentally measured value for our Xanthan gum solutions, but in Eq. C.0.1 we keep it general. Setting $\gamma = \dot{\gamma}u$, we obtain

$$\eta(\dot{\gamma}) = -\mathbb{G}\dot{\gamma}^{\beta-1} \int_0^{\infty} \frac{\gamma^{-\beta}}{1 + a\gamma^2} E_{\alpha-\beta, -\beta} \left(-\frac{\mathbb{G}}{\mathbb{V}} \dot{\gamma}^{\beta-\alpha} \gamma^{\alpha-\beta} \right) d\gamma \quad (\text{C.0.2})$$

As before, we split the integral with limits that range from 0 to ∞ into two different integrals

as follows:

$$\eta(\dot{\gamma}) = -\mathbb{G}\dot{\gamma}^{\beta-1} \left[\int_0^{\gamma^*} \frac{\gamma^{-\beta}}{1+a\gamma^2} \sum_{k=1}^{\infty} \frac{\left(-\frac{\mathbb{G}}{\mathbb{V}}\dot{\gamma}^{\beta-\alpha}\gamma^{\alpha-\beta}\right)^{k-1}}{\Gamma((k-1)(\alpha-\beta)-\beta)} d\gamma \right. \\ \left. + \int_{\gamma^*}^{\infty} -\frac{\gamma^{-\beta}}{1+a\gamma^2} \sum_{k=1}^{\infty} \frac{\left(-\frac{\mathbb{G}}{\mathbb{V}}\dot{\gamma}^{\beta-\alpha}\gamma^{\alpha-\beta}\right)^{-k}}{\Gamma(-k(\alpha-\beta)-\beta)} d\gamma \right] \quad (\text{C.0.3})$$

in which $\gamma^* = (\mathbb{V}/\mathbb{G})^{\alpha-\beta}\dot{\gamma} = \tau\dot{\gamma}$. The decomposition exploits the fact that the Mittag-Leffler function has well defined asymptotes for both small and large arguments, and has the following expansions [82]

$$E_{a,b}(z) = \sum_{k=1}^N \frac{z^{k-1}}{\Gamma(a(k-1)+b)} + \mathcal{O}(z^{N+1}), \quad z \ll 1 \quad (\text{C.0.4})$$

$$E_{a,b}(z) = -\sum_{k=1}^N \frac{z^{-k}}{\Gamma(b-ak)} + \mathcal{O}(z^{-(N+1)}), \quad z \gg 1 \quad (\text{C.0.5})$$

The Mittag-Leffler function smoothly transitions between its small argument power law ($\sim z^0$) to its large argument power law ($\sim z^{-1}$). By separating the integrals into two domains, we assume that the Mittag-Leffler function is piecewise continuous, and transitions from the power law asymptote for $z \ll 1$ to the asymptote for $z \gg 1$ at the discrete point $\gamma = \gamma^*$.

We can solve for the integrals in Eq. C.0.3 in terms of hypergeometric function defined in Eq. 4.3.21 and we obtain

$$\eta(\dot{\gamma}) = \sum_{k=1}^N \left[-\mathbb{G} \left(-\frac{\mathbb{G}}{\mathbb{V}}\right)^{k-1} \frac{\dot{\gamma}^{-p_k}}{\Gamma(p_k-1)} \frac{(\gamma^*)^{p_k}}{p_k} \times {}_2F_1\left(1, \frac{p_k}{2}, 1 + \frac{p_k}{2}; -a(\gamma^*)^2\right) \right. \\ \left. + \mathbb{G} \left(-\frac{\mathbb{G}}{\mathbb{V}}\right)^{-k} \frac{\dot{\gamma}^{q_k-2}}{\Gamma(-q_k+1)} \frac{(\gamma^*)^{-q_k}}{aq_k} \times {}_2F_1\left(1, \frac{q_k}{2}, 1 + \frac{q_k}{2}; \frac{-1}{a(\gamma^*)^2}\right) \right] \quad (\text{C.0.6})$$

in which we have introduced the parameters

$$p_k = \alpha(k - 1) - k\beta + 1 \quad (\text{C.0.7})$$

$$q_k = \alpha k - (k - 1)\beta + 1 \quad (\text{C.0.8})$$

for ease of notation, we obtain

An analytical expression for the first normal stress coefficient $\Psi_1(\dot{\gamma})$, given by 4.3.26, can be derived in an identical fashion, and we obtain

$$\begin{aligned} \Psi_1(\dot{\gamma}) = \sum_{k=1}^N \left[-\mathbb{G} \left(-\frac{\mathbb{G}}{\mathbb{V}} \right)^{k-1} \frac{\dot{\gamma}^{-p_k}}{\Gamma(p_k - 1)} \frac{(\gamma^*)^{p_k+1}}{p_k + 1} \times {}_2F_1 \left(1, \frac{p_k + 1}{2}, \frac{p_k + 3}{2}; -a(\gamma^*)^2 \right) \right. \\ \left. + \mathbb{G} \left(-\frac{\mathbb{G}}{\mathbb{V}} \right)^{-k} \frac{\dot{\gamma}^{q_k-2}}{\Gamma(-q_k + 1)} \frac{(\gamma^*)^{1-q_k}}{a(q_k - 1)} \times {}_2F_1 \left(1, \frac{q_k - 1}{2}, \frac{q_k + 1}{2}; \frac{-1}{a(\gamma^*)^2} \right) \right] \quad (\text{C.0.9}) \end{aligned}$$

Eq. C.0.6 and C.0.9 reduce to Eqs. 4.3.22 and 4.3.27, respectively, by retaining only the lowest order term, *i.e.* the $k = 1$ term and neglecting all higher order terms.

We note that Eq. C.0.5 is strictly valid only in the limit of $z \gg 1$. However, for the purposes of our analytical approximation, we apply this asymptotic limit for $z \geq 1$ (cf. the second integral in Eq. C.0.3; the limits of the argument of the Mittag-Leffler function range from 1 to ∞). In this second integral, as the value of k is increased, the term $1/\Gamma(-\beta - k(\alpha - \beta))$ begins to increase rapidly in magnitude and alternate in sign. This is easily seen by plotting the value of $1/\Gamma(x)$ for $x \leq 0$ (not shown here). Therefore, we in fact obtain poorer approximations for higher orders, beyond a certain value of k . Note that this counter-intuitive result would not have arisen if we had used a larger value of the lower limit in the second integral in Eq. C.0.3, say $\gamma^* \rightarrow 10\gamma^*$, because the z^{-k} term, being large, would damp put these oscillations in the Gamma function. In this case, we could find the approximate solution up to large k , without diminishing accuracy.

However, we note that in practice, we rarely require large k ; to check the accuracy and convergence of our approximation, we compared the exact numerical solution to Eq. C.0.2 with the approximate solution given in Eq. C.0.3 with various randomly generated values of $0 < \beta < \alpha < 1$ and \mathbb{V}, \mathbb{G} . We find that in all cases, we require at most $k = 3$ to get very close agreement between the approximate result and the exact numerical solution, and the $1/\Gamma(-\beta - k(\alpha - \beta))$ is well behaved.

D | *Supplementary Information to Chapter 5*

D.1 *Determination of $I_n(t)$*

We begin with the evaluation of the integral $I_n(t)$ defined as

$$I_n(t) = \int_0^t \left(\frac{\mathbb{V}(t-t')^{-\alpha}}{\Gamma(1-\alpha)} + \frac{\mathbb{G}(t-t')^{-\beta}}{\Gamma(1-\beta)} \right) \cdot \frac{1}{(h_0/u_0 + t')^n} dt' \quad (\text{D.1.1})$$

$$= \int_0^t \frac{\mathbb{V}(t-t')^{-\alpha}}{\Gamma(1-\alpha)(h_0/u_0 + t')^n} + \int_0^t \frac{\mathbb{G}(t-t')^{-\beta}}{\Gamma(1-\beta)(h_0/u_0 + t')^n} dt' \quad (\text{D.1.2})$$

$$= \frac{\mathbb{V}}{\Gamma(1-\alpha)} I_{n\alpha} + \frac{\mathbb{G}}{\Gamma(1-\beta)} I_{n\beta} \quad (\text{D.1.3})$$

Note that $I_{n\alpha}$ is identical to $I_{n\beta}$ in that simply replacing α by β in $I_{n\alpha}$ yields $I_{n\beta}$. Therefore, we only determine one of the integrals here, say $I_{n\alpha}$:

$$I_{n\alpha}(t) = \int_0^t \frac{(t-t')^{-\alpha}}{(h_0/u_0 + t')^n} dt' \quad (\text{D.1.4})$$

Let $t - t' = u$. It can be shown that the integral above reduces to

$$I_{n\alpha}(t) = \int_0^t \frac{u^{-\alpha}}{(h_0/u_0 + t - u)^n} du \quad (\text{D.1.5})$$

$$= \int_0^t \frac{(h_0/u_0 + t)^{-\alpha} \left(\frac{u}{h_0/u_0 + t} \right)^{-\alpha}}{(h_0/u_0 + t)^n \left(1 - \frac{u}{h_0/u_0 + t} \right)^n} du \quad (\text{D.1.6})$$

We now let $u/(h_0/u_0 + t) = v$ to obtain

$$I_{n\alpha}(t) = \frac{1}{(h_0/u_0 + t)^{\alpha+n-1}} \int_0^{\frac{t}{h_0/u_0+t}} v^{-\alpha} (1-v)^{-n} dv \quad (\text{D.1.7})$$

Defining the stretch ratio λ as

$$\lambda = \frac{h_0 + u_0 t}{h_0} = 1 + \frac{u_0}{h_0} t \quad (\text{D.1.8})$$

we can write equation D.1.7 as

$$I_{n\alpha}(t) = \left(\frac{u_0}{h_0} \right)^{\alpha+n-1} \frac{1}{\lambda^{\alpha+n-1}} \mathfrak{B}_{1-1/\lambda}(1-\alpha, 1-n) \quad (\text{D.1.9})$$

where $\mathfrak{B}_x(a, b)$ is the incomplete beta function defined as [204]

$$\mathfrak{B}_x(a, b) = \int_0^x u^{a-1} (1-u)^{b-1} du \quad ; a > 0 \text{ and } x \leq 1 \quad (\text{D.1.10})$$

Replacing α by β in equation D.1.9 we get

$$I_{n\beta}(t) = \left(\frac{u_0}{h_0} \right)^{\beta+n-1} \frac{1}{\lambda^{\beta+n-1}} \mathfrak{B}_{1-1/\lambda}(1-\beta, 1-n) \quad (\text{D.1.11})$$

Substituting D.1.9 and D.1.11 into D.1.3, and letting $n \rightarrow n+1$ for compactness of notation, we arrive at

$$I_{n+1}(t) = \frac{\mathbb{V}}{\Gamma(1-\alpha)} \left(\frac{u_0}{h_0}\right)^{\alpha+n} \frac{1}{\lambda^{\alpha+n}} \mathfrak{B}_{1-1/\lambda}(1-\alpha, -n) + \frac{\mathbb{G}}{\Gamma(1-\beta)} \left(\frac{u_0}{h_0}\right)^{\beta+n} \frac{1}{\lambda^{\beta+n}} \mathfrak{B}_{1-1/\lambda}(1-\beta, -n) \quad (\text{D.1.12})$$

We simply set $n = 2$ above to determine the value of $I_3(t)$ appearing in equation 5.2.45.

D.2 Boundary condition for determining C_1 .

From symmetry arguments, we know that

$$\tau_{zz}(h/2 - \Delta z) = \tau_{zz}(h/2 + \Delta z) \quad (\text{D.2.1})$$

In other words, we observe that the stress in the axial direction is symmetric about the mid plane of the fluid filament. This implies

$$\tau_{zz}(h/2 + \Delta z) - \tau_{zz}(h/2 - \Delta z) = 0 \quad (\text{D.2.2})$$

$$\Rightarrow \frac{\tau_{zz}(h/2 + \Delta z) - \tau_{zz}(h/2 - \Delta z)}{(h/2 + \Delta z) - (h/2 - \Delta z)} = 0 \quad (\text{D.2.3})$$

$$\Rightarrow \lim_{\Delta z \rightarrow 0} \frac{\tau_{zz}(h/2 + \Delta z) - \tau_{zz}(h/2 - \Delta z)}{2\Delta z} = 0 \quad (\text{D.2.4})$$

$$(\text{D.2.5})$$

from which we obtain the boundary condition

$$\boxed{\left. \frac{\partial \tau_{zz}}{\partial z} \right|_{z=h/2} = 0} \quad (\text{D.2.6})$$

E | *An analytical solution to the extended Navier-Stokes equations using the Lambert W function.*

Microchannel gas flows are of importance in a wide range of MEMS devices. In these flows, the mean free path of the gas can be comparable to the characteristic length of the microchannel, leading to strong diffusion-enhanced transport of momentum. Numerical solutions to the Extended Navier Stokes Equations (ENSE) have successfully modeled such microchannel flows. In this paper, we derive analytical solutions to the ENSE for the pressure and velocity field using the Lambert W function. We find that diffusive contributions to the total transport are only dominant for low average pressures and low pressure drops across the microchannel. For large inlet pressures, we show that the expressions involving the Lambert W function predict steep gradients in the pressure and velocity localized near the channel exit. We extract a characteristic length for this boundary layer. Our analytical results are validated by numerical and experimental results available in the literature.

E.1 Introduction

Micro channel gas flows have elicited much research interest in recent years [317]. Such flows are frequently encountered in Micro Electro Mechanical Systems (MEMS) such as in thermal cooling systems for electronic devices [318], air damping of MEMS resonators [319, 320], gas chromatograph analyzers [321] and other applications. Theoretical understanding of macroscale fluid flows, where the continuum approximation holds, has existed for many decades and phenomena appearing at these length scales are well understood and described in classic textbooks [5, 322]. Micro channel flows, however, exhibit many sig-

nificant deviations from the predictions of the Classical Navier–Stokes Equations (CNSE) used to analyze macroscale flows. It has been known from the time of Maxwell [323] that the no-slip boundary condition can be violated in rarefied gas flows. Other deviations from classical macroscale flows include observations of higher mass flow rates through the channel [324] and nonlinear pressure drop along the channel [325]. In a comprehensive overview of the first fifty years of Transport Phenomena [326], Bird highlights as some of the present day challenges: “(e) What boundary and interfacial conditions in transport phenomena need to be clarified by use of molecular dynamics?” and “(h) What is the correct velocity boundary condition at the tube wall when a homogeneous mixture is flowing through the tube?”.

Deviations from the classical results arise from rarefaction of the gas or the shrinking of the characteristic length scales of the flow geometry so that the mean free path λ of the gas becomes comparable to the characteristic length of the flow channel h [327]. Another important source of the deviation of micro scale flows from CNSE predictions is the relative importance of wall effects. The shrinking characteristic length scales of the channel lead to increasing surface to volume ratios, and hence the nature of interaction of the wall with the gas can strongly influence the flow properties. This is essentially a breakdown of the continuum approximation; to be able to neglect microscopic statistical fluctuations, we need a sampling volume with a characteristic length much bigger than the length scale h of the micro channel.

We quantify the deviation from the continuum approximation with the help of the Knudsen number Kn defined as

$$\text{Kn} = \frac{\lambda}{h} \quad (\text{E.1.1})$$

where h is the characteristic length of the channel, and λ is the mean free path of the gas defined as [328]

$$\lambda = \frac{\mu}{P} \sqrt{\frac{\pi RT}{2}} \quad (\text{E.1.2})$$

Here μ is the viscosity of the gas, P is the pressure, R is the gas constant and T is the absolute temperature. In order of increasing Kn , the flow characteristics may be classified as a classical continuum flow, slip flow, transition flow or a free molecular flow [327]. Some typical values of Kn corresponding to these regimes are shown in Figure E.1.1, which has

been adapted from Dongari et al. [329].

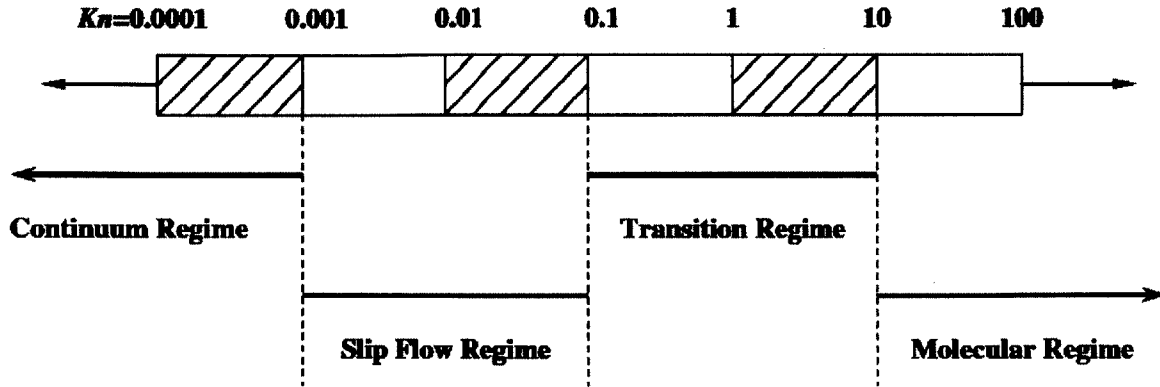


Figure E.1.1: The different regime classifications of micro channel flows based on Knudsen number Kn. Figure is reproduced from [329].

Some of the earliest attempts to account for wall effects and to model the effects of slip in rarefied gas flows were due to Maxwell [323], who modeled the wall surfaces as being intermediate between perfectly reflecting and perfectly absorbing. Due to the roughness of the wall, a fraction σ of the gas molecules impacting it are absorbed by the wall, and subsequently re-emitted in a diffuse manner with a velocity distribution corresponding to a quiescent gas at that particular temperature. The remaining fraction $1 - \sigma$ is reflected specularly. With this assumption, Maxwell showed that the tangential slip velocity at the wall is given by

$$u_{\text{slip}} = \frac{2 - \sigma}{\sigma} \lambda \frac{\partial u}{\partial y} \quad (\text{E.1.3})$$

where $\partial u / \partial y$ is the velocity gradient normal to the flow direction. For high Knudsen number flows, deviations from a first-order derivative model are observed, and hence higher order derivatives are frequently used to model slip in micro channel flows [327, 328, 330, 331]. Extensive reviews on the topic of wall slip and rarefied gas flows in micro channels are available [332].

It has been argued that using the CNSE together with the Maxwell slip velocity formulation is largely an empirical approach to modeling micro channel gas flows [333]. Furthermore, it does not account for local gradients in density which can create local fluxes due to self diffusion [334, 335]. A new approach has been proposed in a series of publications

by Durst and co-workers (see for example [329, 335–337]). The underlying assumption in this theory is that the pressure gradient in the direction of the compressible flow provides an additional diffusive mode of mass transport, which is accounted for analytically by adding an extra term to the CNSE. One therefore eliminates the need to include, in an *ad hoc* manner, the Maxwell slip velocity [329].

A treatment for the self diffusion of gases has been discussed in the landmark transport phenomena text by Hirschfelder, Curtiss and Bird. [338]. They note that in addition to the familiar sources of momentum and mass diffusion that arise from concentration gradients in a multi-component system, there is another contribution to the diffusive flux that arises from the pressure gradient itself. The coefficients of self diffusion can be experimentally measured using, for example, the diffusion of one isotope of a gas into another, if the molecules are sufficiently heavy (see the discussion by Slattery and Bird [339]). These additional modes of transport are accounted for using a rigorous kinetic theory approach, making the mass flux expression significantly more complicated (see, for example, Pg. 516 of Hirschfelder et al. [338]). These additional contributions cannot be neglected when large pressure gradients exist in a rarefied gas flow field. The Extended Navier Stokes Equations (ENSE) proposed by Durst et al. [336] account for this mass and momentum transport due to self diffusion by replacing the velocity in the CNSE with a *total* velocity, that is a sum of convective and diffusive velocity terms.

The problem of pressure driven flow in of a compressible viscous gas through a tube is posed as a detailed exercise (2B.9) in R.B. Bird's second edition of *Transport Phenomena* [322]. Here it is suggested that there is additional contribution to the mass flux along the channel that arises from slip at the wall of the channel. It is suggested (based on empirical evidence) that the slip varies inversely with the pressure in the gas (consistent with equations E.1.2 and E.1.3). The general form of the mass flux variation with pressure is sketched in a figure (Figure 2B.9 of reference [322]), and the insightful student might ask why the sketch shows not just an augmentation in the total flow rate through the channel but also a non-monotonic variation. To quantify and understand such observations it is necessary to have an analytic expression for the mass flux which describes the underlying transport phenomena.

In this paper, we provide for the first time analytical results obtained for micro channel gas flows modeled using the ENSE under the assumptions of the lubrication approximation; currently only semi-analytical or numerical solutions are typically reported. Our presen-

tation is intended to be didactic; we first provide a brief overview of the formulation of the model and the relevant equations. We then present the new analytical expression for the relationship between the total mass flux and the applied pressure difference, and discuss the inherent non-monotonocities and non-linearities that arise. We also compare the results with experimental data to test their predictive ability. The utility of an analytic description of the flow field is demonstrated by using this new formulation to understand the boundary layer structure that can develop near the microchannel exit for sufficiently large inlet pressures. Finally, we use this detailed analytical understanding of this canonical fluid mechanics problem to construct a new flow state map for channel flows of a rarefied gas.

E.2 The Extended Navier Stokes Equations (ENSE)

At steady state and in the absence of any temperature gradients, the system of equations referred to for compactness as the ENSE for a single species are given by [340]

$$\frac{\partial(\rho u_i^T)}{\partial x_i} = 0 \quad (\text{E.2.1})$$

$$\frac{\partial}{\partial x_i} (\rho u_i^T u_i^T) = -\frac{\partial P}{\partial x_j} - \frac{\partial}{\partial x_i} \left(\tau_{ij}^C - \frac{2}{3} \delta_{ij} \dot{m}_k^D u_k^C \right) \quad (\text{E.2.2})$$

$$\tau_{ij}^C = -\mu \left(\frac{\partial u_i^C}{\partial x_j} + \frac{\partial u_j^C}{\partial x_i} \right) + \frac{2}{3} \mu \delta_{ij} \frac{\partial u_k^C}{\partial x_k} \quad (\text{E.2.3})$$

along with the ideal gas equation of state

$$\rho = \frac{P}{RT} \quad (\text{E.2.4})$$

It is assumed that the total mass transport in the extended model consists of a linear sum of convective and diffusive terms. The superscripts C, D and T in the above equations refer to convective, diffusive and total quantities respectively. The total velocity component in the i direction is given by $u_i^T = u_i^C + u_i^D$. The subscripts i, j, k refer to orthogonal coordinate directions and take the values 1, 2 or 3. The other symbols in the above equations are the local density $\rho(\vec{x})$, the local velocity $u(\vec{x})$, the local pressure $P(\vec{x})$, the local dynamic viscosity μ and the self diffusive mass flux in the k direction $\dot{m}_i^D = \rho u_i^D$. The Kronecker delta function

is denoted by δ_{ij} . The self diffusive velocity in the i direction is given by the expression

$$u_i^D = -\frac{\mu}{\rho P} \frac{\partial P}{\partial x_i} \quad (\text{E.2.5})$$

This diffusive velocity u^D is driven by gradients in the pressure and accounts for the Maxwellian slip-like velocity in a natural way, rather than introducing tunable parameters such as the parameter σ in equation E.1.3.

In this paper we consider a rectangular micro channel of length L , width w and height h , with $h \ll w \ll L$. The lubrication approximation holds under these limits [5] and, assuming steady state flow, the ENSE simplify to [337]

$$\frac{\partial}{\partial x} (\rho u^T) + \frac{\partial}{\partial y} (\rho v^T) = 0 \quad (\text{E.2.6})$$

$$\frac{\partial^2 u^T}{\partial y^2} \approx \frac{1}{\mu} \frac{\partial P}{\partial x} \quad (\text{E.2.7})$$

along with the empirical boundary conditions

$$u^T|_{y=\pm h} = -\frac{\mu}{\rho P} \frac{\partial P}{\partial x} \quad (\text{E.2.8})$$

where the walls of the micro channel are located at $y = \pm h$. These boundary conditions arise from the assumption that the no-slip boundary condition applies to the convective velocity u^C at the wall surfaces ($u^C = 0$) so that only a diffusive flux is present locally. It is important to note within the lubrication approximation the mass and momentum equations are not satisfied *exactly*. We ignore terms of order $O(h/L)^2$ and higher. This is a good approximation given the dimensions of the microchannel, and that $h \ll w \ll L$.

Solving equation E.2.7 for u^T and employing the boundary condition E.2.8, Adachi et al. [337] show that

$$\dot{m}^T = \rho u^T = -\frac{\rho}{2\mu} (h^2 - y^2) \frac{dP}{dx} - \frac{\mu}{P} \frac{dP}{dx} \quad (\text{E.2.9})$$

where \dot{m}^T is the local mass flux per unit area and the total mass flow rate \dot{M}^T through any

cross section of the channel is given by

$$\dot{M}^T = w \int_{-h}^h \rho u^T dy \quad (\text{E.2.10})$$

$$= -2hw \left(\frac{h^2 P}{3\mu RT} + \frac{\mu}{P} \right) \frac{dP}{dx} \quad (\text{E.2.11})$$

We now proceed to find analytical expressions for the pressure field and the mass flow rate as well as the velocity field $u(x, y)$ in the channel. Whereas an expression for the total mass flux through the channel may be found by solving equation implicitly [337], previous approaches have solved for the explicit local pressure and velocity fields numerically.

E.3 Results and Discussion

Consider the expression for the total mass flow rate \dot{M}^T derived in equation E.2.11. Because the mass flow rate remains constant through any arbitrary cross-section of the channel, we have $d\dot{M}^T/dx = 0$ and we can write this expression in the form

$$\left(\frac{h^2 P}{3\mu RT} + \frac{\mu}{P} \right) \frac{dP}{dx} = -C' \quad (\text{E.3.1})$$

where $C' = \dot{M}^T/2hw$ is a constant of integration. This equation can be solved for P implicitly, and we determine C' from the boundary conditions at the inlet and outlet of the channel $P(0) = P_i$ and $P(L) = P_o$ to obtain

$$C' = \frac{1}{6RT} \frac{h^2}{L} \left(P_i^2 - P_o^2 + \frac{3\mu^2 RT}{h^2} \ln \frac{P_i^2}{P_o^2} \right) \quad (\text{E.3.2})$$

We now non-dimensionalize equation E.3.1 using $\bar{x} = x/L$ and $\bar{P} = P/P_c$ where L is the length of the micro channel and P_c is a characteristic pressure for an ideal gas given by $P_c = \mu\sqrt{3RT}/h$. As the pressure is increased to P_c , the mean free path given by equation E.1.2 decreases to give a characteristic mean-free path λ_c or, equivalently, a characteristic Knudsen number given by $\text{Kn}_c = \lambda_c/h = \sqrt{\pi/6}$ which characterizes the transition region in figure E.1.1. Substituting these scalings into Equation E.3.1 and E.3.2 results in

the simpler expression

$$\left(\bar{P} + \frac{1}{\bar{P}}\right) \frac{d\bar{P}}{d\bar{x}} = -\bar{C} \quad (\text{E.3.3})$$

where $\bar{C} = (L/\mu)C'$ is dimensionless. Solving this equation for the dimensionless pressure distribution along the channel $\bar{P}(\bar{x})$ with $\bar{P} = P_i/P_c = \bar{P}_i$ at $\bar{x} = 0$ and $\bar{P} = P_o/P_c = \bar{P}_o$ at $\bar{x} = 1$ we obtain the implicit expression

$$\bar{P}_i^2 - \bar{P}^2 + \ln \frac{\bar{P}_i^2}{\bar{P}^2} = \left(\bar{P}_i^2 - \bar{P}_o^2 + \ln \frac{\bar{P}_i^2}{\bar{P}_o^2} \right) \bar{x} \quad (\text{E.3.4})$$

At this point expression E.3.4 can be evaluated using a suitable nonlinear equation solver or root finding algorithm; however additional insight can be gained by seeking an analytic expression for $\bar{P}(\bar{x})$. This equation admits itself to an exact closed form analytical solution given by

$$\frac{P(x/L)}{P_c} \equiv \bar{P}(\bar{x}) = \sqrt{W \left(\exp \left[- \left(\bar{P}_i^2 - \bar{P}_o^2 + \ln \frac{\bar{P}_i^2}{\bar{P}_o^2} \right) \bar{x} + \bar{P}_i^2 + \ln \bar{P}_i^2 \right] \right)} \quad (\text{E.3.5})$$

where $W(x)$ is the Lambert W function defined to be the function $W(x)$ that satisfies the equation

$$W(x) \exp[W(x)] = x \quad (\text{E.3.6})$$

Although it may not be widely known, the Lambert W function is ubiquitous in nature and appears in the solution of a number of mathematical as well as physical problems such as electrostatics, population growth, enzyme kinetics and quantum mechanics. It is similar to the trigonometric functions in the sense that it has no explicit closed form, but a very large number of physical problems are solved with relative ease by employing it in the solution [341]. Furthermore, almost all popular physical computing packages such as Mathematica, Matlab and Maple include full support for the Lambert W function, and utilize efficient algorithms to calculate its value at any point in its domain. Corless et al. [342] provide an excellent summary of the history and applications of $W(x)$.

We may now find explicit solutions for the total mass flow rate \dot{M}^T and the velocity

profile u^T by substituting equation E.3.5 into equations E.2.11 and E.2.9 respectively to obtain

$$\dot{M}^T = \frac{\mu h \omega}{L} \left[\bar{P}_i^2 - \bar{P}_o^2 + \ln \left(\frac{\bar{P}_i}{\bar{P}_o} \right)^2 \right] \quad (\text{E.3.7})$$

$$u^T(\bar{x}, \bar{y}) = \frac{h\sqrt{3RT}}{4L} \frac{\bar{P}(\bar{x})}{[1 + \bar{P}^2(\bar{x})]} \left(\bar{P}_i^2 - \bar{P}_o^2 + \ln \frac{\bar{P}_i}{\bar{P}_o} \right) \left(1 - \bar{y}^2 + \frac{2}{3\bar{P}^2(\bar{x})} \right) \quad (\text{E.3.8})$$

where $\bar{y} = y/h$. To find $u^T(\bar{x})$, we were required to find an analytical expression for the pressure drop $d\bar{P}/d\bar{x}$ (cf. equation E.2.9). We give an explicit expression for the pressure drop later; here we simply note that to find $u^T(\bar{x})$, we have used the fact that the derivative $W'(x)$ of the Lambert function given in equation E.3.6 is given by [342]

$$W'(x) = \frac{W(x)}{x(1 + W(x))}; x \neq 0. \quad (\text{E.3.9})$$

We can now also find the individual contributions to the total mass flux that arise from the diffusive velocity field $u^D(\bar{x})$ and the convective velocity field $u^C(\bar{x}, \bar{y})$ from equation E.2.5:

$$u^D(\bar{x}) = \bar{P}_o^2 \frac{h\sqrt{3RT}}{6L} \left(\frac{\mathcal{P}^2 - 1 + (1/\bar{P}_o^2) \ln \mathcal{P}^2}{\bar{P}(\bar{x})(1 + \bar{P}^2(\bar{x}))} \right) \quad (\text{E.3.10})$$

$$u^C(\bar{x}, \bar{y}) = \bar{P}_o^2 \frac{h\sqrt{3RT}}{4L} \left(\frac{\bar{P}(\bar{x})}{1 + \bar{P}^2(\bar{x})} \right) \left(\mathcal{P}^2 - 1 + (1/\bar{P}_o^2) \ln \mathcal{P}^2 \right) \left(1 - \bar{y}^2 - \frac{1}{3\bar{P}^2(\bar{x})} \right) \quad (\text{E.3.11})$$

For a long narrow channel with $h \ll w$, the pressure gradient is unidirectional (along the channel) and the diffusive contribution does not vary across the channel. The total velocity field in the micro channel is given by $u^T(\bar{x}, \bar{y}) = u^C(\bar{x}, \bar{y}) + u^D(\bar{x})$.

Having derived the solution for the pressure field $\bar{P}(\bar{x})$ (which in turn determines the density field $\rho(\bar{x})$) we now seek to determine the quality of the lubrication approximation used to derive these solutions. To this end, we substitute the density field $\rho(x) = P(x)/RT$ and the velocity field $u^T(x, y)$ using equations (19) and (22) respectively, into the continuity equation (9) to solve for the transverse component of the velocity field, and we obtain

$$v^T = -\frac{\mu RT h}{P_c 4L^2} A^2 \frac{\bar{P}(\bar{x})}{[1 + \bar{P}^2(\bar{x})]^3} (\bar{y}^3 - \bar{y}) \quad (\text{E.3.12})$$

where

$$A = \bar{P}_i^2 - \bar{P}_o^2 + \ln \frac{\bar{P}_i^2}{\bar{P}_o^2} \quad (\text{E.3.13})$$

Equation (10) was obtained from (5) and (6) by neglecting terms of order $(h/L)^2$. We now estimate the magnitude of these neglected terms *a posteriori* by using the obtained solutions for $P(x)$, $u(x, y)$ and $v(x, y)$. We first write out the x component of the momentum equation without neglecting terms of $O((h/L)^2)$:

$$0 = -\frac{\partial P}{\partial x} + \frac{\mu}{3} \left(\frac{\partial^2 u^T}{\partial x^2} + \frac{\partial^2 v^T}{\partial x \partial y} \right) + \mu \left(\frac{\partial^2 u^T}{\partial x^2} + \frac{\partial^2 u^T}{\partial y^2} \right) \quad (\text{E.3.14})$$

Because $h \ll L$, $\frac{\partial^2 u^T}{\partial x^2} \ll \frac{\partial^2 u^T}{\partial y^2}$ and hence we can rewrite the above equation as

$$0 = -\frac{\partial P}{\partial x} + \frac{\mu}{3} \frac{\partial^2 v^T}{\partial x \partial y} + \mu \frac{\partial^2 u^T}{\partial y^2} \quad (\text{E.3.15})$$

Because we have analytical solutions for both $u^T(x, y)$ as well as $v^T(x, y)$ we can calculate the terms $\frac{\mu}{3} \frac{\partial^2 v^T}{\partial x \partial y}$ and $\mu \frac{\partial^2 u^T}{\partial y^2}$ as

$$\mu \frac{\partial^2 u^T}{\partial y^2} = A \frac{P_c}{L} \left(-\frac{\bar{P}(\bar{x})}{2(1 + \bar{P}^2(\bar{x}))} \right) \quad (\text{E.3.16})$$

and

$$\frac{\mu}{3} \frac{\partial^2 v^T}{\partial x \partial y} = -\frac{\mu^2 R T}{12 L^3 P_c} (3\bar{y}^2 - 1) A^3 \left(\frac{(5\bar{P}^2(\bar{x}) - 1) P(\bar{x})}{2(1 + \bar{P}^2(\bar{x}))^5} \right) \quad (\text{E.3.17})$$

To find the relative magnitude of the neglected term in the momentum equation, we divide (31) by (30) and obtain

$$\frac{\frac{\mu}{3} \frac{\partial^2 v^T}{\partial x \partial y}}{\mu \frac{\partial^2 u^T}{\partial y^2}} = \frac{1}{36} \left(\frac{h}{L} \right)^2 (3\bar{y}^2 - 1) A^2 \left(\frac{(5\bar{P}^2(\bar{x}) - 1)}{(1 + \bar{P}^2(\bar{x}))^4} \right) \quad (\text{E.3.18})$$

In the next section, we compare our analytic expression with experiments by Maurer et al[343]. In these experiments, $h = 0.6 \mu\text{m}$ and $L = 10 \text{ cm}$, leading to $(h/L)^2 \sim O(10^{-11})$.

Moreover, for all experimentally accessible parameters, the factor

$$A^2 \left(\frac{5\bar{P}^2(\bar{x}) - 1}{(1 + \bar{P}^2(\bar{x}))^4} \right) \ll 10^{11} \quad (\text{E.3.19})$$

For example, for typical experimental values of $\bar{P}_i/\bar{P}_o = 30$ and $\bar{P}_i = 10$ used by Maurer et al., the magnitude of this term is about $10^3 \ll 10^{11}$. Therefore we are justified in employing the lubrication approximation for typical microchannel geometries over a wide range of magnitudes of the dimensionless pressure field. This conclusion is further supported in the next section by comparing the predictions of our results with experimental data.

E.3.1 Comparison with Data

Equipped with these analytical solutions for the mass flow rate, the pressure field as well as the local velocity field, we next examine the behavior of these expressions under various conditions of inlet and outlet pressures and also compare the analytic expressions with experimental data. In figure E.3.1, we show the scaled pressure $\Delta\bar{P}_s = (\bar{P} - \bar{P}_o)/(\bar{P}_i - \bar{P}_o)$ calculated using equation E.3.5 as a function of position along the channel \bar{x} . The curves correspond to different values of the inlet pressure \bar{P}_i for a fixed (small) value of the outlet pressure \bar{P}_o . It is observed that the nature of the scaled pressure drop $\Delta\bar{P}_s$ strongly depends on the relative values of inlet and outlet pressures. We know that in the classical case the scaled pressure along the channel varies as $\Delta\bar{P}_s = 1 - \bar{x}$, and this linear result is indepen-

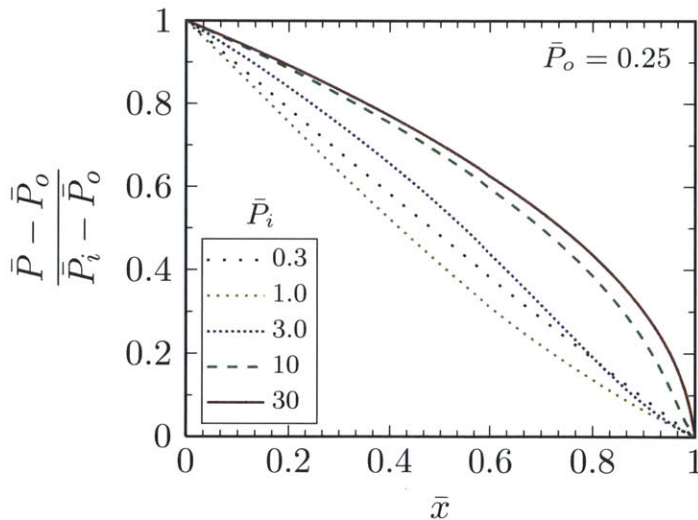


Figure E.3.1

Evolution in the non-dimensional pressure $\bar{P}(\bar{x}) = P(\bar{x})/P_c$ as a function of non-dimensional position $\bar{x} = x/L$ along the micro channel analytically determined from equation E.3.5. We observe that the pressure is a non-monotonic function of \bar{P}_i , and saturates for high inlet pressures \bar{P}_i . Furthermore, an inflection point is present in the curves, some of which are not readily apparent in the plots above on account of being very close to the exit.

dent of the inlet and outlet pressures \bar{P}_i and \bar{P}_o . Accounting for diffusive terms makes the pressure drop highly nonlinear, and it is now a function of both \bar{P}_i and \bar{P}_o . Moreover, for a fixed value of \bar{x} , say $\bar{x} = 0.5$, can be noted that the value of the scaled pressure varies non-monotonically at small values of \bar{P}_i and saturates at high values of \bar{P}_i .

In this Appendix, although we obtain the pressure profiles presented in figure E.3.1 using a lubrication approximation solution to the simplified ENSE, there are other techniques to arrive at an approximate analytic solution for microchannel gas flows. One widely used approach that has led to much success is to obtain a solution for the full Navier-Stokes equations for a compressible fluid using a regular perturbation method[344]. Notably, Venerus and Bugajsky[345] derive expressions for stream-wise as well as transverse pressure and velocity fields for microchannel flows of compressible fluids, and their analytical results agree well with previously published experimental data. However the authors note explicitly that they assume flow conditions such that $\text{Kn} \leq 10^{-3}$ (as opposed to $\text{Kn} \sim 1$ in the present work) and any slip effects are negligible. Qin et al.[346] also present a perturbation solution to the compressible Navier Stokes equations, including the case $\text{Kn} \sim 1$ for both short and long channels. The perturbation solution of Arkilic and Schmidt[347] which applies to long channels ($(h/L)^2 \ll \text{Kn}$) is retrieved by Qin et al. in the appropriate limit. Our analytically derived pressure profiles obtained by utilizing the lubrication approximation (figure 2) also agree with those derived using the perturbation solution in these cited works[346, 347] in the correct limit. However, Qin et al. introduce two additional material constants corresponding to slip boundary conditions (slip coefficients), which are obtained from the literature. Moreover, it is apparent from their results that there is an approach to a boundary layer like region near the channel exit. No detailed comments or analysis are presented for this boundary layer structure. We discuss boundary layer like flow in the results section.

This non-linear evolution of the pressure profile predicted by the ENSE is more readily evident in the pressure *gradient* profiles. A closer examination of the curves in figure E.3.1 shows the existence of an inflection point along the profile, i.e. although the pressure gradient along the channel is always negative, its magnitude may vary non-monotonically. We can easily determine the pressure gradient along the channel by differentiating equation E.3.5 with respect to \bar{x} to obtain

$$\frac{d\bar{P}(\bar{x})}{d\bar{x}} = -\frac{\bar{P}(\bar{x})}{2(1 + \bar{P}^2(\bar{x}))} \left(\bar{P}_i^2 - \bar{P}_o^2 + \ln \frac{\bar{P}_i^2}{\bar{P}_o^2} \right) \quad (\text{E.3.20})$$

Plotting equation E.3.20 in Figure E.3.2 for different values of the dimensionless inlet pressure \bar{P}_i , the non-monotonicity in the pressure gradient is readily apparent. In fact, we analytically find the location of this inflection point \bar{x}^i using equation E.3.20 by setting $d^2\bar{P}/d\bar{x}^2 = 0$ to be

$$\bar{x}^i = \frac{\bar{P}_i^2 + \ln \bar{P}_i^2 - 1}{\bar{P}_i^2 - \bar{P}_o^2 + \ln(\bar{P}_i^2/\bar{P}_o^2)} \quad (\text{E.3.21})$$

and the minimum (most negative) pressure gradient in the micro channel $d\bar{P}/d\bar{x}|_{\bar{x}=\bar{x}^i}$, which occurs at the inflection point, is given by

$$\bar{P}'_{\min} \equiv \left. \frac{d\bar{P}}{d\bar{x}} \right|_{\bar{x}=\bar{x}^i} = -\frac{1}{4} \left(\bar{P}_i^2 - \bar{P}_o^2 + \ln \left(\frac{\bar{P}_i}{\bar{P}_o} \right)^2 \right) \quad (\text{E.3.22})$$

where the prime denotes differentiation with respect to \bar{x} .

Deviations from the classical solution for the mass flow rate of a fluid through a micro channel is a fact that has been experimentally established [317, 325, 343, 347, 348]. The mass flow rate is observed to be higher than that predicted by the CNSE with the no-slip boundary condition. This occurs due to the appearance of the additional ‘slip-like’ velocity contribution near the boundaries of the micro channel. This slip-like flow is modeled in the ENSE with the additional diffusive term without the need for introducing any fitting parameters or additional material constants, and hence this model should be able to predict

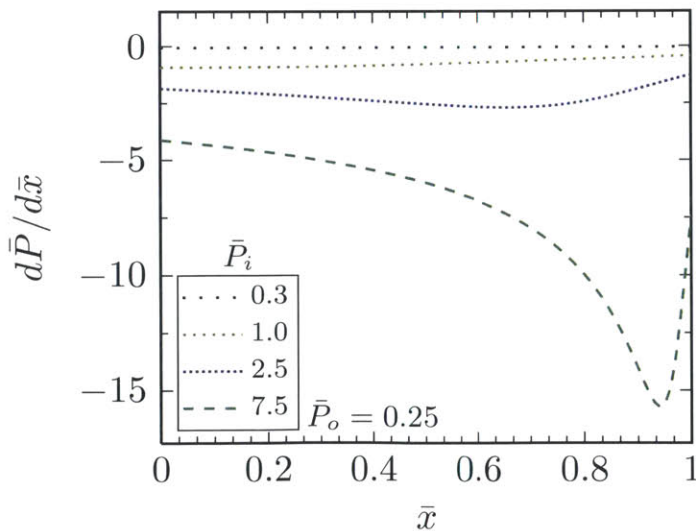


Figure E.3.2

Analytically determined pressure gradient $d\bar{P}/d\bar{x}$ as a function of \bar{x} (equation E.3.20) for a fixed value of the outlet pressure. There exists a point in the channel where the pressure gradient is most favorable (most negative), and the magnitude of the favorable pressure gradient increases with \bar{P}_i . The location \bar{x} at which this occurs is also shifted towards $\bar{x} = 1$ as the pressure is increased (cf. equation E.3.21).

the higher mass flow rate observed experimentally. Indeed, this is the case; in figure E.3.3 we compare experimental measurements of the mass flow rate from Maurer et al. [343] with the predictions of the ENSE presented in this paper (equation E.3.7). The values of channel dimensions and other experimental parameters used in this prediction are the same as those in the work of Maurer et al., and are summarized in the figure caption. We note that the prediction is very good over a wide range of driving pressure differences, and the analytical solutions presented here captures the essential non-linearities and apparent slip phenomena observed in micro channel flows at moderate Knudsen number.

E.3.2 The Conductance

A useful way of representing the overall transport efficiency of the system is in terms of a conductance κ (i.e. the inverse of a flow channel hydrodynamic resistance). For gas flow through a rectangular slit the ENSE predict that the conductance is given by

$$\kappa \equiv \frac{\dot{M}^T}{\Delta P} = \frac{\mu h w}{L P_c} \frac{1}{\bar{P}_i - \bar{P}_o} \left(\bar{P}_i^2 - \bar{P}_o^2 + \ln \frac{\bar{P}_i^2}{\bar{P}_o^2} \right) \quad (\text{E.3.23})$$

The quantity $\bar{P}_i^2 - \bar{P}_o^2$ appears commonly in such problems (for example equation E.3.23 and the abscissa of figure E.3.3). Additional insight can be obtained if we rewrite this expression in terms of an average pressure $\langle P \rangle = (P_i + P_o)/2$ and a pressure difference $\Delta P = P_i - P_o$ such

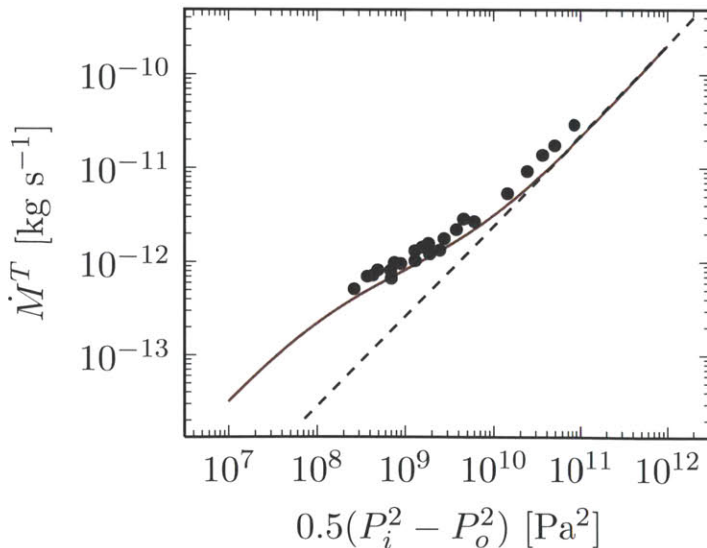


Figure E.3.3

Prediction of the analytically derived solution to the ENSE compared to the experimental measurements taken directly from the values reported by Maurer et al. [343]. The agreement between the prediction and the data is good. The parameters used here are from Maurer et al. $\mu = 19.9 \times 10^{-6}$ Pa s, $h = 0.6 \mu\text{m}$, $w = 200 \mu\text{m}$, $L = 10$ cm, $T = 293$ K. The outlet pressure was held constant at $P_o = 12$ kPa. The black dashed line shows the CNSE solution for the mass flux.

that $\bar{P}_i^2 - \bar{P}_o^2 = (\bar{P}_i + \bar{P}_o)(\bar{P}_i - \bar{P}_o) = \frac{1}{2} \frac{\langle P \rangle}{P_c} \cdot \frac{\Delta P}{P_c}$.

Using these identities we rewrite the conductance in terms of the average pressure $\langle P \rangle$ of the gas to obtain

$$\kappa = \frac{\mu h w}{L} \left(\frac{2\langle P \rangle}{P_c^2} + \frac{1}{\langle P \rangle - P_o} \ln \left(\frac{2\langle P \rangle - P_o}{P_o} \right) \right) \quad (\text{E.3.24})$$

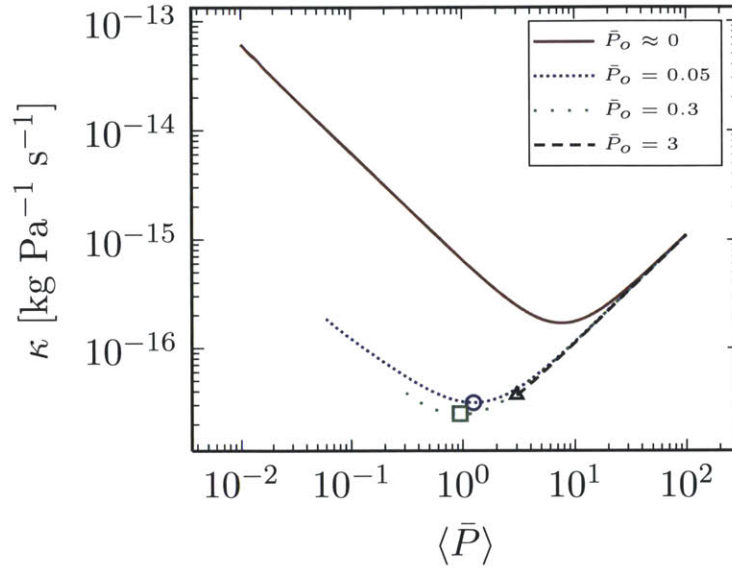
Furthermore, using equation E.1.2, we can define a Knudsen number $\langle \text{Kn} \rangle$ based on the average inlet pressure as

$$\langle \text{Kn} \rangle = \sqrt{\frac{\pi}{24} \frac{P_c}{\langle P \rangle}} \quad (\text{E.3.25})$$

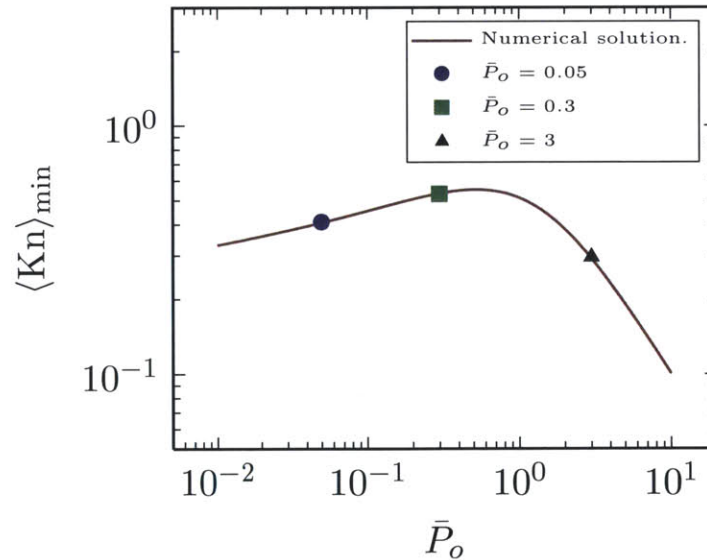
In Figure E.3.4a, we plot the conductance κ as a function of the average dimensionless pressure $\langle \bar{P} \rangle$ in the micro channel. Whereas in the CNSE, the conductance monotonically increases with $\langle \bar{P} \rangle$ (because of the increasing density of the fluid), a distinct non-monotonicity is apparent in the case of ENSE: the conductance of the channel initially decreases with increasing average pressure and then increases to become indistinguishable from the classical limit. This non-monotonicity occurs due to the added diffusion transport mechanism. At low pressure differences, diffusive contributions of the flow resulting from the density gradient along the channel are vastly more efficient at transporting mass and momentum through the micro channel compared to classical convective terms. It can be seen from figure E.3.4(a) that the location of the minimum conductance (indicated by the symbols) is a function of the outlet pressure P_o .

In Figure E.3.4(b) we plot the value of $\langle \text{Kn} \rangle$ at that value of the outlet pressure for which the conductance is a minimum. Note that we are not able to find a simple analytical solution for the value of $\langle P \rangle$ at minimum conductance due to the non-linearity in equation E.3.24. We therefore determine $\langle \text{Kn} \rangle$ as a function of the dimensionless outlet pressure \bar{P}_o numerically. Here we notice another non-monotonicity, and the Knudsen number $\langle \text{Kn} \rangle_{\min}$ defined using the average pressure at which minimum conductance is obtained first increases with increasing outlet pressure and subsequently decreases as $\langle \text{Kn} \rangle_{\min} \sim \bar{P}_o^{-1}$. For larger values of \bar{P}_o (and hence larger $\langle \bar{P} \rangle$), the variation of conductance κ approaches the classical Navier–Stokes case, and κ increases monotonically with increasing $\langle \bar{P} \rangle$. In this limit the average pressure at minimum conductance equals $\langle \bar{P} \rangle \approx \bar{P}_i \approx \bar{P}_o$.

We can also compare the conductance defined by equation E.3.23 with experimen-



(a)



(b)

Figure E.3.4: (a) The conductance κ of the micro channel as a function of the average pressure in the channel. In contrast to the prediction in the classical case in which the conductance increases linearly with average pressure, the CNSE predicts that the conductance varies non-monotonically with $\langle \bar{P} \rangle$. (b) The Knudsen number at minimum conductance calculated using the average pressure as a function of outlet pressure. The Knudsen number at minimum conductance varies non-monotonically with the imposed pressure.

tal measurements of the mass flux through a micro channel as a function of $P_i^2 - P_o^2$. In figure E.3.5 we plot the experimental measurements of Maurer et al. with the analytic expression in equation E.3.23. There are no adjustable parameters in this expression if the inlet and outlet pressures are specified in addition to the channel geometry. It is clear that the ENSE provide an excellent description of the conductance of a rarefied gas through a micro channel, including the appearance of a minimum in the conductance at a specified value of the average pressure $\langle P \rangle = (1/2)(P_i + P_o)$ and the pressure driving force $\Delta P = P_i - P_o$. Also shown on this plot is the CNSE solution (black dashed line), in which κ increases linearly with \bar{P}_o .

E.3.3 Velocity Field in the Channel

We now turn to the velocity field $u^T(x, y)$ given by equation E.3.8. In figure E.3.6, we show the non-dimensional total velocity $\bar{u}^T(\bar{y}) = \frac{u^T}{\mu\sqrt{3RT/4L}}$ at different values of \bar{x} , for two different conditions: (a) $\bar{P}_i = 1$ and (b) $\bar{P}_i = 10$, keeping the outlet pressure fixed at $\bar{P}_o = 0.25$. We observe in Figure E.3.6(a) that the velocity is non-zero at the channel walls, and this slip-like velocity arises from accounting for self-diffusion due to local gradients in pressure. In fact, for these values of \bar{P}_i and \bar{P}_o , the diffusive velocity contribution (given by equation E.3.10) is a significant proportion of the total velocity.

This picture changes when the pressure ratio, which we define as $\mathcal{P} = \bar{P}_i/\bar{P}_o$, is in-

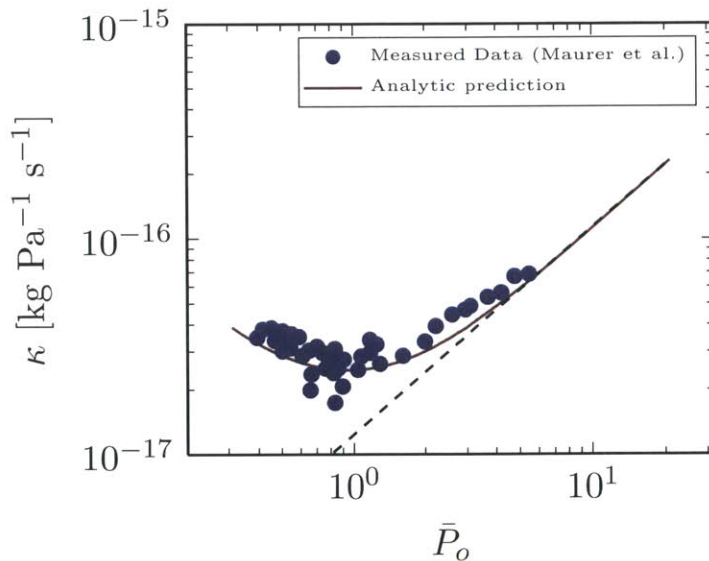
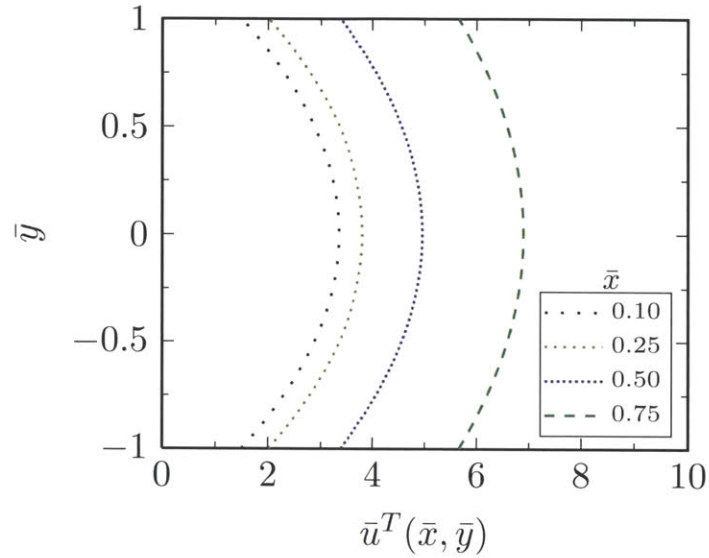
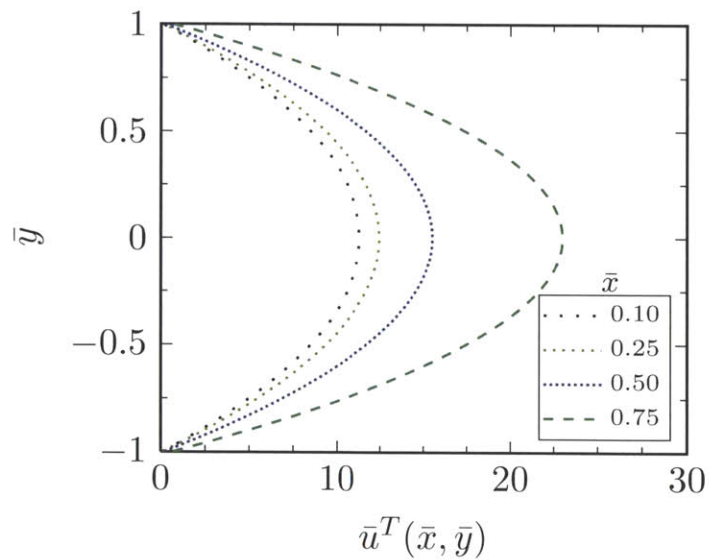


Figure E.3.5

Comparison of the prediction of the analytical expression obtained in the present work for the conductance of a micro channel (equation E.3.24) against experimental data obtained by Maurer et al. [343]. The outlet pressure as well as fluid properties and micro channel geometry is the same as that in [343]. The prediction is very good and closely agrees with the experimental data. The black dashed line shows the CNSE solution.



(a)



(b)

Figure E.3.6: Velocity profiles in the micro channel at different locations \bar{x} . (a) $\bar{P}_i = 1$ and $\bar{P}_o = 0.25$ ($\mathcal{P} = 4$). The contribution of the diffusive velocity terms is a significant proportion of the total velocity and increases along the channel. (b) $\bar{P}_i = 10$ and $\bar{P}_o = 0.25$ ($\mathcal{P} = 40$). In this case, there is still slip at the walls, but its contribution to the total mass flux is negligibly small.

creased. In figure E.3.6(b), we show the same quantity $\bar{u}^T(\bar{y})$ with $\bar{P}_i = 10$ and $\bar{P}_o = 0.25$, corresponding to $\mathcal{P} = 40$. It is immediately observed that in this case, the convective terms in the velocity largely outweigh the diffusive terms. In this regime the slip-like velocity is relatively unimportant; this fact has been noted by other researchers, for example Adachi et al. [337]. The diffusive contribution to the mass flow rate is only important if it is of the same order of magnitude as the convective contribution. For this we require both of the (independently variable) dimensionless pressures \bar{P}_i and \bar{P}_o to be small. With increasing \bar{P}_i , the wall boundary condition begins to approach that of no-slip and the velocity profile becomes parabolic. This is reassuring because in the limit of high pressure, the Knudsen number is small ($\text{Kn} \ll 1$; cf. equation E.1.2), and microscale corrections should become relatively unimportant. However, we also note that because of the compressibility of the gas, there is still a steady increase in the local velocity down the channel in this case as shown in Figure E.3.6(b). Moreover, the pressure profile along the micro channel is still highly non-linear and differs considerably from the CNSE solution, as can be seen from figure E.3.1. As we show later, to approach the classical result $\Delta\bar{P} = 1 - \bar{x}$, we require both $\mathcal{P} \rightarrow 1$ and $P_i \gg P_c$.

To better visualize the evolution in the velocity field along the channel, we consider the quantity $\mathcal{U}(\bar{x}, \bar{y})$, which we call the scaled velocity, defined as

$$\mathcal{U}(\bar{x}, \bar{y}) = \frac{u^T(\bar{x}, \bar{y}) - u_{\min}^T}{u_{\max}^T - u_{\min}^T} \quad (\text{E.3.26})$$

where u_{\min}^T and u_{\max}^T are the minimum and maximum velocities in the micro channel. It is clear from figures E.3.6(a) and E.3.6(b) that the minimum and maximum velocities lie somewhere along the $\bar{y} = \pm 1$ and $\bar{y} = 0$ lines respectively. This is also readily seen from equation E.3.8; If we isolate the terms in equation E.3.8 that depend on \bar{x} and rewrite it as

$$u^T = \xi_1 \frac{\bar{P}(\bar{x})}{1 + \bar{P}^2(\bar{x})} \left(\xi_2 + \frac{2}{3\bar{P}^2(\bar{x})} \right) \quad (\text{E.3.27})$$

where $\xi_1 > 0$ and $\xi_2 \geq 0$ are coefficients independent of \bar{x} , and $\bar{P}(\bar{x})$ is given in terms of the Lambert W function. We can show that u^T is a strictly increasing function of \bar{x} (because the pressure $\bar{P}(\bar{x})$ is a strictly decreasing function of \bar{x}). Therefore, the minimum velocity in the channel is at $(\bar{x} = 0, \bar{y} = \pm 1)$ while the maximum in the velocity occurs at $(\bar{x} = 1, \bar{y} = 0)$, which can now easily be found for any choice of \bar{P}_i and \bar{P}_o .

Figures E.3.7(a)-(d) show shaded plots of the scaled velocity $\mathcal{U}(\bar{x}, \bar{y})$ as a function of the dimensionless channel coordinates. Each panel corresponds to a different value of \bar{P}_i and

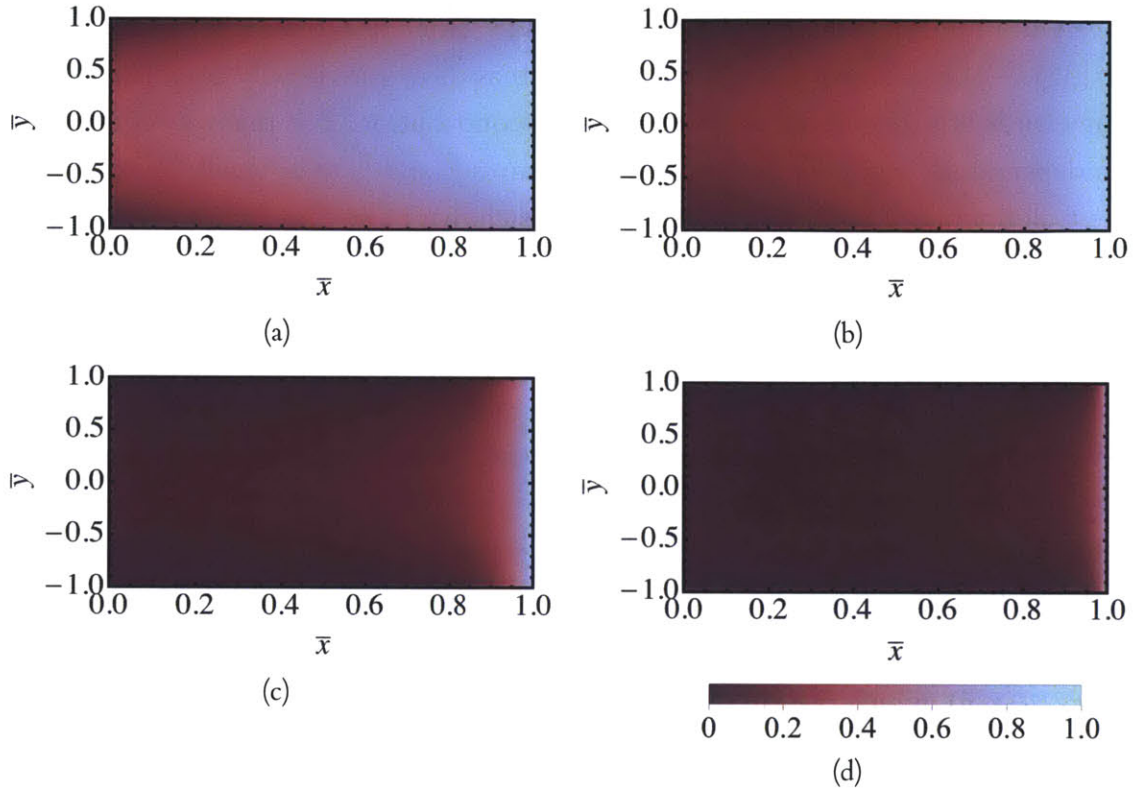


Figure E.3.7: Magnitude of the scaled velocity \mathcal{U} in the micro channel as a function of spatial position for different values of inlet pressure: (a) $\bar{P}_i = 0.3$, (b) $\bar{P}_i = 1.0$, (c) $\bar{P}_i = 5.0$, (d) $\bar{P}_i = 10$ at fixed outlet pressure $\bar{P}_o = 0.25$. For larger values of \bar{P}_i , the fluid undergoes a sudden increase in velocity in the vicinity of $\bar{x} = 1$. Color scale bar shows values of \mathcal{U} ranging from 0 to 1.

the value of the outlet pressure was held to be constant at $\bar{P}_o = 0.25$. We observe that as the driving pressure difference is increased, the scaled velocity increases much more steeply in the vicinity of $\bar{x} \approx 1$.

This behavior can be rationalized from the pressure gradient profiles presented in figure E.3.2; as \bar{P}_i is increased, the magnitude of the pressure gradient along the channel increases rapidly. In addition, equation E.3.21 shows that in the limit of large pressure ratios $\mathcal{P} = \bar{P}_i/\bar{P}_o$, the location of the maximum favorable pressure gradient tends towards $\bar{x}^i \rightarrow 1$. This leads to the rapid increase of the gas velocity in the vicinity of $\bar{x} = 1$ for large \mathcal{P} . To better visualize this sudden change in the velocity near the outlet, in figure E.3.8 we present line scans of the scaled centerline velocity \mathcal{U} at different values of \bar{P}_i . The steep

increase in the scaled velocity is clearly visible. This behavior stands in stark contrast to the classical incompressible solution, where the pressure gradient and the corresponding centerline velocity is constant throughout the channel.

E.3.4 Boundary Layer Analysis

The rapid variation in the velocity field close to $\bar{x} \approx 1$ suggests a boundary layer analysis is appropriate when $\mathcal{P} \gg 1$. Through such an analysis we can extract a characteristic length scale for this boundary layer as well as the asymptotic behavior of pressure and velocity for different limits of \bar{P}_i and \bar{P}_o .

We begin by a consideration of equation E.3.4 which we reproduce here for clarity, with the pressure ratio \mathcal{P} explicitly indicated:

$$\bar{P}_i^2 - \bar{P}(\bar{x})^2 + \ln \frac{\bar{P}_i^2}{\bar{P}^2(\bar{x})} = \bar{P}_o^2 \left(\mathcal{P}^2 - 1 + (1/\bar{P}_o^2) \ln \mathcal{P}^2 \right) \bar{x} \quad (\text{E.3.28})$$

Differentiating this equation with respect to \bar{x} we obtain

$$\bar{P}(\bar{x}) + \frac{1}{\bar{P}(\bar{x})} = -\frac{\bar{P}_o^2}{2} \left(\mathcal{P}^2 - 1 + (1/\bar{P}_o^2) \ln \mathcal{P}^2 \right) \quad (\text{E.3.29})$$

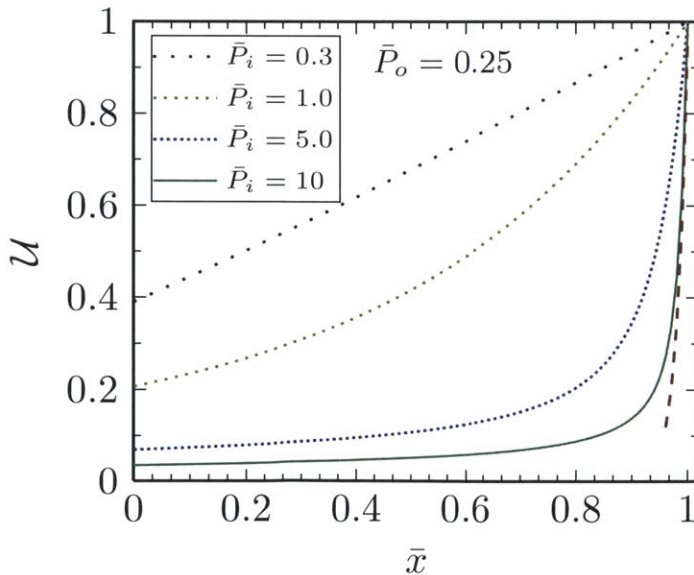


Figure E.3.8

Scaled profiles of the centerline velocity along the micro channel for different values of \bar{P}_i . Increasing \bar{P}_i leads to a steep increase in the scaled velocity close to $\bar{x} = 1$. The red dashed line shows the boundary layer approximation given in Table E.3.1 for $\bar{P}_i = 10 \gg 1$, $\bar{P}_o = 0.25 \ll 1$.

We now perform the variable transformation $\xi = 1 - \bar{x}$ and let $\bar{P}(\bar{x}) = \bar{P}(1 - \xi) = \bar{\psi}(\xi)$. Therefore equation E.3.29 now becomes

$$\left(\bar{\psi} + \frac{1}{\bar{\psi}}\right) \frac{d\bar{\psi}}{d\xi} = \frac{\bar{P}_o^2}{2} (\mathcal{P}^2 - 1 + (1/\bar{P}_o^2) \ln \mathcal{P}^2) \quad (\text{E.3.30})$$

Note that at $\bar{x} = 0$ we have $\xi = 1$ and $\bar{\psi}(1) = \bar{P}_i$. Similarly, $\bar{\psi}(0) = \bar{P}_o$. If desired a full matched asymptotic analysis of this equation can be carried out. Here we are primarily interested in the behavior of the pressure field in the vicinity of the exit of the channel ($\xi \ll 1$), i.e the inner expansion where $\psi(\xi) \approx \bar{P}_o$. We can consider two limits of this nonlinear equation: $\bar{P}_o \ll 1$ and $\bar{P}_o \gg 1$ depending on how large the outlet pressure at the end of micro channel is compared to the characteristic pressure scale $P_c = \mu\sqrt{3RT}/h$. In the former case, equation E.3.30 simplifies to

$$\frac{1}{\bar{\psi}} \frac{d\bar{\psi}}{d\xi} \approx \frac{\bar{P}_o^2}{2} (\mathcal{P}^2 - 1 + (1/\bar{P}_o^2) \ln \mathcal{P}^2) \quad (\text{E.3.31})$$

while for $\bar{P}_o \gg 1$ we obtain

$$\bar{\psi} \frac{d\bar{\psi}}{d\xi} \approx \frac{\bar{P}_o^2}{2} (\mathcal{P}^2 - 1 + (1/\bar{P}_o^2) \ln \mathcal{P}^2) \quad (\text{E.3.32})$$

These differential equations can be easily solved to find the limiting behavior of the pressure field close to $\bar{x} = 1$. These results are presented in tables E.3.1 and E.3.2.

We can apply a similar approximation of the governing differential equation in the vicinity of the channel exit for the velocity field u^T . First we rewrite equation E.2.9 in non-

	$\bar{P}_o \ll 1, \mathcal{P} \gg 1$	$\bar{P}_o \ll 1, \mathcal{P} \sim 1$
$\bar{P}(\bar{x})$	$\bar{P}_o \exp[(1/2)(\bar{P}_o^2(\mathcal{P}^2 - 1) + \ln \mathcal{P}^2)(1 - \bar{x})]$	$\bar{P}_o \exp[(1/2)(\mathcal{P}^2 - 1)(1 - \bar{x})]$
$u^T(\bar{x})$	$\frac{h\sqrt{3RT}}{6L} \frac{\bar{P}_o^2(\mathcal{P}^2 - 1) + \ln \mathcal{P}^2}{\bar{P}_o} \exp[-\frac{1}{2}(\bar{P}_o^2(\mathcal{P}^2 - 1) + \ln \mathcal{P}^2)(1 - \bar{x})]$	$\frac{h\sqrt{3RT}}{6L} \frac{\mathcal{P}^2 - 1}{\bar{P}_o} \exp[-\frac{1}{2}(\mathcal{P}^2 - 1)(1 - \bar{x})]$

Table E.3.1: Limiting expressions for pressure $\bar{P}(\bar{x})$ and velocity $u^T(\bar{x})$ for the case $\bar{P}_o \ll 1$. The expressions in the second column, in which $\mathcal{P} \rightarrow 1$, is obtained by expanding the logarithm for $\mathcal{P} \approx 1$. Equation numbers are given within parentheses.

	$\bar{P}_o \gg 1, \mathcal{P} \gg 1$	$\bar{P}_o \gg 1, \mathcal{P} \sim 1$
$\bar{P}(\bar{x})$	$\bar{P}_o \sqrt{\left(\mathcal{P}^2 - 1 + \frac{1}{\bar{P}_o^2} \ln \mathcal{P}^2\right) (1 - \bar{x}) + 1}$	$\bar{P}_o \sqrt{(\mathcal{P}^2 - 1)(1 - \bar{x}) + 1}$
$u^T(\bar{x})$	$\frac{h\sqrt{3RT}}{4L} \frac{\bar{P}_o \left(\mathcal{P}^2 - 1 + \frac{1}{\bar{P}_o^2} \ln \mathcal{P}^2\right)}{\sqrt{\left(\mathcal{P}^2 - 1 + \frac{1}{\bar{P}_o^2} \ln \mathcal{P}^2\right) (1 - \bar{x}) + 1}}$	$\frac{h\sqrt{3RT}}{4L} \frac{\mathcal{P}^2 - 1}{\bar{P}_o \sqrt{(\mathcal{P}^2 - 1)(1 - \bar{x}) + 1}}$

Table E.3.2: Limiting expressions for pressure $\bar{P}(\bar{x})$ and velocity $u^T(\bar{x})$ for the case $\bar{P}_o \gg 1$. Although there is no exponential behavior in this case, when $\mathcal{P} \gg 1$, the functional dependence of the expressions for pressure and velocity are such that steep gradients occur near the channel exit. As before, the expressions in the second column, in which $\mathcal{P} \rightarrow 1$, is obtained by expanding the logarithm for $\mathcal{P} \approx 1$. Equation numbers are given within parentheses.

dimensional form and apply the same variable transformations described above to obtain

$$u^T = \frac{h\sqrt{3RT}}{2L} \left[1 + \frac{2}{3} \frac{1}{\bar{\psi}^2} \right] \frac{d\bar{\psi}}{d\xi} \quad (\text{E.3.33})$$

which in the limits $\bar{P}_o \ll 1$ and $\bar{P}_o \gg 1$ simplify, respectively, to

$$u^T \approx \frac{h\sqrt{3RT}}{3L} \frac{1}{\bar{\psi}^2} \frac{d\bar{\psi}}{d\xi} \quad (\text{E.3.34})$$

and

$$u^T \approx \frac{h\sqrt{3RT}}{2L} \frac{d\bar{\psi}}{d\xi} \quad (\text{E.3.35})$$

We may now substitute into these equations the asymptotic form of the pressure from tables E.3.1 and E.3.2, according to the relevant magnitude of \bar{P}_o , to find the limiting expressions for the velocity field in the boundary layer near the exit. These results are also summarized in tables E.3.1 and E.3.2.

The exponential dependence of both the pressure field as well as the total velocity field on \bar{x} for low outlet pressures $\bar{P}_o \ll 1$ immediately suggests a characteristic length scale δ

for the boundary layer region given by

$$\frac{\delta}{L} \sim \frac{1}{\bar{P}_o^2 \mathcal{P}^2 + \ln \mathcal{P}^2} = \frac{3\mu^2 RT}{h^2 P_i^2 + 3\mu^2 RT \ln(P_i^2/P_o^2)} \quad (\text{E.3.36})$$

For a fixed value of the outlet pressure \bar{P}_o , the boundary layer thickness decreases with increasing values of the inlet pressure \bar{P}_i and this explains the form of the velocity profiles seen in figure E.3.8. Equivalently, decreasing \bar{P}_o also decreases the boundary layer thickness, although more slowly than increasing \bar{P}_i .

A different structure for the boundary layer at the exit is observed when the outlet pressure is high ($\bar{P}_o \gg 1$). The compressibility of the gas can still be important and there can still be a rapid decrease in the pressure near the exit. In this case, the pressure and velocity profiles have a square root and an inverse square root dependence on the distance from the exit, respectively. However the length scale of the boundary layer remains the same as that of Equation E.3.36. The detailed expressions for this case are given in table E.3.2.

E.4 Conclusion

In this paper we present for the first time analytical solutions to the Extended Navier–Stokes equations and obtain expressions for the pressure field, mass flow rate and velocity field for flow through a rectangular micro channel. The ENSE approach models the apparent slip-like flow of rarefied gases in micro channel geometries by accounting for mass transport due to local pressure gradients. Using the analytical expressions derived here using the Lambert W function, the nonlinear behavior of the pressure field and the resulting velocity field was examined in detail. The analytical expressions derived here are able to successfully capture the anomalous mass flow rate increases observed experimentally.

The ability to obtain an analytic expression for the pressure profile $\bar{P}(\bar{x})$ along the channel E.3.5 in terms of the Lambert W function also helps us construct a more detailed version of the regime map that was shown schematically in Figure E.1.1. This new two dimensional map is best represented in terms of the pressure ratio $\mathcal{P} = P_i/P_o = \bar{P}_i/\bar{P}_o$ that is driving the flow and either the average pressure $\langle P \rangle = (1/2)(P_i + P_o)$ in the channel or the scaled outlet pressure $\bar{P}_o = P_o/P_c$, each of which characterizes the thermodynamic state of the gas and the Knudsen number in the channel. We use the latter representation to construct Figure E.4.1. The two dimensional velocity profile and the pressure profile along the

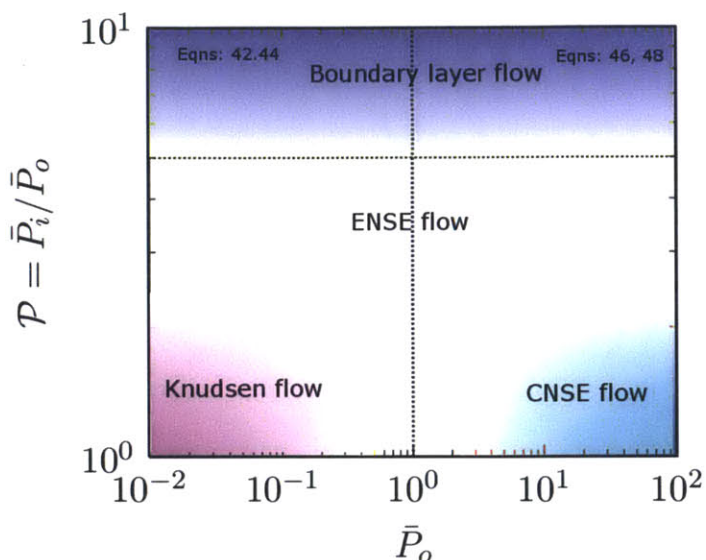


Figure E.4.1

The different flow regimes for micro channel gas flows. Of note is the boundary layer flow regime, in which steep gradients in the pressure field as well as velocity field are localized in the vicinity of the channel exit.

channel are described by equations E.3.5 and E.3.8 for this entire space. For large outlet pressures ($P_o \gg P_c$) and small pressure drops ($\mathcal{P} \approx 1$), the ENSE for compressible viscous flow at moderate Knudsen numbers collapse to the classical Navier-Stokes equations. For low average pressures (corresponding to high Knudsen number) and small pressure differences, the flow approaches the Knudsen regime in which ballistic transport dominates. To describe this regime requires the solution of the Boltzmann equation using appropriate numerical techniques which depend on the Knudsen number range of interest [328].

As the pressure drop along the channel increases ($\mathcal{P} \gg 1$), the flow develops a boundary layer structure in which the largest velocity changes occur in a thin region of width δ near the channel exit. The specific form of the pressure profile or centerline velocity profile in this boundary layer regime depends on the magnitude of the outlet pressure P_o (compared to the characteristic value P_c). The results for both $P_o \gg P_c$ and $P_o \ll P_c$ are given in Tables E.3.1 and E.3.2 respectively. For extremely high pressure ratios, additional effects such as inertial acceleration and viscous heating may further modify the velocity field near the exit. The framework and methodology for dealing with such transport effects have been outlined by Bird and colleagues in numerous publications (see for example [322, 326, 338]) but are beyond the scope of this work.

Bibliography

- [1] B. B. Mandelbrot, *The Fractal Geometry of Nature*, Macmillan, 1983.
- [2] R. F. Voss, “Random fractals: Self-affinity in noise, music, mountains, and clouds”, *Physica D: Nonlinear Phenomena* **1989**, *38*, 362–371.
- [3] D. G. Tarboton, R. L. Bras, I. Rodriguez-Iturre, “The fractal nature of river networks”, *Water Resources Research* **1988**, *24*, 1317–1322.
- [4] S Lovejoy, “Area-perimeter relation for rain and cloud areas”, *Science* **1982**, *216*, 185–187.
- [5] G. K. Batchelor, *An Introduction to Fluid Dynamics*, Cambridge University Press, 1967.
- [6] G. M. Homsy, “Viscous fingering in porous media”, *Annual Review of Fluid Mechanics* **1987**, *19*, 271–311.
- [7] B. B. Mandelbrot, “How long is the coast of britain? Statistical self-similarity and fractional dimension.”, *Science* **1967**, *156*, 636–638.
- [8] F. Labini, M. Montuori, L. Pietronero, “Scale-invariance of galaxy clustering”, *Physics Reports* **1998**, *293*, 61–226.
- [9] J.-F. Gouyet, *Physics and Fractal Structures*, Springer, Paris, 1996.
- [10] H.-O. Peitgen, J. Hartmut, D. Saupe, *Chaos and fractals: new frontiers of science*. Springer, 2004. Springer-Verlag, 2004.
- [11] M. Rubinstein, R. H. Colby, *Polymer Physics*, Oxford University Press, 2003.
- [12] D. Avnir, O. Biham, D. Lidar, O. Malcai, “Is the geometry of nature fractal?”, *Science* **1998**, *279*, 39–40.

- [13] H. H. Winter, M. Mours in *Advances in Polymer Science, Vol. 134*, Springer-Verlag, 1997, pp. 165–234.
- [14] R. J. Metz, R. K. Prud'homme, W. W. Graessley, "Rheology of concentrated microgel solutions", *Rheologica Acta* 1988, 27, 531–539.
- [15] S. A. Khan, C. A. Schnepper, R. C. Armstrong, "Foam rheology: III. Measurement of shear flow properties", *Journal of Rheology* 1988, 32, 69–92.
- [16] T. G. Mason, D. A. Weitz, "Linear viscoelasticity of colloidal hard sphere suspensions near the glass transition.", *Physical Review Letters* 1995, 75, 2770–2773.
- [17] J. P. Rich, G. H. McKinley, P. S. Doyle, "Size dependence of microprobe dynamics during gelation of a discotic colloidal clay", *Journal of Rheology* 2011, 55, 273–299.
- [18] P. Sollich, "Rheological constitutive equation for a model of soft glassy materials", *Physical Review E* 1998, 58, 738–759.
- [19] C. W. Macosko, *Rheology: Principles, Measurements and Applications*, Wiley-VCH, 1994.
- [20] R. G. Larson, *The Structure and Rheology of Complex Fluids*, Oxford University Press, New York, 1999.
- [21] W. Gratzler, *Eurekas and Euphorias: The Oxford Book of Scientific Anecdotes*, Oxford University Press, New York, 2002.
- [22] J. Gribbin, *Science: A History*, Penguin Books, 2009.
- [23] H. Markovitz, "Boltzmann and the beginnings of linear viscoelasticity", *Transactions of the Society of Rheology* 1977, 21, 381–398.
- [24] R. B. Bird, R. C. Armstrong, O. Hassager, *Dynamics of Polymeric Liquids*, John Wiley & Sons, Second, 1987.
- [25] M. Abramowitz, I. A. Stegun, *Handbook of Mathematical Functions*, U.S. National Bureau of Standards, Washington, 1964.
- [26] N. W. Tschoegl, *The Phenomenological Theory of Linear Viscoelastic Behavior*, Springer-Verlag, New York, 1989.
- [27] M. E. Cates, S. J. Candau, "Statics and dynamics of worm-like surfactant micelles", *Journal of Physics: Condensed Matter* 1990, 2, 6869–6892.

- [28] R. G. Larson, "Constitutive relationships for polymeric materials with power-law distributions of relaxation times", *Rheologica Acta* **1985**, *24*, 327–334.
- [29] G. Yin, M. J. Solomon, "Soft glassy rheology model applied to stress relaxation of a thermoreversible colloidal gel", *Journal of Rheology* **2008**, *52*, 785.
- [30] T. S. Ng, G. H. McKinley, "Power law gels at finite strains: The nonlinear rheology of gluten gels", *Journal of Rheology* **2008**, *52*, 417–449.
- [31] L. Ong, R. R. Dagastine, S. E. Kentish, S. L. Gras, "Microstructure of milk gel and cheese curd observed using cryo scanning electron microscopy and confocal microscopy", *LWT - Food Science and Technology* **2011**, *44*, 1291–1302.
- [32] P. Sollich, F. Lequeux, P. Hébraud, M. E. Cates, "Rheology of soft glassy materials", *Physical Review Letters* **1997**, *78*, 2020–2023.
- [33] P. Kollmannsberger, B. Fabry, "Linear and nonlinear rheology of living cells", *Annual Review of Materials Research* **2011**, *41*, 75–97.
- [34] J. G. Curro, P. Pincus, "A theoretical basis for viscoelastic relaxation of elastomers in the long-time limit", *Macromolecules* **1983**, *16*, 559–562.
- [35] H. H. Winter, "Analysis of linear viscoelasticity of a crosslinking polymer at the gel point", *Journal of Rheology* **1986**, *30*, 367–382.
- [36] N. B. Wyatt, A. M. Grillet, "Rheology, adhesion, and debonding mechanisms in fluorosilicone polymer gels", *Journal of Applied Polymer Science* **2014**, *131*, 40034.
- [37] T. G. Mason, K. Ganesan, J. H. van Zanten, D. Wirtz, S. Kuo, "Particle tracking microrheology of complex fluids", *Physical Review Letters* **1997**, *79*, 3282–3285.
- [38] F. Gittes, B. Schnurr, P. D. Olmsted, F. C. MacKintosh, C. F. Schmidt, "Microscopic Viscoelasticity: Shear Moduli of Soft Materials Determined from Thermal Fluctuations", *Physical Review Letters* **1997**, *79*, 3286–3289.
- [39] T. Mason, "Estimating the viscoelastic moduli of complex fluids using the generalized Stokes–Einstein equation", *Rheologica Acta* **2000**, *39*, 371–378.
- [40] A. Einstein, "Über die von der molekularkinetischen theorie der wärme geforderte bewegung von in ruhenden flüssigkeiten suspendierten teilchen", *Annalen der Physik* **1905**, *322*, 549–560.
- [41] M. Kac, "Random walk and the theory of Brownian motion", *American Mathematical Monthly* **1947**, *54*, 369–391.

- [42] R. Metzler, J. Klafter, "The random walk's guide to anomalous diffusion: A fractional dynamics approach.", *Physics Reports* **2000**, *339*, 1–77.
- [43] J.-P. Bouchaud, A. Georges, "Anomalous diffusion in disordered media: Statistical mechanisms, models and physical applications", *Physics Reports* **1990**, *195*, 127–293.
- [44] F. Amblard, A. C Maggs, B. Yurke, A. Pargellis, S. Leibler, "Subdiffusion and anomalous local viscoelasticity in actin networks.", *Physical Review Letters* **1996**, *77*, 4470–4473.
- [45] M. Balland, N. Desprat, D. Icard, S. Féréol, A. Asnacios, J. Browaeys, S. Hénon, F. Gallet, "Power laws in microrheology experiments on living cells: Comparative analysis and modeling", *Physical Review E* **2006**, *74*, 0211911.
- [46] I. Golding, E. Cox, "Physical nature of bacterial cytoplasm", *Physical Review Letters* **2006**, *96*, 098102.
- [47] I. Y. Wong, M. L. Gardel, D. R. Reichman, E. R. Weeks, M. T. Valentine, A. R. Bausch, D. A. Weitz, "Anomalous diffusion probes microstructure dynamics of entangled F-actin networks", *Physical Review Letters* **2004**, *92*, 178101.
- [48] J. Klafter, A. Blumen, G. Zumofen, "Fractal behavior in trapping and reaction: A random walk study", *Journal of Statistical Physics* **1984**, *36*, 561–577.
- [49] I. M. Sokolov, J. Klafter, A. Blumen, "Fractional kinetics", *Physics Today* **2002**, *55*, 48.
- [50] R. Metzler, T. F. Nonnenmacher, "Fractional relaxation processes and fractional rheological models for the description of a class of viscoelastic materials", *International Journal of Plasticity* **2003**, *19*, 941–959.
- [51] H. M. Laun, "Description of the non-linear shear behaviour of a low density polyethylene melt by means of an experimentally determined strain dependent memory function", *Rheologica Acta* **1978**, *17*, 1–15.
- [52] S. M. Fielding, P Sollich, M. E. Cates, "Aging and rheology in soft materials", *Journal of Rheology* **2000**, *44*, 323–369.
- [53] A. Jaishankar, V. Sharma, G. H. McKinley, "Interfacial viscoelasticity, yielding and creep ringing of globular protein-surfactant mixtures", *Soft Matter* **2011**, *7*, 7623–7634.

- [54] V. Sharma, A. Jaishankar, Y. C. Wang, G. H. McKinley, "Rheology of globular proteins: apparent yield stress, high shear rate viscosity and interfacial viscoelasticity of bovine serum albumin solutions", *Soft Matter* **2011**, *7*, 5150–5160.
- [55] H. Schiessel, R. Metzler, A. Blumen, T. Nonnenmacher, "Generalized viscoelastic models: their fractional equations with solutions", *Journal of Physics A: Mathematical and General* **1995**, *28*, 6567–6584.
- [56] R. L. Bagley, P. J. Torvik, "Fractional calculus - A different approach to the analysis of viscoelastically damped structures", *AIAA Journal* **1983**, *21*, 741–748.
- [57] T. F. Nonnenmacher, "Fractional relaxation equations for viscoelasticity and related phenomena", *Rheological Modelling: Thermodynamical and Statistical Approaches* **1991**, 309–320.
- [58] R. Metzler, E. Barkai, J. Klafter, "Anomalous diffusion and relaxation close to thermal equilibrium: a fractional fokker-planck equation approach", *Physical review letters* **1999**, *82*, 3563–3567.
- [59] R. C. Koeller, "Applications of fractional calculus to the theory of viscoelasticity", *Journal of Applied Mechanics* **1984**, *51*, 299–307.
- [60] V. Bertola, F. Bertrand, H. Tabuteau, D. Bonn, P. Coussot, "Wall slip and yielding in pasty materials", *Journal of Rheology* **2003**, *47*, 1211–1226.
- [61] G. H. McKinley, T. Sridhar, "Filament stretching rheometry of complex fluids", *Annual Review of Fluid Mechanics* **2002**, *34*, 375–415.
- [62] S. Haward, V. Sharma, J. Odell, "Extensional opto-rheometry with biofluids and ultra-dilute polymer solutions", *Soft Matter* **2011**, *7*, 9908–9921.
- [63] S. J. Haward, A. Jaishankar, M. S. N. Oliveira, M. A. Alves, G. McKinley, "Extensional flow of hyaluronic acid solutions in an optimized microfluidic cross-slot device", *Biomicrofluidics* **2013**, *7*, 044108.
- [64] R. Lapasin, S. Prich, *Rheology of Industrial Polysaccharides: Theory and Applications*, Blackie Academic and Professional, Glasgow, **1995**.
- [65] T. van Vliet, "On the relation between texture perception and fundamental mechanical parameters for liquids and time dependent solids", *Food Quality and Preference* **2002**, *13*, 227–236.

- [66] M. Padmanabhan, "Measurement of extensional viscosity of viscoelastic liquid foods", *Journal of food engineering* **1995**, *25*, 169–193.
- [67] M. O'Leary, B. Hanson, C. Smith, "Viscosity and non-Newtonian features of thickened fluids used for dysphagia therapy", *Journal of Food Science* **2010**, *75*, E330–8.
- [68] F. García-Ochoa, V. E. Santos, J. A. Casas, E. Gómez, "Xanthan gum: production, recovery, and properties", *Biotechnology Advances* **2000**, *18*, 549–79.
- [69] A. H. Clark, S. B. Ross-Murphy in *Biopolymers*, Springer Verlag, Berlin, **1987**, pp. 57–192.
- [70] G. Kogan, L. Soltés, R. Stern, P. Gemeiner, "Hyaluronic acid: a natural biopolymer with a broad range of biomedical and industrial applications.", *Biotechnology Letters* **2007**, *29*, 17–25.
- [71] K. K. T. Goh, L. Matia-Merino, C. E. Hall, P. J. Moughan, H. Singh, "Complex rheological properties of a water-soluble extract from the fronds of the black tree fern, *Cyathea medullaris*.", *Biomacromolecules* **2007**, *8*, 3414–3421.
- [72] K. K. T. Goh, L. Matia-Merino, D. N. Pinder, C. Saavedra, H. Singh, "Molecular characteristics of a novel water-soluble polysaccharide from the New Zealand black tree fern (*Cyathea medullaris*)", *Food Hydrocolloids* **2011**, *25*, 286–292.
- [73] L. Matia-Merino, K. K. T. Goh, H. Singh, "A natural shear-thickening water-soluble polymer from the fronds of the black tree fern, *Cyathea medullaris*: Influence of salt, pH and temperature", *Carbohydrate Polymers* **2012**, *87*, 131–138.
- [74] S. J. Haward, M. S. N. Oliveira, M. A. Alves, G. H. McKinley, "An optimized cross-slot flow geometry for microfluidic extensional rheometry", *Physical Review Letters* **2012**, *109*, 128301.
- [75] J. C. Maxwell, "On the dynamical theory of gases", *Philosophical Transactions of the Royal Society of London* **1867**, *157*, 49–88.
- [76] M. Wagner, T. Raible, J. Meissner, "Tensile stress overshoot in uniaxial extension of a LDPE melt", *Rheologica Acta* **1979**, *18*, 427–428.
- [77] H. A. Barnes, J. F. Hutton, K. Walters, *An Introduction to Rheology*, Elsevier, Amsterdam, **1989**.
- [78] M. T. Arigo, G. H. McKinley, "The effects of viscoelasticity on the transient motion of a sphere in a shear-thinning fluid", *Journal of Rheology* **1997**, *41*, 103–128.

- [79] J. R. Stokes, G. A. Davies, “Viscoelasticity of human whole saliva collected after acid and mechanical stimulation”, *Biorheology* **2007**, *44*, 141–60.
- [80] G. W. S. Blair, B. C. Veinoglou, J. E. Caffyn, “Limitations of the Newtonian time scale in relation to non-equilibrium rheological states and a theory of quasi-properties”, *Proceedings of the Royal Society A: Mathematical Physical and Engineering Sciences* **1947**, *189*, 69–87.
- [81] H. Schiessel, A Blumen, “Mesoscopic pictures of the sol-gel transition: Ladder models and fractal networks”, *Macromolecules* **1995**, *28*, 4013–4019.
- [82] I. Podlubny, *Fractional Differential Equations*, Academic Press, San-Diego, **1999**.
- [83] T. Surguladze, “On certain applications of fractional calculus to viscoelasticity”, *Journal of Mathematical Sciences* **2002**, *112*, 4517–4557.
- [84] F. Mainardi, *Fractional Calculus and Waves in Linear Viscoelasticity: an Introduction to Mathematical Models*. World Scientific Press, **2010**.
- [85] K. S. Miller, B. Ross, *An Introduction to the Fractional Calculus and Fractional Differential Equations*, John Wiley & Sons, Inc., **1993**.
- [86] I. Podlubny, T. Skovranek, B. M. Vinagre Jara in 2009 IEEE Conference on Emerging Technologies & Factory Automation, Ieee, **2009**, pp. 1–6.
- [87] L. Euler, “De progressionibus transcendentibus seu quarum termini generales algebraice dari nequeunt”, *Commentarii academiae scientiarum Petropolitanae* **1738**, *5*, 36–57.
- [88] J.-L. Lagrange, “Sur une nouvelle espèce de calcul relatif à la différentiation et à l’intégration des quantités variables. (1772): 185–221.”, *Nouveaux Mémoires de l’Académie Royale des Sciences et Belles-Lettres* **1772**, 185–221.
- [89] P. S. Laplace, *Théorie Analytique des Probabilités*, Courcier, Paris, **1820**.
- [90] J. B. J. Fourier, *Theorie Analytique de la Chaleur, par M. Fourier*, Chez Firmin Didot, père et fils, **1822**.
- [91] N. H. Abel, “Solution de quelques problemes a l’aide d’integrales definies”, *Oeuvres Completes* **1881**, *1*, 16–18.
- [92] B. Ross, “The development of fractional calculus 1695–1900”, *Historia Mathematica* **1977**, *4*, 75–89.

- [93] A. Jaishankar, G. H. McKinley, "Power-law rheology in the bulk and at the interface: quasi-properties and fractional constitutive equations", *Proceedings of the Royal Society A: Mathematical Physical and Engineering Sciences* **2013**, 469, 2012.0284.
- [94] C. Friedrich, H. Braun, "Generalized Cole-Cole behavior and its rheological relevance", *Rheologica Acta* **1992**, 31, 309–322.
- [95] H Schiessel, A Blumen, "Hierarchical analogues to fractional relaxation equations", *Journal of Physics A: Mathematical and General* **1993**, 26, 5057–5069.
- [96] P. J. Torvik, R. L. Bagley, "On the appearance of the fractional derivative in the behavior of real materials", *Journal of Applied Mechanics* **1984**, 51, 294–298.
- [97] C. Friedrich, "Relaxation and retardation functions of the Maxwell model with fractional derivatives", *Rheologica Acta* **1991**, 30, 151–158.
- [98] N. Heymans, J. C. Bauwens, "Fractal rheological models and fractional differential equations for viscoelastic behavior", *Rheologica Acta* **1994**, 33, 210–219.
- [99] D. Craiem, R. L. Magin, "Fractional order models of viscoelasticity as an alternative in the analysis of red blood cell (RBC) membrane mechanics.", *Physical Biology* **2010**, 7, 13001.
- [100] V. D. Djordjević, J. Jarić, B. Fabry, J. J. Fredberg, D. Stamenović, "Fractional derivatives embody essential features of cell rheological behavior", *Annals of Biomedical Engineering* **2003**, 31, 692–699.
- [101] L. Ma, G. V. Barbosa-Canovas, "Simulating viscoelastic properties of selected food gums and gum mixtures using a fractional derivative model", *Journal of Texture Studies* **1996**, 27, 307–325.
- [102] C Friedrich in *Rheological Modelling: Thermodynamical and Statistical Approaches*, Springer-Verlag, **1991**, pp. 321–330.
- [103] A. Lion, "On the thermodynamics of fractional damping elements", *Continuum Mechanics and Thermodynamics* **1997**, 9, 83–96.
- [104] R. Kohlrausch, "Theorie des elektrischen Ruckstandes in der Leidener Flasche", *Annalen der Physik* **1854**, 167, 179–214.
- [105] G. Williams, D. C. Watts, "Non-symmetrical dielectric relaxation behaviour arising from a simple empirical decay function", *Transactions of the Faraday Society* **1970**, 66, 80–85.

- [106] R. Metzler, J. Klafter, "From stretched exponential to inverse power-law: fractional dynamics, Cole-Cole relaxation processes, and beyond", *Journal of Non-Crystalline Solids* **2002**, *305*, 81–87.
- [107] W. G. Glockle, T. F. Nonnenmacher, "Fractional integral operators and Fox functions in the theory of viscoelasticity", *Macromolecules* **1991**, *24*, 6426–6434.
- [108] W. G. Glöckle, T. F. Nonnenmacher, "Fractional relaxation and the time-temperature superposition principle", *Rheologica Acta* **1994**, *33*, 337–343.
- [109] W. G. Glöckle, T. F. Nonnenmacher, "A fractional calculus approach to self-similar protein dynamics", *Biophysical Journal* **1995**, *68*, 46–53.
- [110] R. K. Schofield, G. W. S. Blair, "The relationship between viscosity, elasticity and plastic strength of soft materials as illustrated by some mechanical properties of flour doughs, I", *Proceedings of the Royal Society A: Mathematical Physical and Engineering Sciences* **1932**, *138*, 707–718.
- [111] E. Koos, N. Willenbacher, "Capillary forces in suspension rheology.", *Science* **2011**, *331*, 897–900.
- [112] E. Koos, J. Johannsmeier, L. Schwebler, N. Willenbacher, "Tuning suspension rheology using capillary forces", *Soft Matter* **2012**, *8*, 6620–6628.
- [113] E. Koos, N. Willenbacher, "Particle configurations and gelation in capillary suspensions", *Soft Matter* **2012**, *8*, 3988–3994.
- [114] J. Dittmann, E. Koos, N. Willenbacher, "Ceramic capillary suspensions: novel processing route for macroporous ceramic materials", *Journal of the American Ceramic Society* **2013**, *96*, (Ed.: A. Krell), 391–397.
- [115] D. J. McClements, *Food Emulsions: Principles, Practices, and Techniques*, CRC Press, **2005**.
- [116] B. S. Murray, "Interfacial rheology of food emulsifiers and proteins", *Current Opinion in Colloid & Interface Science* **2002**, *7*, 426–431.
- [117] P. Fischer, E. J. Windhab, "Rheology of food materials", *Current Opinion in Colloid & Interface Science* **2011**, *16*, 36–40.
- [118] S. Vandebril, A. Franck, G. G. Fuller, P. Moldenaers, J. Vermant, "A double wall-ring geometry for interfacial shear rheometry", *Rheologica Acta* **2010**, *49*, 131–144.

- [119] G. W. S. Blair, "The role of psychophysics in rheology", *J. Colloid Science* **1947**, *2*, 21–32.
- [120] P. Nutting, "A new general law of deformation", *Journal of the Franklin Institute* **1921**, *191*, 679–685.
- [121] F. Mainardi, R. Gorenflo, "Time-fractional derivatives in relaxation processes: a tutorial survey", *Arxiv preprint arXiv:0801.4914* **2008**.
- [122] G. W. S. Blair, F. M. V. Coppen, "The subjective conception of the firmness of soft materials", *The American Journal of Psychology* **1942**, *55*, 215–229.
- [123] R. L. Bagley, P. J. Torvik, "A theoretical basis for the application of fractional calculus to viscoelasticity", *Journal of Rheology* **1983**, *27*, 201.
- [124] P. E. Rouse, "A theory of the linear viscoelastic properties of dilute solutions of coiling polymers", *The Journal of Chemical Physics* **1953**, *21*, 1272.
- [125] C. Friedrich, H. Schiessel, A. Blumen in *Advances in the Flow and Rheology of Non-Newtonian Fluids*, (Eds.: D. A. Siginer, D. De Kee, R. P. Chhabra), **1999**, pp. 429–266.
- [126] D. A. Edwards, H. Brenner, D. T. Wasan, *Interfacial Transport Processes and Rheology*, Butterworth-Heinemann, Boston, **1991**.
- [127] E. Dickinson, "Adsorbed protein layers at fluid interfaces: interactions, structure and surface rheology", *Colloids and Surfaces B: Biointerfaces* **1999**, *15*, 161–176.
- [128] J. Zasadzinski, J. Ding, H. E. Warriner, F. Bringezu, A. J. Waring, "The physics and physiology of lung surfactants", *Current Opinion in Colloid & Interface Science* **2001**, *6*, 506–513.
- [129] D. L. Leiske, S. R. Raju, H. a. Ketelson, T. J. Millar, G. G. Fuller, "The interfacial viscoelastic properties and structures of human and animal Meibomian lipids.", *Experimental Eye Research* **2010**, *90*, 598–604.
- [130] P. Erni, "Deformation modes of complex fluid interfaces", *Soft Matter* **2011**, *7*, 7586.
- [131] A. W. Adamson, A. P. Gast, *Physical Chemistry of Surfaces*, John Wiley & Sons, New York, 6th, **1997**.
- [132] *Interfacial Rheology*, (Eds.: R. Miller, L. Liggieri), Koninklijke Brill NV, **2009**.

- [133] P. Erni, P. Fischer, E. J. Windhab, V. Kusnezov, H. Stettin, J. LaÛlger, “Stress- and strain-controlled measurements of interfacial shear viscosity and viscoelasticity at liquid/liquid and gas/liquid interfaces”, *Review of Scientific Instruments* **2003**, *74*, 4916.
- [134] L. G. Cascão Pereira, O. Théodoly, H. W. Blanch, C. J. Radke, “Dilatational Rheology of BSA Conformers at the Air/Water Interface”, *Langmuir* **2003**, *19*, 2349–2356.
- [135] L. E. Scriven, “Dynamics of a fluid interface”, *Chemical Engineering Science* **1960**, *12*, 98–108.
- [136] M. A. Bos, T. Van Vliet, “Interfacial rheological properties of adsorbed protein layers and surfactants: a review.”, *Advances in Colloid and Interface Science* **2001**, *91*, 437–71.
- [137] B. Biswas, D. A. Haydon, “The rheology of some interfacial adsorbed films of macromolecules. I. Elastic and creep phenomena”, *Proceedings of the Royal Society A: Mathematical Physical and Engineering Sciences* **1963**, *271*, 296–316.
- [138] D. E. Graham, M. C. Phillips, “Proteins at liquid interfaces V. Shear properties”, *Journal of Colloid and Interface Science* **1980**, *76*, 240–250.
- [139] E. Dickinson, B. S. Murray, G. Stainsby, D. M. W. Anderson, “Surface activity and emulsifying behaviour of some Acacia gums”, *Food Hydrocolloids* **1988**, *2*, 477–490.
- [140] P. Erni, E. J. Windhab, R. Gunde, M. Graber, B. Pfister, A. Parker, P. Fischer, “Interfacial rheology of surface-active biopolymers: Acacia senegal gum versus hydrophobically modified starch.”, *Biomacromolecules* **2007**, *8*, 3458–66.
- [141] M. Elmanan, S. Al-Assaf, G. O. Phillips, P. A. Williams, “Studies on Acacia exudate gums: Part VI. Interfacial rheology of Acacia senegal and Acacia seyal”, *Food Hydrocolloids* **2008**, *22*, 682–689.
- [142] V. Sharma, A. Jaishankar, Y.-C. Wang, G. H. McKinley, “Rheology of globular proteins: apparent yield stress, high shear rate viscosity and interfacial viscoelasticity of bovine serum albumin solutions”, *Soft Matter* **2011**, *7*, 5150–5160.
- [143] C. Sanchez, D. Renard, P. Robert, C. Schmitt, J. Lefebvre, “Structure and rheological properties of acacia gum dispersions”, *Food Hydrocolloids* **2002**, *16*, 257–267.

- [144] T. S. K. Ng, G. H. McKinley, R. H. Ewoldt, "Large amplitude oscillatory shear flow of gluten dough: A model power-law gel", *Journal of Rheology* **2011**, *55*, 627.
- [145] M. Baumgartel, H. H. Winter in Proceedings of the XIth International Congress on Rheology, (Eds.: P. Moldenaers, R. Keunings), **1992**, pp. 893–895.
- [146] J. M. Maloney, D. Nikova, F. Lautenschläger, E. Clarke, R. Langer, J. Guck, K. J. Van Vliet, "Mesenchymal stem cell mechanics from the attached to the suspended state.", *Biophysical Journal* **2010**, *99*, 2479–87.
- [147] A. R. Cameron, J. E. Frith, J. J. Cooper-White, "The influence of substrate creep on mesenchymal stem cell behaviour and phenotype.", *Biomaterials* **2011**, *32*, 5979–5993.
- [148] N. Holten-Andersen, M. J. Harrington, H. Birkedal, B. P. Lee, P. B. Messersmith, K. Y. C. Lee, J. H. Waite, "pH-induced metal-ligand cross-links inspired by mussel yield self-healing polymer networks with near-covalent elastic moduli.", *Proceedings of the National Academy of Sciences of the United States of America* **2011**, *108*, 2651–5.
- [149] K. Walters, *Rheometry*, Chapman and Hall, London, **1975**.
- [150] R. H. Ewoldt, G. H. McKinley, "Creep ringing in rheometry or how to deal with oft-discarded data in step stress tests!", *Rheology Bulletin* **2007**, *76*, 4–6.
- [151] C. Baravian, D. Quemada, "Using instrumental inertia in controlled stress rheometry", *Rheologica Acta* **1998**, *37*, 223–233.
- [152] L. C. E. Struik, "Free damped vibrations of linear viscoelastic materials", *Rheologica Acta* **1967**, *6*, 119–129.
- [153] R. J. Larsen, M. D. Dickey, G. M. Whitesides, D. A. Weitz, "Viscoelastic properties of oxide-coated liquid metals", *Journal of Rheology* **2009**, *53*, 1305.
- [154] N. Heymans, I. Podlubny, "Physical interpretation of initial conditions for fractional differential equations with Riemann-Liouville fractional derivatives", *Rheologica Acta* **2006**, *45*, 765–771.
- [155] C. Friedrich, H. Braun, "Generalized Cole-Cole behavior and its rheological relevance", *Rheologica Acta* **1992**, *322*, 309–322.
- [156] P. Yang, Y. C. Lam, K.-Q. Zhu, "Constitutive equation with fractional derivatives for the generalized UCM model", *Journal of Non-Newtonian Fluid Mechanics* **2010**, *165*, 88–97.

- [157] W. P. Cox, E. H. Merz, "Correlation of Dynamic and Steady Flow Viscosities", *Journal of Polymer Science* **1958**, *28*, 619–622.
- [158] H. M. Laun, "Prediction of elastic strains of polymer melts in shear and elongation", *Journal of Rheology* **1986**, *30*, 459–501.
- [159] P. J. R. Leblans, J. Sampers, H. C. Booij, "The mirror relations and nonlinear viscoelasticity of polymer melts", *Rheologica Acta* **1985**, *24*, 152–158.
- [160] V. Sharma, G. H. McKinley, "An intriguing empirical rule for computing the first normal stress difference from steady shear viscosity data for concentrated polymer solutions and melts", *Rheologica Acta* **2012**, *51*, 487–495.
- [161] H. C. Booij, P. Leblans, "Nonlinear viscoelasticity and the Cox–Merz relations for polymeric fluids", *Journal of Polymer Science: Polymer Physics Edition* **1983**, *21*, 1703–1711.
- [162] M. Renardy, "Qualitative correlation between viscometric and linear viscoelastic functions", *Journal of non-Newtonian Fluid Mechanics* **1997**, *68*, 133–135.
- [163] R. Oertel, W. M. Kulicke, "Viscoelastic properties of liquid crystals of aqueous biopolymer solutions", *Rheologica Acta* **1991**, *30*, 140–150.
- [164] S. B. Ross–Murphy, "Structure–property relationships in food biopolymer gels and solutions", *Journal of Rheology* **1995**, *39*, 1451–1463.
- [165] I. Krieger, "Correspondence : Comments on a manuscript Doraiswamy et al.", *Journal of Rheology* **1992**, *36*, 215–217.
- [166] D. Doraiswamy, A. N. Mujumdar, I. Tsao, A. N. Beris, S. C. Danforth, A. B. Metzner, "The Cox–Merz rule extended: A rheological model for concentrated suspensions and other materials with a yield stress", *Journal of Rheology* **1991**, *35*, 647–685.
- [167] R. I. Tanner, J. M. Simmons, "Combined simple and sinusoidal shearing in elastic liquids", *Chemical Engineering Science* **1967**, *22*, 1803–1815.
- [168] D. A. Rees, E. J. Welsh, "Secondary and Tertiary Structure of Polysaccharides in Solutions and Gels", *Angewandte Chemie* **1977**, *16*, 214–224.
- [169] G. Cuvelier, B. Launay, "Concentration regimes in xanthan gum solutions deduced from flow and viscoelastic properties", *Carbohydrate Polymers* **1986**, *6*, 321–333.

- [170] P. J. Whitcomb, C. Macosko, "Rheology of Xanthan Gum", *Journal of Rheology* **1978**, *22*, 493–505.
- [171] W. E. Rochefort, S. Middleman, "Rheology of xanthan gum: salt, temperature, and strain effects in oscillatory and steady shear experiments", *Journal of Rheology* **1987**, *31*, 337–369.
- [172] S. B. Ross-Murphy, V. J. Morris, E. R. Morris, "Molecular viscoelasticity of xanthan polysaccharide", *Faraday Symposia of the Chemical Society* **1983**, *18*, 115–129.
- [173] M. Tako in *ACS Symposium Series Vol. 489*, **1992**, pp. 268–281.
- [174] V. H. Rolón-Garrido, M. H. Wagner, "The damping function in rheology", *Rheologica Acta* **2009**, *48*, 245–284.
- [175] M. Yalpani, L. D. Hall, M. A. Tung, D. E. Brooks, "Unusual rheology of a branched, water-soluble chitsan derivative", *Nature* **1983**, *302*, 812–814.
- [176] D. Valério, J. J. Trujillo, M. Rivero, J. A. T. Machado, D. Baleanu, "Fractional calculus: A survey of useful formulas", *The European Physical Journal Special Topics* **2013**, *222*, 1827–1846.
- [177] R. G. Larson, *Constitutive Equations for Polymer Melts and Solutions*, Butterworths, Boston, **1988**.
- [178] R. Sharma, B. J. Cherayil, "Polymer melt dynamics: Microscopic roots of fractional viscoelasticity", *Physical Review E* **2010**, *81*, 021804.
- [179] P. R. Soskey, H. H. Winter, "Large step shear strain experiments with parallel-disk rotational rheometers", *Journal of Rheology* **1984**, *28*, 625.
- [180] S. M. Guskey, H. H. Winter, "Transient shear behavior of a thermotropic liquid crystalline polymer in the nematic state", *Journal of Rheology* **1991**, *35*, 1191–1207.
- [181] R. J. English, S. R. Raghavan, R. D. Jenkins, S. A. Khan, "Associative polymers bearing n-alkyl hydrophobes: Rheological evidence for microgel-like behavior", *Journal of Rheology* **1999**, *43*, 1175–1194.
- [182] S. K. Venkataraman, H. H. Winter, "Finite shear strain behavior of a crosslinking polydimethylsiloxane near its gel point", *Rheologica Acta* **1990**, *29*, 423–432.
- [183] J. M. Dealy, K. F. Wissbrun, *Melt Rheology and its Role in Plastics Processing: Theory and Applications*. Van Nostrand Reinhold, New York, **1990**.

- [184] C. J. Dimitriou, R. H. Ewoldt, G. H. McKinley, “Describing and prescribing the constitutive response of yield stress fluids using large amplitude oscillatory shear stress (LAOStress)”, *Journal of Rheology* **2013**, *57*, 27.
- [185] N. Q. Dzuy, “Yield stress measurement for concentrated suspensions”, *Journal of Rheology* **1983**, *27*, 321–349.
- [186] M. H. Wagner, S. E. Stephenson, “The irreversibility assumption of network disentanglement in flowing polymer melts and its effects on elastic recoil predictions”, *Journal of Rheology* **1979**, *23*, 489–504.
- [187] R. B. Bird, “Useful non-Newtonian models”, *Annual Review of Fluid Mechanics* **1976**, *8*, 13–34.
- [188] *Handbook of Pressure Sensitive Adhesive Technology*, (Ed.: D. Satas), Van Nostrand Reinhold, New York, **1989**.
- [189] F. Deplace, C. Carelli, S. Mariot, H. Retsos, A. Chateauminois, K. Ouzineb, C. Creton, “Fine tuning the adhesive properties of a soft nanostructured adhesive with rheological measurements”, *The Journal of Adhesion* **2009**, *85*, 18–54.
- [190] R. Jovanović, M. A. Dubé, “Emulsion-based pressure-sensitive adhesives: a review”, *Journal of Macromolecular Science Part C: Polymer Reviews* **2004**, *44*, 1–51.
- [191] Z. Czech, “Polyacrylate-based water-soluble pressure-sensitive adhesives and their applications”, *European Adhesives and Sealants* **1995**, *2*, 4–10.
- [192] H. Lakrout, C. Creton, D. Ahn, K. R. Shull, “Influence of molecular features on the tackiness of acrylic polymer melts”, *Macromolecules* **2001**, *34*, 7448–7458.
- [193] A. Roos, C. Creton, M. B. Novikov, M. M. Feldstein, “Viscoelasticity and tack of poly(vinyl pyrrolidone)-poly(ethylene glycol) blends”, *Journal of Polymer Science Part B: Polymer Physics* **2002**, *40*, 2395–2409.
- [194] A. Zosel, “Adhesion and tack of polymers: Influence of mechanical properties and surface tensions”, *Colloid and Polymer Science* **1985**, *263*, 541–553.
- [195] P. Tordjeman, E. Papon, J.-J. Villenave, “Tack properties of pressure-sensitive adhesives”, *Journal of Polymer Science Part B: Polymer Physics* **2000**, *38*, 1201–1208.
- [196] C. Gay, “Stickiness—some fundamentals of adhesion.”, *Integrative and Comparative Biology* **2002**, *42*, 1123–6.

- [197] M. Tirumkudulu, W. B. Russel, T. J. Huang, "On the measurement of tack for adhesives", *Physics of Fluids* **2003**, *15*, 1588.
- [198] S. H. Spiegelberg, D. C. Ables, G. H. McKinley, "The role of end-effects on measurements of extensional viscosity in filament stretching rheometers", *Journal of Non-Newtonian Fluid Mechanics* **1996**, *64*, 229–267.
- [199] S. J. Lee, M. M. Denn, M. J. Crochet, A. B. Metzner, "Compressive flow between parallel disks: I. Newtonian fluid with a transverse viscosity gradient", *Journal of Non-Newtonian Fluid Mechanics* **1982**, *10*, 3–30.
- [200] J. M. Kramer, "Large deformations of viscoelastic squeeze films", *Applied Scientific Research* **1974**, *30*, 1–16.
- [201] G. Brindley, J. Davies, K. Walters, "Elastico-viscous squeeze films. Part I", *Journal of Non-Newtonian Fluid Mechanics* **1976**, *1*, 19–37.
- [202] M. A. McClelland, B. A. Finlayson, "Squeezing flow of elastic liquids", *Journal of Non-Newtonian Fluid Mechanics* **1983**, *13*, 181–201.
- [203] J. Engmann, C. Servais, A. S. Burbidge, "Squeeze flow theory and applications to rheometry: A review", *Journal of Non-Newtonian Fluid Mechanics* **2005**, *132*, 1–27.
- [204] J. Spanier, K. B. Oldham, *An Atlas of Functions*, Springer-Verlag, Berlin, **1987**.
- [205] C. M. Bender, S. A. Orszag, *Advanced mathematical methods for scientists and engineers I: Asymptotic methods and perturbation theory*, Springer, New York, **1999**, p. 261.
- [206] H. A. Baghdadi, J. Parrella, S. R. Bhatia, "Long-term aging effects on the rheology of neat laponite and laponite- λ -SPEO dispersions", *Rheologica Acta* **2007**, *47*, 349–357.
- [207] W. Sittikijyothin, D. Torres, M. Gonçalves, "Modelling the rheological behaviour of galactomannan aqueous solutions", *Carbohydrate Polymers* **2005**, *59*, 339–350.
- [208] J. L. Doublier, B. Launay, "Rheology of galactomannan solutions: comparative study of guar gum and locust bean gum", *Journal of Texture Studies* **1981**, *12*, 151–172.
- [209] A. Bourbon, A. Pinheiro, C. Ribeiro, C. Miranda, J. Maia, J. Teixeira, A. Vicente, "Characterization of galactomannans extracted from seeds of *Gleditsia triacanthos* and *Sophora japonica* through shear and extensional rheology: Comparison with guar gum and locust bean gum", *Food Hydrocolloids* **2010**, *24*, 184–192.

- [210] W. Kulicke, R. Porter, "Relation between steady shear flow and dynamic rheology", *Rheologica Acta* **1980**, *605*, 601–605.
- [211] V. Entov, E. Hinch, "Effect of a spectrum of relaxation times on the capillary thinning of a filament of elastic liquid", *Journal of Non-Newtonian Fluid Mechanics* **1997**, *72*, 31–53.
- [212] D. A. Gibbs, E. W. Merrill, K. A. Smith, E. A. Balazs, "Rheology of hyaluronic acid", *Biopolymers* **1968**, *6*, 777–91.
- [213] A. O. Bingöl, D. Lohmann, K. Püschel, W.-M. Kulicke, "Characterization and comparison of shear and extensional flow of sodium hyaluronate and human synovial fluid.", *Biorheology* **2010**, *47*, 205–224.
- [214] *Biochemistry of plant cell walls*, (Eds.: J. R. Hillman, C. T. Brett), Vol. 70, CUP Archive, **1985**.
- [215] N. C. Carpita, D. M. Gibeaut, "Structural models of primary cell walls in flowering plants: consistency of molecular structure with the physical properties of the walls during growth.", *The Plant Journal : For Cell and Molecular Biology* **1993**, *3*, 1–30.
- [216] M. Rinaudo, "Chitin and chitosan: Properties and applications", *Progress in Polymer Science* **2006**, *31*, 603–632.
- [217] B. Weissmann, K. Meyer, "The structure of hyalobiuronic acid and of hyaluronic acid from umbilical cord", *Journal of the American Chemical Society* **1954**, *76*, 1753–1757.
- [218] *Food Polysaccharides and Their Applications*. (Eds.: A. M. Stephen, G. O. Phillips), CRC Press, **2010**.
- [219] H. W. Ducklow, R. Mitchell, "Composition of mucus released by coral reef coelenterates", *Limnology and Oceanography* **1979**, *24*, 706–714.
- [220] L. Gaume, Y. Forterre, "A viscoelastic deadly fluid in carnivorous pitcher plants.", *PloS One* **2007**, *2*, e1185.
- [221] J. Kost, S. Shefer, "Chemically-modified polysaccharides for enzymatically-controlled oral drug delivery", *Biomaterials* **1990**, *11*, 695–698.
- [222] C. D. Melia, "Hydrophilic matrix sustained release systems based on polysaccharide carriers.", *Critical Reviews in Therapeutic Drug Carrier Systems* **1991**, *8*, 395.

- [223] J. F. Morton, "Mucilaginous plants and their uses in medicine", *Journal of Ethnopharmacology* **1990**, *29*, 245–266.
- [224] G. R. Gibson, S. Macfarlane, J. H. Cummings, "The fermentability of polysaccharides by mixed human faecal bacteria in relation to their suitability as bulk-forming laxatives", *Letters in Applied Microbiology* **1990**, *11*, 251–254.
- [225] *Food Stabilizers, Thickeners and Gelling Agents*, (Ed.: A. Imeson), Wiley-Blackwell, Singapore, **2010**.
- [226] I. H. Smith, G. W. Pace, "Recovery of microbial polysaccharides", *Journal of Chemical Technology and Biotechnology* **1982**, *32*, 119–129.
- [227] M. R. Mackley, C. Tock, R. Anthony, S. a. Butler, G. Chapman, D. C. Vadillo, "The rheology and processing behavior of starch and gum-based dysphagia thickeners", *Journal of Rheology* **2013**, *57*, 1533.
- [228] M. Eleya, S. Gunasekaran, "Rheology of barium sulfate suspensions and pre-thickened beverages used in diagnosis and treatment of dysphagia", *Applied Rheology* **2007**, *17*, 33137.
- [229] D. M. Jones, K. Walters, P. R. Williams, "On the extensional viscosity of mobile polymer solutions", *Rheologica Acta* **1987**, *26*, 20–30.
- [230] M. F. Piteira, J. M. Maia, A. Raymundo, I. Sousa, "Extensional flow behaviour of natural fibre-filled dough and its relationship with structure and properties", *Journal of Non-Newtonian Fluid Mechanics* **2006**, *137*, 72–80.
- [231] S. L. Anna, G. H. McKinley, "Elasto-capillary thinning and breakup of model elastic liquids", *Journal of Rheology* **2001**, *45*, 115.
- [232] S. McQueen-Mason, D. J. Cosgrove, "Disruption of hydrogen bonding between plant cell wall polymers by proteins that induce wall extension.", *Proceedings of the National Academy of Sciences of the United States of America* **1994**, *91*, 6574–6578.
- [233] G. H. McKinley, A. Tripathi, "How to extract the Newtonian viscosity from capillary breakup measurements in a filament rheometer", *Journal of Rheology* **2000**, *44*, 653–670.
- [234] B. L. Hager, G. C. Berry, "Moderately Concentrated Solutions of Polystyrene I. Viscosity as a Function of concentration, Temperature, and Molecular Weight", *Journal of Polymer Science: Polymer Physics Edition* **1982**, *20*, 911–928.

- [235] E. R. Morris, A. N. Cutler, S. Ross-Murphy, D. A. Rees, J. Price, "Concentration and shear rate dependence of viscosity in random coil polysaccharide solutions", *Carbohydrate Polymers* **1981**, *1*, 5–21.
- [236] T. E. Newlin, S. E. Lovell, P. R. Saunders, J. D. Ferry, "Long-range intermolecular coupling in concentrated poly-n-butyl methacrylate solutions and its dependence on temperature and concentration", *Journal of Colloid Science* **1962**, *17*, 10–25.
- [237] J. W. van Egmond, "Shear-thickening in suspensions, associating polymers, worm-like micelles, and poor polymer solutions", *Current Opinion in Colloid & Interface Science* **1998**, *3*, 385–390.
- [238] A.-L. Kjøniksen, M. Hiorth, B. Nyström, "Association under shear flow in aqueous solutions of pectin", *European Polymer Journal* **2005**, *41*, 761–770.
- [239] T. A. Witten, M. H. Cohen, "Cross-Linking in Shear-Thickening Ionomers", *Macromolecules* **1985**, *18*, 1915–1918.
- [240] K. Kurita, "Chitin and chitosan: functional biopolymers from marine crustaceans.", *Marine Biotechnology* **2006**, *8*, 203–226.
- [241] A. E. Mirsky, L. Pauling, "On the structure of native, denatured, and coagulated proteins", *Proceedings of the National Academy of Sciences* **1936**, *22*, 439–447.
- [242] S. J. Haward, V. Sharma, C. P. Butts, G. H. McKinley, S. S. Rahatekar, "Shear and extensional rheology of cellulose/ionic liquid solutions.", *Biomacromolecules* **2012**, *13*, 1688–99.
- [243] P. Erni, M. Varagnat, C. Clasen, J. Crest, G. H. McKinley, "Microrheometry of sub-nanolitre biopolymer samples: non-Newtonian flow phenomena of carnivorous plant mucilage", *Soft Matter* **2011**, *7*, 10889.
- [244] R. De Dier, W. Mathues, C. Clasen, "Extensional flow and relaxation of semi-dilute solutions of schizophyllan", *Macromolecular Materials and Engineering* **2013**, *298*, 944–953.
- [245] M. A. Nicosia, J. A. Robbins, "The fluid mechanics of bolus ejection from the oral cavity.", *Journal of Biomechanics* **2001**, *34*, 1537–1544.
- [246] M. R. Duxenneuner, P. Fischer, E. J. Windhab, J. J. Cooper-White, "Extensional properties of hydroxypropyl ether guar gum solutions.", *Biomacromolecules* **2008**, *9*, 2989–2996.

- [247] A. Tripathi, K. C. Tam, G. H. McKinley, "Rheology and dynamics of associative polymers in shear and extension: theory and experiments", *Macromolecules* **2006**, *39*, 1981–1999.
- [248] S. T. J. Peng, R. F. Landel, "Rheological behavior of progressively shear-thickening solutions", *Journal of Applied Physics* **1981**, *52*, 5988.
- [249] L. Leibler, M. Rubinstein, R. H. Colby, "Dynamics of reversible networks", *Macromolecules* **1991**, *24*, 4701–4707.
- [250] L. D. L. Freitas, R. Stadler, "Thermoplastic elastomers by hydrogen bonding. 3. Interrelations between molecular parameters and rheological properties", *Macromolecules* **1987**, *24*, 2478–2485.
- [251] F. Tanaka, S. Edwards, "Viscoelastic properties of physically crosslinked networks", *Journal of Non-Newtonian Fluid Mechanics* **1992**, *43*, 247–271.
- [252] R. F. Greene, C. N. Pace, "Urea and Guanidine Hydrochloride denaturation of ribonuclease, Lysozyme, α -Chymotrypsin, and β -Lactoglobulin", *Journal of Biological Chemistry* **1974**, *249*, 5388–5393.
- [253] J. K. Myers, C. N. Pace, J. M. Scholtz, "Denaturant m values and heat capacity changes: relation to changes in accessible surface areas of protein unfolding.", *Protein Science* **1995**, *4*, 2138–48.
- [254] A. Matouschek, J. T. Kellis, L. Serrano, A. R. Fersht, "Mapping the transition state and pathway of protein folding by protein engineering", *Nature* **1989**, *340*, 122–126.
- [255] L. S. Zamorano, D. G. Pina, J. B. Arellano, S. A. Bursakov, A. P. Zhadan, J. J. Calvete, L. Sanz, P. R. Nielsen, E. Villar, O. Gavel, M. G. Roig, L. Watanabe, I. Polikarpov, V. L. Shnyrov, "Thermodynamic characterization of the palm tree *Roystonea regia* peroxidase stability.", *Biochimie* **2008**, *90*, 1737–49.
- [256] L. M. Mayr, F. X. Schmid, "Stabilization of a protein by guanidinium chloride.", *Biochemistry* **1993**, *32*, 7994–8.
- [257] J. D. Ferry, *Viscoelastic Properties of Polymers*, John Wiley & Sons, **1980**.
- [258] C. N. Pace, D. V. Laurents, J. A. Thomson, "pH dependence of the urea and guanidine hydrochloride denaturation of ribonuclease A and ribonuclease T1.", *Biochemistry* **1990**, *29*, 2564–72.

- [259] C. N. Pace, D. V. Laurents, R. E. Erickson, "Urea denaturation of barnase: pH dependence and characterization of the unfolded state.", *Biochemistry* **1992**, *31*, 2728–34.
- [260] E. Miller, C. Clasen, J. P. Rothstein, "The effect of step-stretch parameters on capillary breakup extensional rheology (CaBER) measurements", *Rheologica Acta* **2009**, *48*, 625–639.
- [261] J. M. Guss, D. W. Hukins, P. J. Smith, W. T. Winter, S. Arnott, "Hyaluronic acid: molecular conformations and interactions in two sodium salts", *Journal of Molecular Biology* **1975**, *95*, 359–84.
- [262] B. Decker, B. F. McKenzie, W. F. McGuckin, C. H. Slocumb, "Comparative distribution of proteins and glycoproteins of serum and synovial fluid.", *Arthritis and Rheumatism* **1959**, *2*, 162–77.
- [263] E. A. Balazs, D. Watson, I. F. Duff, S. Roseman, "Hyaluronic acid in synovial fluid. I. Molecular parameters of hyaluronic acid in normal and arthritic human fluids", *Arthritis and Rheumatism* **1967**, *10*, 357–376.
- [264] A. J. Bollet, "The intrinsic viscosity of synovial fluid hyaluronic acid", *The Journal of Laboratory and Clinical Medicine* **1956**, *48*, 721–728.
- [265] L. B. Dahl, I. M. Dahl, A. Engström-Laurent, K. Granath, "Concentration and molecular weight of sodium hyaluronate in synovial fluid from patients with rheumatoid arthritis and other arthropathies", *Annals of the Rheumatic Diseases* **1985**, *44*, 817–22.
- [266] R. S. Namba, S. Shuster, P. Tucker, R. Stern, "Localization of hyaluronan in pseudocapsule from total hip arthroplasty", *Clinical Orthopaedics and Related Research* **1999**, *363*, 158–162.
- [267] D. Mazzucco, G. H. McKinley, R. D. Scott, M. Spector, "Rheology of joint fluid in total knee arthroplasty patients.", *Journal of Orthopaedic Research* **2002**, *20*, 1157–63.
- [268] D. V. Davies, A. J. Palfrey, "Some of the physical properties of normal and pathological synovial fluids", *Journal of Biomechanics* **1968**, *1*, 79–88.
- [269] S. Al-Assaf, J. Meadows, G. Phillips, P. Williams, "The application of shear and extensional viscosity measurements to assess the potential of hylan in viscosupplementation", *Biorheology* **1996**, *33*, 319–332.

- [270] C. Backus, S. P. Carrington, L. R. Fisher, J. A. Odell, D. A. Rodrigues, *Hyaluronan Volume I: Chemical Biochemical and Biological Aspects*, (Eds.: J. F. Kennedy, G. O. Phillips, P. A. Williams, V. C. Hascall), Woodhead Publishing Ltd, Cambridge, 2002, pp. 209–218.
- [271] P. J. Leider, R. B. Bird, “Squeezing flow between parallel disks. I. Theoretical analysis”, *Industrial & Engineering Chemistry Fundamentals* 1974, 13, 336–341.
- [272] P. G. De Gennes, “Coil-stretch transition of dilute flexible polymers under ultra-high velocity gradients”, *Journal of Chemical Physics* 1974, 60, 5030–5042.
- [273] T. T. Perkins, D. E. Smith, S. Chu, “Single polymer dynamics in an elongational flow”, *Science* 1997, 276, 2016–2021.
- [274] D. E. Smith, H. P. Babcock, S. Chu, “Single polymer dynamics in steady shear flow”, *Science* 1999, 283, 1724–1727.
- [275] J. A. Odell, S. P. Carrington, “Extensional flow oscillatory rheometry”, *Journal of Non-Newtonian Fluid Mechanics* 2006, 137, 110–120.
- [276] Y. Mochimaru, “Fast squeezing flow of viscoelastic fluids”, *Journal of Non-Newtonian Fluid Mechanics* 1987, 9, 157–178.
- [277] S. Chatraei, “Lubricated Squeezing Flow: A New Biaxial Extensional Rheometer”, *Journal of Rheology* 1981, 25, 433.
- [278] D. C. Venerus, T. Y. Shiu, T. Kashyap, J. Hostteler, “Continuous lubricated squeezing flow: A novel technique for equibiaxial elongational viscosity measurements on polymer melts”, *Journal of Rheology* 2010, 54, 1083–1095.
- [279] J. S. Hou, V. C. Mow, W. M. Lai, M. H. Holmes, “An analysis of the squeeze-film lubrication mechanism for articular cartilage.”, *Journal of Biomechanics* 1992, 25, 247–59.
- [280] D. F. James, G. M. Fick, W. D. Baines, “A mechanism to explain physiological lubrication.”, *Journal of Biomechanical Engineering* 2010, 132, 071002.
- [281] C. W. McCutchen, “Mechanism of animal joints: sponge-hydrostatic and weeping bearings”, *Nature* 1959, 184.
- [282] P. R. Lewis, C. W. McCutchen, “Mechanism of animal joints: experimental evidence for weeping lubrication in mammalian joints”, *Nature* 1959, 184.

- [283] K. C. Morell, W. A. Hodge, D. E. Kerbs, R. W. Mann, "Corroboration of in vivo cartilage pressures with implications for synovial joint tribology and osteoarthritis causation", *Proceedings of the National Academy of Sciences* **2005**, 102.
- [284] G. D. Jay, D. A. Harris, C.-J. Cha., "Boundary lubrication by lubricin is mediated by O-linked β (1-3) Gal-GalNAc oligosaccharides", *Glycoconjugate journal* **2001**, 18, 807–815.
- [285] J. Schurz, V. Ribitsch, "Rheology of synovial fluid", *Biorheology* **1987**, 24, 385–399.
- [286] A. J. Müller, J. A. Odell, A. Keller, "Elongational flow and rheology of monodisperse polymers in solution", *Journal of Non-Newtonian Fluid Mechanics* **1988**, 30, 99–118.
- [287] V. Tirtaatmadja, T. Sridhar, "A filament stretching device for measurement of extensional viscosity", *Journal of Rheology* **1993**, 37, 1081–1102.
- [288] C. J. S. Petrie, "One hundred years of extensional flow", *Journal of Non-Newtonian Fluid Mechanics* **2006**, 137, 1–14.
- [289] B. M. Praest, H. Greiling, R. Kock, "Assay of synovial fluid parameters: hyaluronan concentration as a potential marker for joint diseases", *Clinica Chimica Acta* **1997**, 266, 117–128.
- [290] M. G. Levine, D. H. Kling, "Rheologic studies on synovial fluid", *Journal of Clinical Investigation* **1956**, 35, 1419.
- [291] E. Fletcher, J. H. Jacobs, R. L. Markham, "Viscosity studies on hyaluronic acid of synovial fluid in rheumatoid arthritis and osteoarthritis", *Clinical Science* **1955**, 14, 653–660.
- [292] S. J. Falcone, D. M. Palmeri, R. A. Berg, "Rheological and cohesive properties of hyaluronic acid", *Journal of Biomedical Materials Research Part A* **2006**, 76, 721–728.
- [293] K. D. Brandt, J. A. Block, J. P. Michalski, L. W. Moreland, J. R. Caldwell, P. T. Lavin, "Efficacy and safety of intraarticular sodium hyaluronate in knee osteoarthritis", *Clinical Orthopaedics and Related Research* **2001**, 385, 130–143.
- [294] E. Fouissac, M. Milas, M. Rinaudo, "Shear-rate, concentration, molecular weight, and temperature viscosity dependences of hyaluronate, a wormlike polyelectrolyte", *Macromolecules* **1993**, 26, 6945–6951.

- [295] W. E. Krause, E. G. Bellomo, R. H. Colby, "Rheology of sodium hyaluronate under physiological conditions", *Biomacromolecules* **2001**, *2*, 65–69.
- [296] F. Meyer, D. Lohmann, W. M. Kulicke, "Determination of the viscoelastic behavior of sodium hyaluronate in phosphate buffered saline with rheo-mechanical and rheo-optical methods", *Journal of Rheology* **2009**, *53*, 799–818.
- [297] H. Fam, M. Kontopoulou, J. T. Bryant, "Effect of concentration and molecular weight on the rheology of hyaluronic acid/bovine calf serum solutions", *Biorheology* **2009**, *46*, 31–43.
- [298] Y. Mo, K. Nishinari, "Rheology of hyaluronan solutions under extensional flow", *Biorheology* **2001**, *38*, 379–387.
- [299] K. M. N. Oates, W. E. Krause, R. L. Jones, R. H. Colby, "Rheopexy of synovial fluid and protein aggregation.", *Journal of the Royal Society Interface* **2006**, *3*, 167–74.
- [300] O. Regev, S. Vandebril, E. Zussman, C. Clasen, "The role of interfacial viscoelasticity in the stabilization of an electrospun jet", *Polymer* **2010**, *51*, 2611–2620.
- [301] M. Oliveira, F. Pinho, R. Poole, P. Oliveira, M. Alves, "Purely elastic flow asymmetries in flow-focusing devices", *Journal of Non-Newtonian Fluid Mechanics* **2009**, *160*, 31–39.
- [302] H. M. Laun, M. Rady, O. Hassager, "Analytical solutions for squeeze flow with partial wall slip", *Journal of Non-Newtonian Fluid Mechanics* **1999**, *81*, 1–15.
- [303] R. Mendichi, L. Šoltés, A. Giacometti Schieroni, "Evaluation of radius of gyration and intrinsic viscosity molar mass dependence and stiffness of hyaluronan", *Biomacromolecules* **2003**, *4*, 1805–1810.
- [304] C. J. Pipe, T. S. Majmudar, G. H. McKinley, "High shear rate viscometry", *Rheologica Acta* **2008**, *47*, 621–642.
- [305] K. M. N. Oates, W. E. Krause, R. H. Colby in Materials Research Society Symposium Proceedings, Warrendale, Pa., **2002**, pp. 53–58.
- [306] H. R. Kerr, B. Warburton, "Surface rheological properties of hyaluronic acid solutions", *Biorheology* **1985**, *22*, 133–144.
- [307] M. A. Alves in The XVth International Congress on Rheology, The Society of Rheology 80th Annual Meeting, *Vol. 8*, **2008**, pp. 240–242.

- [308] M. Shribak, R. Oldenbourg, “Techniques for fast and sensitive measurements of two-dimensional birefringence distributions”, *Applied Optics* **2003**, *42*, 3009–3017.
- [309] X. Trepas, G. Lenormand, J. J. Fredberg, “Universality in cell mechanics”, *Soft Matter* **2008**, *4*, 1750.
- [310] T. Kim, W. Hwang, H. Lee, R. D. Kamm, “Computational analysis of viscoelastic properties of crosslinked actin networks.”, *PLoS computational biology* **2009**, *5*, e1000439.
- [311] B. Fabry, G. Maksym, J. Butler, M. Glogauer, D. Navajas, J. Fredberg, “Scaling the Microrheology of Living Cells”, *Physical Review Letters* **2001**, *87*, 148102.
- [312] G. Lenormand, E. Millet, B. Fabry, J. P. Butler, J. J. Fredberg, “Linearity and time-scale invariance of the creep function in living cells.”, *Journal of the Royal Society Interface* **2004**, *1*, 91–97.
- [313] K. Kroy, J. Glaser, “The glassy wormlike chain”, *New Journal of Physics* **2007**, *9*, 416.
- [314] K. Kroy, “Dynamics of wormlike and glassy wormlike chains”, *Soft Matter* **2008**, *4*, 2323.
- [315] C. Broedersz, F MacKintosh, “Modeling semiflexible polymer networks”, *arXiv preprint arXiv:1404.4332* **2014**, 1–46.
- [316] R. L. Bagley, P. J. Torvik, “On the fractional calculus model of viscoelastic behavior”, *Journal of Rheology* **1986**, *30*, 133–155.
- [317] C.-M. Ho, Y.-C. Tai, “Micro-Electro-Mechanical-Systems (MEMS) and fluid flows”, *Annual Review of Fluid Mechanics* **1998**, *30*, 579–612.
- [318] Y. Joo, K. Dieu, C.-J. Kim, “Fabrication of monolithic microchannels for IC chip cooling”, *Proc. IEEE* **1995**, *6*, 362–367.
- [319] W. E. Newell, “Miniaturization of tuning forks.”, *Science* **1968**, *161*, 1320–1326.
- [320] C. T. C. Nguyen in Proceedings of the 1995 IEEE International Ultrasonics Symposium, Seattle, WA, **1995**, pp. 489–499.
- [321] S. C. Terry, J. H. Jerman, J. B. Angell, “A Gas chromatographic air analyzer fabricated on a silicon wafer”, *IEEE Transactions on Electron Devices* **1979**, *26*, 1880–1886.

- [322] R. B. Bird, W. E. Stewart, E. N. Lightfoot, *Transport Phenomena*, John Wiley & Sons, Inc., New York, 1960.
- [323] J. C. Maxwell, "On stresses in rarified gases arising from inequalities of temperature", *Philosophical Transactions of the Royal Society* 1879, 170, 231–256.
- [324] J. C. Harley, Y. Huang, H. H. Bau, J. N. Zemel, "Gas flow in micro-channels", *Journal of Fluid Mechanics* 2006, 284, 257–274.
- [325] J. Liu, Y.-C. Tai, C.-M. Ho in IEEE International Conference on Micro Electro Mechanical Systems. Amsterdam, Netherlands, 1995, pp. 209–215.
- [326] R. B. Bird, "Five decades of transport phenomena", *AIChE Journal* 2004, 50, 273–287.
- [327] S. G. Kandlikar, S. Garimella, D. Li, S. Colin, M. R. King, *Heat Transfer and Fluid Flow in Minichannels and Microchannels*, Elsevier, Oxford, 2006.
- [328] N. G. Hadjiconstantinou, "The limits of Navier–Stokes theory and kinetic extensions for describing small-scale gaseous hydrodynamics", *Physics of Fluids* 2006, 18, 111301.
- [329] N. Dongari, A. Sharma, F. Durst, "Pressure-driven diffusive gas flows in micro-channels: from the Knudsen to the continuum regimes", *Microfluidics and Nanofluidics* 2009, 6, 679–692.
- [330] N. G. Hadjiconstantinou, "Comment on Cercignani's second-order slip coefficient", *Physics of Fluids* 2003, 15, 2352.
- [331] S. K. Prabha, S. P. Sathian, "Calculation of thermo-physical properties of Poiseuille flow in a nano-channel", *International Journal of Heat and Mass Transfer* 2013, 58, 217–223.
- [332] W. M. Zhang, G. Meng, X. Wei, "A review on slip models for gas microflows", *Microfluidics and Nanofluidics* 2012, 13, 845–882.
- [333] R. Sambasivam, "Extended Navier–Stokes Equations : Derivations and Applications to Fluid Flow Problems", *Ph.D Thesis Universitat Erlangen-Nurnberg* 2013.
- [334] H. Brenner, "Navier–Stokes revisited", *Physica A: Statistical Mechanics and its Applications* 2005, 349, 60–132.

- [335] S. Chakraborty, F. Durst, "Derivations of extended Navier–Stokes equations from upscaled molecular transport considerations for compressible ideal gas flows: Towards extended constitutive forms", *Physics of Fluids* **2007**, *19*, 088104.
- [336] F. Durst, J. Gomes, R. Sambasivam in Proceeding of the international symposium on turbulence, heat and mass transfer, Dubrovnik, **2006**, pp. 25–29.
- [337] T. Adachi, R. Sambasivam, F. Durst, D. Filimonov in 3rd Micro and Nano Flows Conference, Thessaloniki, Greece, **2011**, pp. 1–10.
- [338] J. O. Hirschfelder, C. F. Curtiss, R. B. Bird, *Molecular Theory of Gases and Liquids*, John Wiley & Sons, Inc., New York, **1954**.
- [339] J. C. Slattery, R. B. Bird, "Calculation of the diffusion coefficient of dilute gases and of the self-diffusion coefficient of dense gases", *AIChE Journal* **1958**, *4*, 137–142.
- [340] R. Sambasivam, S. Chakraborty, F. Durst, "Numerical predictions of backward-facing step flows in microchannels using extended Navier–Stokes equations", *Microfluidics and Nanofluidics* **2013**, DOI 10.1007/s10404-013-1254-1.
- [341] S. R. Valluri, D. J. Jeffrey, R. M. Corless, "Some applications of the Lambert W function to physics", *Canadian Journal of Physics* **2000**, *78*, 823–831.
- [342] R. M. Corless, G. H. Gonnet, D. E. G. Hare, D. J. Jeffrey, D. E. Knuth, "On the Lambert W function", *Advances in Computational Mathematics* **1996**, *5*, 329–359.
- [343] J. Maurer, P. Tabeling, P. Joseph, H. Willaime, "Second-order slip laws in microchannels for helium and nitrogen", *Physics of Fluids* **2003**, *15*, 2613.
- [344] E. G. Taliadorou, M. Neophytou, G. C. Georgiou, "Perturbation solutions of Poiseuille flows of weakly compressible Newtonian liquids", *Journal of Non-Newtonian Fluid Mechanics* **2009**, *163*, 25–34.
- [345] D. C. Venerus, D. J. Bugajsky, "Compressible laminar flow in a channel", *Physics of Fluids* **2010**, *22*, 046101.
- [346] F.-H. Qin, D.-J. Sun, X.-Y. Yin, "Perturbation analysis on gas flow in a straight microchannel", *Physics of Fluids* **2007**, *19*, 027103.
- [347] E. Arkilic, M. Schmidt, K. Breuer, "Gaseous slip flow in long microchannels", *Journal of Microelectromechanical Systems* **1997**, *6*, 167–178.
- [348] J. Pfahler, J. Harley, H. Bau, J. N. Zemel, "Gas and liquid flow in small channels.", *ASME Dynamic Systems and Controls Conference* **1991**, *32*, 49–60.